UNIVERSITAT DE BARCELONA

Advanced TEM imaging tools for Materials Science

Lluís López Conesa

Advanced TEM imaging tools for Materials Science

Lluís López Conesa

Tesi presentada per optar al títol de
Doctor per la Universitat de Barcelona
en el marc del programa de Doctorat en Nanociències

Directores de la tesi:
Dr. Francesca Peiró Martínez
Dr. Sònia Estradé Albiol

LENS-MIND-IN^{2}UB

Dr. Francesca Peiró Martínez,
Professor Titular del Departament d'Electrònica
Dr. Sònia Estradé Albiol,
Professor Lector del Departament d'Electrònica

certifiquen que la tesi "Advanced TEM imaging tools for Materials Science", que presenta Lluís López Conesa per optar al títol de Doctor per la Universitat de Barcelona en el marc del Programa de Doctorat en Nanociències, ha estat realitzada sota la seva direcció.

A Barcelona, 20 d'octubre de 2015

Les directores:

Dr. Francesca Peiró Martínez

Dr. Sònia Estradé Albiol

La tutora:

Dr. Francesca Peiró Martinez

Tribunal:

President: Dr. Virginie Serin
Centre d'Elaboration de Matériaux et d'Etudes Structurales
CEMES-CNRS, Toulouse (France)

Secretari: Dr. Joaquim Portillo Serra
CCiT-UB and Nanomegas SL.

Vocal: Dr. José A. Pérez Omil
Universidad de Cádiz

Membres suplents:

Dr. Jordi Llorca, Universitat Politècnica de Catalunya

Dr. Lluís Yedra Cardona, Luxembourg Institute of Science and Technology

Dr. Sergi Hernández, Universitat de Barcelona

Contents

Chapter 1

Introduction

1.1 Historical overview of TEM

1.1.1 Resolution

Microscopes have been used since the late 16th century in order to extend the resolution limit of the human eye. For most of this time, the illumination source used to obtain images was only visible light. But, in the early 20th century, the development of quantum mechanics, and, in particular, the wave-particle duality proposed by De Broglie (1925) [1], ultimately resulted in the development of an electron microscope by Ruska and Knoll (1931) [2][3].

Since the Rayleigh criterion for the resolution of two punctual objects involves the wavelength of the illumination source, using highly accelerated electrons opened a resolution range which is forbidden to visible light microscopy. Whereas for the shortest range of the visible light spectrum the wavelength is $\lambda = 400nm$, for electrons accelerated at $100keV$ it is $\lambda = 4pm$. Using the magnetic field created by the current running through a copper coil as an electromagnetic lens to focus the electron beam coming from a thermoionic source, Ruska and Knoll built the first Transmission Electron Microscope (TEM) in 1931. The achieved resolution (in the hundreds of nm) was not diffraction-limited by the electron wavelength, but by the quality of the electron optics. Only two years after that, the TEM had surpassed the resolution achievable by the visible light microscope.

Over time, the combination of technical improvements in electron optics and the use of higher accelerating voltages resulted in an ever increasing resolution in the TEM. Contrast fringes that could be related directly to the projected crystal potential were reported by Allpress et al. in 1969 [4]. TEM has been since a capital technique in the study of the structure of materials, being the only real space imaging technique of crystal structures and defects. Following the same basic layout of the Ruska and Knoll design, a major breakthrough was achieved in 1970 by Crewe with the development of the scanning mode of the TEM (STEM) [5]. In STEM, a narrow probe is formed by demagnifying the electron source on top of the specimen. This probe is then scanned across the specimen using the deflection coils. The detector picks up the signal coming from the interaction of the electron beam with a highly localized region of the sample. Following the reciprocity theorem stated by Cowley in 1969 [6], the STEM can be understood as a TEM with an interchanged source and detector. This mode is particularly suited to carry out spectroscopic analyses, obtaining chemical information at the very high spatial resolution that the instrument offers.

1.1.2 Spectroscopy

Together with the STEM mode, the development of the Field Emission Gun (FEG), also in the early 1970s, was a major breakthrough in the spectroscopic techniques related to the TEM. Their combination allowed to obtain a narrow, very bright probe that can be accurately placed on the sample to obtain chemical signals with a sufficient signal to noise ratio in reasonable acquisition times. Two main spectroscopies are carried out in the TEM that allow a quantitative analysis of chemical composition: X ray Energy Dispersive Spectroscopy (EDS) and Electron Energy Loss Spectroscopy (EELS).

EDS analyzes the energies of the characteristic X rays generated when the atoms in the sample return to their ground state after being ionized by the electron beam. Since each element presents its unique range of characteristic ionization energies, elemental identification is straightforward. Given that specimens suitable for TEM are particularly thin, X ray absorption and

fluorescence effects can be neglected and the relative atomic composition can be determined from ionization peak ratios, following the so-called Cliff-Lorimer technique [7][8].

EELS analyzes the energy loss distribution of electrons that have traveled through the sample. Different types of interactions of the impinging electron beam and the atoms of the sample give rise to different regions of the EEL spectrum. Most of the electrons come out of the sample without any detectable energy loss, and contribute to the so-called Zero Loss Peak (ZLP), which is, by a few orders of magnitude, the most intense feature in the EEL spectrum. Next in energy loss appears the low-loss region (5 eV to 100 eV). This corresponds to the interaction of electrons in the beam with valence band electrons in the material. The main feature in this region is the plasmon peak. Since the plasmon energy (plasma frequency) is characteristic for each compound, chemical identification can be obtained. In addition, information on optoelectronic properties of the material (band gap, complex dielectric function, interband and intraband transitions, etc.) can be extracted from the analysis of the energy loss distribution in this region. Also, the intensity ratio between the ZLP and the low-loss region can be used to determine the sample thickness. From 100 eV on, we find the core-loss region, corresponding to the interaction of electrons in the beam with core level electrons from atoms in the sample. Ionization edges are found at characteristic energy losses for each element; thus, elemental identification is straightforward. Quantitative composition determination is a more challenging task, but can also be achieved. The detailed methodology is described in Egerton reference book in the field [9]. From the analysis of the core-loss fine structure (Energy Loss Near Edge Structure, ELNES), quantitative information can also be obtained about the oxidation or bonding state of the atoms.

1.1.3 Aberration correction

Scherzer proved theoretically back in 1936 that rotationally symmetric electromagnetic lenses could not be designed free of aberrations [10]. Thus, a limit for the increase in resolution was expected for TEM. As a method to overcome this limitation, Scherzer himself proposed configurations for spherical aberration

correctors in 1947 [11]. The technical challenge of their practical implementation becomes clear considering that the first demonstrated resolution improvement through the use of an aberration corrector in a TEM was achieved 50 years later, in 1997, by Haider and Rose [12]. Figure 1.1 shows the evolution over time of visible light and electron microscopy, with a closer look at the recent improvements of TEM resolution. The range of length scales that has been opened to real space imaging in a very short period of time is remarkable.

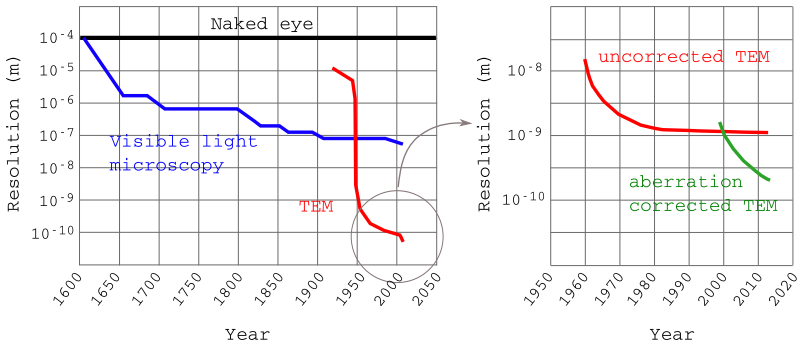

Figure 1.1 Evolution over time of the resolution achievable with the naked eye, a visible light microscope and a transmission electron microscope. The saturation reached for visible light microscopy corresponds to the diffraction limit given by wavelength. For TEM, technical improvements such as aberration correctors (close-up in the right-hand side panel) are still pushing the resolution limit towards the diffraction limit.

Aberration correction is performed in electron optics in a different way than in visible light optics, since it is not possible to implement divergent electromagnetic lenses. The procedure consists, then, in measuring the aberrations present in a given configuration of the optical system and introducing opposite sign aberrations by using non-rotationally symmetric electromagnetic elements. Details on the characterization and correction of aberrations are described in Appendix A.

The use of aberration correction opened a new range of resolution both in TEM and STEM imaging and in spectroscopy, as well as allowing the use of lower voltages without loss of resolution. This results in a greater number of beam sensitive materials becoming suitable for observation. State of the art instrumentation

is still improving mainly through aberration corrector technology. Pushing resolution to the present limits imposes more demanding conditions to environmental variables, such as room temperature stability or mechanical isolation of the microscope, which need to improve accordingly in order to avoid wasting the effects of the correction.

1.2 Contrast in the TEM

In linear optics terms, what a transmission microscope does is transforming each point in the specimen into another object (a spread disk) in the final image. Defining the object as $f(\vec{r})$ and the final image as $g(\vec{r})$, the latter can be defined as the convolution of the object transmission function with a point-spread function $h(r)$ that represents the role of the microscope

$$g(\vec{r}) = \int f(\vec{r'})h(\vec{r} - \vec{r'})d\vec{r'} = f(\vec{r}) \otimes h(\vec{r}) \tag{1.1}$$

A general definition of the object transmission function would be

$$f(x, y) = A(x, y) \cdot e^{-i\Phi_t(x,y)} \tag{1.2}$$

with an amplitude $A(x, y)$ and a phase $\Phi_t(x, y)$. The modulation of the electron beam transmitted through the sample can, thus, occur both in the amplitude and in the phase of the electron wave.

1.2.1 Amplitude contrast

Let us first consider the effect on the amplitude of the electron wave of the scattering by the sample. Amplitude contrast manifests itself in two different forms: mass-thickness contrast and diffraction contrast. Variations of mass and/or thickness of the specimen in conventional, parallel beam TEM give a contrast that can be understood in a similar way as absorption in visible light transmission microscopy. The role of optical absorption would be played in the TEM by the loss of intensity by scattering of the electrons, the process being governed by the Rutherford cross section for scattering by atomic nuclei. Diffraction contrast images

use electrons coherently scattered at different Bragg conditions to obtain images with particular structural information on the specimen.

Mass contrast

Mass-thickness contrast can be described through the Rutherford scattering cross section

$$\sigma_R = 1.62 \times 10^{-24} \left(\frac{Z}{E_0}\right)^2 cot^2\left(\frac{\theta}{2}\right) \tag{1.3}$$

for electrons elastically scattered by nuclei into angles $> \theta$, considering screening of nuclei charge by deep level electrons charge and relativistic corrections. The other dependencies are on the atomic number Z and the energy of incoming electrons E_0, determined by the accelerating voltage. From this cross section, one can see that scattering is strongly forward peaked. However, any quantitative information will come from the small fraction of electrons scattered at large angles, i.e., angles greater than those of Bragg scattering so diffraction contrast will not contribute to the image.

STEM High Angle Annular Dark Field (HAADF) images contain information on the mass-thickness of the specimen, reaching even atomic level resolution. By focusing the electron beam on a small enough probe and collecting the scattered electrons on an annular detector with a sufficiently large hole to avoid Bragg electrons ($> 3^o$), the resulting intensity will depend only on Z and on the thickness of the specimen, t. If the thickness is constant, or changes in a way that can be determined, images can be interpreted in terms of atomic number maps, as shown in figure 1.2. Combined with aberration correction, the chemical sensitivity of HAADF imaging has been successfully used in the characterization of the structure of materials at atomic level. An exemplary case is the determination of the atomic positions of the cation species in the unit cell of the superconductor YBCO [13].

However, the leap from qualitative analysis of HAADF images to quantitative interpretation has to be taken with caution. This will be discussed in more detail in Chapter 2.

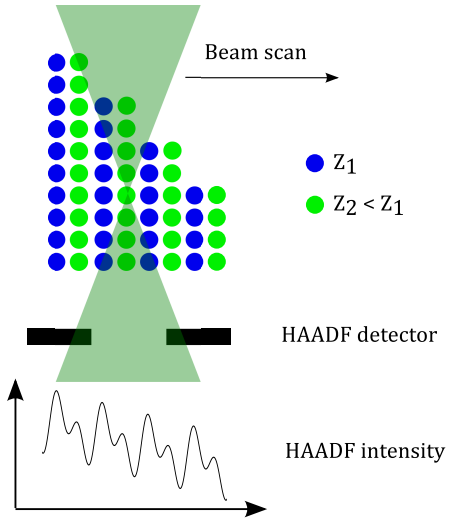

Figure 1.2 Scheme of a 1D HAADF acquisition. Effects of both atomic number and thickness in the HAADF intensity are illustrated.

STEM HAADF images provide useful information about the position of atomic columns in a crystal, and even about their composition through the Z dependence of contrast. However, lighter atoms such as oxygen or lithium, which are of great importance in many functional materials, are invisible to HAADF. The Annular Bright Field (ABF) technique allows the detection of light atoms, in addition to the heavier ones, in STEM images. It can be thought of as a smart acquisition setting used in order to extract further information from the Bright Field (BF) imaging mode. It becomes particularly relevant in aberration corrected STEM.

The signal collected on the BF detector has an annular distribution, despite being *inside* the direct illumination cone (as opposite to HAADF detectors). By placing a circular mask (the beam stopper) on the center of the beam, this angular distribution can be used in order to tune the contrast of the image. ABF images present negative, absorptive-type contrast (*i.e*, dark atomic columns) for a wide range of specimen thicknesses and defocus. To that extent, it is a robust technique with non-oscillating transfer functions, which makes image interpretation much easier, similar to the positive contrast in HAADF. The contrast enhancement

for light atoms can be understood taking into account two main effects:

- Scattering by light atoms is strongly forward peaked towards the central BF region.
- Scattering by heavy atoms is stronger at large angles.

This angular scattering distribution was measured experimentally by Okunishi *et. al.* [14] using the diffracting imaging technique, in which a diffraction pattern can be obtained with the STEM probe placed on a particular atomic column. The theoretical framework was proposed by Findlay *et al.* [15]. The forward peaking of the scattering from light atoms can be explained by the dominance of the s-states channeling process. In this model, electrons couple to the s-type Bloch states, strongly localized around the atoms, and therefore, exit the specimen aligned with the direction of the atomic column. The scattering by heavier atoms is dominated by thermal diffuse scattering (TDS), resulting in larger scattering angles.

Considering the ABF signal as the subtraction of the central region integrated intensity from the large angle integrated intensity (given the non-coherence of STEM imaging), the subsequent darkening of the light atomic columns results in a global contrast enhancement: light atomic columns will i) appear darker against the background signal and ii) will not be shadowed by the contrast from heavier columns. On the downside, the resulting contrast will not have the additional chemical information found in HAADF images. However, if the experimental configuration consists in a purely annular bright field detector or a conventional bright field detector with a mask (as in our case), it is straightforward to acquire ABF and HAADF signals simultaneously. This is not the case if the ABF conditions are achieved by a combination of large camera lenghts and HAADF detectors.

Diffraction contrast

Before getting down to real space imaging, let us first briefly describe how the electron beam is diffracted by the specimen in the TEM. Looking at a single unit cell in a crystalline material, the

amplitude of the electron beam scattered by it can be expressed as

$$A_{cell} = \frac{e^{2\pi i \cdot \vec{k} \cdot \vec{r}}}{r} F(\theta) \tag{1.4}$$

where $F(\theta)$ is the structure factor, containing information on the atomic number and relative positions of all the atoms in the unit cell. The amplitude of a beam diffracted at an angle θ by n unit cells in the specimen will consist of a sum over those unit cells:

$$\phi_g = \frac{i\pi a}{\xi_g} \sum_n e^{-2\pi i \vec{k} \cdot \vec{r_n}} \cdot e^{-2\pi i \cdot \vec{k_D} \cdot \vec{r}} \tag{1.5}$$

where k is defined as $\vec{k} = \vec{k_I} - \vec{k_D}$, the difference between the incident and the diffracted beams. A spot will appear in the diffraction pattern when $\vec{k_D}$ corresponds to scattering in a Bragg angle θ_{Bragg}. The interplanar distance for the given plane family is a. ξ_g is the so called extinction distance for each diffraction vector g:

$$\xi_g = \frac{\pi V_c cos\theta_{Bragg}}{\lambda F_g} \tag{1.6}$$

where V_c is the unit cell volume, θ_{Bragg} is the Bragg angle, λ is the electron wavelength and $F_g = F(\theta_{Bragg})$. It is related to the unit cell dimension through V_c, its composition through F_g and the accelerating voltage through λ. Notice that ξ_g does have dimensions of length and that the amplitude is, thus, dimensionless, as expected.

The electron beam inside the crystal can be thought of as a sum of the direct beam and all the diffracted beams, with amplitudes ϕ_0 and ϕ_{g_i} respectively. As a convenient approximation for this description and also a practical situation in the microscope, let us consider the case where only the direct beam and one diffracted beam are present. In this two beam approximation, only one family of planes is oriented in Bragg conditions. The change in amplitude for the direct and diffracted beams when going through the specimen (z direction) are described by the Howie-Whelan equations [16]

$$\frac{d\phi_g}{dz} = \frac{\pi i}{\xi_g}\phi_0 e^{-2\pi i s z} + \frac{\pi i}{\xi_0}\phi_g \tag{1.7a}$$

$$\frac{d\phi_0}{dz} = \frac{\pi i}{\xi_0}\phi_0 + \frac{\pi i}{\xi_g}\phi_g e^{2\pi i s z} \tag{1.7b}$$

These coupled differential equations describe the continuous (dynamic) exchange of intensity between the direct and diffracted beam. Parameter s is called the excitation error, and corresponds to the distance from the diffracted beam k-vector to the reciprocal lattice node G, as described in figure 1.3.

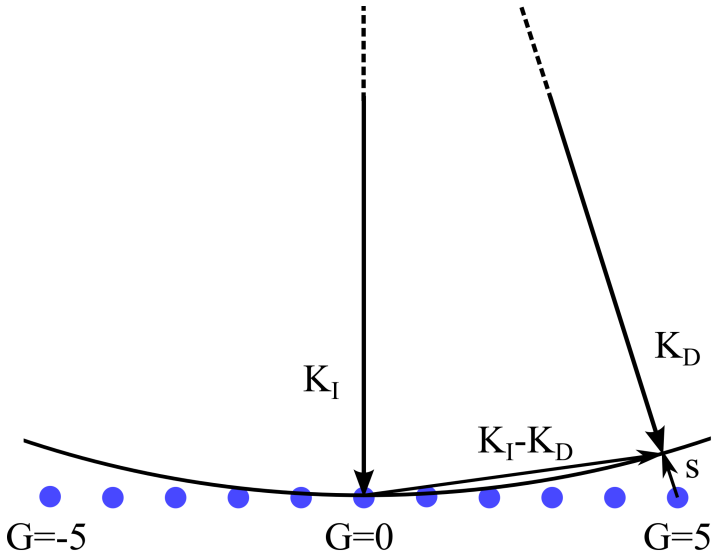

Figure 1.3 Schematic view of the diffraction of the electron beam by the crystal lattice. Blue dots represent nodes in a section of the reciprocal lattice. The momentum of the incident electron is $\vec{K_I}$, and the momentum of a diffracted electron beam is $\vec{K_D}$. The sphere defined by the magnitude of these vectors ($|\vec{K_I}| = |\vec{K_D}| = 1/\lambda$) is called Ewald sphere. When $\vec{K} = \vec{K_D} - \vec{K_I} = \vec{G}$, Ewald sphere intersects with the node and a spot appears in the diffraction pattern. Reflection G is then said to be *strongly excited*. Tilting the specimen allows choosing which reflections are strongly excited. The distance from a node to Ewald sphere is called s, the excitation error.

Solving the Howie-Whelan equations under two beam conditions yields the amplitude of any diffracted beam when in perfect two beam conditions. Then, the actual intensity recorded in the

diffraction pattern can be calculated as the squared modulus of this amplitude

$$|\phi_g|^2 = \left(\frac{\pi t}{\xi_g}\right)^2 \frac{sin^2(\pi t s_{eff})}{(\pi t s_{eff})^2} \tag{1.8}$$

where s_{eff} is an effective excitation error including the effect of the extinction distance of the particular reflection G

$$s_{eff} = \sqrt{s^2 + \frac{1}{\xi_g^2}} \tag{1.9}$$

The diffraction intensity distribution is found at the back focal plane of the objective lens of the TEM. In diffraction mode, the image formation system of the TEM is used to transfer the information on this plane to the detector in order to obtain a diffraction pattern. In image mode, however, the objective aperture in this back focal plane can be used to obtain images with diffraction contrast.

A first distinction has to be made between Bright Field (BF) and Dark Field (DF) imaging, depending on whether the direct beam is included or excluded by the objective aperture. If we set the experimental two beam conditions as discussed before, a *strong beam* DF image is formed by placing the objective aperture around the G reflection. Since electrons on that diffracted beam have been coherently scattered by a given (hkl) family of planes, areas in the image with those planes in zone axis will show bright (diffraction) contrast.

As can be seen from equation 1.8, the parameters that give rise, and therefore can modulate, diffraction contrast in the TEM are changes in thickness, through t, and changes in the diffracting conditions, through $\vec{s}$. A non uniform thickness will cause the presence of thickness fringes in the image, according to the sinusoidal dependence in equation 1.8. A local change in the orientation of the (hkl) planes will cause a tilt with respect to the incident beam and the apparition of bend contours. The latter is a key point in the diffraction imaging of defects in a material. Defects can bend, rotate, or modify the orientation of certain planes in and out of Bragg conditions. These changes can be imaged using

diffraction contrast, thus mapping the variation of the excitation error $\vec{s}$ across the specimen.

The presence of defects in the crystal, either planar (grain boundaries, stacking faults,...) or linear, introduces a translation vector in the exponential terms of the Howie-Whelan equations: $e^{i2\pi(s\cdot z+\vec{g}\cdot\vec{R})}$. The translation term $\alpha = 2\pi\vec{g}\cdot\vec{R}$ will depend on the kind of defect. The particular case in which $\vec{g}\cdot\vec{R} = 0$ means that the defect is out of contrast (invisibility criterion), so the strong reflection to be used in a given orientation must be carefully selected.

In particular, the presence of strain fields around defects indicates the bending of the lattice planes, modifying the Howie-Whelan equation with a continuous variation of $\vec{R}$ with respect to z. The core of the dislocation is located at the $\vec{R}(0)$ position. The excitation error will also change with R as

$$s_R = s + \vec{g}\cdot\frac{d\vec{R}}{dz} \tag{1.10}$$

Setting up a condition with a positive but small s, and placing the objective aperture around the G reflection, the resulting DF image will present strong bright contrast at the areas where the defect brings the planes back into Bragg condition. The complementary BF image will present a dark contrast in the defect regions, where the planes are not in Bragg condition.

The previous description considers the use of strongly excited reflections to form the diffraction contrast image. However, using weakly excited reflections can provide useful information too, in the so called weak-beam dark field mode. By placing the objective aperture in a reflection with a large excitation error s, the image will show bright contrast in the areas in which the defect bends the lattice back to Bragg conditions. A significant amount of intensity is lost, since it decays as $\sim 1/s^2$. The difference with respect to the strong beam situation is that the large value of s means a small coupling of the direct and diffracted beams, so $\vec{g}$ is diffracted more kinematically. Moreover, ξ_{eff} will be small, so the defects will be imaged more sharply and with an intensity independent of ξ_{eff}.

1.2.2 Phase contrast

Let us now consider the phase term in equation 1.2. Since we are considering only the phase contribution to contrast in the image, we can arbitrarily set A to 1. Given the small specimen thickness constraint for TEM observation, we are allowed to express the 3D electrostatic potential in the specimen as a 2D projected potential

$$V_t(x,y) = \int_0^t V(x,y,z)dz \tag{1.11}$$

Electrons in the vacuum (i.e., outside the specimen) have an energy corresponding to the accelerating potential of the microscope, $eV_{acc} = E$. Electrons within the sample will have this energy modified by the projected potential, $E + V(x,y,z)$, at each thickness level in the beam propagation direction, dz. This change in energy can be related to a change in wavelength that causes a change in the phase of the electron wave going through each thickness level dz

$$d\Phi = 2\pi \left(\frac{1}{\lambda'} - \frac{1}{\lambda} \right) dz \tag{1.12}$$

Taking into account the relationship between accelerating voltage and electron wavelength, this phase shift can be expressed in terms of electron energy and wavelength

$$d\Phi = \frac{\pi}{\lambda E} V(x,y,z) = \sigma V(x,y,z) \tag{1.13}$$

where σ is called the interaction constant. Then, the total phase shift of the electron wave after going through the whole thickness of the specimen is

$$\Phi = \sigma \int_0^t V(x,y,z)dz = \sigma V_t(x,y) \tag{1.14}$$

We can introduce this expression for the phase shift in the object transmission function (Eq. 1.2). Considering again the small thickness of the sample, we can truncate the Taylor series expansion of this function at first order to get the weak phase object approximation. In this approximation, the image function,

as described in the linear image model (Eq. 1.1), can be expressed as

$$g(x,y) = [(1 - i\sigma V_t(x,y)) \otimes h(x,y)] \tag{1.15}$$

It is easier to work with the Fourier transform of h(x,y). Equation 1.1 can be expressed in terms of Fourier transforms (G(k)=FT[g(r)], F(k)=FT[f(r)] and H(k)=FT[h(r)]). According to the convolution theorem, convolutions in real space correspond to scalar products in Fourier (or frequency) space

$$G(k) = F(k) \cdot H(k) \tag{1.16}$$

The main contribution to $H(k)$ or *contrast transfer function*, comes from the aberrations of the optical system. Aberrations and aberration correction will be discussed later in more detail, but to illustrate the present section let us assume a simple scenario. Aberrations cause the electron wave to deviate from the ideal spherical wave front by a certain angular value, α. Assuming a perfect rotational symmetry of the electromagnetic lens, the only possible aberrations are defocus (Δf) and spherical aberration (C_s). The change in phase due to these two aberrations can be expressed as

$$\chi(\alpha) = \frac{2\pi}{\lambda}\left(\frac{1}{4}C_s\alpha^4 - \frac{1}{2}\lambda\Delta f\alpha^2\right) \tag{1.17}$$

Since angular deviation and frequency can be related via the electron wavelength ($\alpha = \lambda \cdot k$), equation 1.17 can be expressed in terms of k as

$$\chi(k) = \pi\lambda k^2\left(\frac{1}{2}C_s\lambda^2k^2 - \lambda\Delta f\right) \tag{1.18}$$

The role of the contrast transfer function will be to modulate different spatial frequencies (i.e., different spacings in direct space) by a complex function of the form

$$H(k) = e^{-i\chi(k)} = (cos\,[\chi(k)] - isin\,[\chi(k)]) \tag{1.19}$$

The actual image g(x,y) recorded in the microscope detector will be the intensity, i.e., the squared modulus of the electron

wave function after propagating through the specimen convoluted with the point spread function. Then, from equation 1.15 we have

$$g(x,y) = \psi\psi^* = |1 - i\sigma V_t(x,y) \otimes h(x,y)|^2 \approx 1 + 2\sigma V_t(x,y) \otimes h(x,y) \tag{1.20}$$

Considering the weak phase object approximation, there is no contribution from the amplitude (cosine) term in the complex contrast transfer function in equation 1.19. Only the phase term (sine) remains:

$$H(k) = sin\,[\chi(k)] \tag{1.21}$$

From this oscillatory behavior of the contrast transfer function we can see that different spatial frequencies, i.e., different spacings in the specimen, can be transmitted to the image with different intensities. To prevent the contrast transfer function from changing sign, an objective aperture can be placed in the back focal plane of the objective lens, selecting only spatial frequencies before the first zero of $H(k)$. Although the value of defocus can be optimized to have a region of uniformly transmitted contrast as large as possible, the so-called Scherzer defocus (see figure 1.4), contrast transfer will never be completely flat, and phase contrast HRTEM images will always require a careful interpretation.

Even if the effect of an objective aperture is not included in the CTF shown in figure 1.4, it can be seen that the contrast transfer goes to zero at a given spatial frequency. This is caused by both spatial and temporal incoherence of the illumination, each of them being responsible for an envelope function damping the CTF. Spatial incoherence is introduced by the finite (non-zero) size of the electron source. Temporal incoherence effects can be introduced by instabilities of the accelerating voltage, resulting in electrons with slightly different energies. Since the Scherzer defocus is the condition at which the homogeneous contrast transfer extends to the highest possible spatial frequency, the corresponding real space distance can be used as a way to define the point-resolution of the instrument. However, higher spatial frequencies are still transmitted up to the point at which either the temporal or spatial envelope functions damp the CTF to zero. That spatial frequency

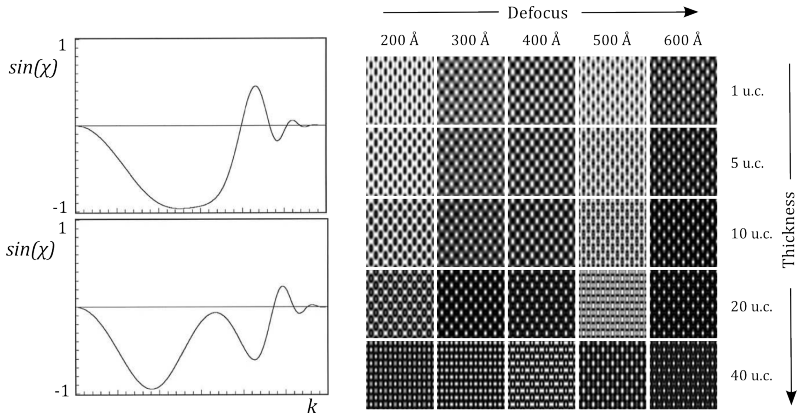

Figure 1.4 a) Phase distortion function in Scherzer (top) and out of Scherzer defocus (bottom) conditions. Contrast is transferred as positive or negative depending on the spatial frequency value k. b) Panel of 25 simulated images of a Si(110) crystal. Depending on the focus and the sample thickness, atoms appear bright or dark.

is called the *information limit* of the instrument. Different approaches exist in order to try to extend the point resolution up to the information limit. From an instrumental point of view, electron holography was devised by Gabor [17] as a way to suppress the effect of the aberrations in the objective system and, therefore, keeping only the specimen-dependent modification of the electron wave, both in amplitude and phase. From an off-line data processing approach, exit wave reconstruction techniques use an acquired HRTEM through-focus series in order to mathematically calculate the effect of the aberrations of the objective system and suppress it. A new image can be generated with higher spatial resolution than any of the acquired images in the series. Two main procedures are used to retrieve the full electron wave (amplitude and phase). The first one relies on the Fourier analysis of the focal series in order to filter out the components that are not sample dependent. The second approach is the iterative modification of the exit wave and comparison with an initial phase guess or simulated electron wave, via the minimization of an error function. Given the fairly small degree of incoherence of the FEG guns and the readily available computational power, the iterative methods are the most commonly used.

We have shown that, even in a scenario with the simplest conditions, we can find atoms as both bright or dark spots in HRTEM images and that, even if the sign is maintained, the intensity recorded will not necessarily be proportional to physical, chemical or structural parameters of the sample. This effect of the contrast transfer function of the microscope has been responsible for keeping HRTEM an almost completely qualitative technique for a long time. In the past few years, however, tools that allow extracting quantitative information from HRTEM images have become more accessible.

1.3 Relevance of advanced TEM modes for materials science

In this introduction to the basic working principles of TEM, the power of the instrument as an ultimate image resolution tool has been established. Stemming from this central aspect, a variety of TEM-related techniques are devoted to reveal properties of materials at the spatial resolution that TEM can provide. Either by the adequate processing of images, the use of particular instrumental configurations or the addition of the needed detectors, it is possible to obtain crucial information to solve challenging materials science problems. Some of these properties, of particular interest in the present thesis are summarized in figure 1.5.

Being able to directly relate the final properties with the intimate structure provides a unique insight into the functionality of materials and devices, especially when compared to the necessarily statistical nature of the information that can be retrieved by macroscopic measurements. The role of defects as non-radiative recombination centers in semiconductors, the free surface structure in oxides for gas sensing or the local magnetic configuration of nanoparticle assemblies for magnetic hyperthermia, for instance, need to be assessed through TEM techniques, which can unveil the local information needed to understand the macroscopic behaviour of these systems.

In particular, the scale reduction associated with the Nanoscience and Nanotechnology revolution demands characterization tools capable of reaching an unprecedented resolution, in a wide

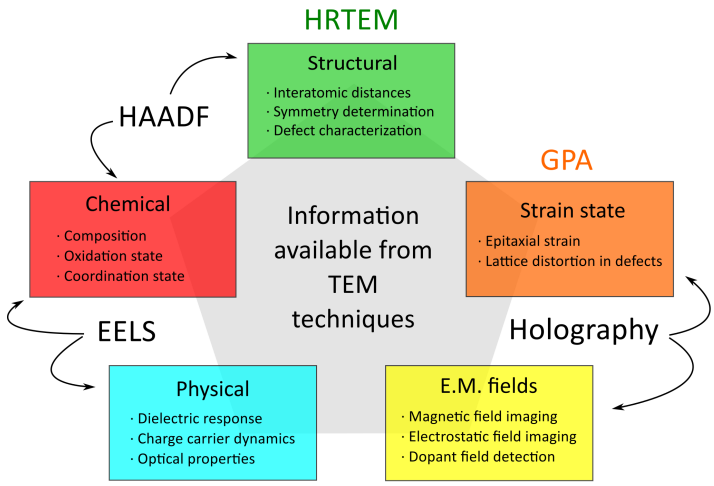

Figure 1.5 Materials properties, as related to TEM techniques

range of fields, not only for standard quality control, but in order to understand the properties of matter at the nanoscale. Going from bigger to smaller devices, but also from elemental building blocks (even atoms) to bigger assemblies, basic properties and device functionalities meet. With its ability to provide different kinds of information at a very high spatial resolution, state-of-the-art TEM and related techniques are in the core of this multidisciplinary and rapidly growing field.

1.4 Summary and scope of this thesis

In the framework of this thesis, different TEM imaging techniques that allow extracting quantitative information will be described, reviewed and applied to solving materials science problems.

The first major topic is related to the assessment of local atomic ordering/disordering phenomena in functional materials. A series of rare earth niobates (RE_3NbO_7) will be studied in order to understand the microstructural origin of their proton conduction properties, that make them excellent candidates to be used as electrode materials in solid oxide fuel cells. Also, single crystals of the tetragonal tungsten bronze (TTB) $Sr_{0.33}Ba_{0.66}Nb_2O_6$ (SBN-67) will be studied by different TEM techniques in order to assess the

possible short range structural and/or chemical disorder. These features are thought to be responsible for the observed macroscopic uniaxial polarization vector of the material as well as its relaxor properties.

A second major topic of interest will be the phenomena taking place at interfaces. This includes the characterization of a set of $LaNiO_3$ perovskite thin films grown on different substrates (LAO, LSAT, STO, YAO). The effect of the substrate-induced compressive/tensile strain, given by lattice mismatch, on the structure of the films will be assessed and related to the observed electric transport properties.

The interfaces in a GaN/InAlN multilayered system designed as a Bragg reflector for laser cavities applications will be investigated in order to account for a lower than expected reflectivity of the devices. The presence of structural defects and the detection of intergrowth of wurtzite and zinc blende phases of GaN in thin films will be addressed.

Also regarding interfaces and strain conditions, the characterization of the free surface of Nb_2O_5 nanorods, as a key point for their humidity sensing properties. Expanding on this, the strain state of Nb_2O_5 when grown on SnO_2 nanowires will also be studied. The coupling of the sensing capabilities of Nb_2O_5 with the electrical transport properties of SnO_2 is of particular interest for functional sensing devices. Therefore, defects at the interface and strain state are of capital interest in order to understand the band structure alignment of the system.

Interfaces in lower dimensionality systems will also be studied, as in the case of $Ag@Fe_3O_4$ dimers for applications in magnetoplasmonics. The epitaxial quality, strain, and the possible chemical diffusion through the contact surface of the two phases of the dimer are key aspects in order to properly tailor their optical properties.

The last major topic is the mapping of magnetic fields at the nanoscale. The magnetic configurations of different geometric arrangements of magnetite Fe_3O_4 nanocubes will be studied. This characterization is aimed at obtaining enhanced responses in magnetic hyperthermia treatments for cancer.

Given the strong interrelationship between the problems under study, the chapter structure follows the dimensionality of the systems under study (3D, 2D, 1D and 0D systems).

In the next Chapter, the TEM-related techniques involved in these studies will be presented in detail.

Bibliography

[1] L. de Broglie. Recherches sur la théorie des quanta. *Ann. de Phys.*, 10e série, t. III, 1925.

[2] M. Knoll and E. Ruska. The electron microscope. *Z. Physik*, 12(78), 1931.

[3] M. Knoll and E. Ruska. Geometric electron optics. *Ann. Physik*, 12(607), 1932.

[4] J.G. Allpress, J.V. Sanders, and Wadsley. Multiple Phase Formation in the Binary System Nb2O5-WO3. VI Electron Microscopic Observation and Evaluation of Non-Periodic Shear Structures. *Acta Cryst. Section B*, (B25), 1969.

[5] A.V. Crewe, M. Isaacson, and D. Johnson. A simple scanning electron microscope. *Rev. Sci. Instrum.*, 40(241), 1969.

[6] J.M. Cowley. Image contrast in a transmission scanning electron microscope. *Appl. Phys. Lett.*, 15(58), 1969.

[7] G. Cliff and G.W. Lorimer. The quantitative analysis of thin specimens. *Journal of Microscopy*, 103(2), 1975.

[8] M. Watanabe and D.B. Williams. The quantitative analysis of thin specimens: a review of progress from the cliff-lorimer to the new eta-factor methods. *Journal of Microscopy*, 221, 2006.

[9] R.F. Egerton. *Electron Energy Loss Spectroscopy in the Electron Microscope*. Springer, 3rd edition, 2011.

[10] O. Scherzer. Über einige fehler von elektronenlinsen. *Zeitschrift für Physik*, 101(9-10), 1936.

[11] O. Scherzer. Sphärische und chromatische korrektur von elektronenlinsen. *Optik*, 2, 1947.

[12] M. Haider, S. Uhlemann, E. Schwan, H. Rose, B. Kabius, and K. Urban. Electron microscopy image enhanced. *Nature*, 392(768), 1998.

[13] M. Varela, A.R. Lupini, S.J. Pennycook, Z. Sefrioui, and J. Santamaría. Nanoscale analysis of $yba_2cu_3o_{7-x}/la_{0.67}ca_{0.33}mno_3$ interfaces. *Solid-State Electronics*, 2003.

[14] E. Okunishi, H. Sawada, and Y. Kondo. Experimental study of annular bright field (abf) imaging using aberration-corrected scanning transmission electron microscopy (stem). *Micron*, 2012.

[15] S.D. Findlay, E. Okunishi, H. Sawada, and Y. Kondo. Dynamics of annular bright field imaging in scanning transmission electron microscopy. *Ultramicroscopy*, 2010.

[16] A. Howie and M.J. Whelan. Diffraction contrast of electron microscope images of crystal lattice defects. ii the development of a dynamical theory. *Proc. Roy. Soc.*, (A263), 1961.

[17] D. Gabor. A new microscopic principle. *Nature*, 777(4098), 1948.

Chapter 2

Quantitative TEM. Imaging and simulation

2.1 Image simulation: basic theoretical concerns

With the ever-increasing access to cheap computational power, image simulation has become a widespread tool to extract quantitative information from HRTEM images. Today, it is possible to create models for the specimen that can be carefully designed atom by atom, if needed. These models can later be simulated to obtain the projected potential map $V_{t(x,y)}$, which is not accessible experimentally, and which can, in turn, be used to simulate images through a range of microscope experimental conditions. The number of available variables that can be addressed by this analysis methodology makes it far more powerful than the analysis of a single HRTEM image. The basic algorithm is described in figure 2.1.

There are a number of available software packages to perform TEM image simulation. JEMS by P. Stadelman or xHREM by HREM Research LLC are commercial packages for Windows; MacTempas by Total Resolution LLC is a commercial option for Mac OS. Free software is also available, for example QSTEM from the ELIM group at Ulm University (for Windows) or the open source code TEM SIM by E.J. Kirkland (for Windows and Unix). In the context of this thesis, simulations have been carried out using the TEM SIM software running on a Linux environment.

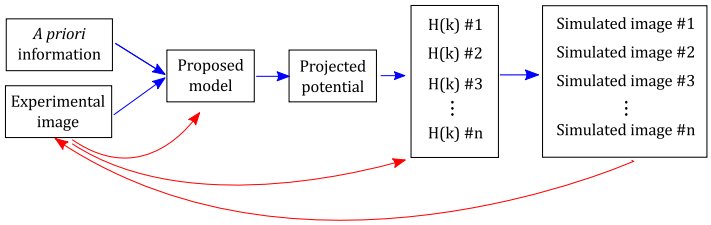

Figure 2.1 Basic algorithm for extracting quantitative information from image simulation. A first model is proposed using qualitative information from the experimental image or other inputs (if available). The projected potential is calculated and propagated through different transfer functions. The resulting simulated images are compared to the original ones and this information is used to apply changes, that can be precisely quantified, to the model and/or the transfer functions.

2.1.1 Creating the model

The model represents the TEM specimen including, at least, the minimal features of interest that we want to study. It is the input information for the image simulation software. The TEM SIM software uses .xyz files as an input. This file format consists of the dimensions of the object to simulate and a list containing the 3D position of each atom, identified by its atomic number Z. To create the models, two software packages developed at University of Cádiz have been used: EJE Z and RHODIUS [1, 2].

EJE Z is the software package used to create crystallographic phases. Unit cell parameters, space group symmetry and atoms in the asymmetric unit are introduced to create a phase. The unit cell can be visualized and rotated in 3D, with the possibility to include coordination polyhedra. An example is shown in figure 2.2(a). Plane spacings and angles, interatomic distances, metric tensors and other interesting parameters can be listed. The reciprocal lattice of the crystal can also be visualized in 3D. The unit cell can be projected along any given direction and repeated periodically, if needed, to create a model of the perfect crystal that can be recorded in the .xyz format, ready to be simulated.

In order to create more complex structures including interfaces, defects, faceting or any other structural or compositional feature of interest, RHODIUS uses the supercell approach. RHODIUS supercells are boxes that can be filled using the crystallographic

phases in EJE Z. After filling this box with the considered phase, the material can be precisely sculpted by imposing geometric constraints. Supercells of the same dimensions can be summed up, as illustrated in figure 2.2(b), to create structures as complex as the problem at hand requires, even atom by atom if necessary.

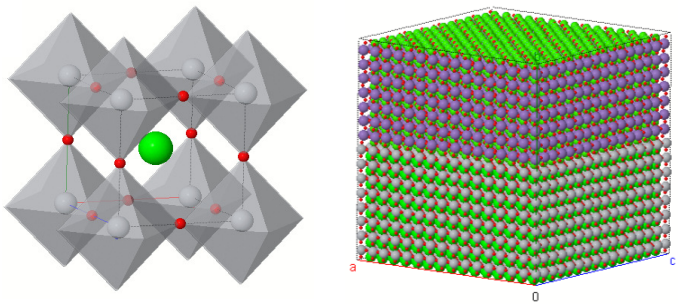

Figure 2.2 a) Unit cell of $SrTiO_3$ created and visualized in EJE Z showing Ti coordination octahedra. b) Model of an interface between a $SrTiO_3$ substrate and a $La_{0.5}Ca_{0.5}MnO_3$ film

2.1.2 HRTEM simulations

The electron beam in HRTEM can be assumed to be almost parallel when entering the specimen. The incident electron wave, then, can be expressed as a plane wave. This wave will travel through the potential in the sample and will emerge modified by this interaction. Then, an image of this exit electron wave will be formed by the objective system. The process of simulating an image will focus on this segment of the trajectory of the electrons in the microscope; effects of the electron gun and condenser system will be taken into account in the form of the incident electron wave, and the effect of the intermediate and projector systems, (magnification and shift) can be neglected since they can be addressed in the calibration and processing of the resulting simulated image.

The first step in HRTEM simulation is, then, calculating the propagation of the incident plane wave through the specimen potential. Two main approaches are used to do so, namely the Bloch waves method and the multislice method.

Bloch wave method

The Bloch wave method relies on the fact that the potential that the electrons of the beam see when traveling inside the specimen has the same periodicity as the Bravais lattice of the crystal i.e., $V(\vec{r}+\vec{R}) = V(\vec{r})$, where $\vec{R}$ is a vector of the Bravais lattice. Independent electrons, each one obeying a one-electron Schrödinger equation

$$H\varphi = \left(\frac{\hbar^2}{2m}\nabla^2 + V(\vec{r})\right)\varphi = E\varphi \tag{2.1}$$

are called Bloch electrons and their stationary states can be expressed in the form of a plane wave times a function with the periodicity of the Bravais lattice

$$\varphi_k = e^{i\cdot\vec{k}\cdot\vec{r}}u_k(\vec{r}) \tag{2.2}$$

This result is known as Bloch theorem, and wave functions with this form are called Bloch waves. The periodic function $u_k(\vec{r})$ can be expressed as a Fourier series

$$u_k(\vec{r}) = \sum_K c_{k-K}e^{-i\cdot\vec{K}\cdot\vec{r}} \tag{2.3}$$

where vectors $\vec{K}$ belong to the reciprocal lattice of the crystal due to the periodicity condition. The periodic potential can also be expanded in a similar way following the same argument

$$V_k(\vec{r}) = \sum_K V_K e^{i\cdot\vec{K}\cdot\vec{r}} \tag{2.4}$$

Substituting equations 2.2 and 2.3 for the Bloch waves and equation 2.4 for the potential in the Schrödinger equations yields

$$\sum_K e^{i(\vec{k}-\vec{K})\vec{r}}\left\{\left(\frac{\hbar}{2m}(\vec{k}-\vec{K})^2 - E\right)c_{k-K} + \sum_K U_{K'-K}c_{k-K'}\right\} = 0 \tag{2.5}$$

and since the plane waves $e^{i(\vec{k}-\vec{K})\cdot\vec{r}}$ satisfying the periodicity of the crystal form an orthogonal basis set, coefficients for each term must vanish

$$\left[\frac{\hbar}{2m}(\vec{k}-\vec{K})^2 - E\right] c_{k-K} + \sum_K U_{K'-K} c_{k-K'} = 0 \qquad (2.6)$$

By imposing just the periodicity of the potential, the problem of finding the allowed Bloch waves in the specimen has become N independent eigenvalue problems, one for each value of $\vec{k}$. For each $\vec{k}$, only the c coefficients corresponding to a vector $\vec{K}$ belonging to the reciprocal lattice of the crystal will be non-zero. Notice that no particular description of the form of the potential has been used so far, besides the assumption of periodicity.

Of all the possible combinations of Bloch waves inside the specimen, only some of them will be compatible with the incident electron wave. This electron wave can be expressed in a basis of Bloch waves as

$$\psi(\vec{r}) = \sum_k \alpha_k \varphi_k(\vec{k}, \vec{r}) \qquad (2.7)$$

If the weighting coefficients α_k are known, the electron wave is determined at any point in the specimen. Equating the solution of equation 2.6 at z = 0 (specimen entrance surface) to the known incident wave (plane wave for HRTEM), coefficients can be determined. Then, for the particular case of $z = t$, where t is the specimen thickness, the exit electron wave can be calculated. Figure 2.3 shows a descriptive diagram of the Bloch wave method.

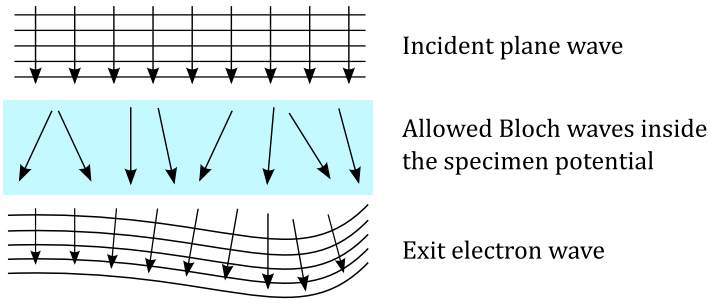

Figure 2.3 Schematic of the Bloch wave method to calculate the exit electron wave. Schrödinger equation is solved in the specimen to obtain the allowed Bloch waves. They are later set to match the plane wave at the entrance surface and propagated to the exit surface

A first problem with this approach is the starting assumption of the periodicity of the potential. This will not be true in the presence of defects or interfaces in the model, which are common situations of interest for simulation. Computationally, the problem of calculating the N Bloch waves (eigenvalues and eigenvectors, N-beam problem) requires the storage of N^2 elements in memory, and CPU time scales as N^3. Given these limitations, the Bloch wave method is restricted to problems with perfect symmetry of crystals with small and highly symmetric unit cells, i.e., where a small number of beams is needed for the calculation.

Multislice method

The multislice method is used to solve the propagation of a quantum mechanical wave package through a medium. In the case of simulation of electron microscopy images, it consists in slicing the specimen potential into thin slices containing a projected potential each. The electron wave is transmitted through each slice and propagated in vacuum to the next one. Each slice acts as a weak phase object, as described in Chapter one. Dynamical scattering effects due to specimen thickness can be taken into account by iteration, despite each transmission step being a kinematical process. The resulting exit wave can be obtained by this method for specimens as thick as ~ 100 nm. The method is summarized in figure 2.4.

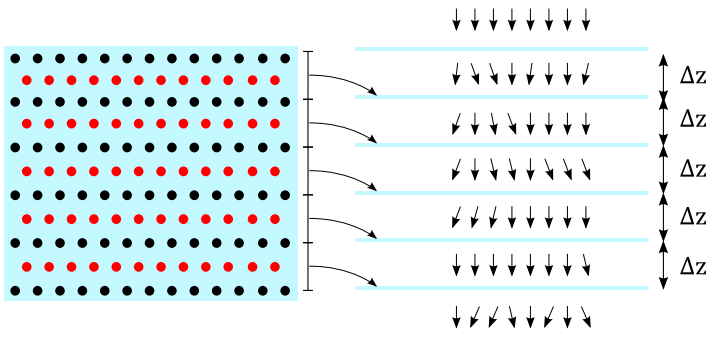

Figure 2.4 Schematic of the multislice method. The incident plane wave is transmitted through each potential slice. The modified wave is propagated to the next slice till the exit surface is reached

The wave equation for the propagation of electrons in the z direction can be written as

$$\frac{\partial\psi(x,y,z)}{\partial z} = \left[\frac{i\lambda}{4\pi}\nabla^2_{xy} + i\sigma V(x,y,z)\right]\psi(x,y,z) \tag{2.8}$$

where σ is the interaction parameter. The solution of this differential equation has the form

$$\psi(x,y,z+\Delta z) = exp\left[\int_z^{z+\Delta z} \frac{i\lambda}{4\pi}\nabla^2_{xy} + i\sigma V(x,y,z')dz'\right]\psi(x,y,z) \tag{2.9}$$

Imposing the geometry of the multislice approach, Δz will be a thin slice of the specimen, and the solution can be further simplified as

$$\psi(x,y,z+\Delta z) = exp\left[\frac{i\lambda}{4\pi}\nabla^2_{xy} + i\sigma v_{\Delta z}(x,y)\right]\psi(x,y,z) \tag{2.10}$$

where $v_{\Delta z}$ is the projected potential of a slice of thickness Δz

$$v_{\Delta z} = \int_z^{z+\Delta z} V(x,y,z')dz' \tag{2.11}$$

Making use of the Zassenhaus theorem for the exponentiation of operators and neglecting terms of second order and higher, equation 2.10 can be written as

$$\begin{aligned}\psi(x,y,z+\Delta z) &= exp\left(\frac{i\lambda}{4\pi}\Delta z\nabla^2_{xy}\right) exp\left[i\sigma v_{\Delta z}(x,y,z)\right]\psi(x,y,z) = \\ &= exp\left(\frac{i\lambda}{4\pi}\Delta z\nabla^2_{xy}\right) t(x,y,z)\psi(x,y,z)\end{aligned} \tag{2.12}$$

where $t(x,y,z)$ is the transmission function for a slice of thickness Δz, as defined in section 1.2 for a weak phase object. By taking

the Fourier transform of equation 2.12, after some further manipulations, the remaining exponential operator can be interpreted as a propagator function $P(k, \Delta z)$

$$FT\left[exp\left(\frac{i\lambda}{4\pi}\Delta z\nabla^2_{xy}\right)t(x,y,z)\psi(x,y,z)\right] = \\ = P(k,\Delta z)FT\left[t(x,y,z)\psi(x,y,z)\right] \quad (2.13)$$

Since a product in Fourier space is a convolution in real space, equation 2.12 can be rewritten as

$$\psi_{n+1}(x,y) = p(x,y,\Delta z_n) \otimes t_n(x,y)\psi_n(x,y) \quad (2.14)$$

which is the real space multislice equation. The iterative process of transmission and propagation, starting with the incident electron wave $\psi_0(x,y)$, ends with the exit electron wave at the exit surface of the specimen. Computationally, the calculation of equation 2.14 is carried out both in real and Fourier spaces, since the transmission function is a diagonal matrix in real space and the propagation function is a diagonal matrix in Fourier space

$$\psi_{n+1}(x,y) = FT^{-1}\left\{P_n(k_x,k_y,\Delta z_n)FT\left[t_n(x,y)\psi_n(x,y)\right]\right\} \quad (2.15)$$

If the electron wave function is sampled for $N_x \times N_y$ points, there will be as many Fourier coefficients to calculate. Using the Fast Fourier Transform algorithms, CPU time scales as $Nlog2(N)$ instead of N^3 as in the Bloch waves eigenvalue problem.

Effect of the objective system

Once the exit electron wave function has been calculated, the only remaining calculation is the (much faster and simpler) addition of the effect of the objective lens. This is done by a direct product of the Fourier Transform of the exit wave and the Contrast Transfer Function defined by the microscope parameters

$$\Psi(k) = FT\left[\psi(x,y)\right]H(k) \quad (2.16)$$

By inverse Fourier transformation of $\Psi(k)$ and the subsequent calculation of its squared modulus, the final image intensity is obtained

$$I(x,y) = |FT^{-1}\left[\Psi(k)\right]|^2 \tag{2.17}$$

A single calculated exit wave can be used to produce as many simulated images as necessary, under different objective lens conditions. Table 2.1 summarizes the parameters involved in a HRTEM simulation and its relationship with the actual instrument.

In the multislice approach, including defects and interfaces in the model is possible. However, the calculation using the FFT algorithms imposes periodic boundary conditions to the supercell. If non-periodic features are present, the supercell size should be large enough as to keep those away from the edges of the simulation ($\sim 5nm$), where a second cell will be repeated generating a new interface. These edges will have to be discarded later.

Parameter	**Effect on the simulation**
Accelerating voltage (V_0)	Defines the incident wavelength of the electron beam
Wavefunction size (N_x, N_y)	Number of pixels used to sample the transmission function of the model and the incident plane wave
Slice thickness	Determines the thickness of each slice of projected potential
Spherical aberration C_{s3}, C_{s5}	Determines the contrast transfer function
Defocus	Defines the contrast transfer function
Objective aperture size	Sets a cut-off point in the contrast transfer function
Illumination semi-angle	Defines the shape of the incident electron wave
Defocus spread	Integration over a range of defocus values due to high voltage or lens current instabilities

Table 2.1 HRTEM image simulation parameters

2.1.3 STEM simulation

The case of image simulation in the STEM mode using the multislice method can be understood as a slight variation of what has been just explained for the HRTEM case, just substituting the incident electron wave, $\psi(x, y)$, which is a plane wave in HRTEM, for a focused probe in STEM. In a STEM calculation, the probe function has to be propagated through the specimen in each pixel. So if the specimen is sampled in $N_x \times N_y$ pixels, there will be as many calculations equivalent to those described for HRTEM, with the corresponding increase in computer time. Once the exit wave is calculated, its integrated intensity in the back focal plane, applying the geometric constraint of the detector (BF, ABF, ADF, HAADF), will be the image intensity for that particular pixel. A comparative diagram between HRTEM and STEM image simulation is presented in figure 2.5. Table 2.2 summarizes the parameters involved in a multislice STEM simulation.

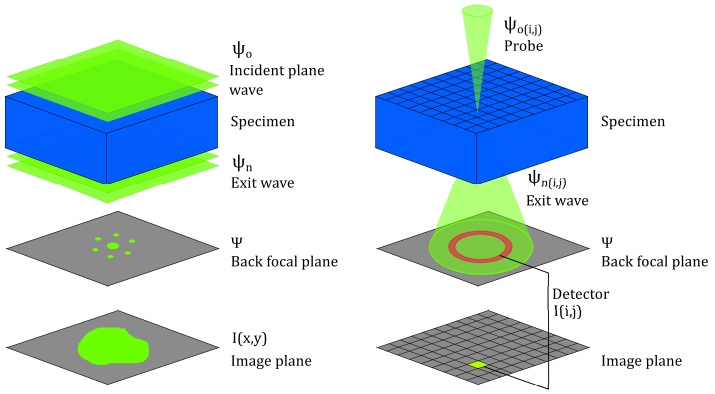

Figure 2.5 Schematic view of the steps in a) a HRTEM simulation and b) a STEM simulation

2.1.4 Image simulation. State of the art

HRTEM simulation

Computer simulation of the contrast of HRTEM images has been used since the early 80s [3]. However, the quantitative analysis of HRTEM images has greatly benefited from the incorporation of C_s

Parameter	Effect on the simulation
Accelerating voltage (V_0)	Defines the incident wavelength of the electron beam
Probe wavefunction size (N_x, N_y)	Sampling in pixels of the focused incident probe $\psi_0(x, y)$
Object transmission function size (N_x, N_y)	Sampling in pixels of the object transmission function $t_n(x, y)$
Condenser aperture angle	Limits the number of beams in the probe function
Spherical aberration C_{s3}, C_{s5}	Determines the shape of the probe
Defocus	Determines the shape of the probe
Detector geometry	Inner and outer radius, allows choosing between BF, ABF, ADF, HAADF, ...
Object size	Real space dimensions of the object
Object sampling (N_x, N_y)	Number of pixels in the final image
Slice thickness	Defines the thickness of each slice of projected potential

Table 2.2 STEM image simulation parameters

correctors. The reduction in size of the point spread function of the microscope, besides facilitating the interpretation by eliminating delocalization effects, avoids the intermixing of the intensity of neighboring atomic columns.

Applications of image simulation for uncorrected HRTEM mainly focus on the determination of the structure of defects by comparison of simulated images from proposed models and experimental images.

The cation sublattice of oxides was studied, for example, by Daneu et al. in 2007 [4] for the characterization of (111) twin boundaries in spinel $MgAl_2O_4$. The detailed composition at the defects was found by the combination of multislice simulations from different models and EDS chemical maps.

Regarding the characterization of defects in semiconductors, Pailloux et al.[5] described 2D defects ('nanoplatelets') in germanium after ion implantation. The procedure consisted in simulating an initial model and applying strain field analysis to both experimental and simulated images. Their results stress the need

for HRTEM image simulations, given the variation in the apparent size of the defects with defocus and sample thickness.

Despite not being a widely used technique for chemical characterization, HRTEM images have been used to study the composition of ternary III-V structures through lattice parameter distortion. For example, Ruterana et al.[6] used Finite Element calculations to characterize the relaxation of In clusters in a GaN matrix.

As already mentioned, the use of aberration correctors opened new possibilites for extracting of information from HRTEM. In particular, the introduction of small negative C_s values was found to enhance contrast for lighter elements. This technique, known as Negative C_s Imaging (NCSI), was introduced in 2004 by Jia and Urban. [7]

Besides improving the procedure already in use for the characterization of defects in oxides [8] and semiconductors [9], the possibility to access lighter atoms allows studying the oxygen sublattice in oxides. In the seminal paper by Jia and Urban[7], the particular problem under study was the oxygen concentration in twin boundaries in $BaTiO_3$ crystals. Multislice image simulation was used to calibrate the relationship between the oxygen occupancy in a given site and the HRTEM image intensity. More recently, in 2013, An et al.[10] studied twin boundaries in yttria stabilized zirconia (YSZ) regarding the simultaneous effects of anion site occupancy and atomic displacements on the image contrast.

HAADF simulation

HAADF image simulation has also been much more extensively used in recent years, with the increasing availability of probe corrected STEM systems. The possibility to use Z-contrast to identify composition at atomic column level has made it clear that it is necessary to compare experimental images with simulated ones. There are two main ways to obtain compositional information from HAADF images, by using either relative or absolute intensity scales.

Relative composition analysis of the HAADF intensity relies in the use of a model-based technique in which the composition

of unknown atomic columns can be obtained from hypothesis testing statistical methods, as introduced by Van Aert et al. in 2009 [11]. In this work, a $LaAlO_3/SrTiO_3$ multilayer was characterized. Regions far removed from the interfaces were used as a reference and introduced in the parametric model to identify mixed composition interface layers. Simulations were used to assess the effect of thermal diffuse scattering and the cross talking between neighboring columns, which was found to be especially important for low signal-to-noise ratios. With this method, differences of $\Delta Z = 3$ in average column atomic number could be discriminated. Further work in the same group by Martinez et al. in 2014 [12], on $Pb_{1.2}Sr_{0.8}Fe_2O_5$, expanded this method by using simulated images from varying composition models as references instead of reference regions. The statistical model used a linear combination of these compositions. This method proved to be accurate up to a given thickness, where non-linear effects became important.

The feasibility of an absolute quantification of the HAADF intensity was demonstrated by LeBeau et al. in 2008. [13, 14]. By obtaining a response map of the annular detector that can be compensated for, the experimental intensity can be normalized and directly compared with simulations from models with a given composition. The initial work on $SrTiO_3$ [13, 14] was later extended in 2009 to $PbWO_4$, showing good results also for heavier elements [15]. Rosenauer et al. used this approach in 2011 [16] to characterize the composition of InGaN quantum wells and quantum dots. In all these studies, the importance of including thermal diffuse scattering to obtain comparable results in the simulation is stressed. This can be achieved in multislice calculations by averaging over a number of different phonon configurations (frozen phonon approximation). In this sense, the main problem outlined in these works is the precise knowledge of the Debye-Waller factors governing thermal atomic displacements, since they are obtained from bulk measurements but could be rather different in nanoscale objects, interfaces or epitaxially strained thin films.

The effect of thermal diffuse scattering in the HAADF intensity was thoroughly studied by Blom et al. in 2012 [17] when characterizing the M1 phase of catalyst Mo-V-Nb-Te-O through HAADF

experiments and simulation. The use of great computing capabilities allowed studying systematically the role of a wide range of detector geometries and Debye-Waller factors via the HAADF simulation. Applying different detector geometries for the analysis of the same specimen was proposed as an experimental way of accessing Debye-Waller factors in the nanoscale.

Further results concerning the effect of the annular detector were given in the 2013 paper by Findlay and LeBeau[18]. The lack of rotational symmetry of the HAADF detector was found to be unimportant for HAADF at short camera lengths, provided the intensity is normalized. On the contrary, for longer camera lengths, the particular symmetry of the detector should be included in the simulations if a precision of around $\sim 5\%$ was required. This is important in Annular Bright Field (ABF) experiments if they are carried out using HAADF detectors and long camera lengths.

An alternative method for composition quantification was proposed by E et al. in 2013 [19]. A calculated Probe Integrated Scattering Cross Sections (PICS) is used for quantification instead of HAADF intensity. Through image simulation, PICS signal was proven to be more linear with composition than peak intensity and insensitive to defocus, making it a very useful tool for quantification. Results showed $\Delta Z = 1$ sensitivity and the possibility to identify single atoms of unknown elements, where spectroscopic techniques could suffer from too low a signal-to-noise ratio.

The detection of single atoms of dopants in amorphous materials was demonstrated by Mizoguchi et al. in 2013 [20]. The apparent non-homogeneous distribution of dopants was ruled out through image simulation by showing the effects of depth of focus and specimen thickness on the visibility of the embedded dopant atoms. Only atoms in a $\Delta z = 5$ nm from the beam waist and in a thin area could be imaged.

STEM HAADF simulation has also been used as a diagnostic technique for determining experimental conditions, both for the microscope and for the TEM specimen. In 2009, Grillo [21] used HAADF image simulations to study the effect of strain relaxation and bending on HAADF intensity. He showed the effect of surface relaxation due to sample preparation in a strained InGaAs/GaAs quantum well system. The acquisition of HAADF tilt series was

proposed as a method to map surface strain. Kauko et al. reported in 2013 [22] these strain relaxation effects in the quantification of Sb content in GaAs/GaAsSb nanowires from HAADF intensities.

Regarding the characterization of the STEM probe itself, HAADF image simulation was used by Kim et al. in 2012 [23] in order to assess the effect of probe current on the spatial coherence of the beam. The effect in the blurring of the image of a finite source size could be added to the simulation as a convolution with a Gaussian function with a probe current-dependent FWHM.

2.2 Electron holography

Whereas image simulation methods offer an indirect access to the real electron wave, electron holography allows obtaining experimentally both the amplitude and the phase of the electron wave. The development in recent years of highly coherent electron sources (the Schottky Field Emission Gun (FEG), and, especially, the Cold Field Emission Gun (c-FEG)) has made the acquisition of electron holograms possible in a considerable fraction of the commercial TEMs.

Holography is an interferometry technique, initially proposed by Denis Gabor in 1947 to overcome the inherent aberrations of the electron microscope. It consists in the retrieval of the complete object wave function through the acquisition of the interference pattern arising from the interference of the object wave and a reference wave. In the TEM, the most widely used configuration to obtain an hologram is the so-called off-axis electron holography, as described in figure 2.6. An electrostatic biprism is placed in the column in order to split the electron beam. A part of the beam will travel through vacuum ($\psi_0(\vec{r})$, reference wave) and the other one through the specimen ($\psi(\vec{r})$, object wave), suffering a phase shift Φ_s

$$\psi_0(\vec{r}) = e^{i(\vec{k}\cdot\vec{r})} \tag{2.18}$$

$$\psi(\vec{r}) = A(\vec{r})e^{i(\vec{k}\cdot\vec{r}+\Phi_s)} \tag{2.19}$$

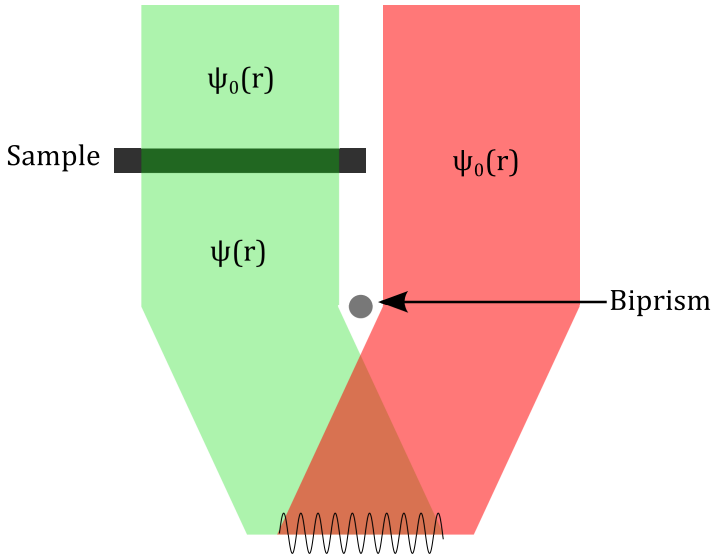

Figure 2.6 Off axis electron holography basic diagram. The electron wave resulting from the interaction of the electron beam with the sample and a reference electron wave from the electron beam going through vacuum are made to interfere using an electrostatic biprism. The resulting interference fringe pattern is studied.

The intensity recorded by the detector in the overlapping region of these two waves will be, then, the square modulus of the resulting wave $\psi_0(\vec{r}) + \psi(\vec{r})$

$$I(x,y) = |\psi_0 + \psi|^2 = 1 + A^2 + 2Acos(2i\pi r k_h + \Phi_s) \qquad (2.20)$$

where k_h is the carrier spatial frequency, corresponding to the holographic fringes spacing. We can see that the phase shift term, Φ_s, survives the recording process. Taking the Fourier Transform of this recorded intensity we obtain

$$FT\left[I(x,y)\right] = FT\left[1 + A^2\right] + FT\left[A(\vec{r})e^{i\varphi_s}\right] \otimes \delta(k - k_h) + \\ + FT\left[A(\vec{r})e^{-i\varphi_s}\right] \otimes \delta(k + k_h) \qquad (2.21)$$

The three terms in equation 2.21 are the three bands of the hologram power spectrum. The first term is the center band that corresponds to the classical TEM image. It contains both elastic

and inelastic contributions and no phase information at all. The two sidebands, which are redundant since they carry the same information, are the power spectrum of the complete electron wave. By inverse Fourier Transform of one sideband, the complete wave function, amplitude and phase, can be obtained in real space. By acquiring a reference hologram of a completely empty region, a reference electron wave can be obtained under the same experimental conditions and used to correct for any distortion of the optic system, i.e., aberrations of the electromagnetic lenses, CCD camera response, etc.

Up to this point, the only mechanism considered in the image formation process resulting in a phase shift has been the electrostatic potential in the sample. However, the given description of electron holography is far more general and many other physical phenomena causing a phase shift in the electron wave can be studied and quantified, giving rise to different types of electron holography techniques depending on the considered phase shift contribution, as well as the size scale of the studied system. There are four main contributions to the phase shift term

$$\varphi_s = \varphi_C + \varphi_G + \varphi_E + \varphi_M \tag{2.22}$$

namely *crystalline*, *geometric*, *electrostatic* and *magnetic* phases. High resolution electron holography is given directly by this description when considering only the crystalline phase term. The main interests of this technique are the improvement of spatial resolution in HRTEM images by the elimination of aberrations and the possibility of quantification, since *i)* the transfer of amplitude and phase from the object to the reconstructed electron wave is linear and *ii)* all inelastically scattered electrons are filtered out.

Dark field electron holography allows studying the geometric phase term, arising from strain and displacement fields in the sample ($\vec{u}$), which is

$$\varphi_G = -2\pi \vec{g} \cdot \vec{u} \tag{2.23}$$

for a given diffracted beam $\vec{g}$. This mode of electron holography uses the interference fringes coming from the overlapping of two diffracted beams, since the direct beam ($\vec{g} = 0$) carries no information about displacement fields. One of these beams is taken as a

reference of an unstrained region of the sample, instead of using the vacuum. After retrieving the phase, the displacement field can be obtained from equation 2.23 and the strain tensor can be calculated. This technique has been applied with great success to the characterization of strain fields of electronic devices [24, 25].

The electrostatic and magnetic phase terms are studied in the so-called medium resolution electron holography techniques. The resolution limitation comes from the need to switch off the objective lens to avoid the effect of its strong magnetic field on the sample. The after-specimen Lorentz lens, with a much larger focal length, is used to form the image, thus reducing the resolution by an order of magnitude. On the other hand, a much larger field of view can be recorded (up to a few microns). The phase shift resulting from both electrostatic and magnetic fields acting simultaneously on electrons traveling through the sample will be

$$\varphi_{E+M} = C_E \int V(x,y,z)dz - \frac{e}{\hbar}\int\int B_x(x,y,z)dxdz \qquad (2.24)$$

where C_E is a constant depending on the accelerating voltage and B is the magnetic field of the sample. The analysis of the electrostatic contribution to the phase shift allows, for example, detecting dopant potentials in semiconductor devices. If the mean inner potential can be assumed to be constant along the beam propagation direction z, the electrostatic phase shift can give 3D morphological information. The magnetic part can be used to obtain quantitative maps of magnetic induction (direction and intensity), local switching in spintronic devices, etc. [26–29]

2.2.1 Obtaining an electron hologram

The first requirement for electron holography, being an interferometry technique, is a highly coherent electron source. The most spatially coherent source available in a TEM is the Cold Field Emission Gun (cFEG). It is, thus, the adequate choice for holography experiments although not the most widespread. The Schottky Field Emission Gun (SFEG, or just FEG) is the most commonly used one and still provides a coherent enough source to perform electron holography. The emission process diagram for

these two sources is depicted in figure 2.7. As can be seen, the effect of the Schottky barrier potential ϕ_B is to extend the size of the electron source, i.e., to reduce the spatial coherence.

In order to obtain a large coherent illumination with a high enough intensity, the beam shape is made elliptical using the stigmators. Given the uniaxial symmetry of the biprism, the illumination is set to have the major axis (large coherent area) perpendicular to the biprism direction and the minor axis (small area to have a high intensity) along the biprism direction. This configuration is shown in figure 2.8.

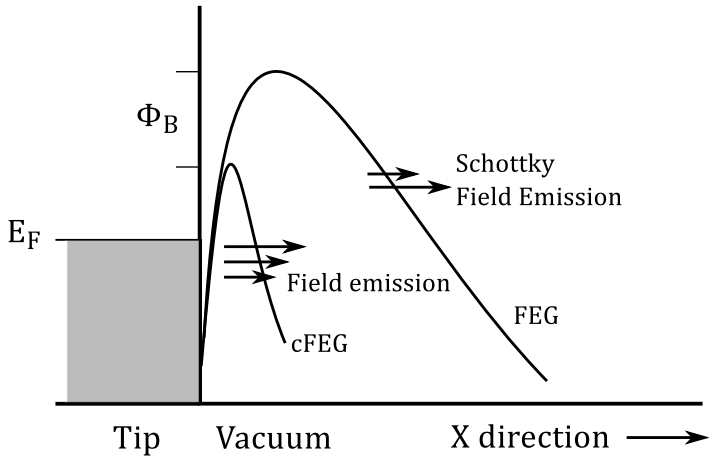

Figure 2.7 Energy potential landscape of the tip-vacuum interface for cFEG and FEG electron sources. The cFEG source is the smallest source and therefore, the most spatially coherent

The image is formed using the Lorentz lens as an objective lens, in order to avoid the strong magnetic field of the regular objective lens on the sample. By applying a voltage to the biprism, electrons that traveled through the sample and electrons that traveled through vacuum are made to overlap on the detector. This results in the recording of the interferometric fringe pattern superimposed to the image. By changing the voltage applied to the biprism, the size of the overlapping area and the spacing of the fringes (resolution) can be adjusted. After the object/vacuum hologram is acquired, a reference vacuum/vacuum hologram is also acquired in the same conditions.

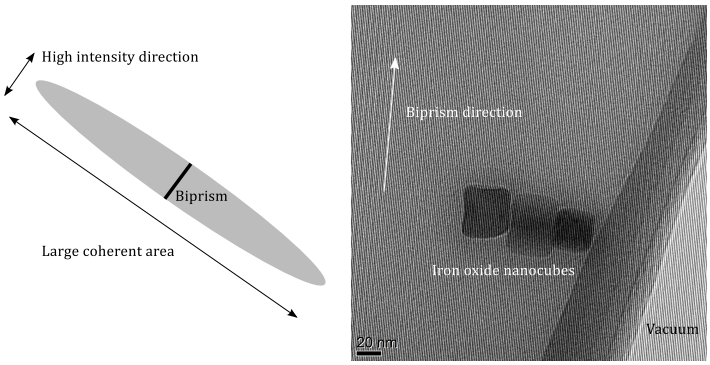

Figure 2.8 a) Elliptical illumination created to obtain a large coherent region and high intensity. b) Example hologram showing the orientation of the biprism and the corresponding interference fringes

As described in section 1.2, the phase shift suffered by electrons travelling through the sample has contributions from both the electrostatic and the magnetic fields in it. In order to make it possible to separate both contributions, two acquisitions are necessary to reverse the vector magnetic field, while the scalar mean inner potential remains the same. The flipping process needed to revert the direction of the magnetic field can be the mechanical flipping of the TEM grid between two hologram acquisitions of the same object. Hopefully, and with a considerable effort, the object can be located in the grid after putting the specimen back in the TEM. This procedure results in 4 holograms for each object of interest: up and down orientations and corresponding vacuum references.

2.2.2 Processing the hologram

The first step in the processing of the hologram is the correction of instrumental artifacts using the reference vacuum hologram

$$\frac{I}{I_{ref}} = \frac{A}{A_{ref}} e^{i(\varphi - \varphi_{ref})} \tag{2.25}$$

As seen in equation 2.21, the FFT of the hologram contains three bands: the center band (the classical TEM image) and two redundant sidebands. A mask is placed in the FFT selecting

either one of the sidebands, excluding the center band and the Fresnel fringes coming from the biprism, as depicted in figure 2.9. The corresponding amplitude and phase images are obtained for both the up and down holograms.

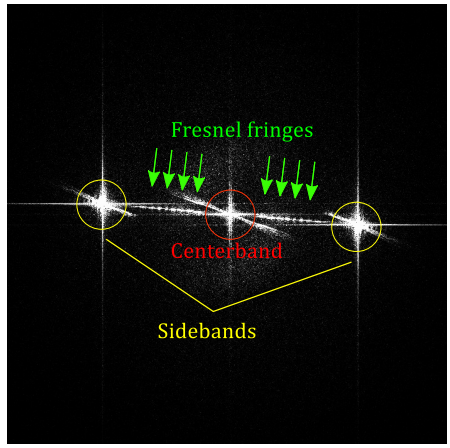

Figure 2.9 FFT of the hologram highlighting the main features. Only one of the sidebands is used in the analysis

The field flipping process results in mirror symmetry and, most likely, a rotation between up and down holograms, which need to be compensated for. Other possible effects, such spatial drift or changes in magnification due to defocus, must also be corrected. The optimum alignment parameters are found when the amplitude difference between the up and down images is nearly zero.

With the correctly aligned up and down phase images, either the electrostatic or the magnetic contribution to the phase shift can be obtained. From equation 2.24, and taking into account the introduced field reversal, we have

$$\varphi_M = \frac{\varphi_{up} - \varphi_{down}}{2} \tag{2.26}$$

$$\varphi_E = \frac{\varphi_{up} + \varphi_{down}}{2} \tag{2.27}$$

Then, the resulting phase images can be unwrapped, i.e., normalized between phases $-\pi$ and π.

2.2.3 Electron holography. State of the art

Off-axis electron holography has been used for the characterization of magnetic, electrostatic and strain fields in the nanoscale for the last decade.

The magnetic configurations of different geometric arrangements of nanoparticles have been studied by electron holography. A first example is the 2008 work by Snoeck et al. [27]. Vortex states were found in single nanocubes. Magnetic field lines coupling in chains of aligned nanoparticles and closed circuits for square arrangements of particles were also unveiled. Ammar et al. [28, 30] studied Permalloy ($Fe_{30}Ni_{70}$) round nanoparticles, finding vortex states and coupling between adjacent nanoparticles.

For nanowires and similar aspect ratio objects, the internal magnetic structure has been extensively studied by electron holography. A groundbreaking work in terms of spatial resolution was carried out by Snoeck et al. in 2003 [26], reporting on the magnetization state of 4 nm diameter cobalt nanowires. Isolated, branched and bundles of nanowires were characterized and shown to be fully magnetized. More recently, Ni nanocylinders 85 nm and 55 nm wide were studied by Biziere et al. [31]. The internal structure of domain walls (DWs) was imaged. Differences in diameter showed a transition from mixed vortex-transverse DWs for the 85 nm cylinders to purely transverse DWs for the 55 nm cylinders. Also in 2013, Murakami et al [32] reported on the effect of antiphase boundaries (APBs) on the size of ferromagnetic domains in $Fe_{2.5}Zn_{0.5}O_4$ nanowires, by means of HRTEM and electron holography.

In thin films, several studies have been carried out on the *in situ* switching of magnetic structures. For instance Javon, in 2010 [33], imaged the local switching of a Magnetic Tunneling Junction (MTJ) consisting in a multilayer of Au/Co/Fe/MgO/-FeV/MgO(001). By acquiring holograms with different magnetic fields applied by a low excitation of the objective lens, a full local hysteresis loop was recorded. A systematic study was presented in 2013 by Rodriguez et al.[29]. After a careful calibration of the objective lens magnetic field with respect to the two tilt axes of the specimen holder, the effect of the out-of-plane component was assessed. It was found that coercive fields in LSMO and

LCMO suffered a variation of up to 10% with the out-of-plane component of the applied magnetic field. A detailed procedure on getting hysteresis loops from electron holography was described and applied to Fe/MgO/FeV MTJ.

In situ polarization experiments in the TEM on a magnetic recording head were reported by Goto et al. in 2013 [34]. The effect on the fringing magnetic field of the bias voltage applied to the writing tip was characterized.

Regarding the electrostatic contribution to the phase shift, one of the first applications was the direct imaging of dopant-related potentials in semiconductor devices. Rau et al. reported for the first time, in 1999 [35], the mapping of electrostatic potentials in the p, n, and depletion regions of a MOSFET transistor, reaching 10 nm spatial resolution and 0.1 V sensitivity. In 2002, Twitchett et al. [36] reported the first *in situ* polarization results, studying the effect of the applied bias voltage on samples with different thicknesses.

In situ polarization experiments were also carried out by de Knoop et al. [37] to characterize the electric field around a carbon nanocone tip, to be used as a cold emitter for electron guns. Besides the mapping of the electric field around the *in situ* polarized tip, I-V curves were acquired and used to determine the work function of the tip, in the Fowler-Nordheim formalism for tunneling current.

Ferroelectric ordering has also been assessed thorough electron holography. The ferroelectric ordering of $BaTiO_3$ nanoparticles has also been studied by *in situ* polarization holography experiments by Polking et al. in 2012 [38]. The structural distortion responsible for ferroelectric ordering could be imaged by exit wave reconstruction techniques. In addition, *in situ* heating experiments in the TEM showed the loss of ferroelectricity above its Curie temperature. Room temperature switching was also shown via *in situ* holography polarization experiments that allowed imaging the fringing field around the cubic particles. A size limit of around 5 nm was determined for the ferroelectric ordering of the particles.

The characterization of charge distribution by electron holography recently reached single elementary charge resolution. In

a work in 2013 by Gatel et al., MgO nanoparticles were studied by aberration corrected electron holography [39]. By directly applying Gauss law at the nanoscale, the contribution to the electrostatic phase shift of the mean inner potential (MIP) and any possible additional charge could be separated and evaluated by a contour integral.

Working at low accelerating voltages, holography can be performed also on beam sensitive carbon based materials. In 2011, Ortolani [40] used holography with a 100 kV electron beam to map and quantify the surface electrostatic potential of Multi Wall Carbon Nanotubes (MWCNTs) and graphene. The number of walls in the nanotubes and the number of layers in graphene was found to be related to the potential.

Dark field holography has been used since 2008 [24] for the characterization, through the geometric phase, of strain fields mainly in semiconducting devices, where strain engineering is crucial for carrier mobility enhancement. The technique is described in detail in [25].

2.3 Geometric Phase Analysis (GPA)

Analysis of the geometric phase can also be performed from HRTEM images. Compared to dark field holography, GPA data from HRTEM is limited to smaller fields of view and is more restrictive with sample thickness. However, the obtained information is equally reliable. The analysis methodology was described in 1998 in a paper by Hÿtch et al.[41], and will be summarized here.

GPA is a Fourier space technique that uses the power spectrum of a lattice image. Two strong reflections in the power spectrum, corresponding to two reciprocal lattice vectors, define a reference framework, a projected 2D unit cell from which to measure distortions. A perfect, long range ordered crystal would produce ideally sharp reflections in the power spectrum. Local distortions in the lattice, on the contrary, give rise to diffuse intensity surrounding the main peaks. GPA consists in filtering the power spectrum and obtaining images from the main reflection and the diffuse scattering. Hence the field of view limitation when compared

with dark field holography: any non-homogeneity in the contrast transfer process (thickness, bending, contamination,...) that can produce contrast reversals can introduce artifacts. The acceptable field of view is limited to regions with image coherence.

Mathematically, the image can be expressed as a Fourier series as

$$I(\vec{r}) = \sum_{g} H_g e^{2\pi(i\cdot\vec{g}\cdot\vec{r})} \tag{2.28}$$

where $\vec{r}$ are the real space (x,y) coordinates and g are the reciprocal lattice vectors corresponding to the reflections in the power spectrum. Fourier coefficients H_g are complex, with the amplitude (A_g) and phase (ϕ_g) of each lattice fringes set. Since the image is a real function, the conjugate symmetry of the Fourier components can be assumed, and the Fourier series can be expressed in a *cos* form

$$I(\vec{r}) = A_0 \sum_{g>0} 2A_g cos(2\pi\vec{r}\cdot\vec{g} + \phi_g) \tag{2.29}$$

where each term in the sum corresponds to the lattice fringes from the lattice vectors $\vec{g}$ and $-\vec{g}$. If we consider now a lattice distortion

$$\vec{g} \rightarrow \vec{g} + \Delta\vec{g} \tag{2.30}$$

the intensity expression for a particular lattice fringes set will be

$$I(\vec{r}) = 2A_g cos(2\pi\vec{r}\cdot\vec{g} + 2\pi\Delta\vec{g}\cdot\vec{r} + \phi_g) \tag{2.31}$$

Comparing this with equation 2.28, the lattice distortion introduces a position dependant phase term (setting the arbitray value of $\varphi_g = 0$)

$$\phi_g(\vec{r}) = 2\pi\Delta\vec{g}\cdot\vec{r} \tag{2.32}$$

In order to construct a phase image, a mask is set in an intense reflection in the power spectrum of the image, and the selected area is inverse Fourier transformed. The gradient of this geometric phase term will be a distortion map for the given lattice fringes set

$$\nabla\phi_g(\vec{r}) = 2\pi\Delta\vec{g} \tag{2.33}$$

From two non co-linear fringes sets, g_1 and g_2, the local r-dependent displacement field can be obtained as

$$\begin{pmatrix} u_x \\ u_y \end{pmatrix} = -\frac{1}{2\pi}\begin{pmatrix} g_{1x} & g_{1y} \\ g_{2x} & g_{2y} \end{pmatrix}\begin{pmatrix} \phi_{g1} \\ \phi_{g2} \end{pmatrix} \tag{2.34}$$

For small displacements, the strain field will be the gradient of the displacement field

$$\epsilon = \begin{pmatrix} \epsilon_{xx} & \epsilon_{xy} \\ \epsilon_{yx} & \epsilon_{yy} \end{pmatrix} = -\frac{1}{2\pi}\begin{pmatrix} g_{1x} & g_{1y} \\ g_{2x} & g_{2y} \end{pmatrix}\begin{pmatrix} \frac{\partial\phi_{g1}}{\partial x} & \frac{\partial\phi_{g1}}{\partial y} \\ \frac{\partial\phi_{g2}}{\partial x} & \frac{\partial\phi_{g2}}{\partial y} \end{pmatrix} \tag{2.35}$$

The symmetric term of this tensor corresponds to strain (ϵ) and the antisymmetric term corresponds to a rigid body rotation (ω). Figure 2.10 summarizes the steps in the GPA analysis of a defect in Te-doped GaAs.

Similar results can be obtained from real space processing of high resolution images. Whereas GPA relies on the analysis in the Fourier space, Peak Pairs Analysis [42] uses intensity peak recognition algorithms. A non-strained area of the specimen is set as a reference, and used to create a square lattice via an affine transformation. When analyzing the image, defects and displacements can be easily detected when peaks fall in non-integer coordinates of the reference lattice. From the displacement field, strain can be calculated in the same way as explained for GPA.

2.3.1 GPA. State of the art

Geometric Phase Analysis (GPA) has been extensively used since its introduction in 1998 by Hÿtch et al. [41]. Originally, it was intented as a tool to be used on HRTEM images, but the incorporation of C_s probe corrected STEMs opened the possibility to apply GPA to any high resolution image.

The 1998 seminal paper reported on the characterization of a domain wall in the perovskite $PbTiO_3$ as a test system. However, a major field of application for GPA has been the characterization

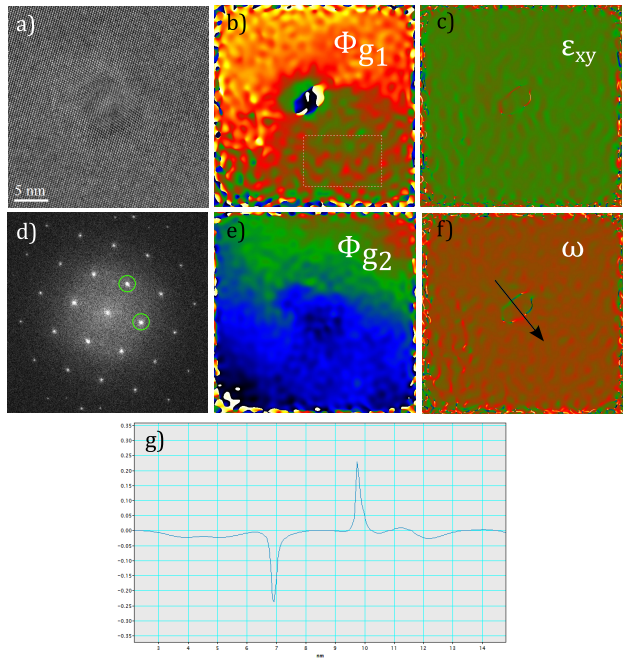

Figure 2.10 a) and d) HRTEM image and power spectrum of a defect in GaAs:Te. Circled spots in the power spectrum are the selected g1 and g2 vectors. b) and e) Mapped phase distortion for g_1 and g_2. e) Strain map. f-g) Lattice rotation map and line profile showing the rotation at both sides of the defect

of semiconducting materials and devices, a field in which strain engineering is a key point. Hÿtch reported in 2003 [43] on the displacement field around a dislocation in Si observed edge-on using HRTEM. The comparison of the calculated displacement fields with simulation allowed the detection of atomic displacements up to a resolution of 0.03Å. For functional semiconducting devices, aberration corrected HRTEM images were used by Hüe et al.[44] to assess the strain in the channel of a Si MOSFET, induced by the SiGe source and drain terminals. The results were in excellent agreement with linear elasticity theory calculations performed using finite element methods. High angle grain boundaries in Si, formed in the direct bonding of $\sim 90^o$ Si(100) and Si(110) wafers, were studied by Cherkashin et al. in 2012 [45]. The surface reconstruction of this interface has a prominent effect on the hole mobility in advanced CMOS circuits. This atomic reconstruction

was characterized through HRTEM images and GPA was used to determine the lattice expansion and rotation.

Heterointerfaces formed by Si and Ge have also been a subject of study. Liu et al.[46] reported on a Si/Ge interface in thin film geometry. The GPA strain maps obtained from the misfit dislocation areas in HRTEM images were compared with the maps calculated using different P-N and Foreman models for pure edge dislocations, in order to choose the best fitting description. More recently, Si/Ge/Si heterointerfaces in nanowires were characterized by Wen et al. [47] by aberration corrected STEM-HAADF. GPA was applied to assess the growth of thin Ge quantum wells, fully stressed in-plane to Si, with an out-of-plane relaxation. A critical thickness of around 3 nm of the Ge layer for the relaxation of both radial and growth direction strain was found. The two latter examples illustrate the importance of dimensionality (2D vs 1D) when studying properties of materials at the nanoscale.

III-V semiconducting systems have also been studied through GPA, mainly from aberration corrected STEM-HAADF images, since Z contrast is of particular interest in binary and ternary compounds. Li et al.[48] studied dislocation cores with different structures in InAs at the atomic level. GPA strain maps showed that dislocation cores act as sources of strain inversion. Stacking faults, on the contrary, leave the strain state unaffected. Also in III-V systems, Zhao et al.[49] studied an AlAsSb/InAs/AlAsSb system with an InAs quantum well. GPA strain mapping showed an out-of-plane variation in the lattice parameter not matching the expected InAs one. This would be in good agreement with the possible segregation of In and/or Sb, resulting in the formation of transient layers at both interfaces of the quantum well.

2.4 Instrumentation used in this thesis

The experimental images and data analyzed in this thesis have been obtained from the following instruments:

- JEOL JEM 2010F, Schottky field emission gun, 200kV, and coupled to a Gatan GIF imaging filter. Located at the Scientific and Technological Centers of Universitat de Barcelona
- JEOL JEM 2100, LaB_6 cathode, 200kV. Located at the Scientific and Technological Centers of Universitat de Barcelona
- FEI Low Base TITAN, equipped with a high brightness Schottky field emission gun (X-FEG), a monochromator and a condenser lens Cs corrector, 80 kV-300 kV. Coupled to a Gatan Tridiem EEL spectrometer. Located at Laboratorio de Microscopías Avanzadas, Instituto de Nanociencia de Aragón, Zaragoza
- FEI TITAN^3, Schottky field emission gun, equipped with an objective lens Cs corrector. 80 kV-300 kV. Equipped with a Lorentz lens and an electrostatic biprism. Located at Laboratorio de Microscopías Avanzadas, Instituto de Nanociencia de Aragon, Zaragoza
- FEI TECNAI F30, Schottky field emission gun, operated at 300 kV and coupled to a Gatan GIF Tridiem energy filter. Located at Laboratorio de Microscopías Avanzadas, Instituto de Nanociencia de Aragón, Zaragoza
- Hitachi HF3300-I2TEM, cold field emission gun, 300 kV, equipped with an objective lens Cs corrector and four electrostatic biprisms. Located at Centre d'Elaboration des Matériaux et d'Etudes Structurales (CEMES-CNRS), Toulouse
- FEI SACTEM TECNAI F20, Schottky emission gun, 200 kV. Located at Centre d'Elaboration des Matériaux et d'Etudes Structurales (CEMES-CNRS), Toulouse
- FEI TITAN^3, equipped with a high brightness Schottky field emission gun (X-FEG) and a condenser lens Cs corrector, 80 kV-300 kV. Located at École Centrale des Arts et Manufactures, Paris

- JEOL JEM 3000F, equipped with a Schottky field emission gun, 300 kV. Located at Centro Nacional de Microscopía Electrónica, Madrid.
- JEOL ARM 200cF, equipped with a cold Field Emission Gun (cFEG), 200 kV, Cs aberration corrector in the condenser lens system and a Quantum Gatan Imaging Filter. Located at Centro Nacional de Microscopía Electrónica, Madrid.

Bibliography

[1] S. Bernal, F. Botana, J. Calvino, C. Lopez-Cartes, J. Perez-Omil, and J. Rodriguez-Izquierdo. The interpretation of HREM images of supported metal catalysts using image simulation: Profile view images. *Ultramicroscopy*, 72(3-4):135–164, 1998.

[2] J. Pérez-Omil. *Interpretación sistemática de imágenes de microscopía electrónica de alta resolución de materiales policristalinos. Estudio de catalizadores metálicos soportados.* PhD thesis, Universidad de Cádiz, 1994.

[3] S. Horiuchi. Effect of the phase shift due to dynamical scattering on the contrast of crystal structure images. *Ultramicroscopy*, 10:229–236, 1982.

[4] N. Daneu, A. Rečnik, T. Yamazaki, and T. Dolenec. Structure and chemistry of (111) twin boundaries in $MgAl_2O_4$ spinel crystals from Mogok. *Physics and Chemistry of Minerals*, 34(4):233–247, 2007.

[5] F. Pailloux, M.L. David, and L. Pizzagalli. Quantitative HRTEM investigation of nanoplatelets. *Micron*, 41(2):135–142, 2010.

[6] P. Ruterana, P. Singh, S. Kret, G. Jurczak, G. Maciejewski, P. Dluzewski, H.K. Cho, R.J. Choi, H.J. Lee, and E.K. Suh. Quantitative evaluation of the atomic structure of defects and composition fluctuations at the nanometer scale inside InGaN/GaN heterostructures. *Physica Status Solidi (B)*, 241(12):2735–2738, 2004.

[7] C.L. Jia and K. Urban. Atomic-resolution measurement of oxygen concentration in oxide materials. *Science*, 303(5666):2001–4, 2004.

[8] L. Houben. Aberration-corrected HRTEM of defects in strained La_2CuO_4 thin films grown on $SrTiO_3$. *Journal of Materials Science*, 41(14):4413–4419, 2006.

[9] M. Texier, B. Pichaud, M.F. Beaufort, and J.F. Barbot. Structural disordering and extended defects produced by He-implantation in silicon carbide. *Journal of Physics D: Applied Physics*, 46(48):485105, 2013.

[10] J. An, A.L. Koh, J.S. Park, R. Sinclair, T.M. Gür, and F.B. Prinz. Aberration-corrected TEM imaging of oxygen occupancy in YSZ. *The Journal of Physical Chemistry Letters*, 4(7):1156–1160, 2013.

[11] S. Van Aert, J. Verbeeck, R. Erni, S. Bals, M. Luysberg, D. Van Dyck, and G. Van Tendeloo. Quantitative atomic resolution mapping using high-angle annular dark field scanning transmission electron microscopy. *Ultramicroscopy*, 109(10):1236–44, 2009.

[12] G.T. Martinez, A. De Backer, A. Rosenauer, J. Verbeeck, and S. Van Aert. The effect of probe inaccuracies on the quantitative model-based analysis of high angle annular dark field scanning transmission electron microscopy images. *Micron*, 63:57–63, 2014.

[13] J.M. Lebeau and S. Stemmer. Experimental quantification of annular dark-field images in scanning transmission electron microscopy. *Ultramicroscopy*, 108(12):1653–8, 2008.

[14] J. LeBeau, S. Findlay, L. Allen, and S. Stemmer. Quantitative atomic resolution Scanning Transmission Electron Microscopy. *Physical Review Letters*, 100(20):206101, 2008.

[15] J. LeBeau, S. Findlay, X. Wang, A. Jacobson, L. Allen, and S. Stemmer. High-angle scattering of fast electrons from crystals containing heavy elements: Simulation and experiment. *Physical Review B*, 79(21):214110, 2009.

[16] A. Rosenauer, T. Mehrtens, K. Müller, K. Gries, M. Schowalter, P.V. Satyam, S. Bley, C. Tessarek, D. Hommel, K. Sebald, M. Seyfried, J. Gutowski, A. Avramescu, K. Engl, and S. Lutgen. Composition mapping in InGaN by scanning transmission electron microscopy. *Ultramicroscopy*, 111(8):1316–27, 2011.

[17] D.A. Blom. Multislice frozen phonon high angle annular dark-field image simulation study of Mo-V-Nb-Te-O complex oxidation catalyst "M1". *Ultramicroscopy*, 112(1):69–75, 2012.

[18] S.D. Findlay and J.M. LeBeau. Detector non-uniformity in scanning transmission electron microscopy. *Ultramicroscopy*, 124:52–60, 2013.

[19] H. E, K.E. Macarthur, T.J. Pennycook, E. Okunishi, A.J. D'Alfonso, N.R. Lugg, L.J. Allen, and P.D. Nellist. Probe integrated scattering cross sections in the analysis of atomic resolution HAADF STEM images. *Ultramicroscopy*, 133:109–19, 2013.

[20] T. Mizoguchi, S. D Findlay, A. Masuno, Y. Saito, K. Yamaguchi, H. Inoue, and Y. Ikuhara. Atomic-scale identification of individual lanthanide dopants in optical glass fiber. *ACS Nano*, 7(6):5058–5063, 2013.

[21] V. Grillo. The effect of surface strain relaxation on HAADF imaging. *Ultramicroscopy*, 109(12):1453–64, 2009.

[22] H. Kauko, T. Grieb, R. Bjø rge, M. Schowalter, A.M. Munshi, H. Weman, A. Rosenauer, and A.T. J. van Helvoort. Compositional characterization of GaAs/GaAsSb nanowires by quantitative HAADF-STEM. *Micron*, 44:254–60, 2013.

[23] S. Kim, Y. Oshima, Y. Tanishiro, and K. Takayanagi. Study on probe current dependence of the intensity distribution in annular dark field images. *Ultramicroscopy*, 121:38–41, 2012.

[24] M. Hÿtch, F. Houdellier, F. Hüe, and E. Snoeck. Nanoscale holographic interferometry for strain measurements in electronic devices. *Nature*, 453(7198):1086–9, 2008.

[25] M.J. Hÿtch, F. Houdellier, F. Hüe, and E. Snoeck. Dark-field electron holography for the measurement of geometric phase. *Ultramicroscopy*, 111(8):1328–37, 2011.

[26] E. Snoeck, R.E. Dunin-Borkowski, F. Dumestre, P. Renaud, C. Amiens, B. Chaudret, and P. Zurcher. Quantitative magnetization measurements on nanometer ferromagnetic cobalt wires using electron holography. *Applied Physics Letters*, 82(1):88, 2003.

[27] E. Snoeck, C. Gatel, L.M. Lacroix, T. Blon, S. Lachaize, J. Carrey, M. Respaud, and B. Chaudret. Magnetic configurations of 30 nm iron nanocubes studied by electron holography. *Nano letters*, 8:4293–4298, 2008.

[28] M. Ammar, M. LoBue, E. Snoeck, M. Hÿtch, Y. Champion, R. Barrué, and F. Mazaleyrat. A quantitative analysis of magnetic vortices in Permalloy nanoparticles characterized by electron holography. *Journal of Magnetism and Magnetic Materials*, 320(20):e716–e719, 2008.

[29] L.A. Rodríguez, C. Magén, E. Snoeck, C. Gatel, L. Marín, L. Serrano-Ramón, J.L. Prieto, M. Muñoz, P.A. Algarabel, L. Morellon, J.M. De Teresa, and M.R. Ibarra. Quantitative in situ magnetization reversal studies in Lorentz microscopy and electron holography. *Ultramicroscopy*, 134:144–54, 2013.

[30] M. LoBue, F. Mazaleyrat, M. Ammar, R. Barrué, Y. Champion, S. Faure, M. Hÿtch, E. Snoeck, J. Steiner, and F. Alouges. Observation and modelling of magnetic vortex core structure in Permalloy nanoparticles. *Journal of Magnetism and Magnetic Materials*, 322(9-12):1290–1292, 2010.

[31] N. Biziere, C. Gatel, R. Lassalle-Balier, M.C. Clochard, J.E. Wegrowe, and E. Snoeck. Imaging the fine structure of a magnetic domain wall in a Ni nanocylinder. *Nano letters*, 13(5):2053–7, 2013.

[32] Y. Murakami, A. Ohta, T. Kanki, S. Aizawa, T. Tanigaki, H.S. Park, H. Tanaka, and D. Shindo. Revealing magnetic domain

structure in functional $Fe_{2.5}Zn_{0.5}O_4$ wires by transmission electron microscopy. *Acta Materialia*, 64:144–153, 2014.

[33] E. Javon, C. Gatel, A. Masseboeuf, and E. Snoeck. Electron holography study of the local magnetic switching process in magnetic tunnel junctions. *Journal of Applied Physics*, 107(9):09D310, 2010.

[34] T. Goto, J.S. Jeong, W. Xia, Z. Akase, D. Shindo, and K. Hirata. Electron holography of magnetic field generated by a magnetic recording head. *Microscopy*, 62(3):383–9, 2013.

[35] W. Rau, P. Schwander, F. Baumann, W. Höppner, and A. Ourmazd. Two-dimensional mapping of the electrostatic potential in transistors by electron holography. *Physical Review Letters*, 82(12):2614–2617, 1999.

[36] A. Twitchett, R. Dunin-Borkowski, and P.A. Midgley. Quantitative electron holography of biased semiconductor devices. *Physical Review Letters*, 88(23):238302, 2002.

[37] L. de Knoop, F. Houdellier, C. Gatel, A. Masseboeuf, M. Monthioux, and M. Hÿtch. Determining the work function of a carbon-cone cold-field emitter by in situ electron holography. *Micron*, 63:2–8, 2014.

[38] M.J. Polking, M.G. Han, A. Yourdkhani, V. Petkov, C.F. Kisielowski, V.V. Volkov, Y. Zhu, G. Caruntu, A.P. Alivisatos, and R. Ramesh. Ferroelectric order in individual nanometre-scale crystals. *Nature materials*, 11(8):700–9, 2012.

[39] C. Gatel, A. Lubk, G. Pozzi, E. Snoeck, and M. Hÿtch. Counting elementary charges on nanoparticles by electron holography. *Physical Review Letters*, 111(2):025501, 2013.

[40] L. Ortolani, F. Houdellier, M. Monthioux, E. Snoeck, and V. Morandi. Surface electrostatic potentials in carbon nanotubes and graphene membranes investigated with electron holography. *Carbon*, 49(4):1423–1429, 2011.

[41] M.J. Hÿtch, E. Snoeck, and R. Kilaas. Quantitative measurement of displacement and strain fields from HREM micrographs. *Ultramicroscopy*, 74(3):131–146, 1998.

[42] P. Galindo, S. Kret, A.M. Sánchez, J. Laval, A. Yáñez, J. Pizarro, E. Guerrero, T. Ben, and S.I. Molina. The Peak Pairs algorithm for strain mapping from HRTEM images. *Ultramicroscopy*, (107):1186–1193, 2007.

[43] M. Hytch, J.L. Putaux, and J.M. Penisson. Measurement of the displacement field of dislocations to 0.03 by electron microscopy. *Nature*, 423(May):270–273, 2003.

[44] F. Hüe, M. Hÿtch, H. Bender, F. Houdellier, and A. Claverie. Direct mapping of strain in a strained silicon transistor by high-resolution electron microscopy. *Physical Review Letters*, 100(15):28–31, 2008.

[45] N. Cherkashin, O. Kononchuk, S. Reboh, and M. Hÿtch. Application of the O-lattice theory for the reconstruction of the high-angle near 90 degree tilt Si(110)(001) boundary created by wafer bonding. *Acta Materialia*, 60(3):1161–1173, 2012.

[46] Q.L. Liu, C.W. Zhao, Y.M. Xing, S.J. Su, and B.W. Cheng. Quantitative strain analysis of misfit dislocations in a Si / Ge heterostructure interface by geometric phase analysis. *Optics and Lasers in Engineering*, 50(5):796–799, 2012.

[47] C.Y. Wen, M.C. Reuter, D. Su, E.A. Stach, and F.M. Ross. Strain and stability of ultrathin Ge layers in Si/Ge/Si axial heterojunction nanowires. *Nano Letters*, page 150212153538002, 2015.

[48] L. Li, Z. Gan, M.R. McCartney, H. Liang, H. Yu, Y. Gao, J. Wang, and D.J. Smith. Atomic configurations at InAs partial dislocation cores associated with Z-shape faulted dipoles. *Scientific reports*, 3:3229, 2013.

[49] Y. Zhao, J. Nicolaï, N. Bertru, H. Folliot, M. Perrin, C. Gatel, B. Warot-Fonrose, and Anne. Ponchet. Sb surfactant mediated growth of InAs/$AlAs_{0.56}Sb_{0.44}$ strained quantum well for intersubband absorption at 1.55 micron. *Applied Physics Letters*, 106(8):081908, 2015.

Chapter 3

3D materials: ordering/disordering in cationic or anionic sublattices

3.1 Introduction

In this chapter we are involved in the occurrence of local order/disorder (either structural, chemical, or both) in the framework of long range ordered crystals. In particular, rare earth niobates (RE_3NbO_7, RE = Y, Yb, Er, Lu) as well as strontium barium niobate ($Sr_{0.67}Ba_{0.33}Nb_2O_6$) will be investigated using TEM techniques. We will consider these systems as 3D nanomaterials since, in spite of not having any dimensions constrained under 100 nm, they present structural features in the nano and sub-nano length scales that play an important role in the properties of the bulk material, and require the appropriate nano-tools to access local information.

Rare earth niobates are investigated mainly by diffraction techniques. The analysis of the SAED patterns obtained in transmission mode allows for the characterization of local ordering phenomena, through the study of diffuse scattering intensity. A reciprocal space model can be obtained and subsequently tested by comparison of experimental and simulated HRTEM images. The

characterization of the local structure of the material is crucial for understanding its functionality and performance as a proton conducting electrolyte for solid oxide fuel cells (SOFCs).

In the case of strontium barium niobate, the study of diffuse scattering intensity in SAED patterns is used to assess the presence of a structural disorder. In addition to uncorrected TEM and STEM, the capabilities of aberration corrected STEM are used in full. By using aberration corrected STEM-HAADF imaging, the cation sublattice can be imaged in direct space at the atomic level. Through ABF imaging, the anion sublattice can be also imaged, completing a full structural characterization. In addition, aberration corrected STEM combined with EELS spectrum imaging allows assessing the degree of chemical disorder in the structure. Local disorder phenomena in this material are critical to understand the origin of its ferroelectric relaxor properties.

3.2 RE_3NbO_7

3.2.1 Solid Oxide Fuel Cells. Proton conductors

Solid oxide fuel cells (SOFCs) are a promising source of electrical power for a wide range of applications. They provide high efficiency and very low environmental impact without involving any combustion process. However, the high operating temperatures, leading to problems involving the cost and aging of devices, is one of the main issues regarding this technology. In this sense, proton conducting materials allow for lower operating temperatures with a higher conductivity, proton transport being a lower activation energy process than oxygen ion transport [1].

The first proton conductor materials were acceptor doped ABO_3 perovskites (*i.e.*, barium cerates and barium zirconates) [2–4], and they remain the most studied systems. Although for these materials low doping values (8–10%) of Ga, Sc, In, or other trivalent atoms are needed in order to avoid the formation of ordered domains of vacancies, other inherently defective oxides can present oxygen ion/proton conductivity with no doping [5, 6]. The best known inherently defective compound is probably $Ba_2In_2O_5$, which presents a brownmillerite type structure with oxygen-vacancy ordering at low temperature but becomes fully disordered at high temperature, with a great amount of "free" oxygen vacancies, with no need for doping.

The rare earth niobates RE_3NbO_7 studied here are also inherently defective oxides and belong to the so-called defect-fluorite family. Considering the AO_2 fluorite generic formula, RE_3NbO_7 are intrinsic defective oxides since they present, with no doping, one oxygen vacancy every eight oxygen sites. Within this family, Y_3NbO_7 studies have been reported in the literature [7–10]. It has been shown that Y_3NbO_7 is a pure oxygen ion conductor in a wide range of oxygen partial pressures which remains stable at high temperatures under both oxidizing and reducing atmospheres [7]. The level of conductivity at 800^oC is still, nevertheless, much below that of 8% yttria-doped zirconia (YSZ). It has also been shown by transmission Electron Microscopy (TEM) that Y_3NbO_7 presents, locally, superstructure features which are attributed to oxygen vacancies ordering [9]. This ordering would explain the

low level of conductivity observed in spite of the high amount of oxygen vacancies.

In this section, we extend this study to other RE_3NbO_7 compounds, also with a fluorite structure. The objective here is to determine whether the conclusions drawn for the Y_3NbO_7 compound are still valid for smaller rare-earth atoms, i.e., to find out whether the observed vacancy ordering depends on the rare-earth cation or is essentially related to the 1/8 fraction of oxygen vacancies in oxygen sites. A series of four rare earth (Y, Er, Yb, and Lu) compounds with the general formula RE_3NbO_7 have been studied by TEM.

3.2.2 Sample growth and preliminary characterization

The series of RE_3NbO_7 compounds with RE = Y, Er, Yb, Lu were obtained by the group of Prof. Dezanneau at Laboratoire Structures Propriétés et Modélisation des Solides (SPMS), École Centrale Paris, by the self-propagating high-temperature synthesis (SHS) technique, or combustion route [1]. They also carried out the X-Ray diffraction and Raman characterization of the samples. X-ray diffraction indicated a fluorite structure (space group $Fm\bar{3}m$) for the whole series, with a cell parameter which increases with rare earth ion radius, as can be seen in figure 3.1(a), and table 3.1. Regarding Raman spectroscopy results, in the samples under study, four low intensity peaks with diffuse maxima were found in the spectra at low frequencies, in addition to the expected fluorite mode at around 800 cm^{-1}, as shown in figure 3.1b. It can also be seen that the fluorite mode increases in intensity with RE ion radius.

Given the limited spatial resolution of both XRD and Raman spectrosocopy, TEM techniques are needed to unveil the relevant local structural information.

3.2.3 Superstructure modulation in HRTEM images

Samples were prepared for TEM observation by solution of the powder in ethanol and subsequent dispersion on a holey carbon film covered copper mesh grid. Additionally, samples were also prepared from sintered pellets by using the FIB *in situ* lift-out

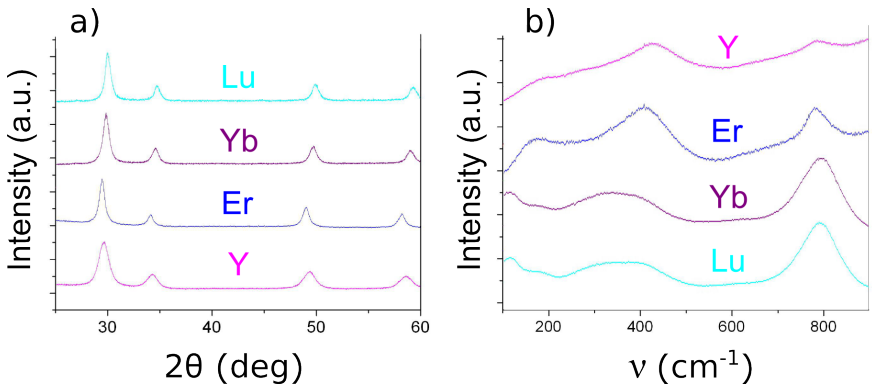

Figure 3.1 a) XRD patterns for the four studied rare earth compounds. The measured cell parameter increases according to the RE ion radius. There is an increase in the broadening of the peaks from Lu_3NbO_7 to Y_3NbO_7. b) Raman spectra for the four compounds. Besides the expected fluorite mode at around 800 cm^{-1}, lower frequency modes are excited. The expected fluorite mode increases in intensity with RE ion radius.

Compound	RE ionic radius (Å)	a (Å)
Lu_3NbO_7	1.11(7)	5.18(0)
Yb_3NbO_7	1.12(5)	5.20(0)
Er_3NbO_7	1.14(4)	5.22(9)
Y_3NbO_7	1.15(0)	5.25(9)

Table 3.1 Rare earth ion radii from [11] and [12] and cell parameters obtained for the four compounds from XRD experiments. The tabulated ionic radii correspond to the RE^{3+} in octahedral coordination. Ionic radius for Nb^{5+} in octahedral coordination is 0.86 Å.

technique. See Appendix B for the sample preparation details. TEM observations were carried out in a JEOL 2100 microscope operating at 200 kV and in a JEOL J3000F microscope operating at 300 kV.

Figure 3.2 shows high resolution transmission electron microscopy (HRTEM) images of the Er, Y and Lu compounds in powder form. They all present regions with a superstructure contrast modulation when indexed according to the ideal fluorite cell. For the Er_3NbO_7 compound (Fig. 3.2(a,d)), a superstructure contrast modulation is visible in the (111) planes of the HRTEM image taken along the [011] zone axis. In the close up view in panel (d), the presence of two differently oriented modulated regions

and of regions with no modulation is illustrated. For Y_3NbO_7 (Fig. 3.2(b)) a 2x superstructure modulation occurring on the (111) planes is also apparent in the HRTEM image taken along the [211] zone axis. As it can be seen, some of these modulation lines form zig-zag structures, going from a dark/bright to a bright/dark contrast, corresponding to antiphase boundaries (APB). For Lu_3NbO_7 (3.2(c)) an equivalent contrast modulation is found. APBs are also observed.

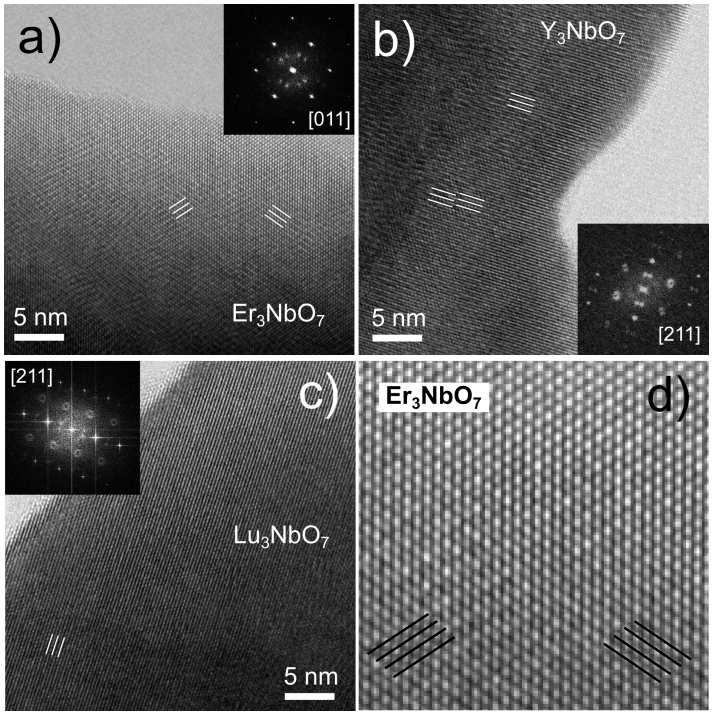

Figure 3.2 a) HRTEM image of the Er_3NbO_7 powder sample oriented along the [011] zone axis and corresponding FFT. White lines highlight the $2 \times d_{111}$ modulation in two different orientations. b) Y_3NbO_7 powder sample viewed along the [211] zone axis and corresponding FFT. In addition to the $2 \times d_{111}$ superstructure modulation, APBs are evidenced by the contrast inversion highlighted by the two sets of white lines. c) Lu_3NbO_7 powder sample viewed along the [211] zone axis and corresponding FFT. Equivalent superstructure modulation and APBs are found. d) Close-up view of the region highlighted in (a) showing the coexistance of small domains with no modulation, and modulations with two different <111> orientations.

FFTs obtained from the HRTEM images are shown in the insets in figure 3.2. They all present the expected reflections for a fluorite structure and additional diffuse scattering features. In the case of the Er_3NbO_7 compound viewed along the [011] direction, split spots appear at half the reciprocal distances of the fluorite reflections. For the Y_3NbO_7 and Lu_3NbO_7 compounds, both observed along the [211] zone axis, diffuse features consist in split spots and rings located also at half the reciprocal distances of the fluorite reciprocal lattice.

3.2.4 Diffuse scattering in SAED patterns

In order to identify the structural features related to the additional diffuse scattering observed in the FFTs of HRTEM images, SAED experiments in several zone axis orientations were also performed. Electron diffraction patterns were obtained for all the studied compounds from powder samples. As for the FFTs, they all show the characteristic reflections of the fluorite structure as well as diffuse scattering features consisting in split spots and diffuse rings. Considering the fluorite reciprocal lattice vectors, $\vec{G_F}$, diffuse scattering can be described using a modulation vector $\vec{q}$, as $\vec{G_F} \pm \vec{q}$.

Figure 3.3b shows the diffraction pattern of the Y_3NbO_7 sample along the [211] zone axis. Split spots appear at both sides of $\vec{G_F} \pm \frac{1}{2}(111)$ and equivalent directions, and diffuse rings appear at $\vec{G_F} \pm \frac{1}{2}(11\bar{3})$ and equivalent directions.

Figure 3.4 shows three diffraction patterns collected along different zone axes for the Er_3NbO_7 compound. In the $[0\bar{1}1]$ zone axis, split spots appear at both sides of $\vec{G_F} \pm \frac{1}{2}(111)$ and equivalent directions, but no diffuse rings are present. In the [031] zone axis, split spots appear at $\vec{G_F} \pm \frac{1}{2}(3\bar{1}\bar{3})$ and equivalent directions. For the [211] zone axis, the same diffraction results as for the Y_3NbO_7 sample are recovered: split spots appear at both sides of $\vec{G_F} \pm \frac{1}{2}(111)$ and equivalent directions, and diffuse rings appear at $\vec{G_F} \pm \frac{1}{2}(11\bar{3})$ and equivalent directions.

Figure 3.5 shows four diffraction patterns collected along different zone axes for the Lu_3NbO_7 sample. In the [233] zone axis, split spots appear again at $\vec{G_F} \pm \frac{1}{2}(111)$, and diffuse rings appear

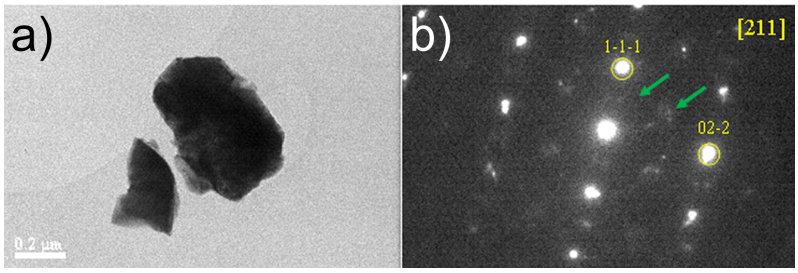

Figure 3.3 a) BF image of the powder Y_3NbO_7 sample. b) SAED of the Y_3NbO_7 powder sample along the [211] zone axis. Fluorite lattice reflections are circled in the diffraction pattern, while additional spots are highlighted with arrows.

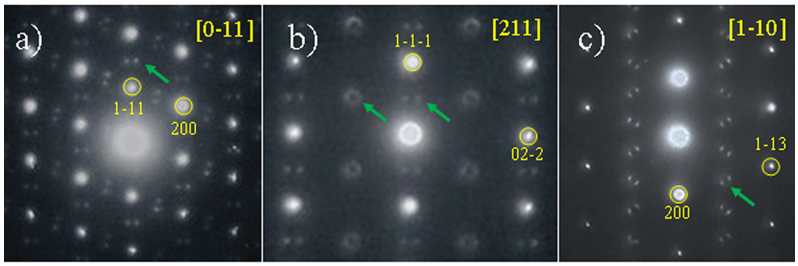

Figure 3.4 Diffraction patterns obtained along different zone axes of the Er_3NbO_7 powder sample. Fluorite lattice reflections are circled and diffuse scattering features are highlighted with arrows.

at $\vec{G_F} \pm \frac{1}{2}(1\bar{1}3)$. In the [031] zone axis, split spots appear at $\vec{G_F} \pm \frac{1}{2}(3\bar{1}\bar{3})$ and equivalent directions. In the $[0\bar{1}1]$ zone axis, split spots appear at both sides of $\vec{G_F} \pm \frac{1}{2}(111)$ and equivalent directions, but no diffuse rings are present. In the [211] zone axis split spots appear at both sides of $\vec{G_F} \pm \frac{1}{2}(111)$ and equivalent directions, and diffuse rings appear at $\vec{G_F} \pm \frac{1}{2}(11\bar{3})$ and equivalent directions.

In order to rule out structural changes induced by the sintering process, equivalent SAED experiments were also performed for the sintered pellets. In this case, TEM samples were prepared by the FIB lift-out method, as illustrated in 3.6. Panels (a) and (b) show secondary electron images obtained during the FIB preparation process, with the lamella cut on the Er_3NbO_7 pellet and attached to the copper grid, respectively. Panel (c) shows a BF TEM image of the final electrotransparent sample. Diffraction contrast from

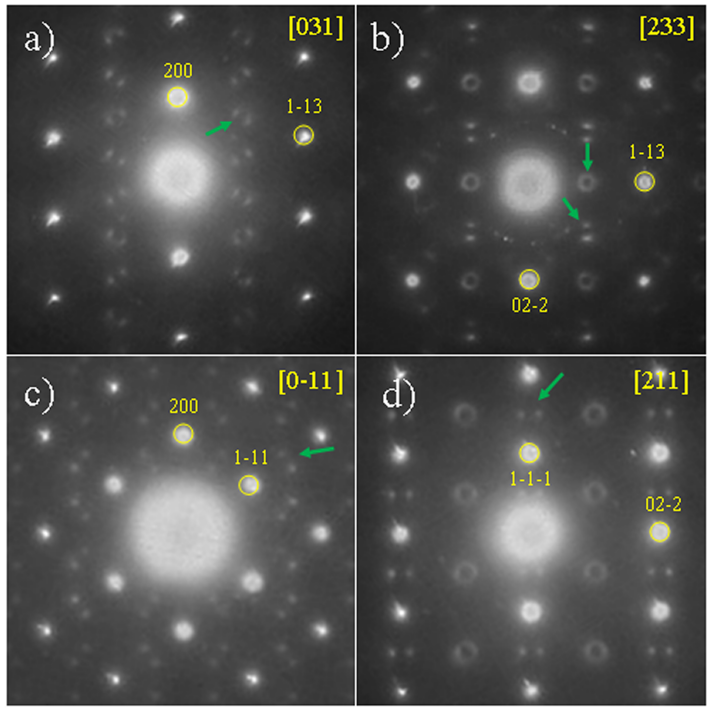

Figure 3.5 Diffraction patterns along different zone axes of the Lu_3NbO_7 powder sample. Fluorite lattice reflections are circled and diffuse scattering features are highlighted with arrows.

grains with different orientations is apparent. Panel (d) shows a BF image of the lamella obtained from the Y_3NbO_7 pellet. Setting up the proper two beam conditions (as explained in Chapter 1), and placing an objective aperture in the $\vec{G} \neq 0$, the resulting DF image presents bright contrast only for the grain in a strong Bragg condition for the selected reflection. Panels (e-g) display the DF images obtained selecting different reflections. Grains with no contrast difference in BF image can be seen in sharp contrast in DF. Grain sizes below 1μm were found for all samples.

SAED patterns for the sintered pellets are shown in figure 3.7. Panel (a) shows the SAED for Y_3NbO_7 oriented along the [211] zone axis. Diffuse scattering features appear as split spots at both sides of $\vec{G_F} \pm \frac{1}{2}(1\bar{1}\bar{1})$ and as rings located at $\vec{G_F} \pm \frac{1}{2}(11\bar{3})$. Panel (b) shows a SAED pattern from the Yb_3NbO_7 sintered pellet sample oriented along the $[0\bar{1}1]$ zone axis. Diffuse scaterring consists in

split spots at both sides of $\vec{G_F} \pm \frac{1}{2}(1\bar{1}1)$. Diffuse scattering found along with the fluorite lattice reflections for all the samples cut from sintered pellets can be described by the same modulation vector as was found for the powder samples.

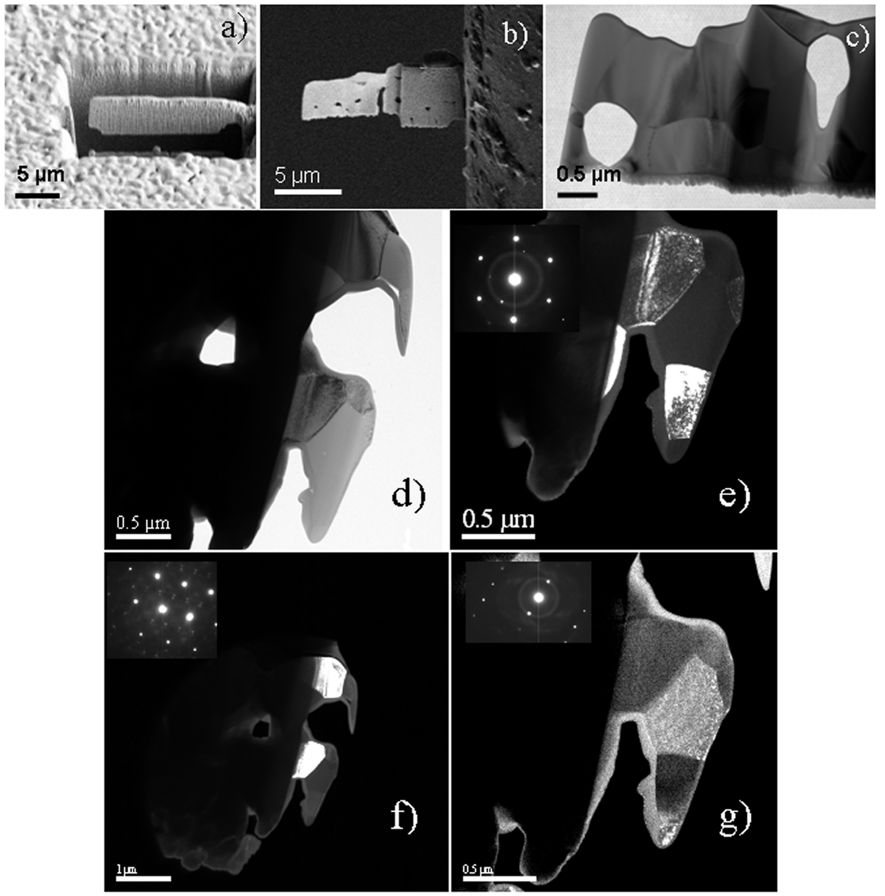

Figure 3.6 a-c) Different steps of the FIB lift-out TEM sample preparation process of the Er_3NbO_7 sintered pellet. (a) and (b) are secondary electron images and (c) is a BF image taken in the TEM. Notice the preservation of grain boundaries after the preparation of the thin lamella. d-g) Y_3NbO_7 sintered sample as prepared by FIB. Grain boundaries are visible in the bright field image (d), and particular grains in diffracting conditions are highlighted in dark field images (e), (f) and (g).

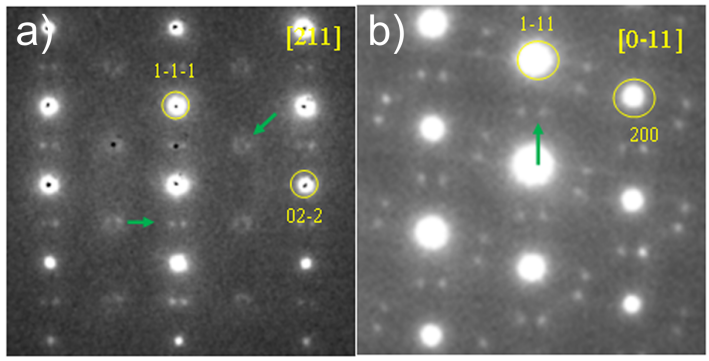

Figure 3.7 SAED patterns from the Y_3NbO_7 (a) and Yb_3NbO_7 (b) sintered samples.

3.2.5 Interpreting diffraction patterns. Local ordering effects.

A reciprocal space model is needed to interpret the data from the extensive SAED study carried out on the series of rare earth niobates. Pyrochlore ($A_2B_2O_7$) is a second order superstructure of fluorite, with a stacking of half the fluorite periodicity along the $[111]_F$ direction. In pyrochlore, pairs of layers with cation coordination numbers 8 and 6, respectively, are stacked along $[111]_F$, while in perfect fluorite all cations are in an 8-coordination cubic environment, as depicted in figure 3.8. In the system under study, the inherent oxygen deficiency of the RE_3NbO_7 with respect to the ideal fluorite structure could lead to the formation of a pyrochlore phase by the local ordering of the oxygen vacancies on one of the corners of the cubes along the $[111]_F$ direction.

Long range pyrochlore ordering is to be avoided mainly by the difference in ionic radius between the large rare earth and the smaller niobium cations sharing the same crystallographic site, which should cause a deformation of the coordination polyhedra.

The proposed microstructure of the material should consist, then, in somewhat small domains of the pyrochlore phase embedded in a fluorite matrix. Scattering of the electron beam by such a system is illustrated in figure 3.9(b). The presence of multiple, randomly oriented, pyrochlore domains results in an annular diffuse scattering intensity distribution around the expected long-range order spot for the pyrochlore phase. The finite size of

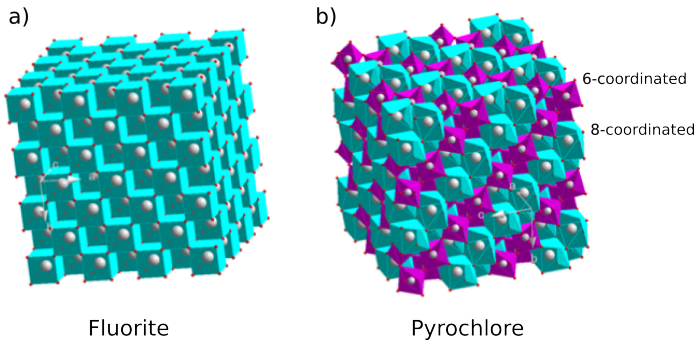

Figure 3.8 a) Fluorite structure (AO_2, space group $Fm\bar{3}m$). A cations are in an 8-coordinated cubic environment. b) Pyrochlore ($A_2B_2O_7$, space group $Fd\bar{3}m$) is a second order superstructure of the fluorite structure. Layers of 6-coordinated and 8-coordinated atoms are stacked alternately along the [111] direction.

the domains is responsible for the spread of the reflection, and the random orientation is responsible for the annular symmetry. Figure 3.9 also shows the two extreme cases: the perfect fluorite and pyrochlore structures. Should the pyrochlore domain size increase in the sample, the radius of the diffuse scattering ring would decrease until collapsing in the superstructure spot for the long-range ordered, monodomain pyrochlore.

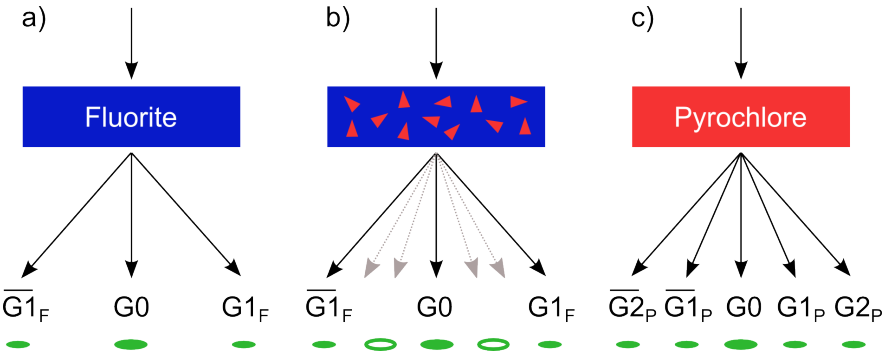

Figure 3.9 Scheme of the diffraction of the electron beam by a) a fluorite crystal, b) a fluorite matrix with randomly oriented pyrochlore domains and c) a pyrochlore crystal.

By drawing the corresponding diffuse rings around the $\frac{1}{2}(hkl)_F$ positions, the reciprocal space configurations corresponding to each of the cases in figure 3.9 can be obtained. They are shown

in figure 3.10. In the experimental SAED patterns, diffuse rings and split spots appear at the expected positions for the ideal pyrochlore superstructure reflections, doubling the fluorite cubic cell. Remarkably, all the experimental results can be explained in terms of the reciprocal space model in figure 3.10(b): diffuse rings appear whenever the Ewald sphere is tangent to them, and pairs of spots appear whenever the sphere cuts the rings in the reciprocal space.

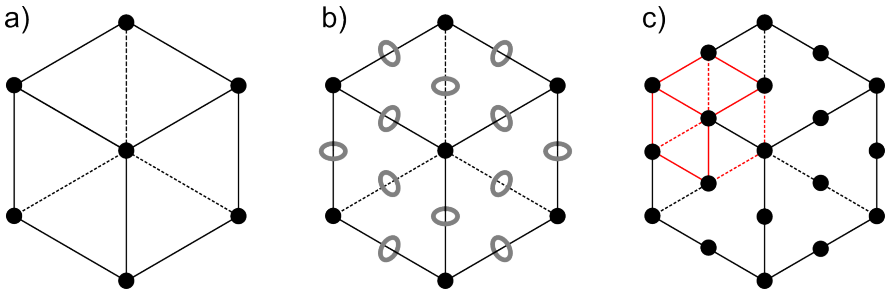

Figure 3.10 Qualitative reciprocal space models for a) fluorite, b) randomly oriented pyrochlore domains in a fluorite matrix and c) pyrochlore. The finite size and random orientation of the pyrochlore ordered domains in b) is responsible for the ring shaped diffuse scattering features.

HRTEM images show direct evidence of these local ordered domains, with contrast modulation occurring along the <111> directions of the fluorite unit cell, as expected for pyrochlore.

Raman spectroscopy results are consistent with the presence of short-range ordered domains. For a perfect fluorite structure, a single phonon mode is expected to be Raman active, while pyrochlore structure presents six Raman active normal vibration modes. This is in good agreement with the lower frequency modes observed in the Raman spectra shown in figure 3.1(b). As for XRD results, it is worth noticing that lateral resolution lies in the range of microns. Small domains of pyrochlore phase with sizes below the XRD sensitivity threshold (*i.e.*, <300 Å) are still consistent with the observations. The broadening of the XRD fluorite peak with RE cation radius can be understood as the result of an increasing disorder: the larger the difference between RE and Nb, the sooner the pyrochlore ordering is suppressed, resulting in smaller domains. The same argument stands for the

lower intensity of the fluorite Raman mode with increasing RE radius. This formation of domains of local order is characteristic of oxygen-deficient compounds [13] and a number of systems closely related to the ones under study, such as certain fluorite zirconias, have been shown to present an average cubic fluorite structure, whilst the local structure is dominated by microdomain formation [14].

3.2.6 Conclusions

- A series of rare earth niobates (RE_3NbO_7, RE = Y,Er,Yb,Lu), synthesized by the self-propagating high-temperature synthesis (SHS) technique, with applications as proton conductors in SOFCs, have been studied by HRTEM and SAED.
- HRTEM results show the presence of a superstructure contrast modulation for all compounds. This modulation consists in the doubling of the periodicity in the <111> directions, and is found in the form of small domains in the crystal.
- SAED diffraction patterns have been acquired from powder samples and sintered pellets. Diffuse scattering features are found for all samples in the form of split spots and/or diffuse rings located around the $\frac{1}{2}(hkl)_F$ fluorite reflections. No significant differences in the strength of the diffuse scattering between the sintered pellets and the nanopowder samples are observed.
- A microstructure of randomly oriented domains of pyrochlore phase embedded in the fluorite matrix is proposed. The finite size of the domains accounts for the diffuse nature of the pyrochlore reflections, and the random orientation accounts for the ring symmetry. All the experimental diffraction patterns can be explained by the cuts of the Ewald sphere with the fluorite spots and diffuse pyrochlore rings.
- The proposed model is found to be in good agreement with previous results from Raman spectroscopy and XRD characterization.

3.3 $Sr_{0.67}Ba_{0.33}Nb_2O_6$

3.3.1 Relaxor ferroelectrics

Ferroelectricity is the property by which certain materials present a spontaneous polarization ($\vec{P}$) without any applied external electric field ($\vec{E}$), below a transition temperature (Curie temperature, T_C). Figure 3.11a represents the polarization mechanism of perovskite ferroelectrics, such as the well known $BaTiO_3$. At T_C, a structural phase transition occurs, displacing all the B cations in the same direction from the center of the unit cell. When an external electric field is applied, the polarization state is modified in a way that depends not only on the applied electric field but also on the previous history of the material, resulting in a hysteresis loop for the $\vec{P}(\vec{E})$ curve. This non-linear response, combined with the high values of dielectric constant, refractive index and electromechanical coupling coefficients as compared to other oxides (especially near T_C), make ferroelectrics very useful in the fabrication of innovative devices. The hysteresis effect can be used as a memory function in the fabrication of ferroelectric RAM memories.

Relaxors are a class of ferroelectric materials with important technological applications [15]. Unlike regular ferroelectrics, they present a broad, diffuse ferroelectric to paraelectric phase transition, resulting in a Curie 'range' of temperatures instead of a Curie temperature [16]. As a consequence, the dielectric constant, electro-optic, photorefractive, pyro- and piezo- electric coefficients stay high for a wider temperature range, making them excellent candidates for applications in optical communications, spatial light modulators, sensors and actuators, etc [17][18][19].

Materials exhibiting relaxor properties can be divided in two main groups, according to their structure. A first group is formed by materials related to the cubic perovskite structure, ABO_3, being its classic example PMN ($PbMg_{0.33}Nb_{0.66}O_3$) [20]. Figure 3.11(b) illustrates the polarization mechanism of a cubic relaxor. Chemical disorder in the B positions of the perovskite unit cell is responsible for the electric charge disorder and the formation of random electric fields. The cubic structure provides eight easy polarization axes, along the equivalent <111> directions. Therefore, the theoretical framework for their description is a

spherical random bond - random field model for the formation of polar nanoregions with a polarization vector pointing towards a random direction.

A second group is that of uniaxial relaxors, which present the tetragonal tungsten bronze (TTB) structure (see figure 3.12). The TTB structure can be derived from the perovskite unit cell by rotating octahedra by approximately 45^{o}, forming a corner sharing octahedral network with triangular, square and pentagonal tunnels that can be occupied by metal cations of different sizes [21][22]. The general structural formula is $[(A1)_2(A2)_4C_4]\,[(B1)_2(B2)_8]\,O_{30}$, being A, B and C the pentagonal, square and triangular sites, respectively. A-type sites are occupied by alkaline earth metals, B-type sites are occupied by transition metals and C-type sites are usually empty or occupied by small radii alkali metals [23]. By choosing the appropriate cations, including mixing and substitutions, the functional properties can be modulated or stabilized [24]. Relaxor behaviour arises from the random occupation by different cations of interoctahedral $A1$ and $A2$ sites. The presence of atoms with different radii randomly occupying equivalent crystallographic sites (disorder) suppresses any long range ferroelectric order, allowing local polarization in weakly interacting nanodomains only [25]. For any given temperature in the Curie range, some domains will be polarized and some will not, being the macroscopic behaviour an envelope of the response of each individual region, leading to the diffuse nature of the transition [26]. The polarization mechanism for an uniaxial relaxor is illustrated in figure 3.11(c).

For uniaxial relaxors, there is only one easy polarization axis, the tetragonal axis $\vec{c}$, containing 180^{o} domain walls. These materials constitute, thus, the first known materialization of a ferroic three-dimensional random field Ising model ($\vec{c}$ or $-\vec{c}$ orientations of $\vec{P}$) [27]. The study of these systems is of great interest both from the applied and the theoretical point of view.

3.3.2 Uniaxial relaxors: the case of SBN

The solid solution $Sr_xBa_{1-x}Nb_2O_6$ presents stronger relaxor properties as strontium content increases. The ratio between Sr and Ba has been shown to shift the transition T range and the dielectric

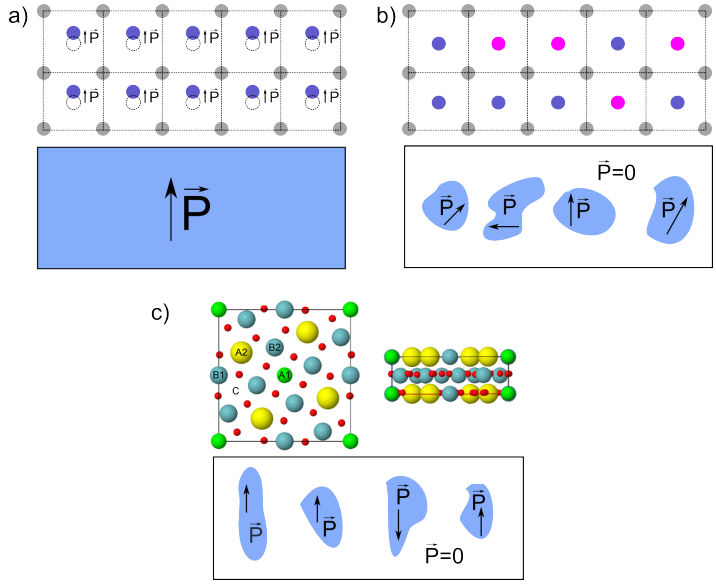

Figure 3.11 a) Polarization mechanism in a regular ferroelectric, such as $BaTiO_3$. Below T_C, the whole material is polarized. b) Polarization mechanism in a cubic relaxor. Chemical disorder in the B positions of the perovskite generates random electric fields, with no structural transition involved. c) Polarization mechanism in a uniaxial relaxor. The random fields arising from the chemical disorder are constrained in one direction ($\vec{c}$) due to the unit cell symmetry.

permittivity, through the octahedral distortion induced by the atomic radii difference.

As stated above, the origin of the relaxor properties is linked to a disorder in the crystal structure. In SBN, regardless of the Sr/Ba ratio, A1 sites are occupied by Sr, A2 sites are occupied randomly by Sr or Ba, and C sites are empty [28]. A total of 1/6 of (A1+A2) sites are empty, resulting in the so-called *unfilled* TTB structure. The resulting electric charge disorder is responsible for the creation of quenched local random electric fields, the formation of polar nanodomains and, ultimately, the spontaneous polarization of the material. The orientation of this polarization always happens to be along $\vec{c}$ due to the crystal symmetry.

The first report of an incommensurate modulation in SBN comes from XRD experiments in the early 1980s [29], and it has been frequently found in all the TTB family. Electron diffraction experiments have proven much more useful than XRD or neut-

ron diffraction for the detection of weaker symmetry elements superimposed on a framework structure [30][31]. In the following sections, we will address the characterization of the structural and chemical disorder in the structure of $Sr_{0.67}Ba_{0.33}Nb_2O_6$ (SBN-67). We complement electron diffraction experiments with the capabilities of aberration corrected STEM and EELS spectroscopy, in order to understand these disorder features locally in direct space.

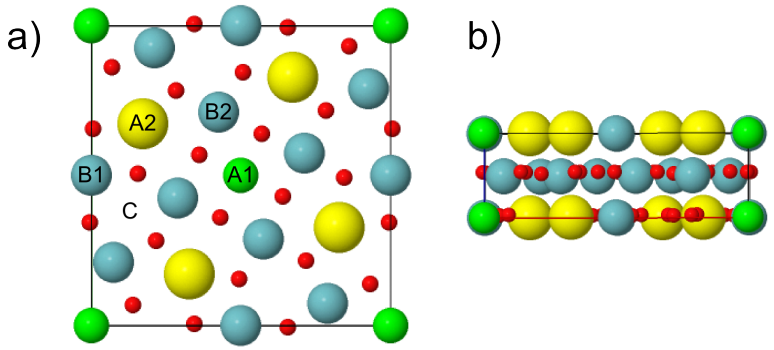

Figure 3.12 a) Tetragonal Tungsten Bronze (TTB) cell viewed along the [001] zone axis. Crystallographic sites in the structural formula are indicated. b) TTB cell viewed along the [100] zone axis.

3.3.3 Structural characterization of SBN-67

A [001] oriented monocrystal of SBN-67 was provided by the group of Prof. Dezanneau at the Laboratoire Structures, Propriétés et Modélisation des Solides (SPMS), École Centrale Paris. Specimens were prepared for TEM observation either by mechanical polishing and subsequent ion milling or through FIB *in situ* lift-out. Sample preparation details can be found in Appendix B. Observations were carried out in a JEOL J2100 for SAED experiments, in a FEI Titan^3 for HAADF experiments and in a JEOL ARM 200cF for ABF and EELS experiments.

Diffuse scattering: incommensurate structural modulation

Figure 3.13(a) shows an electron diffraction pattern obtained from an SBN single crystal along the [001] zone axis. Although not fully kinematical (some of the forbidden $h00$ and $0k0$ for $h, k = 2n + 1$

reflections are faint but still visible), the presence of an intensity modulation according to the structure factor evidences the small thickness of the TEM specimen. From the [001] projection, the measured a and b parameters of the tetragonal unit cell are 12.6 Å.

Figure 3.13(b) shows an electron diffraction pattern obtained from an SBN single crystal along the [100] zone axis. From the [100] projection, the measured c parameter is 3.9 Å. SAED experiments confirm the tetragonal tungsten bronze (TTB) structure of the crystal. A clear streaking of the scattering intensity along the [010] direction can be observed. Streaking corresponds to the elongation of Bragg maxima, and can arise from an unidimensional disorder occurring in the direction perpendicular to the diffuse intensity distribution. This is a first indication of the presence of A-site vacancies inducing strain in the structure.

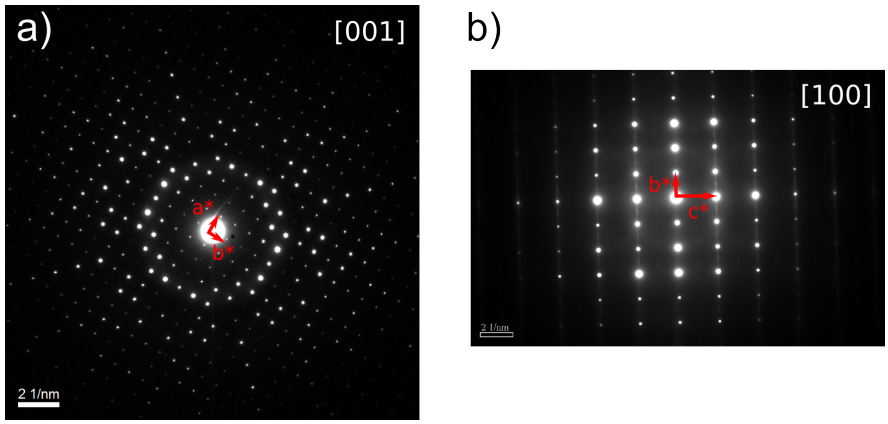

Figure 3.13 SAED patterns for the SBN-67 crystal along the a) [001] and b) [100] zone axes. Reciprocal unit cell vectors in each zone axis are superimposed on the image. The measured cell parameters are a = b = 12.6 Å, and c = 3.9 Å.

Figure 3.14 shows a close-up view of the SAED pattern obtained along the [100] zone axis, in a region far away from the direct spot. Weaker diffuse scattering features can be observed. Besides the streaking along [010], superstructure spots are found in lines parallel to [010] doubling the periodicity of the c axis. These superstructure spots present a much weaker intensity than the main reflections. It is readily apparent that spots are not distributed equidistantly in the superstructure line, which is a

signature of incommensurate structural modulations. Also, no streaking of the scattering intensity is found in the superstructure lines.

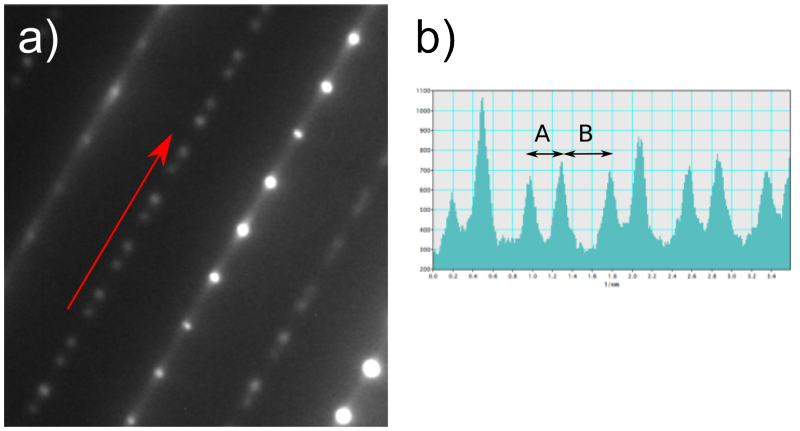

Figure 3.14 a) Close-up view of the SAED pattern acquired along the [100] zone axis. b) Intensity profile along the highlighted line in (a).

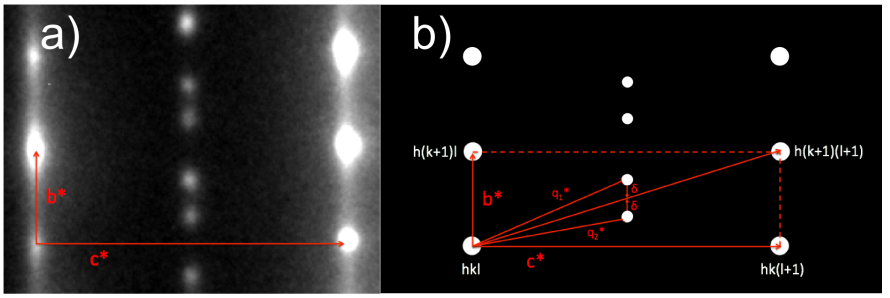

Figure 3.15 a) Experimental SAED pattern b) Scheme of the reciprocal unit cell and the superstructure modulation vectors needed to describe the experimental diffraction patterns.

Because of the presence of incommensurate superstructure spots (not appearing at multiples of the TTB reciprocal lattice vectors), two additional modulation vectors need to be introduced in order to fully describe the reciprocal unit cell, ($\vec{q_1^*}$ and $\vec{q_2^*}$), resulting in a 5-D reciprocal superspace. A scheme showing the relationship of the modulation vectors needed to describe the incommensurate superstructure spots with the reciprocal unit cell vectors of the TTB structure is given in figure 3.15,

where a region of the SAED pattern obtained along the [100] zone axis is shown. The incommensuration parameter, δ, can be calculated from the distance relationships of the superstructure spots [30], which can be measured on the intensity profile in figure 3.14(b) as $\delta = \frac{B-A}{A+B} = \frac{1}{5}$. This parameter describes how much the spots deviate from the commensurate modulation case. For $\delta = 0$ both spots would collapse in the reciprocal space position corresponding to the exact doubling of the TTB unit cell. As can be geometrically derived from the diagram in figure 3.14(b), the resulting modulation vectors are

$$\vec{q_1^*} = \frac{1}{2}(\vec{b^*} + \vec{c^*}) + \delta\vec{b^*} = \frac{7}{10}\vec{b^*} + \frac{1}{2}\vec{c^*} \tag{3.1a}$$

$$\vec{q_2^*} = \frac{1}{2}(\vec{b^*} - \vec{c^*}) + \delta\vec{b^*} = \frac{3}{10}\vec{b^*} + \frac{1}{2}\vec{c^*} \tag{3.1b}$$

The presence of an incommensurate structural modulation points towards a locally disordered crystal structure. The random occupation of crystallographic sites by different atoms should lead to a structural variation that may be just compositional but is also likely to be displacive [31]. The random nature of this variation leads to a fluctuation which is not a multiple of the TTB structure, resulting in the incommensurate superlattice spots.

The cation and anion sublattices. HAADF and ABF imaging.

Direct images of the cation sublattice were obtained by STEM HAADF. In the [001] zone axis, the fluctuation in the structure caused by the incommensurate modulation can be seen as sinusoidal contrast waves, highlighted along the [010] direction in figure 3.16.

Figure 3.17(a) shows a HAADF image of the SBN-67 single crystal viewed along the [001] zone axis at the unit cell level. The different intensities and shapes of the atomic columns can be distinguished. The structural channels formed by the NbO_6 octahedra and the corresponding crystallographic positions are highlighted in figure 3.17(b) by superimposing a model of one unit cell: A1-type cation sites, in square tunnels and occupied by Sr, with expected random vacancies; A2-type sites, in pentagonal

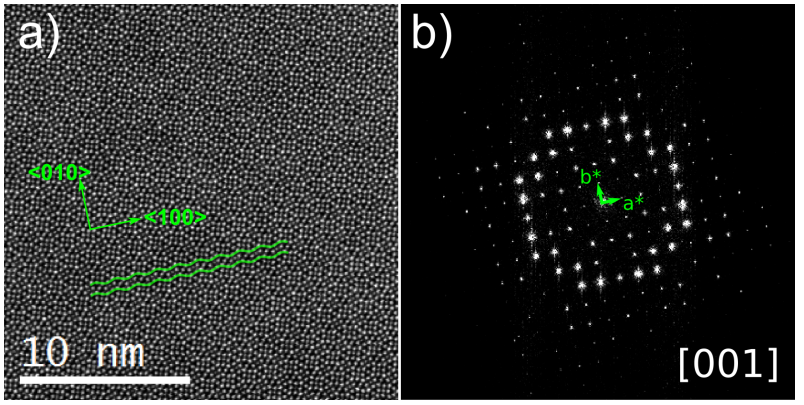

Figure 3.16 a) HAADF image of the SBN-67 crystal along the [001] zone axis, and b) corresponding FFT. Incommensurate modulation appears as a sinusoidal contrast wave, as highlighted in the image.

tunnels and expected to be occupied by randomly distributed Ba and Sr atoms; and Nb columns, at the B-type sites at the center of the octahedra. Figure 3.17(c) shows the same image highlighting the shapes of the atomic columns. Columns showing a circular symmetry correspond to A1 and B sites. A1 sites columns present a smaller radius, as expected from the smaller size of Sr atoms. The elongation of the spots corresponding to A2 columns supports the possibility of a structural modulation, as it corresponds to the projected view of the preferential atom displacements in these columns. This is in good agreement with results reported in the literature from XRD structural refinements [32]. Figure 3.17(d) shows the 70% probability anisotropic displacement ellipsoids (adapted from [32]) corresponding to the A2 sites superimposed to the same image. Remarkably, these ellipsoids present the same orientation and asymmetry as the experimental image of the elongated columns.

Figure 3.18 shows a HAADF image from the SBN-67 single crystal oriented along the [100] zone axis. Panel (a) shows a Fourier filtered image with two superimposed unit cells. A1-type cation sites, in square tunnels and occupied by Sr, with expected random vacancies; A2-type sites, in pentagonal tunnels and expected to be occupied by randomly distributed Ba and Sr atoms; and Nb columns, at the B-type sites, are visible. Planes

consisting solely of Nb and O atoms are denser and present the shortest interatomic distances in this projection. Atomic columns are not fully resolved in these planes. Planes consisting of Sr, Ba and Nb atoms present larger interatomic distances and are fully resolved. Ba atoms appear in pairs, with a larger diameter and a brighter contrast, and separated alternatively by a Sr and a Nb atom, which present a similar contrast due to their similar atomic numbers (Z_{Ba}=56, Z_{Sr}=38, Z_{Nb}=41). Panel (b) shows an unfiltered image taken along the same projection. Empty A1 sites can be seen in the image. The decrease in HAADF intensity at the vacancy sites is clear from the intensity profiles. The set of HAADF images taken along the [100] zone axis allows confirming the presence of random empty sites on the A-type cation columns. Whereas all the previous results were consistent with structural disorder in the crystal, this is the first direct evidence.

ABF images allow imaging the oxygen sublattice in the [001] zone axis projection, as shown in figure 3.19. Oxygen atoms are visible in the shared corners of the NbO_6 octahedra, as expected.

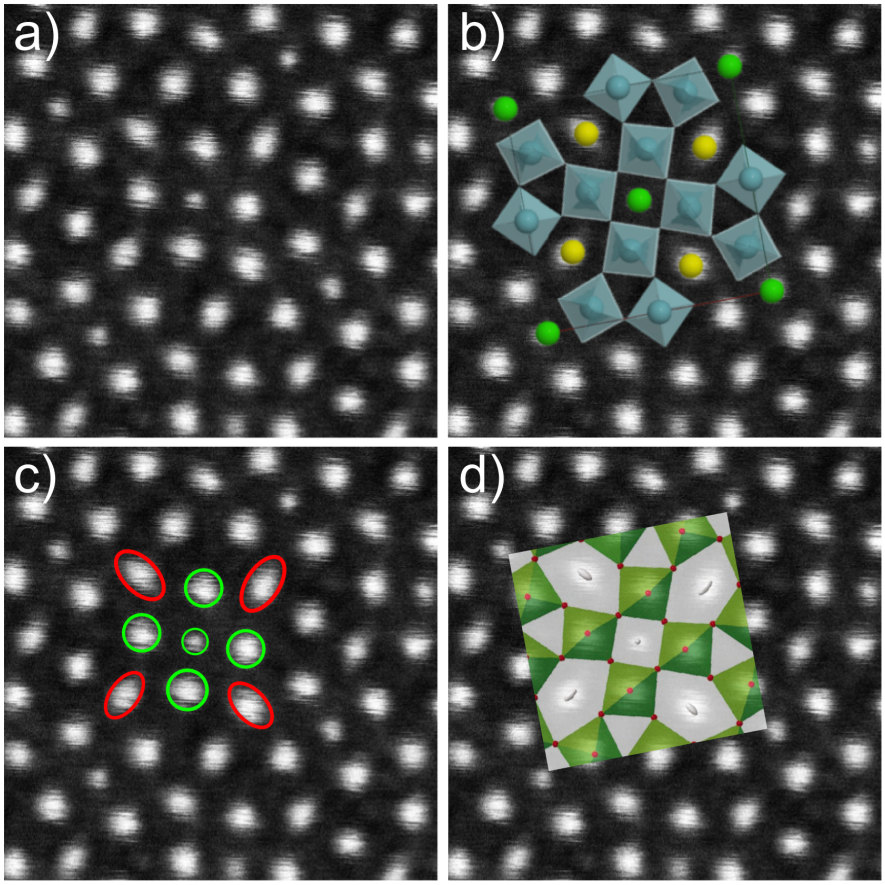

Figure 3.17 a) Higher magnification HAADF image taken along the [001] zone axis. b) The same image with the structural channels formed by the NbO_6 octahedra in the TTB unit cell superimposed. c) The same image highlighting the elongation of the A2-type cation columns (in red). d) The same image with the 70% probability of displacement ellipsoids calculated by Woicke et al. [32] superimposed.

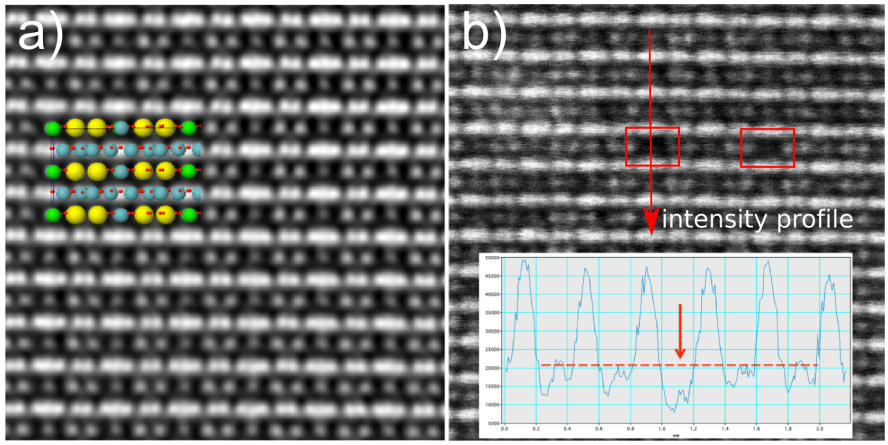

Figure 3.18 a) Fourier filtered HAADF image along the [100] zone axis with a superimposed schematic view of two unit cells. Green dots represent the A1-type cation site, in square tunnels and occupied by Sr, with expected random vacancies; yellow dots represent the A2-type sites, in pentagonal tunnels and expected to be occupied by randomly distributed Ba and Sr atoms. Nb columns are represented in blue, at the B-type sites. b) Unfiltered HAADF image. Inset: intensity profile of the HAADF image along the vertical direction. The presence of A-site vacancies is visible in the image and confirmed by the decrease in the HAADF intensity profile at the expected vacancy sites (as highlighted by square sections in the HAADF image and by an arrow in the intensity profile.

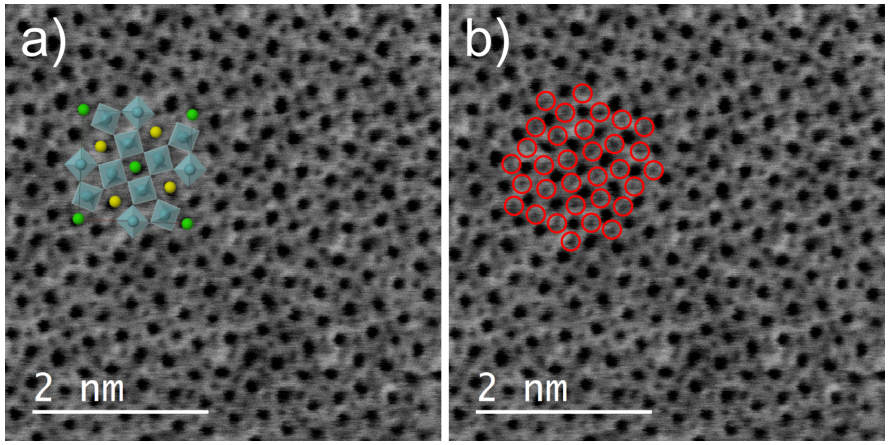

Figure 3.19 Annular Bright Field (ABF) image of the SBN-67 crystal along the [001] zone axis. a) ABF image with a structural model superimposed, showing the cation sites and the NbO_6 octahedra. b) ABF image with the oxygen atoms highlighted with red circles at the corners of the NbO_6 octahedra.

3.3.4 Chemical characterization: EELS spectrum imaging

In order to assess the possible chemical disorder in the structure, atomically resolved EELS spectrum images (SI) were acquired with the crystal oriented along the [001] zone axis. With an energy loss window ranging from 600 eV to 2600 eV, it was possible to cover core loss edges for the 3 cations in the structure: Ba $M_{4,5}$, Sr $L_{2,3}$ and Nb $L_{2,3}$.

Mapping large areas with atomic column resolution requires short acquisition times for each individual pixel/spectrum, since long experiments increase the effect of a possible mechanical drift of the sample holder, which may compromise the spatial resolution. The combination of the high brightness of a cold FEG gun and a very fast and sensitive detector allowed obtaining a useful signal even for acquisition times as low as 0.005 s/pixel. However, the acquired SI present a low signal-to-noise ratio, especially for higher energy losses. Since we need atomic resolution, experimental data needs to be processed in order to reduce the noise level.

Multivariate analysis. Principal Component Analysis for noise reduction.

Multivariate analysis techniques are used to extract relevant information from different kinds of datasets by their adequate representation in a vector space. For an EELS SI datacube, each basis vector (component) is a spectrum, and the weights to be applied in order to reconstruct the data are known as loadings and represent the abundance of each component in the map.

In particular, Principal Component Analsis (PCA) consists in the projection of the data in a coordinate system chosen through variance criteria. The first component of the new orthogonal basis is the one with maximum data variance. The following components are, then, the n-th components with n-th maxium variance and orthogonal to the previous n-1 components. Mathematically, this is equivalent to solving the eigenvector problem of the covariance matrix of the data. The symmetry of this matrix assures the orthogonality of the new coordinate system. Once the decomposition has been performed, the dimensionality of the

problem can be reduced by keeping only the components that account for most of the variance in the data, discarding the rest as noise contribution. In our case, the datacube dimensions are 120 pixels × 120 pixels × 2048 channels, covering a region of about 5 nm × 5 nm, resulting in a sub-Å sampling. The details of the data processing are summarized in figure 3.20. Panel (a) shows the simultaneously acquired HAADF image for reference. Panel (b) is the raw spectrum image. Panel (c) shows two individual spectra corresponding to the indicated pixel coordinates in the spectrum image. From the co-acquired HAADF, it can be seen that they correspond to two different crystallographic sites. However, no information can be extracted from these individual spectra since they are too noisy. Panel (e) shows the explained variance ratio, or Scree plot, of the SI. The component carrying most of the variance in the data is assigned a value of 1 and the rest of the components are ordered according to the relative fraction of the data variance that they account for. From the 4th component and beyond, saturation at what we can call 'noise level' is reached. Therefore, a new datacube is reconstructed using only the first three components, filtering the noise out. Panel (d) shows the two individual spectra from the same pixel coordinates as in panel (c), but extracted from the reconstructed data cube after the PCA processing. The signal-to-noise ratio is remarkably improved and modulation in the chemical information between spectra corresponding to two crystal sites is apparent. As a sanity check, panel (f) shows the integrated intensity from the whole spectrum image in panel (b) before processing. It is clear that chemical information is present in the data and that the signal-to-noise ratio can be improved by statistical methods, especially given the large amount of data points in the spectrum images, which constitute an ideal system for the machine learning algorithm. In this sense, by just integrating the signal, atomic resolution is lost, whereas by PCA processing we are able to improve the signal-to-noise ratio while retaining the spatial resolution of the experimental acquisition.

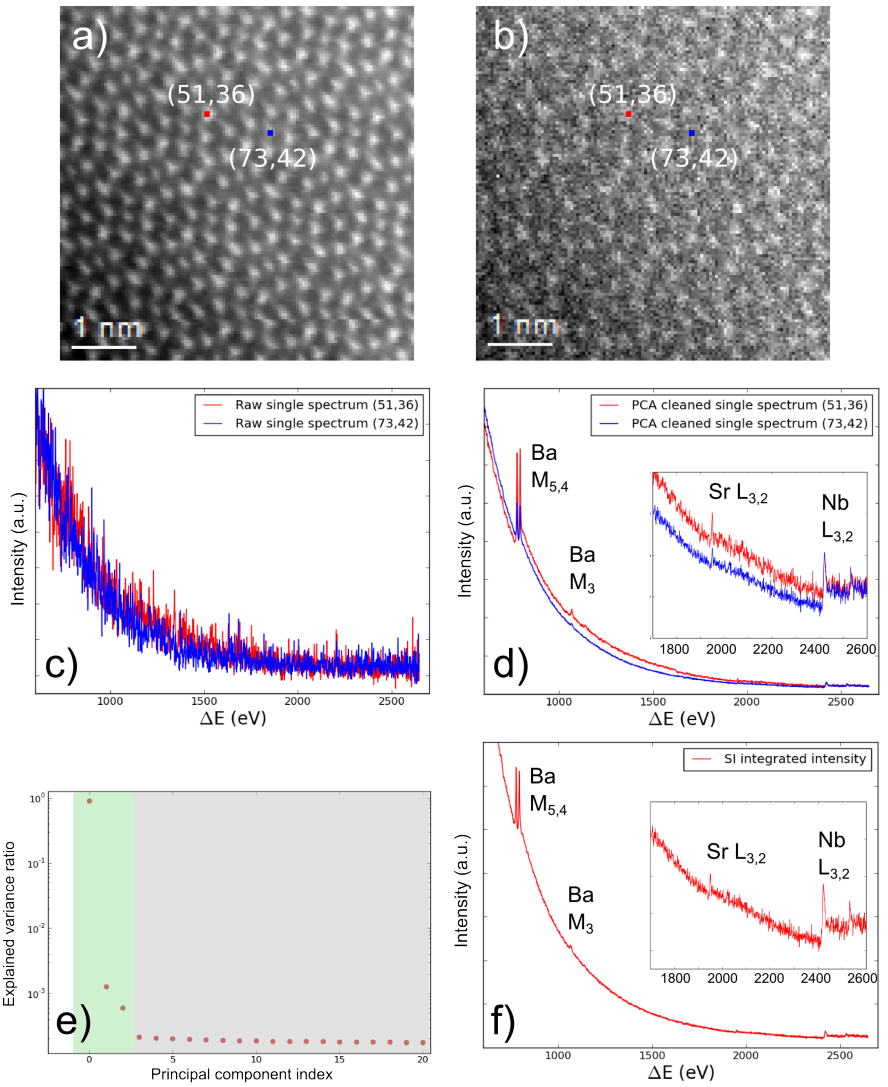

Figure 3.20 a) HAADF image, acquired simulatenously to the EELS SI. b) Raw spectrum image. c) Individual spectra from two pixels in the raw spectrum image, as indicated in panels (a) and (b). d) Explained variance ratio figure. e) Resulting spectra from the same pixels after PCA processing. The noise reduction allows obtaining information of the spatial distribution of the signal. f) Integrated signal from the whole spectrum image in panel (b).

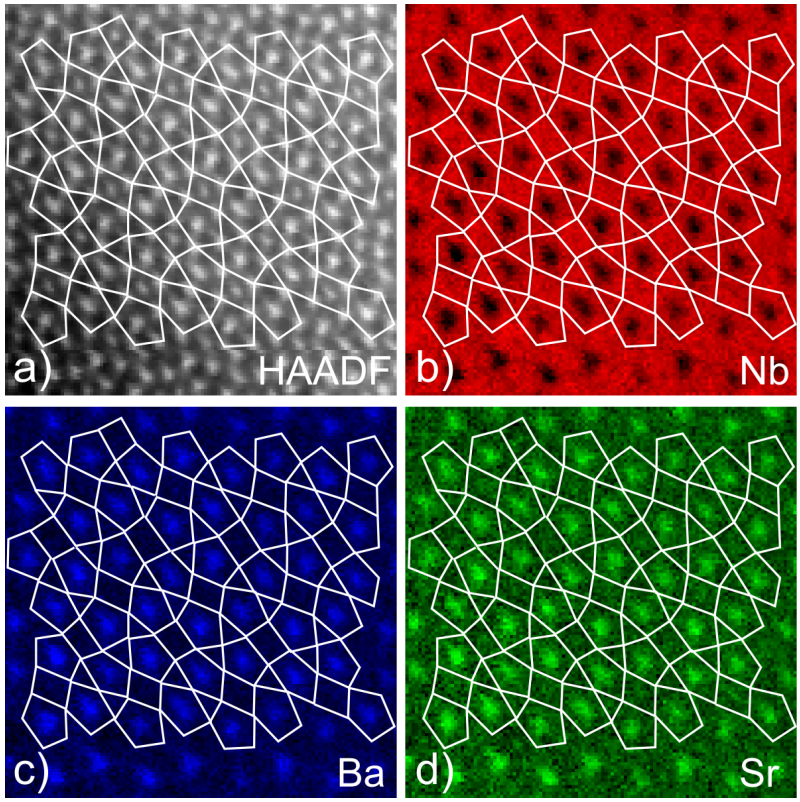

Figure 3.21 a) HAADF image, acquired simulatenously to the EELS SI. The structural channels formed by the corner sharing NbO_6 octahedra are drawn on the image. b) Nb, c) Ba and d) Sr relative composition maps with the structural channels superimposed. The presence of Ba and Sr in the A2 pentagonal sites is clearly visible. Triangular C sites are empty, as expected.

Elemental mapping

After cleaning the dataset by means of PCA, the spectrum image was analyzed to assess a possible chemical disorder. Using the usual Egerton [33] quantification for the core-loss edges, relative composition maps could be obtained for a region of about 3x3 unit cells, as shown in figure 3.21. For clarity, the channel structure is drawn on the co-acquired HAADF image and on the compositional maps. The image is slightly distorted due to drift during acquisition. Qualitatively, it is apparent from visual inspection that the pentagonal A2 sites are indeed shared by Ba and Sr. Nb signal is not atomically resolved; it is found distributed all over the background but for the bigger structural channels (A2 sites).

The main point of interest is the analysis of the Sr/Ba relationship, which determines the relaxor properties of the material. From the Egerton quantification on the spatially resolved compositional maps, the relative composition, taking into account that there are twice as many A2 sites than A1 sites, is $\left[\frac{Sr}{Ba}\right] = 2$, in good agreement with the nominal composition for $Sr_{0.67}Ba_{0.33}Nb_2O_6$.

As a sanity check, the same quantification process was carried out on the integrated signal for the whole unprocessed spectrum image and equivalent results were obtained. This is to confirm that PCA processing is successful in recovering atomic resolution for the chemical maps without a significant modification of the chemical data.

3.3.5 Conclusions

- A single crystal of the ferroelectric relaxor $Sr_{0.67}Ba_{0.33}Nb_2O_6$ (SBN-67), prepared for TEM observation in the [001] and [100] zone axes of the Tetragonal Tungsten Bronze (TTB) structure, was studied by SAED, HAADF, ABF and EELS in order to assess a possible local disorder in the structure, and to correlate it with the macroscopic relaxor behavior of the material.

- Diffuse scattering in [100] SAED patterns was found in the form of streaking of the scattering intensity along the [010] direction and elongation of the Bragg maxima, which

are compatible with strain in the structure, arising from vacancies in A1 sites.

- A direct evidence of A1 site vacancies was obtained from aberration corrected STEM HAADF images taken along the [100] zone axis. Randomly distributed vacant A1 sites were found all over the crystal.

- Superstructure spots were also found in the [100] SAED patterns, doubling the periodicity of the (001) planes, consisting in non-equidistantly distributed spots along the [010] direction. This incommensurate superstructure modulation requires two additional modulation vectors to describe the reciprocal space of the crystal, resulting in a 5-D reciprocal space.

- The incommensurate modulation of the structure found in SAED patterns is compatible with chemical disorder in A2 sites, resulting in a structural fluctuation which is not a multiple of the TTB unit cell. In direct space, this incommensurate modulation is seen as a sinusoidal contrast wave in the HAADF images taken along the [001] zone axis.

- The random occupation of A2 sites by Ba or Sr is also in good agreement with the observed elongation of the corresponding atomic columns in the HAADF images taken along the [001] zone axis, produced by the slight displacements of the atoms in the column.

- Atomically resolved EELS chemical maps, showing the random occupation of Ba and Sr in the A2 sites, give a direct evidence of this chemical disorder.

- The structural reasons of the macroscopic relaxor behaviour of SBN-67, namely, random A1 vacancies and Sr/Ba mixing in A2 sites, are determined from aberration corrected STEM HAADF and EELS experiments.

Bibliography

[1] M.D. Braida. *Noveaux conducteurs protoniques de structure fluorite*. PhD thesis, École Centrale Paris, 2010.

[2] H. Iwahara. Proton conduction in sintered oxides based on $BaCeO_3$. *Journal of The Electrochemical Society*, 135(2):529, 1988.

[3] H. Hiwahara, T. Esaka, H. Uchida, and N. Maeda. *Solid State Ionics*, 1981.

[4] H. Iwahara T. Takahashi. *Rec. Chem. Miner.*, 1980.

[5] J.B Goodenough, J.E. Ruiz-Diaz, and Y.S. Zhen. Oxide-ion conduction in $Ba_2In_2O_5$ and $Ba_3In_2MO_8$ (M = Ce, Hf or Zr). *Solid State Ionics*, 1990.

[6] S.B. Adler, J.A. Reimer, J. Baltisberger, and U. Werner. Chemical Structure and Oxygen Dynamics in $Ba_2In_20_5$. *J. Am. Chem. Soc.*, 1994.

[7] J. Lee, M. Yashima, and M. Yoshimura. Ionic conductivity of fluorite-structured solid solution $Y_{0.8}Nb_{0.2}O_{1.7}$. *Solid State Ionics*, 107:47–51, 1998.

[8] R. Miida, F. Sato, and M. Tanaka. Locally modulated structure of fluorite-related Y_2O_3-Nb_2O_5 solid solutions. *Journal of applied Crystallography*, 8898:272–279, 1997.

[9] S. Garcia-Martin, M.A. Alario-Franco, D.P. Fagg, and J.T.S. Irvine. Evidence of three types of short range ordered fluorite structure... *Journal of Materials Chemistry*, 15(19):1903, 2005.

[10] S. Garcia-Martin, D.P. Fagg, and J.T.S. Irvine. Characterization of diffuse scattering in Yttria-stabilized zirconia by electron diffraction and high-resolution transmission electron microscopy. *Chemistry of Materials*, (2):5933–5938, 2008.

[11] Shannon, R.D. and Prewitt, C.T. Effective ionic radii in oxides and fluorides. *Acta Cryst.*, (B25):925–946, 1969.

[12] Shannon, R.D. and and Prewitt, C.T. Revised values of effective ionic radii. *Acta Cryst.*, (B26):1048–1048, 1970.

[13] S.A. Kovyazina, L.A. Perelyaeva, and I.A. Leonidov. High-temperature structural disorder in R_3NbO_7. *Journal of Structural Chemistry*, 44(6):975–979, 2003.

[14] J. Irvine. Structural studies on the optimisation of fast oxide ion transport. *Solid State Ionics*, 136-137(1-2):879–885, 2000.

[15] W. Kleemann. The relaxor enigma - Charge disorder and random fields in ferroelectrics. *Journal of Materials Science*, 41(1):129–136, 2006.

[16] Y. J. Qi, C. J. Lu, J. Zhu, X. B. Chen, H. L. Song, H. J. Zhang, and X. G. Xu. Ferroelectric and dielectric properties of $Ca_{0.28}Ba_{0.72}Nb_2O_6$ single crystals of tungsten bronzes structure. *Applied Physics Letters*, 87(8):082904, 2005.

[17] S. Sakamoto and T. Yazaki. Anomalous electro optic properties of ferroelectric strontium barium niobate and their device applications. *Applied Physics Letters*, (22):429, 1973.

[18] M. Horowitz, A. Bekker, and B. Fischer. Broadband second-harmonic generation in $Sr_xBa_{1-x}Nb_2O_6$ by spread spectrum phase matching with controllable domain gratings. *Applied Physics Letters*, 62(21):2619–2621, 1993.

[19] M. Cuniot-Ponsard, J.M. Desvignes, A. Bellemain, and F. Bridou. Simultaneous characterization of the electro-optic, converse-piezoelectric, and electroabsorptive effects in epitaxial (Sr,Ba)Nb_2O_6 thin films. *Journal of Applied Physics*, 109(1), 2011.

[20] R.A. Cowley, S.N. Gvasaliya, S.G. Lushnikov, B. Roessli, and G.M. Rotaru. Relaxing with relaxors: a review of relaxor ferroelectrics. *Advances in Physics*, 60(2):229–327, 2011.

[21] M. Eber, M. Burianek, D. Klimm, and M. Mühlberg. Single crystal growth of the tetragonal tungsten bronze $Ca_xBa_{1-x}Nb_2O_6$ ($x = 0.28$; CBN-28). *Journal of Crystal Growth*, 240(1-2):1–5, 2002.

[22] X. Kuang, F. Pan, J. Cao, C. Liang, M.R. Suchomel, F. Porcher, and M. Allix. Defect structure, phase separation, and electrical properties of nonstoichiometric tetragonal tungsten bronze $Ba_{(0.5-x)}TaO_{(3-x)}$. *Inorganic Chemistry*, pages 2–10, 2013.

[23] K.C. Mouli, K. H. Rao, P.S.V. Subba Rao, and A. Bhanumathi. Ferroelectric properties of modified strontium barium niobate ceramics. *Ferroelectrics*, 67(1):169–171, 1986.

[24] S. Lanfredi, C. Darie, F.S. Bellucci, C.V. Colin, and M.A.L. Nobre. Phase transitions and interface phenomena in the cryogenic temperature domain of a niobate nanostructured ceramic. *Dalton Transactions*, 43(28):10983, 2014.

[25] C. L. Jia, J. Schubert, T. Heeg, S. B. Mi, H. Y. Chen, B. Joschko, M. Burianek, M. Mühlberg, and K. Urban. Tailoring the orientations of complex niobate films on perovskite substrates. *Acta Materialia*, 54(9):2383–2391, 2006.

[26] L.A. Bursill and P.J. Lin. Chaotic states observed in strontium barium niobate. *Philosophical Magazine B*, 54(2):157–170, 1986.

[27] W. Kleemann, J. Dec, V.V. Shvartsman, Z. Kutnjak, and T. Braun. Two-dimensional Ising model criticality in a three-dimensional uniaxial relaxor ferroelectric with frozen polar nanoregions. *Physical Review Letters*, 97(6):1–4, 2006.

[28] S.N. Gvasaliya, R.A. Cowley, L.I. Ivleva, S.G. Lushnikov, B. Roessli, and A. Zheludev. Phase transition of the uniaxial disordered ferroelectric $Sr_{0.61}Ba_{0.39}Nb_2O_6$. *Journal of physics. Condensed matter*, 26(18):185901, 2014.

[29] J. Schneck, J. C. Toledano, R. Whatmore, and F. W. Ainger. Incommensurate phases in ferroelectric tetragonal tungsten bronzes. *Ferroelectrics*, 36(1):327–330, 1981.

[30] L.A. Bursill and P.J. Lin. Incommensurate superstructures and phase transition of strontium barium niobate (SBN). *Acta Crystallographica Section B: Structural Science*, 43(1):49–56, 1987.

[31] E. Martiínez, A. Fundora, H. Amorin, J. Portelles, and J. M. Siqueiros. Study by high resolution electron microscopy and electron diffraction of the $La_{0.03}Sr_{0.255}Ba_{0.7}Nb_{2-y}Ti_yO_{6-y/2}$ ferroelectric ceramic. *Journal of Applied Physics*, 91(5):3154, 2002.

[32] T. Woike, V. Petrícek, M. Dusek, N.K. Hansen, P. Fertey, C. Lecomte, A. Arakcheeva, G. Chapuis, M. Imlau, and R. Pankrath. The modulated structure of $Ba_{0.39}Sr_{0.61}Nb_2O_6$. I. Harmonic solution. *Acta crystallographica. Section B: Structural crystallography and crystal chemistry*, 59(Pt 1):28–35, 2003.

[33] R.F. Egerton. *Electron Energy Loss Spectroscopy in the Electron Microscope*. Springer, 3rd edition, 2011.

Chapter 4

2D materials: HRTEM simulation of film defects

4.1 Introduction

In this chapter we will cover the identification of strain state and defects in materials with only one dimension constrained in the nanoscale: thin films. Thin film technology allows depositing very thin layers of material on top of a substrate; the resulting nanostructures present interesting properties different from their bulk counterparts, or improve the properties of the substrate material. Thin films are commonly used in industry for the enhancement of mechanical properties of surfaces, such as hardness or friction response, for magnetic switching data storage devices, for ligthing applications such as LEDs [1] or lasers [2], or in the photovoltaics field in tandem solar cells [3], amongst others.

The first section of this chapter will be devoted to the perovskite oxide $LaNiO_3$, an interesting material to be used as an electrode in ferroelectric devices because of its charge transport properties. These properties can be tuned through strain engineering. The main target of the study will be, thus, the characterization of the strain state of LNO films grown epitaxially on substrates that exert different compressive or tensile stresses on the films through crystal lattice mismatch.

The second section focuses on III-V semiconducting materials. The system under study is a multilayer of alternating InAlN/GaN

periods in a Bragg reflector configuration. The microstructure of the GaN layers will be studied in order to understand the lower than expected reflectivity of the device. Polytypism and structural defects will be assessed by HRTEM and HRTEM image simulation techniques.

4.2 $LaNiO_3$ thin films

The series of rare earth nickelates ($RENiO_3$) presents one of the richest phase diagrams among the transition metal oxides due to the interplay of charge, orbital, spin and crystal lattice degrees of freedom. Even moreso when considering epitaxial thin films for which additional new phases, different from the bulk ones, must be taken into consideration. The case of $LaNiO_3$ (LNO) is of particular interest as a highly conducting electrode, since it is one of the few oxides for which resistivity levels below 100 $\mu\Omega\times$cm have been reported [4, 5]. In addition, it is the only member of the $RENiO_3$ series that keeps its metallic character for all temperatures, with no metal-insulator (MI) transition, except for ultrathin films of less than eight unit cells [6].

LNO belongs to the perovskite family of oxides, with a general formula ABO_3. The ideal unit cell is cubic, with the A-site cation placed in the center of the cube and the B-site cations occupying its corners. Oxygen atoms are arranged forming a network of corner sharing octahedra enclosing the B-site cations. A generic perovskite unit cell is depicted in figure 4.1. The metallic behaviour of LNO comes from the hybridization of O 2p and Ni 3d orbitals. Therefore, structural parameters such as the Ni-O distances and Ni-O-Ni angles, which govern the transfer integral between these orbitals, play a key role in determining the transport properties of the material [7]. A way to tune these transport properties is through the epitaxial stress exerted by a substrate with a given lattice parameter mismatch [8–10].

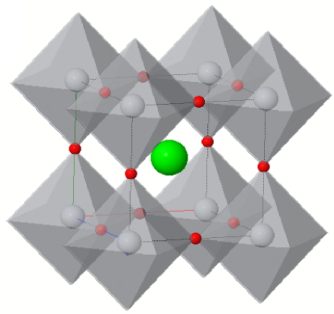

Figure 4.1 Perovskite unit cell. Coordination polyhedra around the B cations (in green) are drawn. The green sphere corresponds to the central A cation and the small red spheres correspond to the oxygen atoms.

In order to study LNO thin films under different strain states, a series of films were grown by the group of Professor Josep Fontcuberta at Institut de Ciència dels Materials the Barcelona. Films were grown by Pulsed Laser Deposition (PLD) on top of different substrates (LAO, LSAT, YAO and STO), using a KrF excimer laser ($\lambda = 248$ nm) with a fluence of 1.5 J $\cdot$ cm^{-2} and a repetition rate of 5 Hz. Deposition was performed at an oxygen pressure P = 0.15 mbar and keeping the substrate at a temperature T = 700 ^{o}C. The number of laser pulses was varied to obtain films with nominal thicknesses of 14 nm and 35 nm, according to previous growth-rate calibrations. Lattice mismatch values with respect to bulk LNO range from -3.1% to +2%, covering both compressive and tensile strain. The theoretical lattice parameter values for each substrate and bulk LNO are shown in figure 4.2, as well as a schematic view of the expected LNO elastic deformation, asuming volume conservation of the unit cell.

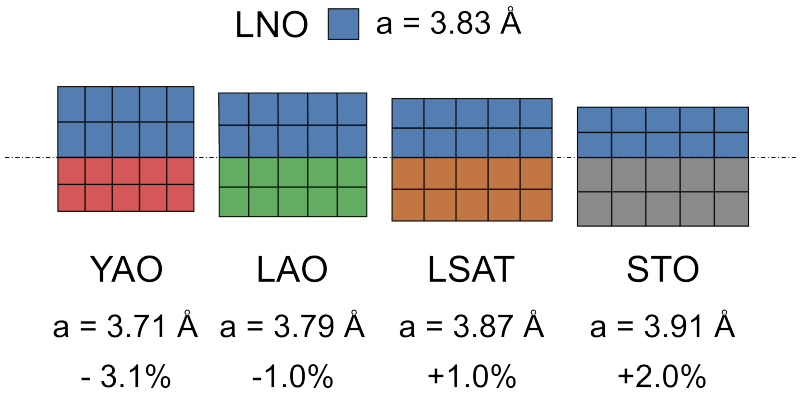

Figure 4.2 Summary of the different substrates used to grow the epitaxial LNO thin films, with the corresponding cell parameters and lattice mismatch with respect to the bulk value for LNO. The cartoon qualitatively represents the expected unit cell deformation according to the compressive (LAO, YAO) or tensile (LSAT, STO) strain exerted by the substrate.

4.2.1 Substrate-induced strain characterization

The 14 nm LNO films grown on LAO, LSAT and STO substrates present good crystalline quality and a thickness close to nominal, with a surface roughness of about ± 1 nm. A good cube-on-cube

growth fulfilling the [001]LNO(010)//[001]substrate(010) epitaxial relationship is observed, with atomic-sharp interfaces. Figure 4.3 shows three HAADF images of 14 nm LNO films, grown on LAO, LSAT and STO. The corresponding FFTs show the good epitaxial growth of the films on the substrates, with no detectable crystal symmetry change between the compressive and tensile cases for the strained LNO films. Planar defects are observed throughout the films and are highlighted by dashed lines in figure 4.3. These defects are Ruddlesden-Popper faults and will be discussed in detail in the following subsection.

Geometric Phase Analysis was used to generate strain tensor maps for the in-plane (ϵ_{xx}) and out-of-plane (ϵ_{yy}) components, using the substrate region as a reference. The maps are shown in figure 4.3, superimposed to the experimental HAADF images. From the GPA results, it can be seen that films grow fully adapted to the substrate in the in-plane direction. Since the used reference region is the substrate, and not bulk LNO, the obtained values for the ϵ_{yy} component need to be further analyzed. Taking into account the difference between the lattice parameters of each substrate and the bulk LNO lattice parameter, it is found that all films present out of plane parameters which lie very close to LNO bulk values. The difference is of 0.7% for LNO on LAO, 0.1% for LNO on LSAT and 0.5% for LNO on STO.

In the case of LNO grown on YAO, the 14 nm film is fully relaxed both in the in-plane and out-of-plane directions. Besides the larger lattice mismatch when compared to the other substrates in the series, YAO is a distorted perovskite with the orthorhombic space group Pnma, so the growth of cubic LNO (space group $Pm\bar{3}m$) is not isostructural. The expected epitaxial relationship would be [001]LNO(100) // [010]YAO(101). Figure 4.4 shows an HRTEM image of the 14 nm LNO film on YAO taken along the [001] zone axis of LNO. The corresponding FFT shows the 45 ^{o} rotation between the YAO and LNO unit cells, as expected from the *a priori* epitaxial relationship. Split spots corresponding to the lattice parameters of the two structures are clearly observed. Splitting is evident between the 202 and 200 reflections of YAO and LNO, respectively, which present a lattice mismatch of 3.6%.

A rotation is also apparent, in the in-plane direction, between the $10\bar{1}$ and 020 reflections of YAO and LNO, respectively.

Thicker films of 35 nm grown on LAO and LSAT were also characterized. The strain states found by GPA are equivalent to the ones found in the 14 nm films.

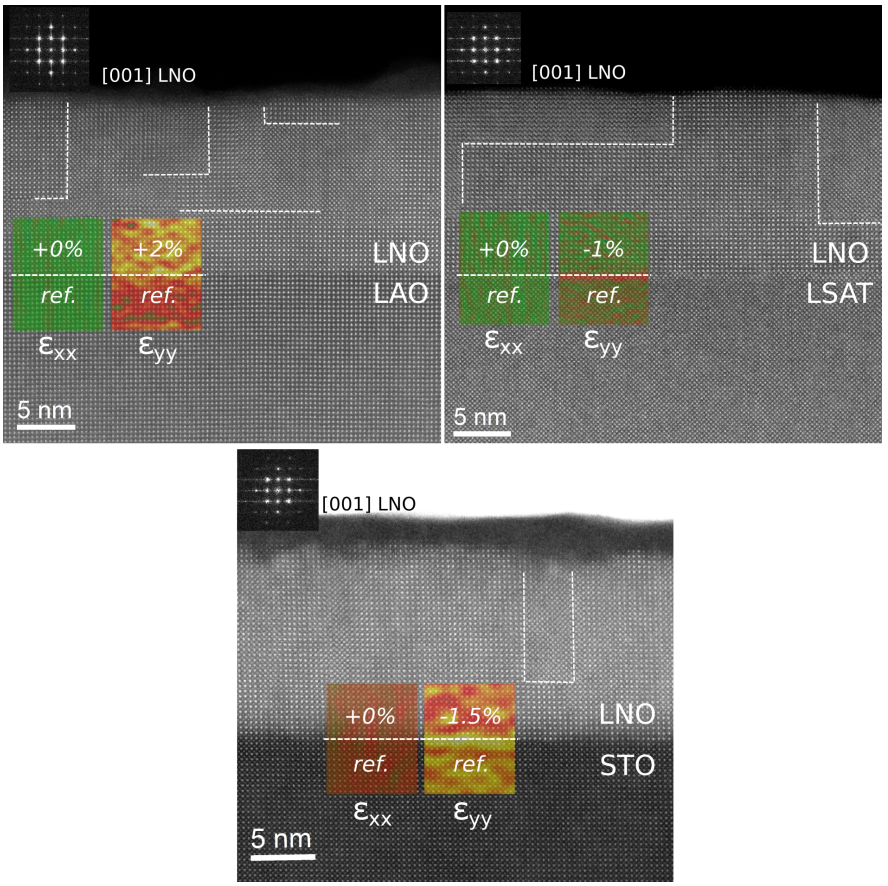

Figure 4.3 HAADF images of 14 nm LNO films grown on LAO, LSAT and STO. Insets show the corresponding FFTs obtained from the film region in each case. All the LNO films present the same structure, with an elastically deformed unit cell due to the substrate-induced strain. Superimposed in false colour, GPA maps for the in-plane (ϵ_{xx}) and out-of-plane (ϵ_{yy}) components of the strain tensor, taking the substrate region as a reference. In-plane components show a fully adapted film. Ruddlesden-Popper type defects in the LNO films are indicated by dashed lines.

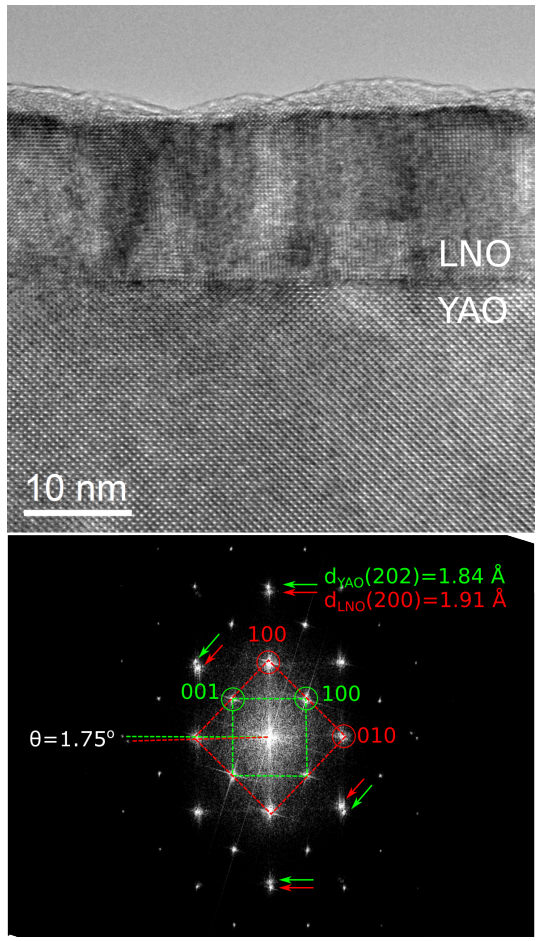

Figure 4.4 HRTEM image of the 14 nm LNO film grown on YAO and corresponding FFT. LNO (cubic, space group $Pm\bar{3}m$) and YAO (orthorhombic, space group Pnma) reciprocal unit cells are highlighted on the FFT in red and green, respectively. Split spots corresponding to characteristic spacings of both structures are indicated by arrows. A rotation of the spots in the in-plane direction is also indicated.

4.2.2 Ruddlesden-Popper faults

Disregarding the LNO/YAO system, both 14 nm and 35 nm LNO films show a fully adapted, defect-free growth for the first 3-5 nm. Beyond that thickness, planar defects start to appear in the film, oriented either parallel or perpendicular to the substrate-film interface. They are indicated in figure 4.3 by dashed white lines. These planar defects consist in the displacement of the crystal by half a unit cell along a <111> direction and are known as Ruddlesden-Popper (RP) faults [11][12].

The crystal displacement can be easily seen in HAADF contrast. A close up view of one of these planar defects is shown in figure 4.5. The defect is highlighted by a dashed line and the crystal displacement is shown schematically by a superimposed structural model. Blue spheres correspond to La columns and green spheres correspond to Ni columns. In order to emphasize the Z-contrast difference between the A and B sites of the perovskite, the same image is shown in colour scale.

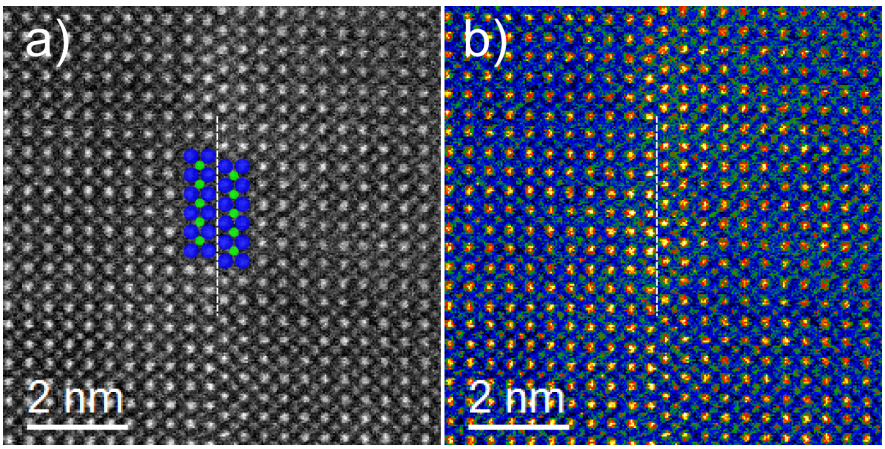

Figure 4.5 a) HAADF image of a RP fault in the 35 nm LNO film grown on LAO substrate with a structural model superimposed. Blue circles correspond to La columns and green circles correspond to Ni columns, considering the Z dependence of the HAADF intensity. b) The same HAADF image, temperature color coded to visualize more easily that no A/B contrast is lost across the RP fault.

A second type of RP faults is found surrounding rectangular regions in the film for which the contrast difference between the

A and B sites of the perovskite is lost, as seen in the domain highlighted in figure 4.3(c).

Other RP faults constitute domain boundaries marking the separation of regions with and without A/B contrast but with a gradual transition. Figure 4.6(a) shows a HAADF image of a RP domain boundary in the 35 nm LNO film on LAO. Panel (b) contains the same HAADF image in a colour scale in order to help visualize the contrast difference, or lack therof, between the A and B sites of the perovskite unit cell. Both the upper and lower parts of the image correspond to the LNO film. The loss of HAADF contrast between the A and B sites is clearly observed in the upper part of the image, i.e., inside the RP domain. Panel (c) shows a wider field of view containing the region in panels (a) and (b). It can be observed in the colour coded HAADF intensity that the loss of contrast between the A and B sites of the perovskite is sharp in the out-of-plane direction, taking place in just one atomic plane. On the other hand, the loss of A/B contrast in the lateral direction is gradual.

The differences observed in HAADF contrast for the RP faults can be understood in terms of the 3D position of the domains inside the films and the relative orientation of the planar defects with respect to the electron beam. The first situation is the most simple one: two displaced domains are observed side by side and they constitute the totality of the TEM specimen thickness. This corresponds to the case schematically shown in figure 4.7(a). In the second case, the loss of A/B contrast is due to the superposition of two domains. The displacement by half a unit cell means that A sites of one domain will be in the positions expected for B cations in the other domain. The projected view yields an average HAADF contrast. This situation happens when the displaced domain defined by the RP faults is embedded in the non-displaced LNO and the electron beam travels through both domains, as shown in figure 4.7(b). In the third case, the gradual loss of A/B contrast is explained by the planar defect not being oriented parallel to the electron beam, as depicted in figure 4.7(c).

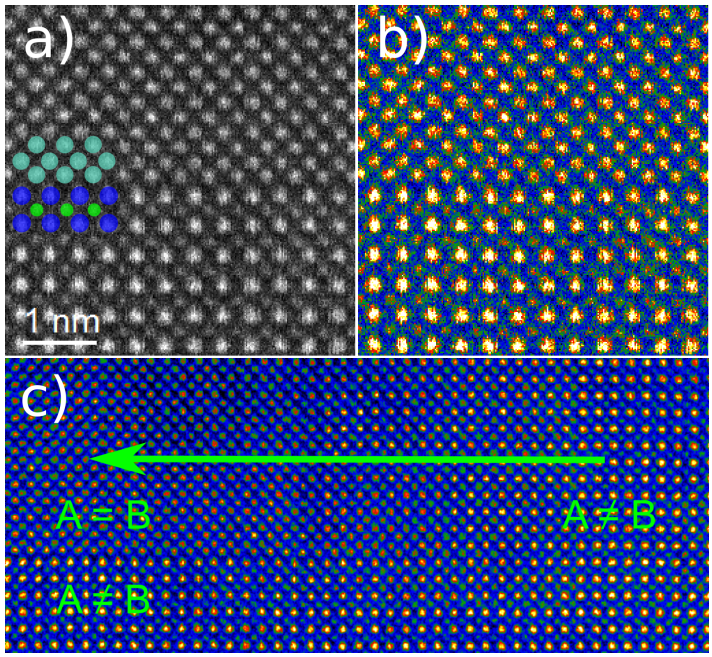

Figure 4.6 a) HAADF image of a RP fault in the 35 nm LNO film grown on LAO substrate with a structural model superimposed. Blue circles correspond to La columns, green circles correspond to Ni columns and turquoise circles correspond to the overlapping La and Ni columns. b) The same HAADF image using a temperature colour code for the HAADF intensity. c) Wider field of view containing the region shown in (a) and (b). The loss of A/B HAADF contrast is sharp in the out-of-plane direction but gradual in the in-plane direction.

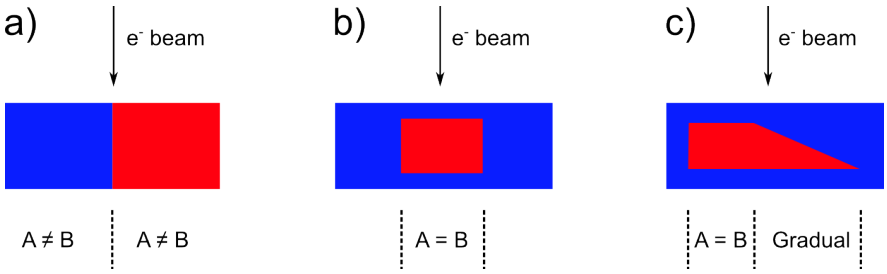

Figure 4.7 Cartoon displaying a) a RP fault separating two domains through the whole TEM specimen thickness. b) RP faults enclosing a domain embedded in the non-displaced LNO. c) a RP domain with one boundary not parallel to the electron beam.

4.2.3 Non-stoichiometry in LNO thin films

Superstructure modulation in complex oxides with a perovskite, or a related, structure is rather common. The extremely large flexibility of the perovskite unit cell, which allows it to accommodate cations of very different sizes, results in a broad landscape of possible superstructures for distorted perovskites.

The distortion of the coordination polyhedra might consist in just a collective rotation pattern of the BO_6 octahedra [13] or in the formation of different coordination environments for all or some of the cations, if vacancies are introduced. The relaxation of the cations around a structural defect, such as an oxygen vacancy, results in the rearrangement of the remaining oxygen atoms to create new coordination polyhedra [14, 15]. In the films under study, a superstructure modulation doubling the periodicity of the LNO unit cell was observed in HRTEM and HAADF images in regions of the 35 nm LNO films grown on LAO and LSAT. Figure 4.8 shows an HRTEM image of the 35 nm LNO film on LAO observed along the [100] zone axis with the superstructure modulation oriented perpendicular to the substrate-film interface, doubling the d_{010} spacing. In the well known series of defective perovskites described by the formula $A_nB_nO_{3n-1}$, there is a variety of local minima for the energy corresponding to the rearrangement of the structure when oxygen atoms are taken away. Given the inherent thermodynamic instability of the Ni^{3+} state, let us now consider the n = 2 member of the series. This gives us the oxygen defficient $LaNiO_{2.5}$ phase. The interplay of the Ni oxidation state and the oxygen content in the material is also a key factor for understanding the transport properties of the material.

Investigations on the structure of the $LaNiO_{2.5}$ sub-stoichiometric phase go back to the 1980s when an XRD pattern was first reported by Crespin *et al.* [16] and indexed as a monoclinic perovskite superstructure with cell parameters $2\sqrt{a_o}, 2\sqrt{a_o}, 2a_o$, a_o being the cell parameter of the ideal cubic perovskite. Although the structure could not be solved, a model based on the brownmillerite structure was proposed. Brownmillerite is a perovskite superstructure in which the B cation adopts both tetrahedral and octahedral coordinations due to the ordering of the oxygen vacancies. However, given that a tetrahedral environment is par-

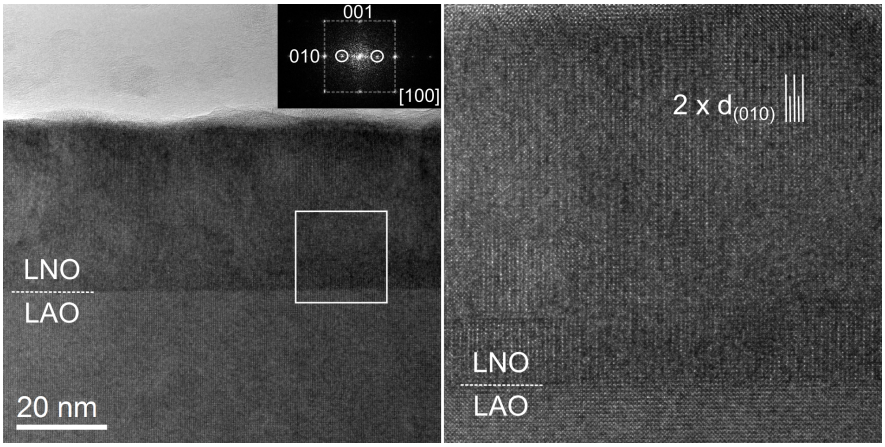

Figure 4.8 a) HRTEM image of the 35 nm LNO film grown on LAO taken along the [100] zone axis. Inset: FFT of the highlighted region. A superstructure modulation is observed over extended regions of the film, consisting in a doubling of the periodicity of the unit cell in the in-plane [010] direction. This can be seen as the 1/2x(010) spot in the FFT and in real space as the doubling of the d_{010} spacing, as indicated in panel (b). b) Close-up view from the highlighted region.

ticularly unfavorable in the case of Ni, tetragonal structures were proposed by Vidgasayar and Rao [8], in which the ordering of oxygen vacancies occurs in the [110] direction, forming chains of NiO_6 octahedra and NiO_4 square planes aligned along the c axis. Based on electron diffraction experiments, González-Calbet *el al.* [17] adopted the octahedral-square planes description but in the framework of a monoclinic cell with $2\sqrt{a_o}, 2\sqrt{a_o}, 2a_o$ cell parameters. Later, Moriga *et al.*[18] determined the correct unit cell symmetry from XRD data, which was found to be monoclinic but with a relationship to the ideal perovskite of the form $2a_o, 2a_o, 2a_o$. Given that the finer structural details are determined by the arrangements of oxygen atoms, which are weak scatterers for X-rays, the final refinement of the structure including the polyhedra tilt patterns was reported by Alonso *et al.* [7, 19] from high resolution neutron diffraction experiments. Their results also proved, based on the Brown bond model, that Ni atoms are divalent in both octahedral and planar coordination environments.

Figure 4.9(a) shows the unit cell for the oxygen deficient $LaNiO_{2.5}$, including the Ni coordination polyhedra only. The lattice parameters are $a_m = b_m = 7.8$, $c_m = 7.40$ and $\beta = 94^o$,

where the subindex m stands for monoclinic. The shortening of the $\vec{c}$ axis is a result of the missing two apical oxygens in the square planar columns, as shown in figure 4.9(b). When these apical oxygens are missing, the equatorial oxygens are drawn closer to the central Ni atom. As a result, the equatorial planes of the adjacent octahedral units are expanded and the apical oxygens are drawn closer to the central Ni atom to compensate for this [7].

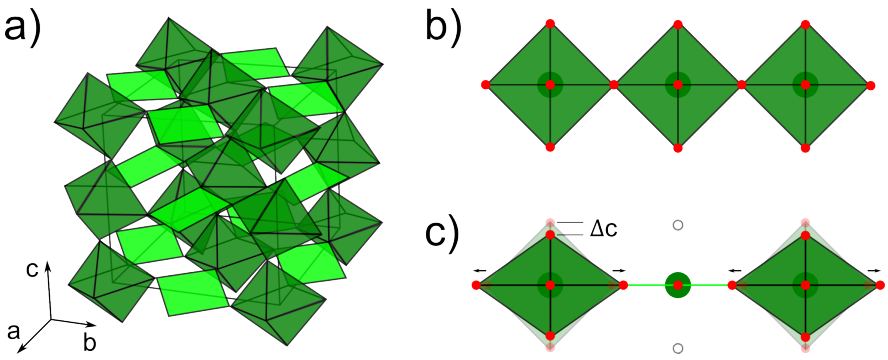

Figure 4.9 a) $LaNiO_{2.5}$ monoclinic unit cell showing the two different coordination environments for Ni atoms: octahedra and square planes. Adapted from [7]. b) Schematic view of the Ni coordination polyhedra in the ideal perovskite structure. c) Schematic view of the distortion of the Ni coordination polyhedra caused by the missing apical oxygens in every second Ni position along [110]. This distortion is responsible for the shortening of the c axis of the monoclinic phase when compared to the ideal perovskite.

Considering the HRTEM image of the 35 nm LNO film grown on LAO shown in figure 4.8, taken along the [100] zone axis, and the unit cell of the $LaNiO_{2.5}$ phase, the observed superstructure modulation can be explained as an octahedral tilt arrangement resulting from the missing oxygen atoms. However, images taken along the [100] zone axis can not provide direct imaging of the octahedral and planar coordinated columns, since they alternate along the [110] direction.

Taking into acount the compressive strain exerted by the LAO substrate, the shorter $\vec{c}$ axis of the monoclinic, oxygen defficient $LaNiO_{2.5}$ is expected to lay in plane. Given the cube-on-cube epitaxial relationship, when preparing a cross-section TEM specimen so that one of the faces of the LAO cubic cell is perpendicular to the electron beam, the $\vec{c}$ axis of the monoclinic

phase can end up lying either parallel or perpendicular to the electron beam. Figure 4.10 shows HRTEM images from two cross sections, both corresponding to 35 nm LNO films grown on a LAO substrate, perpendicular from each other. The experimental image in figure 4.10(a), as the one in figure 4.8, is compatible with the monoclinic $\vec{c}$ axis being oriented perpendicular to the electron beam. Therefore, by preparing a new TEM specimen from the same sample, cut at 90^o from the first one, it is expected to get the monoclinic $\vec{c}$ axis parallel to the electron beam. In this situation, the chains of NiO_6 octahedra and NiO_4 square planes would be apparent in the image. The corresponding HRTEM image from the 90^o rotated TEM specimen is shown in figure 4.10(b). A region with a contrast modulation consisting in a checkerboard pattern oriented at 45^o with respect to the substrate-film interface is clearly visible. This pattern corresponds to the doubling of the (110) interplanar distances, as predicted for the ordering of the oxygen vacancies in $LaNiO_{2.5}$ resulting in the chains of octahedra and square planes along the $\vec{c}$ axis. Figure 4.10(c) shows the structural models with the octahedra and square planes as seen in each one of the orientations related by a 90^o rotation.

Figure 4.11(a) shows an HRTEM image of the 35 nm LNO film grown on LSAT. A superstructure modulation doubling the perovskite unit cell is observed in this film too, but oriented parallel to the substrate-film interface. Considering again the $LaNiO_{2.5}$ phase, this can be understood in terms of the epitaxial strain exerted by the substrate. If the compressive LAO favoured the in-plane orientation of the monoclinic $\vec{c}$ axis, the tensile LSAT favours its out-of-plane orientation. In this situation, irrespective of the face of the cube of the LSAT substrate chosen to be oriented parallel to the electron beam in the cross-section TEM specimen, the ordered columns with oxygen vacancies will not be directly visible. Again, the observed superstructure corresponds to the octahedral tilt pattern, as depicted in figure 4.11(c), where the structural model with the coordination polyhedra is shown. By cutting a 45^o oriented specimen so that the (110) planes, in which the ordering occurs, are visible, a new superstructure modulation is expected to be seen, perpendicular to the substrate-film interface, coexisting with the parallel one, which corresponds to

the octahedral tilts. The experimental HRTEM image obtained from the 45^o rotated TEM specimen is shown in figure 4.11(b). The two contrast modulations are observed, corresponding to the octahedral and square plane columns oriented out of plane as is apparent in the structural model in figure 4.11(c).

In summary, the observed superstructure modulation in LNO thin films is found to be compatible with a lower symmetry, oxygen defficient, monoclinc $LaNiO_{2.5}$ phase. The octahedral tilt induced by the oxygen vacancies is observed in different orientations depending on the sign of the stress exerted by the substrate. This is related to the in-plane or out-of-plane orientation of the shorter monoclinic $\vec{c}$ axis. By choosing an adequate geometry for the TEM specimen preparation in each case, the crystal orientations revealing the alternating octahedral and planar square coordinated columns can be made accessible. However, this phase is not found everywhere in the films; in other words, $LaNiO_{2.5}$ does not constitute the totality of the films. This is in good agreement with the macroscopic conduction measurements. A metallic behaviour is found for all the studied layers. This would not be possible if only $LaNiO_{2.5}$ was present in these samples, as the Ni coordination environment and octahedral connectivity is crucial for the transport properties of $LaNiO_3$. Indeed, known oxygen deficient phases ($LaNiO_{3-\delta}$) are reported to be insulating.

Regarding the 14 nm films, no superstructure modulation is observed. However, the same arguments concerning the thermodynamic instability of Ni^{3+} and the subsequent presence of oxygen vacancies still hold. Considering that the 14 nm films have been grown under the same conditions as the 35 nm films, a certain degree of non-stoichiometry due to oxygen vacancies is expected. It is thus implied that a critical thickness exists for the ordering of the vacancies.

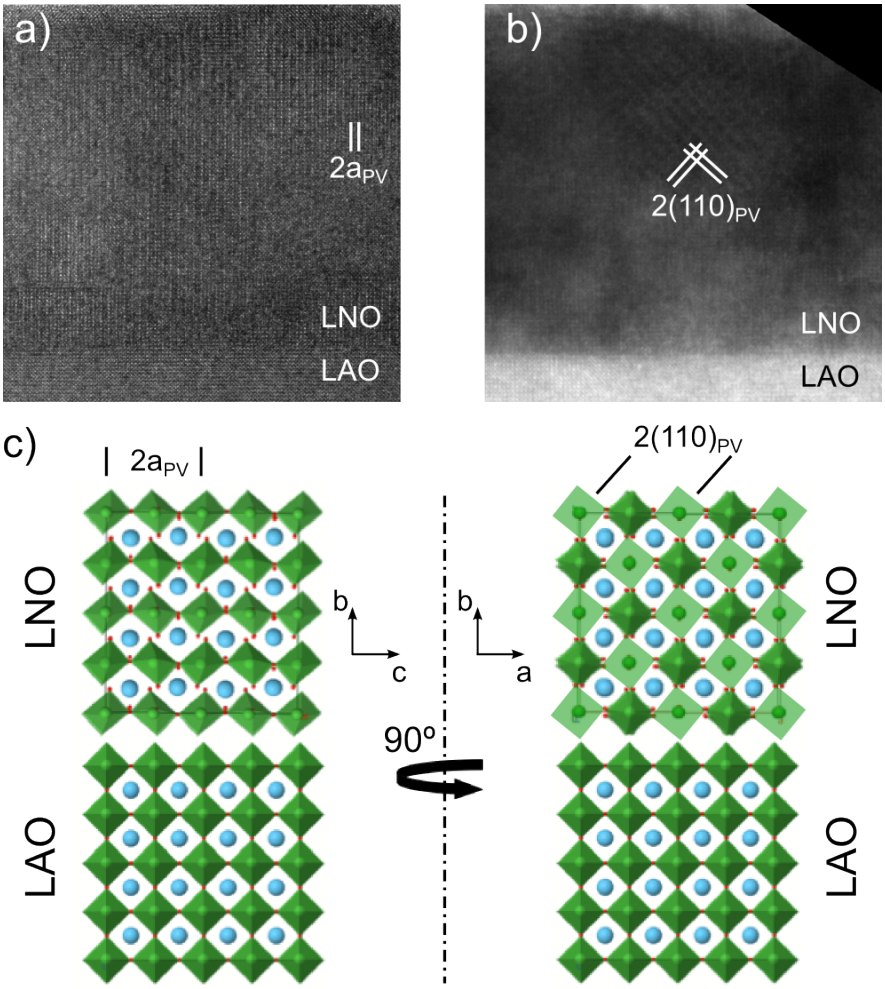

Figure 4.10 a,b) Pair of HRTEM images of the 35 nm LNO film on LAO related by a 90^o rotation of the sample preparation direction. c) Structural model of the $LaNiO_{2.5}$/LAO interface showing the octahedral tilt pattern of $LaNiO_{2.5}$, viewed along the $\vec{a}$ axis, and the alternating octahedral and planar columns, viewed along the c axis.

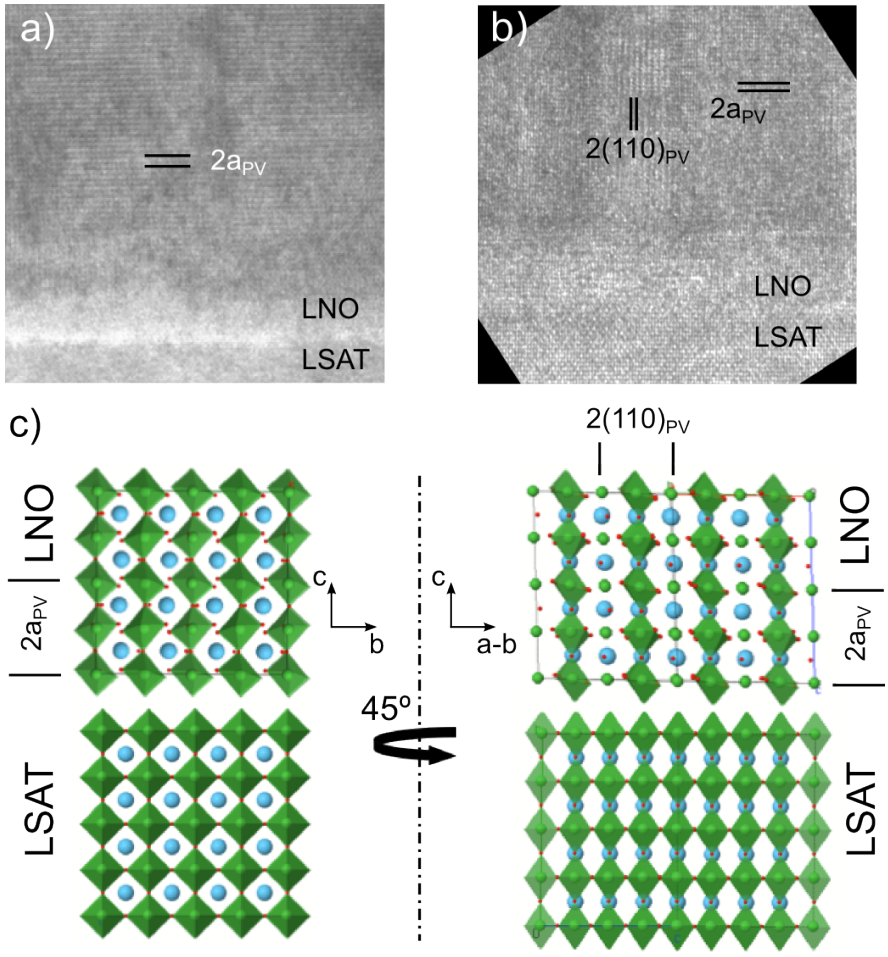

Figure 4.11 a) HRTEM image of the 35 nm LNO film on LSAT observed along the [100] direction. b) HRTEM image of the same film, from a TEM specimen prepared at 45^o from the one in (a), thus observed along the [110] direction. c) Structural model of the $LaNiO_{2.5}$/LSAT interface showing the origin of the modulations in (a) and (b): the effect of alternating columns of octahedral and planar columns is superimposed to that of the octahedral tilt pattern.

4.2.4 Conclusions

- 14 and 35 nm thick LNO films grown by PLD on LAO, LSAT, STO and YAO substrates have been characterized to study the different epitaxial strain states induced in the LNO films by the crystal lattice mismatch with each substrate.

- A good epitaxial growth of the films is confirmed from HRTEM and HAADF experiments. Thicknesses close to nominal are observed, with (14±1) nm and (35±5) nm for the two series, respectively. From the digital diffractograms (FFTs), LNO films grown on LAO, LSAT and STO are found to be completely adapted to the substrate. On the other hand, LNO grown on YAO is fully relaxed due to the larger lattice mismatch and the different structure of the orthorhombic substrate and the cubic LNO.

- The strain state of the LNO films grown on LAO, LSAT and STO has been studied by GPA. The results show fully strained LNO films in the in-plane direction and values close to those of bulk LNO for the out-of-plane parameter.

- Planar defects are found after the first 3 to 5 nm in all films. These defects are Ruddlesden-Popper faults, consisting in the displacement of the crystal lattice by half the unit cell along the [111] direction. Different orientations of the RP faults have been assessed by the study of the HAADF intensity. In particular, the presence, or lack, of a contrast difference between the A and B sites of the perovskite structure across a RP fault has been useful in determining the overlapping of different domains in the films.

- A local superstructure modulation has been observed in the 35 nm LNO films grown on LAO and LSAT, which has been found to correspond to $LaNiO_{2.5}$, a monoclinic oxygen defficient phase. The difference in the sign of the strain exerted by the LAO and LSAT substrates is found to lead to two different orientations of the monoclinic axes of $LaNiO_{2.5}$. Through an adequate TEM specimen preparation process, different zone axes of the oxygen deficient phase have been made accessible for observation.

- Both the strain exerted by the substrate, that affects the Ni-O angles and distances and, therefore, the orbital hybridization, and the non-stoichiometry of the films, that affects the octahedral network connectivity, are major aspects affecting the electrical transport properties of LNO.

4.3 InAlN/GaN Distributed Bragg reflectors

The series of III-V nitrides (AlN, InN, GaN) have attracted a great deal of attention, especially since the successful realization of the GaN-based high intensity blue LED by Nakamura in 1993 [20]. This breakthrough received the Nobel Prize in Physics in 2014. The possibility to tune the optical properties of functional devices in the visible range of the spectrum make them key building blocks in the field of optoelectronics. However, one of the main issues regarding the fabrication of efficient devices is the large lattice mismatch between the binary compounds. A solution is the use of ternary compounds (InAlN, AlGaN, InGaN) with different stoichiometries, which allow tuning the lattice parameter to meet the particular needs of a given application. Other problems still remain, such as the difference in optimal growth temperatures for each compound, which can lead, for instance, to a spinodal decomposition.

Distributed Bragg reflectors (DBRs) consist in multilayer devices containing alternating layers of materials with high and low refractive index values. By properly choosing the refractive indexes and the thicknesses of the semiperiods, it is possible to select the range of wavelengths to be reflected, through the phenomenon of constructive interference [21][22]. DBRs are used as highly efficient reflectors, for example, in resonant cavity LEDs [23] or in vertical cavity surface emitting lasers (VCSELs) [24][25]. The reflectivity values depend on the structural homogeneity of the layers, their flatness and the abruptness of the interfaces. [26]

4.3.1 Sample growth and preliminary characterization

In this section, the characterization of an InAlN/GaN ten-period DBR will be addressed. The device under study was grown by the group of Prof. Enrique Calleja at Instituto de Sistemas Optoelectrónicos y Microtecnología (ISOM), from Universidad Politécnica de Madrid (UPM). The vertical stacking of the device consists in a sapphire substrate on top of which a 4 μm GaN template is grown by Metalorganic Vapour Phase Epitaxy (MOVPE). Then, a 100 nm GaN buffer layer is grown by plasma assisted Molecular Beam Epitaxy (MBE) at a temperature of 700^o in order to

minimize the surface roughness, as it might propagate into the multilayer structure. InAlN semiperiods were grown at 535^o. A nominal composition of $In_{17}Al_{83}N$ whas chosen in order to achieve in-plane lattice matching with GaN, thus optimizing the crystalline quality of the system. GaN semiperiods were grown at the same temperature and in an In rich environment so that liquid In would act as a surfactant, enhancing Ga adatoms surface mobility. An annealing process at 600^o was carried out after every GaN semiperiod growth in order to desorb the accumulated In and improve GaN crystalline quality. The targeted thicknesses are 43 nm for the InAlN semiperiod and 40 nm for the GaN semiperiod to achieve the maximum reflectivity at a wavelength of 400 nm. Further details of the growth procedure can be found in references [27] and [28].

Figure 4.12(a) shows a HAADF image of the resulting DBR stacking. The expected 10 InAlN/GaN bilayers are successfully grown, with thickness values very close to nominal. XRD studies carried out at ISOM, already revealed a good stacking with a periodicity of 83 nm, as expected for the 43 nm InAlN/40 nm GaN bilayers. XRD also showed a perfect in-plane lattice matching of the two compounds. Using a linear Vegard law to relate the lattice parameters obtained from XRD with In content, the estimated value was found to be 18.4%. With the measured layer thicknesses and known refractive indexes for the layer compositions [29][30], the corresponding calculated reflectivity curve is obtained, as shown in figure 4.12(b). However, the experimentally measured reflectivity is below the expected value ($\sim$60% vs $\sim$75%). In order to determine the origin of the depleted optical properties of the device, TEM experiments were carried out to analyze the microstructure of the DBR device.

Samples for TEM observation were prepared in cross section geometry by mechanical polishing and subsequent Ar^+ ion milling up to electrotransparency, as described in Appendix B. HRTEM experiments were carried out in a JEOL 2010F microscope.

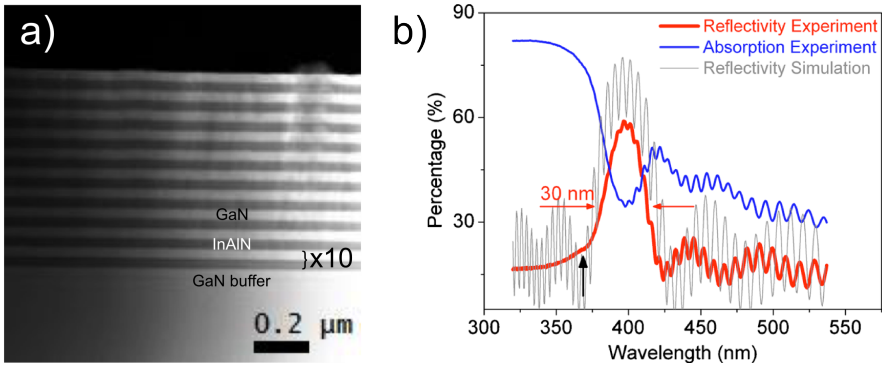

Figure 4.12 a) HAADF image of the InAlN/GaN DBR stacking. Dark layers correspond to the InAlN semiperiods and bright layers correspond to GaN semiperiods, given the atomic number dependence of the HAADF intensity. b) Reflectivity and absorption spectra measured for the studied device. Reflectivity spectrum calculated from known layer thickness and refractive indexes. A significantly lower value for the reflectivity is found ($\sim$ 60%), compared to the calculated curve. Reproduced from [28]

4.3.2 GaN polytypism: wurtzite and zinc blende phases

HRTEM images show a perfect, defect-free wurtzite structure for the InAlN layers. This is not he case for the GaN layers, where Moirée fringes with different perodicities as well as planar defects are apparent (see figure 4.13) in extended regions. In particular, it is evident from the difference in the stacking sequence of the growth direction planes that zinc blende GaN is also present in the GaN semiperiods.

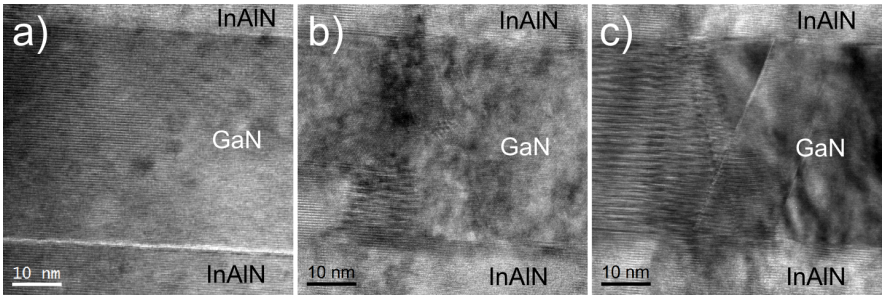

Figure 4.13 a) HRTEM image of a GaN semiperiod and corresponding bottom and top InAlN semiperiods. In this case only defect-free wurtzite is observed in the GaN layer. b-c) Examples of GaN layer regions where Moirée fringes and planar defects are apparent.

Figure 4.14 shows an HRTEM image from a GaN semiperiod region containing both wurtzite (W) and zinc blende (ZB) phases. The two phases are related by the epitaxial relationship $[110]GaN_W$-$(002)//\ [011]GaN_{ZB}(1\bar{1}0)$. As can be seen in the indexed FFT in panel (b), both phases are lattice-matched in the in-plane direction. However, some reflections corresponding to W and ZB are split in the out-of-plane direction. Vector addition of the reciprocal vectors of the split spots from the two phases results in the spots corresponding to the superposition Moirée pattern observed in the image.

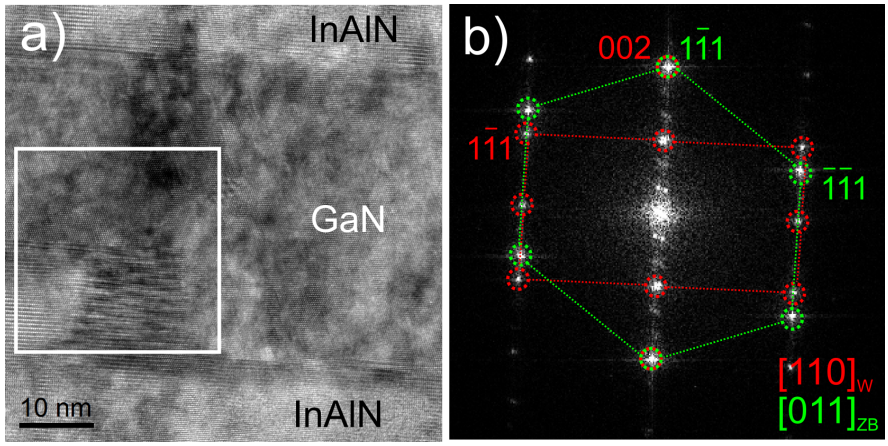

Figure 4.14 a) HRTEM image of a GaN semiperiod showing wurtzite (W) and zinc blende (ZB) GaN, as well a superposition region with Moirée fringes. b) FFT corresponding to the region higlighted in (a), showing the overlapping W and ZB GaN reciprocal cells. Spots corresponding to the superposition Moirée pattern are described by the out-of-plane lattice mismatch.

Following the indexation of the FFT in figure 4.14(b), a structural model for the contact surfaces between wurtzite and zinc blende GaN is proposed in figure 6.2. As stated above, the growth planes are the (001) plane of the wurtzite structure and a $\{111\}_{ZB}$ plane, respectively. However, the stacking sequence changes between the two structures, as can be seen in figure 6.2(a) that corresponds to the cross section view of the interface, as in the experimental HRTEM images. The wurtzite phase shows an *ababab*... type stacking sequence, or 2H (2 for the periodicity, H for hexagonal). Zinc blende phase has an *abcabcabc*... type stack-

ing, or 3C (3 for the periodicty, C for cubic). For the in-plane orientation, 3 rotations for the growth of $\{111\}_{ZB}$ zinc blende are possible, as shown in figure 4.15(b).

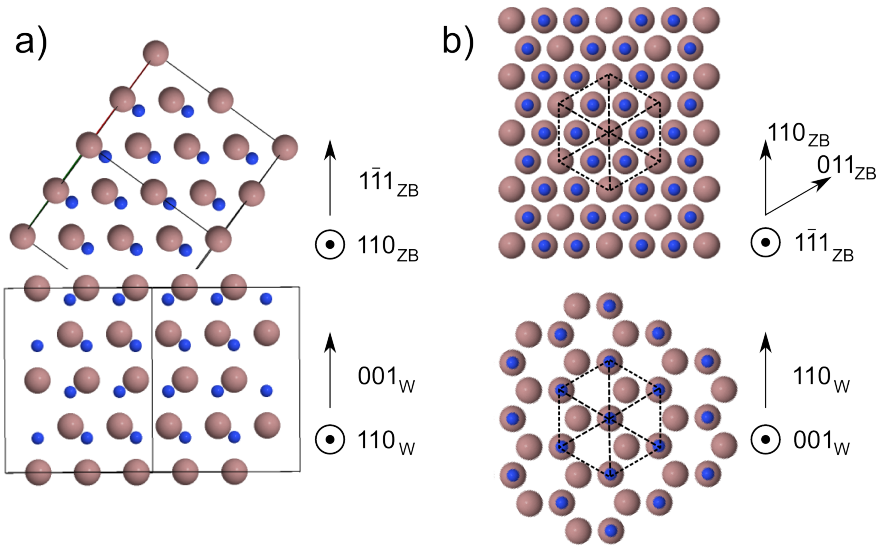

Figure 4.15 Model for the contact surfaces between wurtzite and zinc blende GaN. Large grey circles correspond to Ga atoms and small blue circles correspond to N atoms. a) Front view, as in the cross section experimental HRTEM images. b) Top view of the proposed contact surfaces. The highlighted hexagon indicates the alignment between the two phases. Notice that the ZB structure can be rotated by 120^o increments.

Figure 4.16(a) shows a lateral frontier, inside a GaN semiperiode, between wurtzite and zinc blende phases, including a small superposition region presenting Moirée fringes. Considering the structural model just described and the indexation of the pure phases in the image (panels (c) and (d), a model consisting in the superposition of a block of $[110]_W$ GaN and a block of $[011]_{ZB}$ GaN was created. An HRTEM image was simulated for this block and is presented superimposed to the experimental image in 4.16(b). The simulated image matches the experimentally observed Moirée fringes, with a 6-fold periodicty pattern with respect to the zinc blende structure.

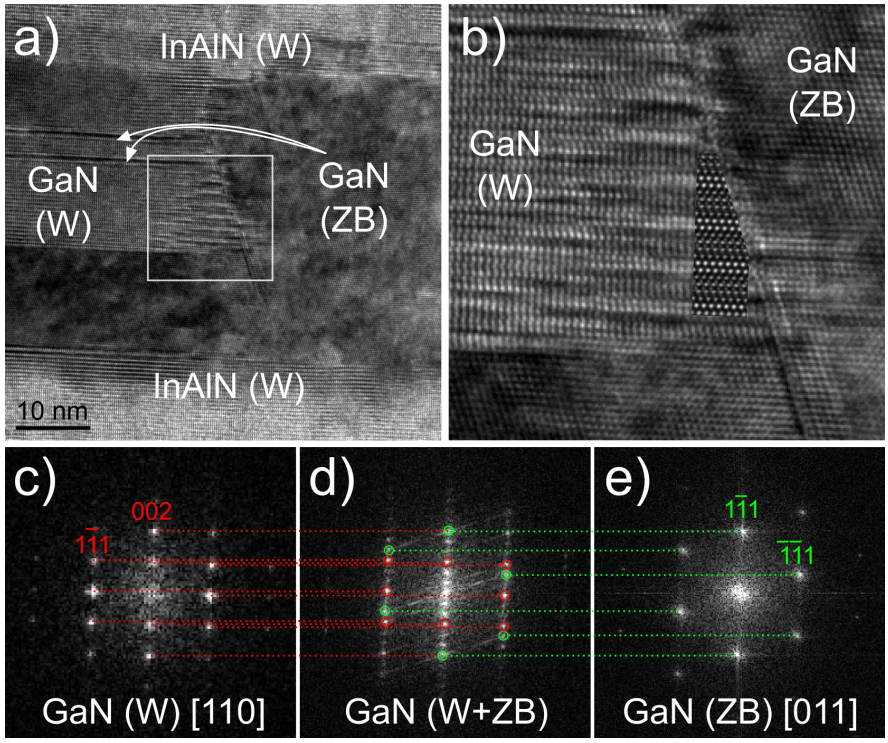

Figure 4.16 a) HRTEM image of a GaN layer with a superposition region of wurtzite and zinc blende phases. b) Close up view of the highlighted superposition region presenting Moirée fringes. Superimposed, a simulated HRTEM image obtained from the proposed structural model. c) FFT from the W region. d) FFT from the superposition region. e) FFT from the ZB region.

4.3.3 GaN twinning

Figure 4.17 shows an HRTEM image of the top GaN semiperiod of the stacking, containing only zinc blende GaN. A high density of planar defects is observed, as well as a region showing a different lattice periodicity (highlighted by a white square). Analysis of the FFT of this region, shown in panel (b), reveals the presence of two different orientations for the zinc blende GaN. Both orientations, $[110]_{ZB}$ and $[011]_{ZB}$, share the $[1\bar{1}1]_{ZB}$ growth direction and are related by a 60^o in-plane rotation. By vector adding the reciprocal lattice vectors from both zone axes, the additional spots in the FFT can be obtained, and the different periodicity in the region of overlapping can be understood as a Moirée pattern.

Considering the growth of GaN in this system, always on top of an hexagonal wurtzite InAlN layer, the same argument as applied for the construction of the contact surfaces model between wurtzite and zinc blende phases is still valid for the ZB semiperiod. Zinc blende GaN growing on top of [001] oriented wurtzite InAlN is expected to follow the epitaxial relationship in figure 4.15. Considering the hexagonal symmetry of the $[1\bar{1}1]_{ZB}$ growth direction planes, as can be seen in figure 4.15(b), all $[1\bar{1}1]_{ZB}$ orientations related by a 120^o in-plane rotation will be, in principle, equally likely to happen (e.g. the $[110]_{ZB}$ and $[011]_{ZB}$ drawn in panel (b)). This is in good agreement with the high density of twin defects that can be seen in the zinc blende GaN regions.

Taking this into account, a structural model was built in which a block of $[110]_{ZB}$-oriented GaN and a block of $[011]_{ZB}$-oriented GaN were superimposed in the direction of the electron beam. HRTEM images from this superposition region were simulated and the obtained three-fold periodicity of the Moirée fringes matches the experimental HRTEM image, as shown in figure 4.17(d).

4.3.4 Discussion

Polytypism in III-V compounds has been extensively reported in the literature for a long time, and stays nowadays an active topic of interest [31–39]. The presence of zinc blende GaN can be explained in the present case by the low growth temperature (535^oC), chosen to avoid the decomposition of the InAlN semiperiods [40]; the optimum temperature for wurtzite GaN growth being $\sim 700^o$C [41, 42].

Both the presence of polytipism and a high density of twin defects in the GaN layers compromise the homogeneity of the periods which, as stated above, is crucial for the performance of the device. The additional interfaces generated both at the boundaries between the two phases or at the twin planes separating the rotated domains of ZB GaN act as absorption and/or scattering centers for photons with energies below the bandgap. These defects would contribute to the residual absorption of the device, which would, in turn, lead to a decrease in reflectivity.

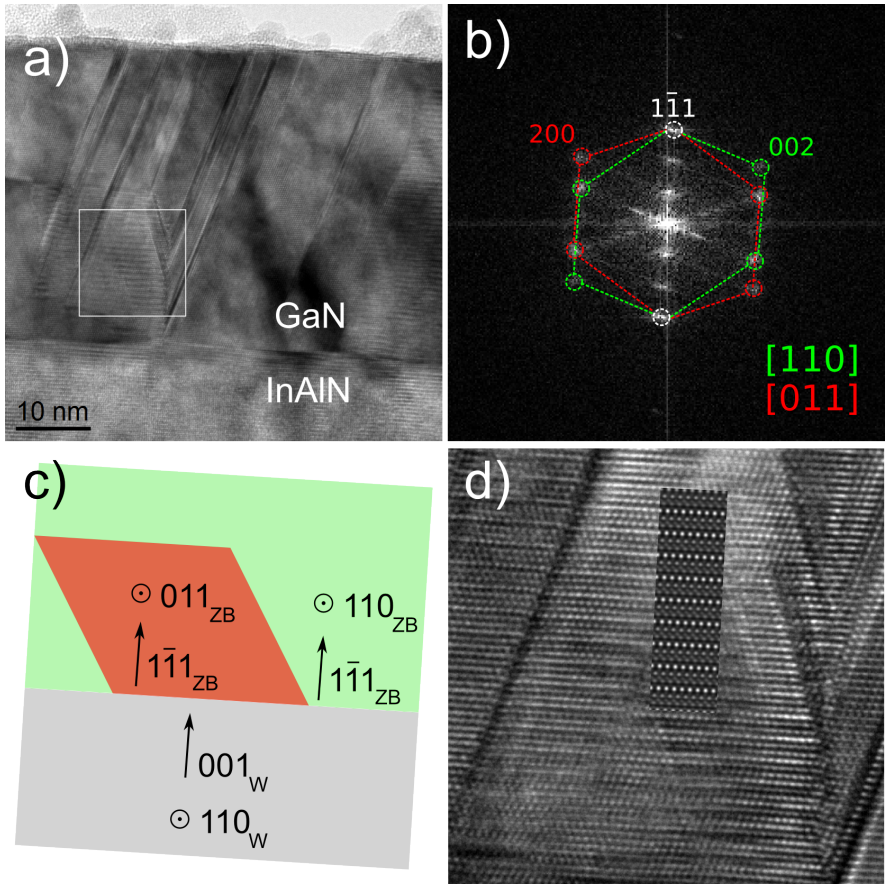

Figure 4.17 a) HRTEM image of a zinc blende GaN region showing twinning and Moirée fringes in the highlighted area. b) FFT from the highlighted area, with a 60^o twinning. c) Proposed structural model for the superposition region. d) Close up view of the region highlighted in (a) with a superimposed HRTEM simulated image obtained from the model. The simulated image reproduces the 3-fold periodicity corresponding to the Moirée fringes pattern.

4.3.5 Conclusions

- A DBR device consisting of alternating layers of InAlN and GaN, grown by plasma assisted MBE, has been studied by HRTEM in order to assess the presence of microstructural features that might account for the lower than expected reflectivity of the device.

- Defect-free InAlN semiperiods with wurtzite structure were observed. However, a high degree of structural inhomogeneity was found in the GaN semiperiods. Coexistence of wurtzite and zinc blende GaN was observed, as well as a number of planar defects in both phases. The presence of zinc blende GaN is attributed to the low growth temperature employed in order to avoid decomposition of the InAlN semiperiods.

- A structural model for the contact surfaces between wurtzite and zinc blende GaN is proposed considering the indexation of the experimental images and the unit cell symmetry.

- A high density of twin defects was observed in zinc blende GaN. The presence of these twins is explained in terms of the proposed structural model, as different in-plane rotations for the growth of ZB on top of W are possible.

- HRTEM image simulations were carried out in order to validate the proposed model for the contact surfaces and the orientation of the observed defects in the layers. Simulated images successfully reproduce the experimental HRTEM contrast for the case of overlapping wurtzite and zinc blende GaN as well as for the case of overlapping zinc blende domains with different in-plane orientations.

- The presence of these structural defects in the GaN layers explains the low reflectivity of the DBR device, since they act as absorption and/or scattering centers for photons with energies below the bandgap energy, thus increasing the residual absorption in the device.

Bibliography

[1] J. M. Ramírez, Y. Berencén, L. López-Conesa, J. M. Rebled, F. Peiró, and B. Garrido. Carrier transport and electroluminescence efficiency of erbium-doped silicon nanocrystal superlattices. *Appl. Phys. Lett.*, 103(8):081102, 2013.

[2] A. Eljarrat, L. López-Conesa, J.M. Rebled, Y. Berencén, J.M. Ramírez, B. Garrido, C. Magén, S. Estradé, and F. Peiró. Structural and compositional properties of Er-doped silicon nanoclusters/oxides for multilayered photonic devices studied by STEM-EELS. *Nanoscale*, 5(20):9963–70, 2013.

[3] J. López-Vidrier, S. Hernández, J. Samà, M. Canino, M. Allegrezza, M. Bellettato, R. Shukla, M. Schnabel, P. Löper, L. López-Conesa, S. Estradé, F. Peiró, S. Janz, and B. Garrido. Structural, optical and electrical properties of silicon nanocrystals embedded in Si_xC_{1-x}/SiC multilayer systems for photovoltaic applications. *Materials Science and Engineering: B*, 178(9):639–644, 2013.

[4] X.Q. Xu, J.L. Peng, Y. Li, H.L. Ju, and R.L. Greene. Resistivity, thermopower, and susceptibility of $RNiO_3$ (R = La, Pr). 48(2):1112–1118, 1993.

[5] M. Zhu, P. Komissinskiy, A. Radetinac, M. Vafaee, Z. Wang, and L. Alff. Effect of composition and strain on the electrical properties of $LaNiO_3$ thin films. *Applied Physics Letters*, 103(14):141902, 2013.

[6] R. Scherwitzl, P. Zubko, C. Lichtensteiger, and J.M. Triscone. Electric-field tuning of the metal-insulator trans-

ition in ultrathin films of $LaNiO_3$. *Applied Physics Letters*, 95(22):222114, 2009.

[7] J.A. Alonso, M.J. Martínez-Lope, J.L. García-Muñoz, and M.T. Fernández-Díaz. A structural and magnetic study of the defect perovskite $LaNiO_{2.5}$ from high-resolution neutron diffraction data. *J. Phys. Condens. Matter*, pages 6417–6426, 1997.

[8] M.K. Kinyanjui, Y. Lu, N. Gauquelin, M. Wu, A. Frano, P. Wochner, M. Reehuis, G. Christiani, G. Logvenov, H.U. Habermeier, G.A. Botton, U. Kaiser, B. Keimer, and E. Benckiser. Lattice distortions and octahedral rotations in epitaxially strained $LaNiO_3/LaAlO_3$ superlattices. *Applied Physics Letters*, 104(22):221909, 2014.

[9] J. Hwang, J. Son, J Zhang, A. Janotti, C. Van de Walle, and S. Stemmer. Structural origins of the properties of rare earth nickelate superlattices. *Physical Review B*, 87(6):060101, 2013.

[10] E. Sakai, M. Tamamitsu, K. Yoshimatsu, S. Okamoto, K. Horiba, M. Oshima, and H. Kumigashira. Gradual localization of Ni 3d states in $LaNiO_3$ ultrathin films induced by dimension. *Physical Review B*, 87(7):075132, 2013.

[11] T. Suzuki, Y. Nishi, and M. Fujimoto. Ruddlesden–Popper planar faults and nanotwins in heteroepitaxial nonstoichiometric barium titanate thin films. *Journal of the American ...*, 95:3185–3195, 2000.

[12] E. Detemple, Q.M. Ramasse, W. Sigle, G. Cristiani, H.U. Habermeier, B. Keimer, and P.A. van Aken. Ruddlesden-Popper faults in $LaNiO_3/LaAlO_3$ superlattices. *Journal of Applied Physics*, 112(1):013509, 2012.

[13] D.I. Woodward and I.M. Reaney. Electron diffraction of tilted perovskites. *Acta crystallographica. Section B, Structural science*, 61(4):387–99, 2005.

[14] S. Stølen, C.E. Mohn, P. Ravindran, and N.L. Allan. Topography of the potential energy hypersurface and criteria for

fast-ion conduction in perovskite-related $A_2B_2O_5$ oxides. *The journal of physical chemistry. B*, 109(25):12362–5, 2005.

[15] S. Stølen, E. Bakken, and C.E. Mohn. Oxygen-deficient perovskites: linking structure, energetics and ion transport. *Physical chemistry chemical physics : PCCP*, 8(4):429–47, 2006.

[16] M. Crespin, P. Levitz, and L. Gatineau. *J. Chem. Soc. Faraday Trans.*, 1983.

[17] J.M. González-Calbet, M.J. Sayagués, and M. Vallet-Regi. An electron diffraction study of new phases in the lanio$_{3-x}$ system. *1989*, Solid State Ionics.

[18] T. Moriga, O. Usaka, T. Inamura, I. Nakabayashi, I. Matsubara, T. Kinouchi, S. Kikkawa, and F. Kanamaru. *1994*, Bull. Chem. Soc. Japan.

[19] J.A. Alonso and M.J. Martínez-Lope. Preparation and crystal structure of the deficient perovskite $LaNiO_{2.5}$, solved from neutron powder diffraction data. *Journal of the Chemical Society, Dalton Transactions*, (17):2819, 1995.

[20] *The Blue Laser Diode. The Complete Story.* Springer-Verlag Berlin Heidelberg, 2000.

[21] T. Ive, O. Brandt, X. Kong, A. Trampert, and K. Ploog. (Al,In)N layers and (Al,In)N/GaN heterostructures grown by plasma-assisted molecular beam epitaxy on 6H-SiC(0001). *Physical Review B*, 78(3):1–9, 2008.

[22] Ž. Gačević, S. Fernández-Garrido, E. Calleja, E. Luna, and A. Trampert. Growth and characterization of lattice-matched InAlN/GaN Bragg reflectors grown by plasma-assisted molecular beam epitaxy. *Physica Status Solidi (C)*, 6(S2):S643–S645, 2009.

[23] J.F. Carlin and M. Ilegems. High-quality AllnN for high index contrast Bragg mirrors lattice matched to GaN. *Applied physics letters*, 83(4):668–670.

[24] E. Feltin, R. Butte, J.F. Carlin, J. Dorsaz, N. Grandjean, and M. Ilegems. Lattice-matched distributed Bragg reflectors for nitride-based vertical cavity surface emitting lasers. 41(2), 2005.

[25] E. Feltin, G. Christmann, J. Dorsaz, A. Castiglia, J.F. Carlin, R. Butte, N. Grandjean, S. Christopoulos, G. Baldassarri Höger von Högersthal, A.J.D. Grundy, P.G. Lagoudakis, and J.J. Baumberg. Blue lasing at room temperature in an optically pumped lattice-matched AlInN/GaN VCSEL structure. 43(17), 2007.

[26] C.M. Wu, B.P. Zhang, J.Z. Shang, L.E. Cai, J.Y. Zhang, J.Z. Yu, and Q.M. Wang. High-reflectivity AlN/GaN distributed Bragg reflectors grown on sapphire substrates by MOCVD. *Semiconductor Science and Technology*, 26(5):055013, 2011.

[27] S. Fernández-Garrido, Ž. Gačević, and E. Calleja. A comprehensive diagram to grow InAlN alloys by plasma-assisted molecular beam epitaxy. *Applied Physics Letters*, 93(19):2006–2009, 2008.

[28] Ž. Gačević, S. Fernández-Garrido, D. Hosseini, S. Estradé, F. Peiró, and E. Calleja. InAlN / GaN Bragg reflectors grown by plasma-assisted molecular beam epitaxy. *Journal of Applied Physics*, 108(113117):1–7, 2010.

[29] D. Brunner, H. Angerer, E. Bustarret, F. Freudenberg, R. Hopler, R. Dimitrov, O. Ambacher, and M. Stutzmann. Optical constants of epitaxial AlGaN films and their temperature dependence. *Journal of Applied Physics*, 82(10):5090–5096, 1997.

[30] R. Butté, J.F. Carlin, E. Feltin, M. Gonschorek, S. Nicolay, G. Christmann, D. Simeonov, A. Castiglia, J. Dorsaz, H.J. Buehlmann, S. Christopoulos, G. Baldassarri Höger von Högersthal, a.J.D. Grundy, M. Mosca, C. Pinquier, M.A. Py, F. Demangeot, J. Frandon, P.G. Lagoudakis, J.J. Baumberg, and N. Grandjean. Current status of AlInN layers lattice-matched to GaN for photonics and electronics. 6328, 2007.

[31] X.H. Wu, L.M. Brown, D. Kapolnek, S. Keller, B. Keller, S.P. DenBaars, and J.S. Speck. Defect structure of metal-organic chemical vapor deposition-grown epitaxial (0001) GaN/Al_2O_3. *Journal of Applied Physics*, 80(6):3228, 1996.

[32] T. Ito. Simple criterion for wurtzite - zinc-blende polytypism in semiconductors. *Japanese Journal of Applied Physics*, 37, 1998.

[33] L. Mancera, J.A. Rodríguez, and N. Takeuchi. Theoretical study of the stability of wurtzite, zinc-blende, NaCl and CsCl phases in group IIIB and IIIA nitrides. *Physica Status Solidi (B)*, 241(10):2424–2428, 2004.

[34] E. Monroy, M. Hermann, E. Sarigiannidou, T. Andreev, P. Holliger, S. Monnoye, H. Mank, B. Daudin, and M. Eickhoff. Polytype transition of N-face GaN:Mg from wurtzite to zinc-blende. *Journal of Applied Physics*, 96(7):3709, 2004.

[35] J.H. Kim and P.H. Holloway. Wurtzite to zinc-blende phase transition in gallium nitride thin films. *Applied Physics Letters*, 84(5):711, 2004.

[36] B.W. Jacobs, V.M. Ayres, M.A. Crimp, and K. McElroy. Internal structure of multiphase zinc-blende wurtzite gallium nitride nanowires. *Nanotechnology*, 19(40):405706, 2008.

[37] H.Y. Xu, Z. Liu, Y. Liang, Y.Y. Rao, X.T. Zhang, and S.K. Hark. Structure and photoluminescence of wurtzite/zinc-blende heterostructure GaN nanorods. *Applied Physics Letters*, 95(13):133108, 2009.

[38] G. Jacopin, L. Rigutti, L. Largeau, F. Fortuna, F. Furtmayr, F. H. Julien, M. Eickhoff, and M. Tchernycheva. Optical properties of wurtzite/zinc-blende heterostructures in GaN nanowires. *Journal of Applied Physics*, 110(6):064313, 2011.

[39] W.Y. Pang, I. Lo, S. Wu, Z.X. Lin, C.H. Shih, Y.C. Lin, Y.C. Wang, C.H. Hu, and G.Z.L. Hsu. Growth of wurtzite and zinc-blende phased GaN on silicon (100) substrate with sputtered AlN buffer layer. *Journal of Crystal Growth*, 382:1–6, 2013.

[40] Takashi Matsuoka and Takashi Matsuoka. Calculation of unstable mixing region in wurtzite $In_{1-x-y}Ga_xAl_yN$. *Applied Physics Letters*, 71(1997):105–106, 1997.

[41] B. M. Shi, M. H. Xie, H. S. Wu, N. Wang, and S. Y. Tong. Transition between wurtzite and zinc-blende GaN: An effect of deposition condition of molecular-beam epitaxy. *Applied Physics Letters*, 89(15):151921, 2006.

[42] S. Suandon, S. Sanorpim, K. Yoodee, and K. Onabe. Effect of growth temperature on polytype transition of GaN from zincblende to wurtzite. *Thin Solid Films*, 515(10):4393–4396, 2007.

Chapter 5

1D materials: localized strain fields in core-shell nanowires

5.1 Introduction

In this chapter we will focus on nanostructures with 2 dimensions confined in the nanoscale. Nanowires, nanotubes, nanorods, etc. find a lot of applications on their own and, in addition, are suitable to be tailored to form heterostructures (either radial or longitudinal), functionalized with organic molecules, decorated or filled (in the case of nanotubes) [1–4].

Semiconductor nanowires have attracted much attention over the past few years. From a technological point of view, advantages such as the possibility to use crystal phases that are not stable in bulk, the easier lattice matching between different phases or materials due to the lack of lateral relaxation, or the related strain engineering in such interfaces opens a wide field of possibilities, all this, combined with the prospect of the possible integration in the already developed and scalable semiconductor industry. On the other hand, the resulting quantum confinement of charge carriers in space gives rise to interesting new phenomena and new applications [5].

Last, but not least, the high surface to volume ratio of 1D nano objects allows for a very high efficiency in applications such

as catalysis or sensing, where performance is controlled by the reactivity of the surface and the contribution of the bulk is rather unimportant or even a drawback [6–8].

This chapter will be devoted to the study of Nb_2O_5 and Nb_2O_5/SnO_2 core shell heterostructures, with applications in humidity sensing. It will focus on the characterization of the surfaces, both the free surface of the Nb_2O_5 nanorods and the Nb_2O_5/SnO_2 heterojunction, which are critical for the humidity sensing properties of the nanostructures, mostly through HRTEM. Interpretation and analysis of the images will be carried out by means of HRTEM image simulation and GPA.

5.2 Nb_2O_5 for humidity sensing

The research into solid-state sensors with higher sensitivity, better selectivity, and long-term stability has significantly increased in recent years [9–11]. In particular, humidity sensing is receiving significant attention given its technological potential, as it is needed in many areas of industrial processing, environmental control, and medical applications [12, 13]. Nanostructured metal oxides are ideally suited for the fabrication of sensors with improved performances due to the confinement effects and the possibility to tailor their surface and charge-transport properties by adjusting their size and shape [14–17]. Humidity sensors based on the most widely used metal oxide, SnO_2, mostly operate at relatively high temperatures (>200 ^{o}C), and they are known to suffer from undesired cross-sensitivity effects in the presence of other gases [18, 19]. The sensor response is commonly explained by chemisorption of water molecules onto the SnO_2 surface, which alters the electronic conduction by depleting the metal oxide of charge carriers and inhibiting the charge-transduction processes with analyte molecules. This response is, thus, rather irregular.

Nb_2O_5 is a less-studied but promising ceramic material for sensing applications due to its good response to moisture even at room temperature [20–22]. Stoichiometric Nb_2O_5 is an insulator, but it becomes an n-type semiconductor at very low oxygen deficiency levels, with a conduction band formed by Nb-3d orbitals and a valence band formed by O-2p orbitals. The humidity detection mechanism is usually described as the condensation of water molecules onto the NbO_x surface, which induces proton conduction and, as a result, a change in the net electrical conductivity [22]. Consequently, the morphology of the NbO_x surface critically influences the final response of this material toward moisture.

The reduction of energy consumption in sensor devices demands materials that can deliver optimal sensing behavior at low or room temperature. In general, sensors based on ionic conduction mechanisms show a higher sensitivity toward water vapor than those based on electronic conduction [23]. However, most of the wideband semiconductors such as Nb_2O_5 exhibit low mobility of charge carriers, leading to a high resistivity, which

makes them less attractive for their implementation in devices. Heterostructured nanomaterials, based on engineered metal-oxide or oxide-oxide multimaterial junctions, can enhance the functional performance by combining individual material characteristics, which have shown significant advantages when compared with their single-component counterparts. In the case of Nb_2O_5 as a humidity sensor, the pairing with SnO_2 allows combining the high sensitivity of the former with the good electrical conductivity and device integrability of the latter.

5.2.1 Synthesis and preliminary characterization

As previously described, ceramic materials such as Nb_2O_5 detect humidity at low temperatures following ionic conduction mechanisms: when the Nb_2O_5 nanorods are exposed to humidity, the water molecules dissociate, resulting in hydroxyl groups attached to their surface. If only hydroxyl groups are present in the surface, then protons hop between adjacent hydroxyl groups, leading to protonic conduction. If enough water molecules are available, then a second layer of water molecules is formed, which is stagnant and cannot move freely due to the bonding to the two hydrogen atoms. Further layers of water molecules subsequently adsorbed allow the free movement of the protons through the network formed by water molecules, leading to an effective ionic conduction as a function of the humidity content in air (Grotthuss mechanism). However, the high resistivity of Nb_2O_5 at 60^oC prevents any realistic implementation of a device. Hence the use of Nb_2O_5@SnO_2 heterostructures is proposed in order to take advantage of the good transport properties of SnO_2.

Nb_2O_5 nanorods were grown by the group of Professor Sanjay Mathur at Köln University [24], through the CVD controlled decomposition of $[Nb(O^iPr)_5]_2$ precursor at 950 ^oC on top of polycrystalline alumina substrate. One dimensional growth was promoted by adjusting the precursor flow and the substrate temperature, which lead to the formation of needle-like deposits. Nb_2O_5@SnO_2 heterostructures were also grown at Köln University. SnO_2 nanowires were synthesized by decomposition of $[Sn(O^tBu)_4]$ precursor at 750 ^oC on gold-sputtered aluminum oxide substrates through the vapor-liquid-solid (VLS) growth mechanism. The

growth of SnO2/Nb_2O_5 core-shell heterostructures was achieved by CVD, via the decomposition of $[Nb(O^iPr)_5]_2$ at 950 ^oC onto the as-grown crystalline SnO_2 nanowires. The deposition of the Nb_2O_5 shell was carried out in the same conditions as the bare Nb_2O_5 nanorods, to allow comparing their performances.

In order to assess the effectiveness of this approach, the humidity sensing response of three different systems was measured at the Nb_2O_5 optimal temperature of 60^{o}C. First, bare Nb_2O_5 nanorods. Second, Nb_2O_5-covered SnO_2 nanowires with a low-density coverage. Finally, Nb_2O_5-covered SnO_2 nanowires with a high-density coverage. The compared results are shown in figure 5.1. Remarkably, the fully covered Nb_2O_5@SnO_2 heterostructures present an equivalent value for the sensitivity as the bare Nb_2O_5 nanorods, but a three times shorter recovery time.

The heterostructure strategy is, thus, proven useful. The TEM structural characterization aims at explaining the origin of this improved functionality down to atomic level. Samples were prepared for TEM observation by scratching of the deposited nanostrutures from the substrates with a razor, suspension of the obtained powder in hexane and subsequent dispersion of a droplet on top of a holey carbon-covered copper grid. HRTEM experiments were carried out in the JEOL J2100 and JEOL J2010F microscopes at CCiT-UB, and the FEI Tecnai F30 microscope at LMA-INA.

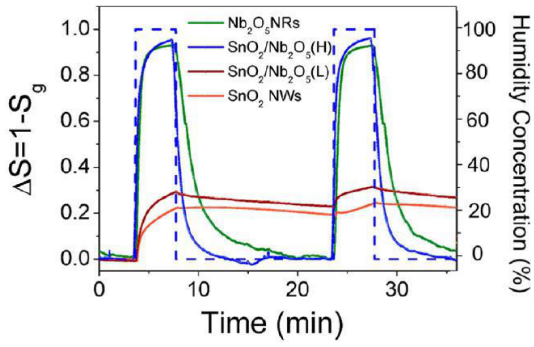

Figure 5.1 Humidity sensing behavior of Nb_2O_5, SnO_2, and Nb_2O_5/SnO_2 (H) and (L) heterostructures with high and low Nb_2O_5 content, respectively.

5.3 Nb_2O_5 nanorods

A general view of the synthesized Nb_2O_5 nanorods is shown in figure 5.2. They present lengths under 500 nm and diameters ranging from 30 nm to 50 nm. Contrast fringes along the growth direction are observed in all nanorods. They are more clearly visible in the higher magnification HRTEM images in figure 5.3, resulting in a streaking of the intensity in the FFTs. Streaking patterns are often related to planar defects in crystals, such as twins or stacking faults.

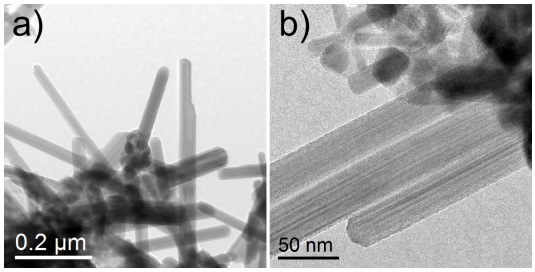

Figure 5.2 a) General BF image of the Nb_2O_5 nanorods. b) Higher magnification image. All the nanorods present contrast fringes oriented along the growth direction.

The indexation of the FFTs of the Nb_2O_5 nanorods is far from straightforward. Nb_2O_5 presents a large number of crystal modifications, depending strongly on the employed synthesis method and conditions. The high temperature forms expected from the synthesis of the nanorods present rather similar block structures, defined by the arrangement and connectivity of $n \times n$ blocks of NbO_6 octahedra. Two monoclinic space groups, C2 (#5) and C2/m (#12), are consistent with the obtained digital diffraction patterns. The structure described according to space group C2 presents a unit cell with $a = 5.2$, $b = 4.7$ $c = 5.9$, $\beta = 108.6^o$. The unit cell of the structure described according to space group C2/m presents a unit cell with $a = 28.5$, $b = 3.8$ $c = 17.5$, $\beta = 120.8^o$. In a monoclinic axes set, the NbO_6 building blocks form infinite chains along the $\vec{b}$ axis. Therefore, observation along the [010] zone axis should provide the necessary information to elucidate the structure of the nanorods. However, and rather logically considering their uniaxial symmetry, all nanorods present the monoclinic $\vec{b}$ axis oriented along the growth direction, contained in-plane and not accessible for observation.

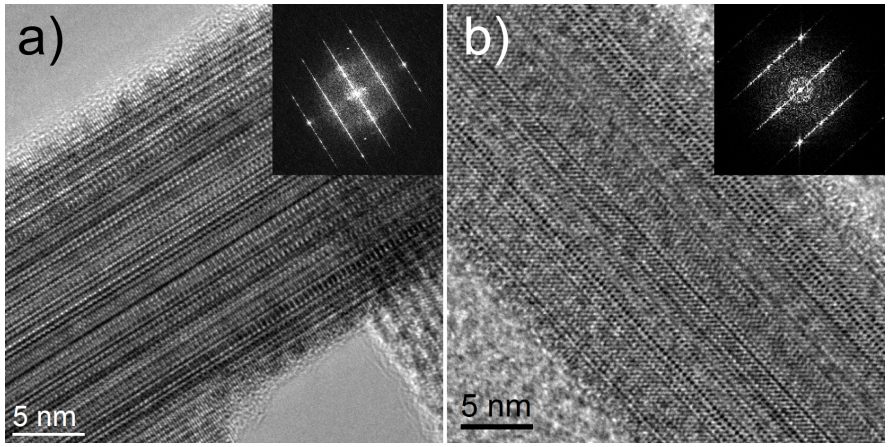

Figure 5.3 HRTEM image of two Nb_2O_5 nanorods. A complex contrast modulation is observed, perpendicular to the growth direction of the nanorod.

A direct experimental strategy for solving this problem would be the preparation of a cross-section TEM specimen from a nanowire, thus making the [010] accessible for observation. Although this is feasible, *e.g.* by using FIB sample preparation (see Appendix B), it is a sophisticated and time consuming approach. On the other hand, HRTEM simulation offers the possibility to tackle this problem with no need for new sample preparations and additional experiments. Therefore, atomic models were created for the considered phases of Nb_2O_5, and HRTEM images were simulated for different crystal orientations and microscope conditions.

Considering the streaking patterns in the FFTs, twin defects were introduced in the crystallographically perfect monoclinic C2 structure in order to take into account the contrast modulation. However, no successful match with the experimental HRTEM contrast was achieved. On the other hand, the intrinsically twinned C2/m phase successfully reproduced the experimental contrast, as shown by the simulations superimposed to the experimental image in figure 5.4.

HRTEM image simulation thus confirmed the formation of Nb_2O_5 nanorods corresponding to space group 12 phase (C2/m, $a = 28.5$, $b = 3.8$ $c = 17.5$, $\beta = 120.8^o$). In spite of not being a direct structural determination technique (as explained in Chapter

1) HRTEM proved a useful technique in order to discriminate between possible known structures for a given compound, involving just offline analysis of the data. After HRTEM simulation results allowed a proper indexation of two disctint regions of the nanorod, a twin defect could be structurally described, as shown in panel (a). The defect plane is marked by a dashed line. Both domains share the (020) planes in the growth direction, but are rotated with respect to each other and are observed along [301] and [101] directions, respectively.

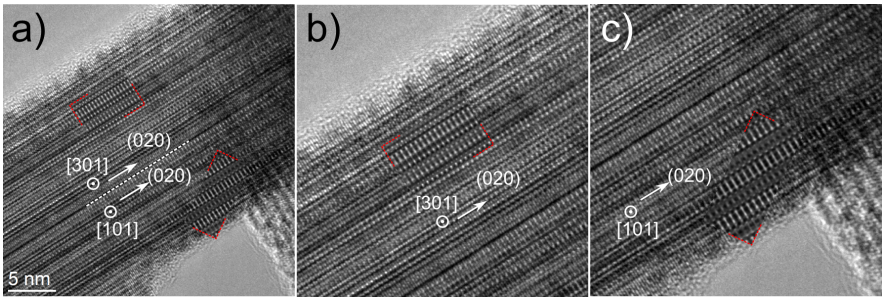

Figure 5.4 a) HRTEM image of a Nb_2O_5 nanorod with superimposed HRTEM simulations for the C2/m structure. The presence of a twin defect is indicated. b-c) Close-up views of the two regions of the nanorod separated by the twin defect, with superimposed HRTEM simulations.

5.4 Nb_2O_5@SnO_2 heterostructures

The resulting fully covered core-shell nanowire heterostructure is shown in figure 5.5. The Nb_2O_5 coverage is not homogeneous, but in the form of connected islands.

In order to have an easier access to the interface between the two materials, core-shell nanorods with a low-density Nb_2O_5 coverage were studied. The resulting heterostructures are shown in figure 5.6. Nb_2O_5 islands are almost isolated on the SnO_2 nanowire at this stage. Morphologically, these Nb_2O_5 islands are found in the form of truncated pyramids. Some of them present dark contrast bands perpendicular to the interface.

HRTEM images of the interfaces, and corresponding FFTs, reveal the epitaxial growth of monoclinic C2 (#5) Nb_2O_5 on top of rutile SnO_2, with an epitaxial relationship $[103]SnO_2(00\bar{1})$ //

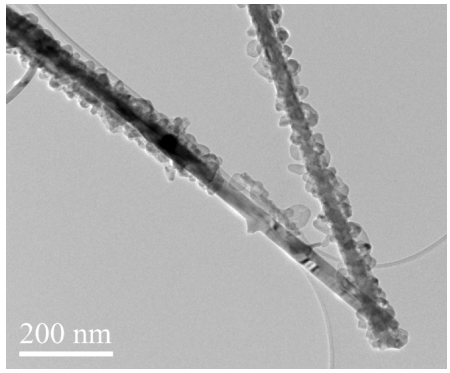

Figure 5.5 BF image showing two fully Nb_2O_5-covered SnO_2 nanowires forming core-shell heterostructures. The shells are not homogeneous, but formed by small crystals.

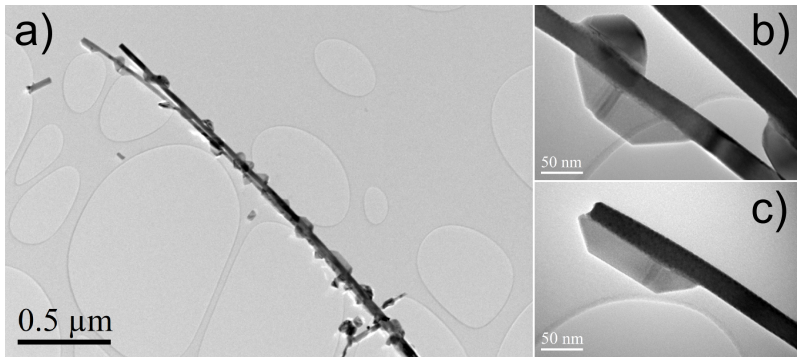

Figure 5.6 BF images of the low density Nb_2O_5/SnO_2 nanowires. a) General view of a nanowire. b-c) Close-up view of the Nb_2O_5 islands showing a truncated pyramid morphology. Largest pyramid in panel (b) shows dark contrast bands perpendicular to the interface.

$[100]Nb_2O_5(\bar{3}01)$, as shown in figure 5.7. The Nb_2O_5 structure appears to be relaxed, as can be seen in the splitting of the SnO_2 $00\bar{1}$ and Nb_2O_5 $\bar{3}01$ out-of-plane spots and the 040 in-plane spots in the FFTs (highlighted by arrows in figure 5.7). Periodic dark contrast features are visible along the two interfaces. By placing a mask on the in-plane shared 020 reflections and computing the inverse FFT (IFFT), dislocation networks at the interfaces are revealed (figures 5.7(c) and 5.7(f)). These dislocations result in the dark contrast features observed at the interfaces in the HRTEM images, due to the lack of crystal coherence at the defects and the subsequent loss of phase contrast.

Further analysis of the strain state of the Nb_2O_5 islands was carried out using Geometric Phase Analysis (GPA). Figure 5.8

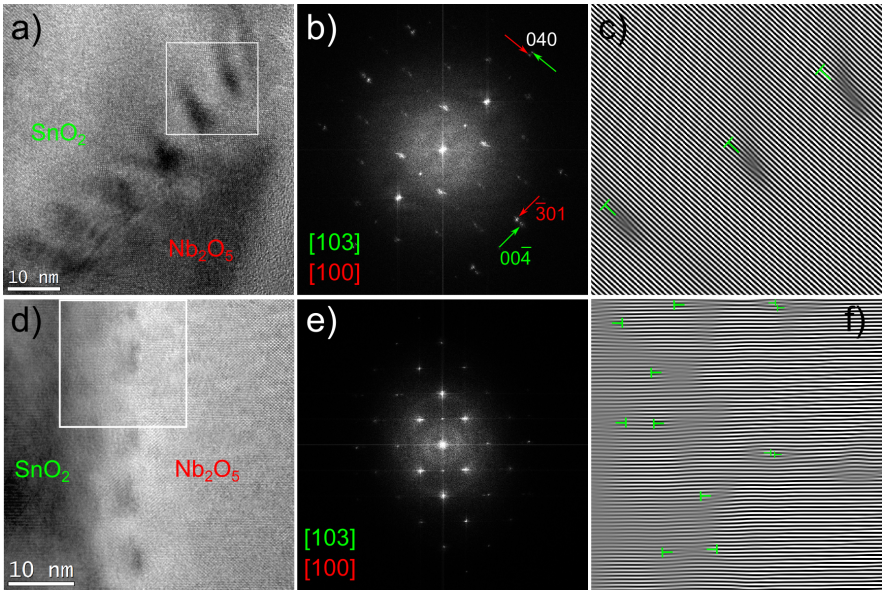

Figure 5.7 a-d) HRTEM images of two Nb_2O_5/SnO_2 interfaces. b,e) Corresponding FFTs showing splitting of the spots due to the relaxation of the grown Nb_2O_5. c,f) IFFTs of the regions highlighted by white squares in (a,d), selecting the 020 reflections only, and showing a network of dislocations at the interfaces.

shows an HRTEM image of a Nb_2O_5/SnO_2 interface and the calculated map for the in-plane component of the strain tensor (ϵ_{xx}). The resulting strain map shows the dislocations as bright contrast due to lattice planes bending at the defect sites. In good agreement with the IFFT analysis of HRTEM images, dislocations are found at the interface with a periodicity of ~ 10 nm.

More interestingly, the ϵ_{xx} map in figure 5.8b shows that the Nb_2O_5 is not fully relaxed through the formation of interface dislocations. It is clear that strain propagates into the island in vertical bands perpendicular to the interface. The in-plane strain relaxation can be quantified at $\sim 3\%$, at its lowest, from a strain profile drawn across the interface. A strain profile drawn across the bands in the Nb_2O_5 island yields an additional strain relaxation variation of $\sim 2\%$ in the perpendicular direction.

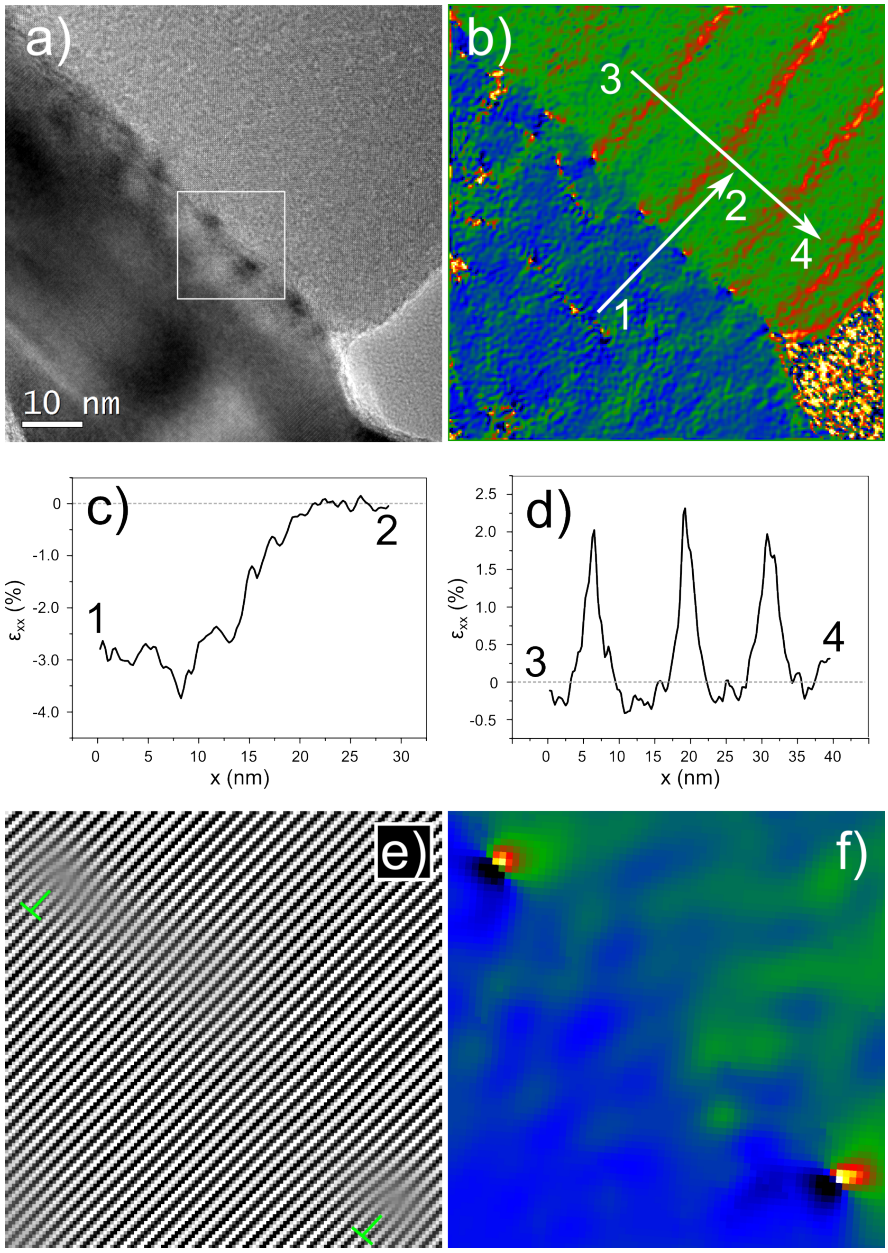

Figure 5.8 a) HRTEM image of a Nb_2O_5/SnO_2 interface showing periodic dark contrast features. b) Corresponding GPA map calculated for the in-plane component of the strain tensor ϵ_{xx}. c-d) Intensity profiles along the highlighted lines in b), showing that, in spite of the presence of dislocations, strain still propagates into the island in vertical bands. e) IFFT image from the 020 reflections of Nb_2O_5 and SnO_2 showing dislocations. f) ϵ_{xx} map showing the strain at the dislocation sites.

Twin defects are also observed at the interfaces of other Nb_2O_5 islands instead of the dislocations described thus far. Some of these twins are oriented parallel to the nanowire-island interface, as the one shown in figure 5.9. In this case, the growth of the Nb_2O_5 starts along the orientation given by the epitaxial relationship with SnO_2. Growth continues for 1-2 nm before rotating in plane; then, the twinned domain grows in the full extension of the island for another 1-2 nm and it rotates again to the original growth direction. The subsequent growth of the Nb_2O_5 island is defect free.

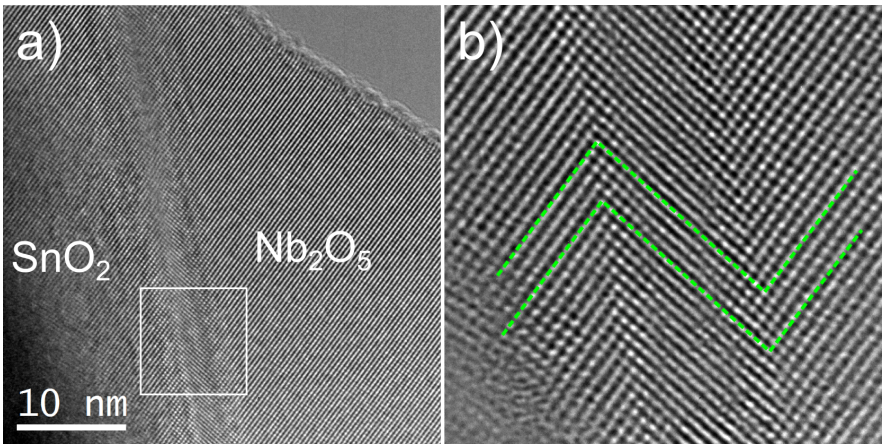

Figure 5.9 a) HRTEM image of a Nb_2O_5 island on a SnO_2 nanowire. A twinned region of the Nb_2O_5 of about 2 nm lays very close and parallel to the interface, for the whole extension of the island. b) Higher magnification image of the region highlighted in (a), evidencing the rotation of the planes at the boundaries of the twinned region.

Twinning occurring perpendicular to the nanowire-island interface is more common, and it corresponds to the dark contrast bands perpendicular to the interface observed in the general BF images (Fig. 5.6). HRTEM images and FFTs of these twinned regions, as the ones shown in figure 5.10, reveal the coexistence of two domains. These two domains are observed along the same zone axis and are rotated in plane with respect to one another. This rotation is visible in the FFT in figure 5.10(b). By masking the FFT for the sets of spots corresponding to each domain and

getting the IFFT in both cases, maps of the two regions in the Nb_2O_5 island can be generated, as shown in panels (c) and (d).

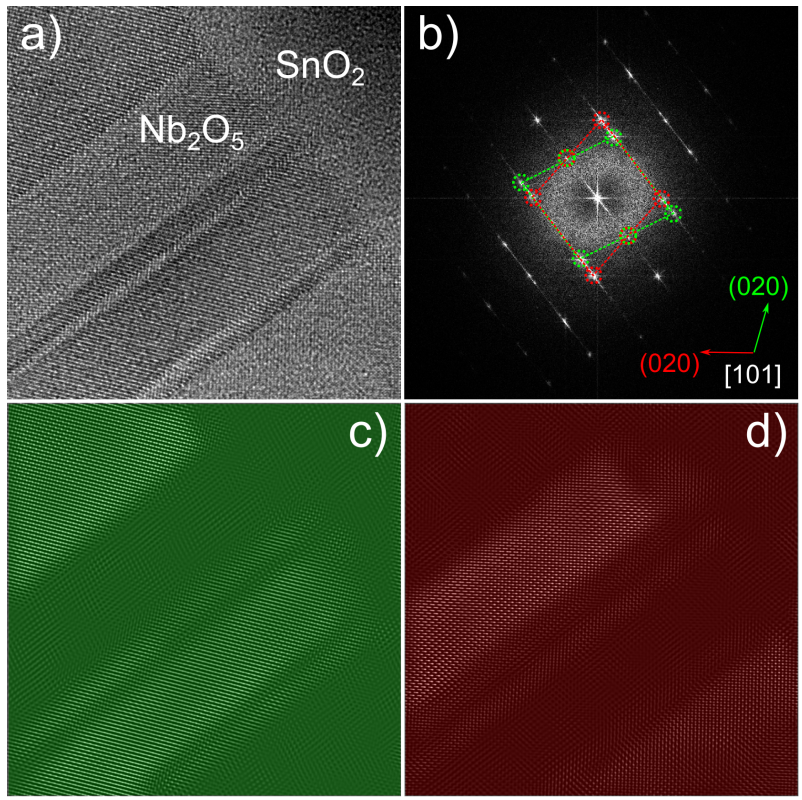

Figure 5.10 a) HRTEM image of a twinned region of a Nb_2O_5 island on top of SnO_2, with the twin planes oriented perpendicular to the interface. b) FFT of the HRTEM image in (a), with highlighted spots corresponding to the two domains related by the twin defects. c,d) IFFT images obtained using the reflections belonging to each domain.

A number of detached Nb_2O_5 crystals were also found, as shown in figure 5.11. These crystals present a nanorod morphology and HRTEM contrast modulation fringes along the growth direction. They are ascribed to the C2/m phase of Nb_2O_5 that was also found for the Nb_2O_5 nanorods (section 5.3). Considering our findings concerning the presence of interface defects, the out-of-plane propagation of strain inside the Nb_2O_5 and the out-of-plane alignment of the twinned regions, the presence of C2/m nanorods is likely to be the final stage of a strain relaxation process. At early

growth stages, the structure is governed by the underlying SnO_2 nanowire. Beyond a critical nanowire length, the accumulated strain results in the structural transition to C2/m Nb_2O_5.

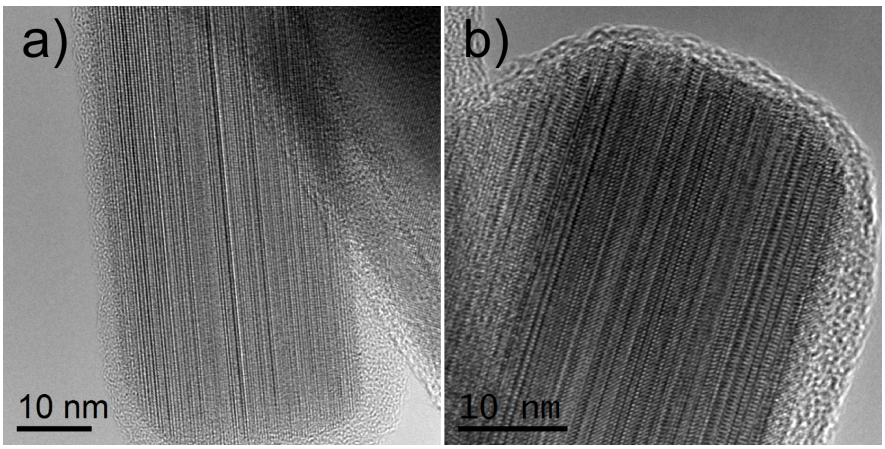

Figure 5.11 a,b) HRTEM images of detached Nb_2O_5 crystals. Contrast modulation fringes are observed along the growth direction of the crystals, as for the C2/m nanorods in section 5.3.

5.4.1 Discussion

Defects in Nb_2O_5 are ascribed to oxygen deficient sites; in particular, twins are often attributed to a whole row of missing oxygen atoms [25, 26], which results in the non-stoichiometry of Nb_2O_5 with excess of Nb cations and defines the n character of the semiconductor. Those oxygen-vacancy-related defects such as deformation twins are known to considerably increase the electron transport properties in resistive-type gas sensors [27]. Moreover, the small electronic contribution of electrons tunneled throughout the Nb_2O_5 could be efficiently transported to the conduction band of SnO_2 according to the theoretical band gap alignment between Nb_2O_5 and SnO_2 at the heterostructure interface shown in figure 5.12. When the two semiconductors are brought into physical contact through epitaxial growth of the Nb_2O_5 shell onto the SnO_2 core, their Fermi level is aligned according to the well-accepted electron affinity model [28]. As a consequence, electrons could transfer from the conduction band of Nb_2O_5 to SnO_2. The con-

centrations of the charge carriers are directly related to the defect structure of the metal oxide. Therefore, the defects and strain between the two materials at the heterojunction are to facilitate the carrier transport from the shell to the core.

This would explain the reduced recovery time for the heterostructures when compared to Nb_2O_5 nanorods.

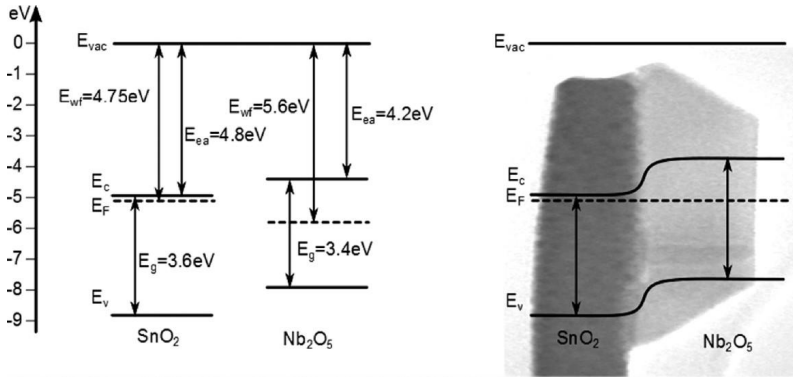

Figure 5.12 Theoretical band energy diagram (based on bulk values) of SnO_2/Nb_2O_5 39,36,40-43 and band gap alignment of SnO_2/Nb_2O_5 heterostructures.

5.5 Conclusions

- Three different systems have been studied in order to relate their structure with their humidity sensing response: Nb_2O_5 nanorods and Nb_2O_5@SnO_2 heterostructures with two different coverage densities.

- CVD grown Nb_2O_5 nanorods were characterized by HRTEM. Contrast modulation and streaking patterns in the FFTs suggested a high density of planar defects such as twins or stacking faults.

- HRTEM simulation was used as a tool to discriminate between possible crystal structures of Nb_2O_5, equally compatible with the data obtained from the accessible crystal orientations. The nanorods were ascribed to the N modification of Nb_2O_5 (space group 12, C2/m). This resulted in a much lower density of defects than expected from a

first examination of HRTEM contrast. Twin defects were characterized using the image simulation results.

- Nb_2O_5@SnO_2 heterostructures were studied by HRTEM in order to characterize the heterojunction between the two materials. Nb_2O_5 grown epitaxially on top of SnO_2 was indexed according to the monoclinic space group C2, in contrast with the studied nanorods.

- Nb_2O_5 was found to grow in the shape of truncated pyramidal islands on top of SnO_2 nanowires. GPA strain mapping revealed strain relaxation in the Nb_2O_5 islands via the formation of dislocations at the interface between the two materials. This dislocations were mapped by Fourier filtering of the HRTEM images, as well.

- GPA also showed strain propagation inside the Nb_2O_5 islands in bands perpendicular to the interface. This means that strain is not fully relaxed through the formation of dislocations at the interface. HRTEM images of many islands showed the presence of twin defects with the twin plane laying perpendicular to the interface. The corresponding vertically oriented twin domains were mapped by Fourier filtering of the HRTEM images. A minority of islands showed twin defects with the twinning plane laying parallel to the interface.

- A number of detached Nb_2O_5 crystals were found. All the free standing crystals were ascribed to the monoclinic C2/m space group, as the bare nanorods.

- The obtained defect characterization allowed explaining the enhancement of the sensor functionality achieved by the engineered core-shell heterostructure under the considered sensing and charge transport mechanisms.

Bibliography

[1] S. Park, M. Vosguerichian, and Z. Bao. A review of fabrication and applications of carbon nanotube film-based flexible electronics. *Nanoscale*, 5:1727–1752, 2013.

[2] L. Huang and J.G. Lu. Synthesis, characterizations and applications of cadmium chalcogenide nanowires: a review. *Journal of Materials Science and Technology*, 31(6):556–572, 2015.

[3] J. Briscoe and S. Dunn. Piezoelectric nanogenerators - a review of nanostructured piezoelectric energy harvesters. *Nano Energy*, 14:15–29, 2015.

[4] Q. Liu, R. Zou, Y. Bando, D. Golberg, and J. Hu. Nanowires sheathed inside nanotubes: manipulation, properties and applications. *Progress in Materials Science*, 70:1–49, 2015.

[5] L. Dong, D. Juan, and P.A.G. Xuan. Inas nanowire devices with strong gate tunability: fundamental electron transport properties and application prospects: a review. *Journal of Materials Science and Technology*, 31(6):542–555, 2015.

[6] C. Li, H. Yamahara, Y. Lee, H. Tabata, and J.J. Delaunay. CuO nanowire/microflower/nanowire modified cu electrode with enhanced electrochemical performance for non-enzymatic glucose sensing. *Nanotechnology*, 26(30):305503, 2015.

[7] M. Huang, Y. Wu, and W. Hu. A facile synthesis of reduced graphene oxide-wrapped wo_3 nanowire composite and its enhanced electrochemical catalysis properties. *Ceramics International*, 40(5):7219–7225, 2014.

[8] J. Xu, J. Cai, J. Wang, L. Zhang, Y. Fan, N. Zhang, H. Zhou, D. Chen, Y. Zhong, H. Fan, H. Shao, J. Zhang, and C. Cao. Facile synthesis of hierarchically porous co_3o_4 nanowire arrays with enhanced electrochemical catalysis. *Electrochemistry Communications*, 25:119–123, 2012.

[9] C. Wang, L. Yin, L. Zhang, D. Xiang, and R. Gao. Metal oxide gas sensors: sensitivity and influencing factors. *Sensors*, (10):2088–106, 2010.

[10] J. Huang and Q. Wan. Gas sensors based on semiconducting metal oxide one-dimensional nanostructures. *Sensors*, (10):9903–9924, 2009.

[11] S. M. Kanan, O. M. El-Kadri, I. A Abu-Yousef, and M. C. Kanan. Semiconducting metal oxide based sensors for selective gas pollutant detection. *Sensors*, (9):8158–96, 2009.

[12] E. Traversa, G. Gnappi, A. Montenero, and G. Gusmano. Ceramic thin films by sol-gel processing as novel materials for integrated humidity sensors. *Sens. Actuators, B*, (23):135–156, 1995.

[13] N. Yamazoe and Y. Shimizu. Humidity sensors: principles and applications. *Sens. Actuators*, (10):379–398, 1986.

[14] A. Vomiero, A. Ponzoni, E. Comini, M. Ferroni, G. Faglia, and G. Sberveglieri. Direct integration of metal oxide nanowires into an effective gas sensing device. *Nanotechnology*, (21):145502, 2010.

[15] J. D. Prades, R. Jiménez-Díaz, M. Manzanares, F. Hernández-Ramírez, A. Cirera, A. Romano-Rodríguez, S. Mathur, and J. R. Morante. Toward a systematic understanding of photodetectors based on individual metal oxide nanowires. *Phys. Chem. Chem. Phys.*, (11):10881–9, 2009.

[16] S. Barth, F. Hernández-Ramírez, J. D. Holmes, and A. Romano-Rodríguez. Synthesis and applications of one-dimensional semiconductors. *Phys. Chem. Chem. Phys.*, (55):563–627, 2010.

[17] F. Hernández-Ramírez, J. D. Prades, A. Hackner, T. Fischer, G. Mueller, S. Mathur, and J. R. Morante. Miniaturized ionization gas sensors from single metal oxide nanowires. *Nanoscale*, (3):630–4, 2011.

[18] M. Batzill and U. Diebold. The surface and materials science of tin oxide. *Prog. Sur., Sci.*, (79):47–154, 2005.

[19] F. Hernández-Ramírez, A. Tarancón, O. Casals, E. Pellicer, J. Rodríguez, A. Romano-Rodríguez, J. Morante, S. Barth, and S. Mathur. Electrical properties of individual tin oxide nanowires contacted to platinum electrodes. *Phys. Rev. B*, (76):1–5, 2007.

[20] A. Kohli, C.C. Wang, and S.A. Akbar. Niobium pentoxide as a lean-range oxygen sensor. *Sens. Actuators, B*, (56):121–128, 1999.

[21] A. L. Chambon, A. Maleysson, A. Pauly, A. Germain, B. Demarne, and A. Grisel. Investigation, for NH_3 gas sensing applications, of the Nb_2O_5 semiconducting oxide in the presence of interferent species such as oxygen and humidity. *Sens. Actuators, B*, (45):107–114, 1997.

[22] N. Kurioka, D. Watanabe, T. S. Haneda Masaaki, T. Mizushima, N. Kakuta, and T. Hanaoka. Preparation of niobium oxide films as a humidity sensor. *Catal. Today*, (16):495–501, 1993.

[23] Z. Chen and C. Lu. Humidity sensors: a review of materials and mechanisms. *Sens. Lett.*, (3):274–295, 2005.

[24] R. Fiz, F. Hernández-Ramírez, T. Fischer, L. López-Conesa, S. Estradé, F. Peiró, and S. Mathur. Synthesis, characterization, and humidity detection properties of Nb_2O_5 nanorods and SnO_2/Nb_2O_5 heterostructures. *J. Phys. Chem. C*, (117):10086–10094, 2013.

[25] T. Kikuchi and M. Goto. Oxygen vacancies in $Nb_{22}0_{(54-x)}$, $Nb_{25}0_{(62-x)}$, and $Nb_{28}0_{(70-x)}$. *J. Solid State Chem.*, (16):363–371, 1976.

[26] W.K Chen. Diffusion of oxygen in near-stoichiometric α-Nb_2O_5. *J. Chem. Phys.*, (47):47, 1967.

[27] D. Rosenfeld, P. E. Schmid, V. Demarne, and A. Grisel. Electrical transport properties of thin-film metal-oxide-metal Nb_2O_5 oxygen sensors. *Sens. Actuators, B*, (37):83–89, 2000.

[28] N. Yamazoe and K. Shimanoe. Theory of power laws for semiconductor gas sensors. *Sens. Actuators, B*, (128):566–573, 2008.

Chapter 6

0D materials: strain and magnetic fields in nanoparticle assemblies

This chapter will be focused on the characterization of strain and magnetic fields in objects having all their dimensions confined in the nanoscale (*i.e.*, under 100 nm). Nanoparticles are one of the most studied systems in the history of nanoscience, and they are at the very core of the development of this field, even before the term emerged: the first systematic study of the interaction of metallic particles with light was carried out by Michael Faraday in the 1850s, using a colloidal suspension of what we now call Au nanoparticles.

The change in the optical and electronic properties of nanoparticles compared to their bulk counterparts is due to the quantum confinement effect. The confinement of electrons in real space causes their delocalization in momentum space, according to Heisenberg uncertainty principle, thus modifying their band structure. This size dependence allows tuning their functional properties by adjusting their size or shape, with no need to alter their composition. This has been widely exploited in the field of semiconducting materials, with nanoparticles (in this case, quantum dots) usually found embedded in larger structures with a higher dimensionality.

Their size scale also makes nanoparticles good candidates for biomedical applications. They can be introduced in the organism and targeted to specific locations by proper functionalization. They can be used as drug delivery systems, contrast enhancement agents for imaging tehcniques, or as a treatment, such as in magnetic hyperthermia for cancer therapy.

The first section of the chapter is devoted to the examination of dimer structures combining a Fe_3O_4 nanoparticle and a metallic Ag nanoparticle. In this system, a detailed characterization of the contact surface (defects, strain, possible chemical interdiffusions) is crucial for its application in magnetoplasmonics. This task will be addressed through aberration corrected HRTEM experiments, simulations and GPA analysis.

The second section of the chapter is focused on the determination of the magnetic state of Fe_3O_4 nanoparticles designed for medical applications. In particular, electron holography will be used to assess the magnetic configurations of the nanoparticle ensembles in order to optimize their magnetic response for hyperthermia cancer treatment.

6.1 $Ag@Fe_3O_4$ dimers

6.1.1 Magnetoplasmonic coupling

The effect that an external magnetic field has on the electron plasma of a metal has found important technological applications, mainly in information storage devices using magneto-optical (MO) recording [1, 2]. In the search for improving the performance of magneto-optical activity, the use of systems with combined magnetic and plasmonic functionality has attracted much interest to the field of mangnetoplasmonics.

Surface plasmons formed at the interface between two media with opposite sign permittivities are strongly localized excitations that are able to confine electromagnetic fields in small nanoregions [3–8]. This local field enhancement increases the MO response for any given material [9]. At the same time, an external magnetic field can be used to control the plasmonic properties.

The possibility to create active optical devices by applying a magnetic field as an external source can be used in the development of integrated nanophotonic chips [10]. Magnetic field offers not only a fast response, in the range of the femtoseconds [11], but the possibility to use both its magnitude and orientation as an input.

The local field enhancement achieved by the surface plasmon results in an increased interaction with molecules present at the surface. In addition to this, the high sensitivity of the surface plasmon to changes in the optical parameters of the media, such as refraction index, make these systems very powerful in the field of sensing [12].

The increasing capabilities of nanofabrication techniques allow for the fine tuning of the magnetoplasmonic properties of structures by precisely controling their size and shape. When choosing which material to use for these kinds of applications, two phenomena need to be taken into account: magneto-optical response and optical losses.

Regarding magneto-optical activity, ferromagnetic materials present the highest values when compared to paramagnetic and diamagnetic materials. However, they show large optical lossses and very broad plasmon ressonances. On the other hand, noble

metals present very low optical losses and very well defined plasmon ressonances. Yet, their diamagnetic nature leads to low values for their magneto-optical activity. The combination of noble metals and ferromagnetic materials seems, thus, a suitable strategy to obtain an optimal magnetoplasmonic behaviour [13–16].

In the case under study, Ag/Fe_3O_4 dimers were synthesized at University of Stockholm by Dr. Marta Estrader and Dr. Germán Salazar-Álvarez. First, in order to obtain Fe_3O_4 nanoparticles, a solution of iron oleate (FeOL) (1 mmol), sodium oleate (NaOL) (43.5 mg, 0.143 mmol) and oleic acid (OA) (50.5 μL, 0.143 mmol) with 10 mL of 1-octadecene (ODE) was stirred at 70^{o}C during 1 hour until complete dissolution of reactants. A thermal ramp was applied from 100^{o}C, at a 2,5^{o}C/min speed, up to the ODE boiling point of 320^{o}C under N_2 atmosphere and reflux conditions, and kept at that temperature for 30 min. To form the dimers, a solution of Fe_3O_4 nanoparticles (0.33 mmol), silver acetate (AgAc) (26.8 mg, 0.16 mmol), oleylamine (OAM) (2.2 mL, 6.7 mmol) and 13 mL of toluene was stirred at 60^{o}C under N_2 atmosphere during 6 hours. Reaction was quenched adding 15 mL of ethanol to the reaction flask. Precipitation of the dimers was forced using a strong magnet. The precipitate was dispersed in toluene and kept in a shaker device for 12 h.

Samples for TEM observation were prepared by dispersion of a droplet of the solution on a carbon coated copper grid. HRTEM observations were carried out in a FEI TITAN^3 equipped with a FEG gun and an aberration corrector in the objective system, located at LMA-INA in Zaragoza.

6.1.2 Dimer morphology and faceting

General TEM images shown in figure 6.1 reveal a dimer structure formed by a cubic Fe_3O_4 particle of $\sim$10 nm and a $\sim$5 nm Ag particle. Fe_3O_4 cube faces correspond to {100}-type planes. Cubes are faceted at the corners, resulting in a cuboctahedral geometry. Ag particles present an irregular faceting.

All Ag particles are attached to the corresponding Fe_3O_4 cube on one of its faces, terminated by {100}-type planes, following the epitaxial relationship [020]Ag(002) // [040]Fe_3O_4(004), as can be

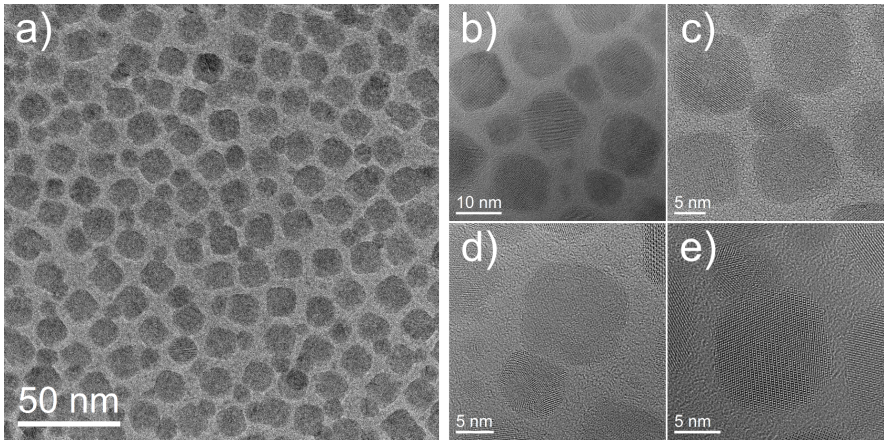

Figure 6.1 a) General image showing the densely distributed dimers. Only two nanoparticles are found for each nanostructure. b-e) HRTEM images from different dimers. Ag particles present an irregular faceting.

seen in figure 6.2. The complex faceting of the Ag particle of the dimer means that only the first ∼10 atomic planes of the particle remain in zone axis coherently with the Fe_3O_4 cube. However, atomic planes are visible all over the pyramidal shape of the Ag particle confirming its crystallinity. An atomic model following the described epitaxial relationship and crystal surfaces was created and used to generate a simulated HRTEM image. The model and the resulting simulated image are shown in figure 6.3 superimposed to the experimental image. The simulated HRTEM image matches the experimental contrast for both components of the dimer and also at the contact interface. Notice the lack of delocalization effects at the surfaces due to the use of an aberration corrected instrument.

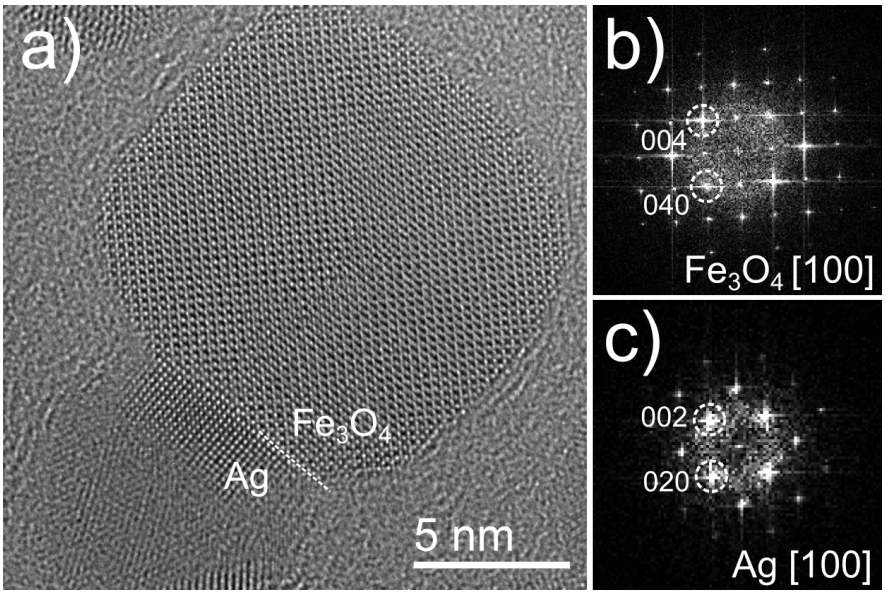

Figure 6.2 a) HRTEM image of a dimer observed along the [100] zone axis for both the Fe_3O_4 nanoparticle and the first section of the Ag nanoparticle. b) FFT from the Fe_3O_4 nanoparticle and c) FFT from Ag showing the epitaxial relationship between the two materials.

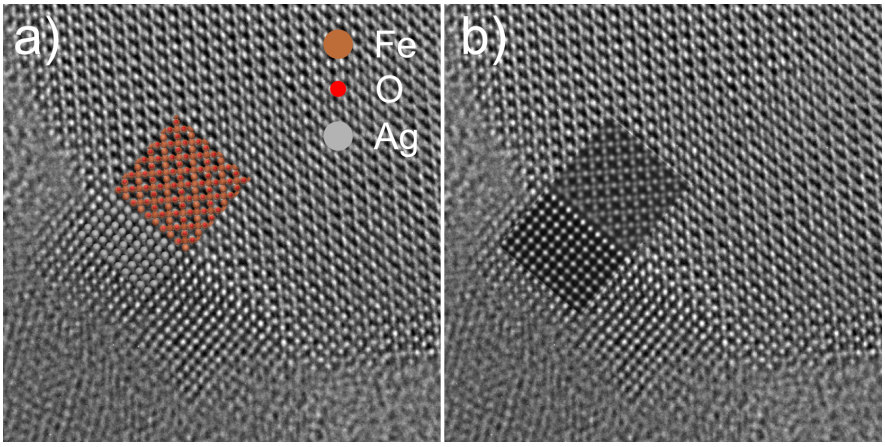

Figure 6.3 a) Structural model created according to the observed epitaxial relationship, superimposed to the experimental HRTEM image. b) Corresponding simulated HRTEM image, showing a good agreement with the experimental HRTEM contrast.

6.1.3 Epitaxial strain

Having established the epitaxial relationship between the two components of the dimer, the strain state across the interface was studied by GPA. By selecting the common reflections, phase shifts and amplitudes could be mapped. Amplitude of the selected reflection maps the spatial distribution of that particular reflection on the image. The amplitude images corresponding to the coincident 002 and 020 reflections of Ag and 004 an 040 reflections of Fe_3O_4 are shown in figure 6.4, together with the power spectrum. Amplitude maps show the continuity of the lattice planes corresponding to the aforementioned reflections through the interface, constituting the epitaxial relationship between the two materials.

By processing the phase shift map as described in Chapter 2, the strain tensor can be retrieved. The studied interface area is highlighted in figure 6.5(a), and the obtained maps for the in-plane (ϵ_{xx}) and out-of-plane (ϵ_{yy}) components of the strain tensor are shown in panels (c) and (d). Setting the Fe_3O_4 cube as the reference area, the Ag particle is found to be fully strained in the in-plane direction and relaxed in the out-of-plane direction. The intensity profile of ϵ_{yy} across the interface shows a strain peak in the first two atomic planes and a subsequent strain relaxation. This peak matches an observed increase in HRTEM intensity, attributed to the change in interplanar distance. Profiles for the strain maps and HRTEM intensity are overlapped in panel (b) for clarity.

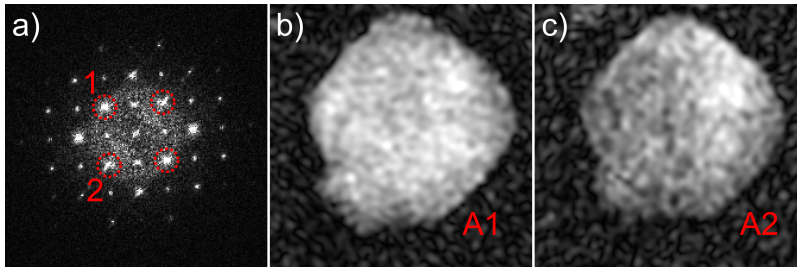

Figure 6.4 a) Power spectrum from the whole dimer. Highlighted in red, common reflections for both materials. b-c) Amplitude maps for the labeled reflections in the power spectrum, showing the continuity of the corresponding atomic planes across the interface.

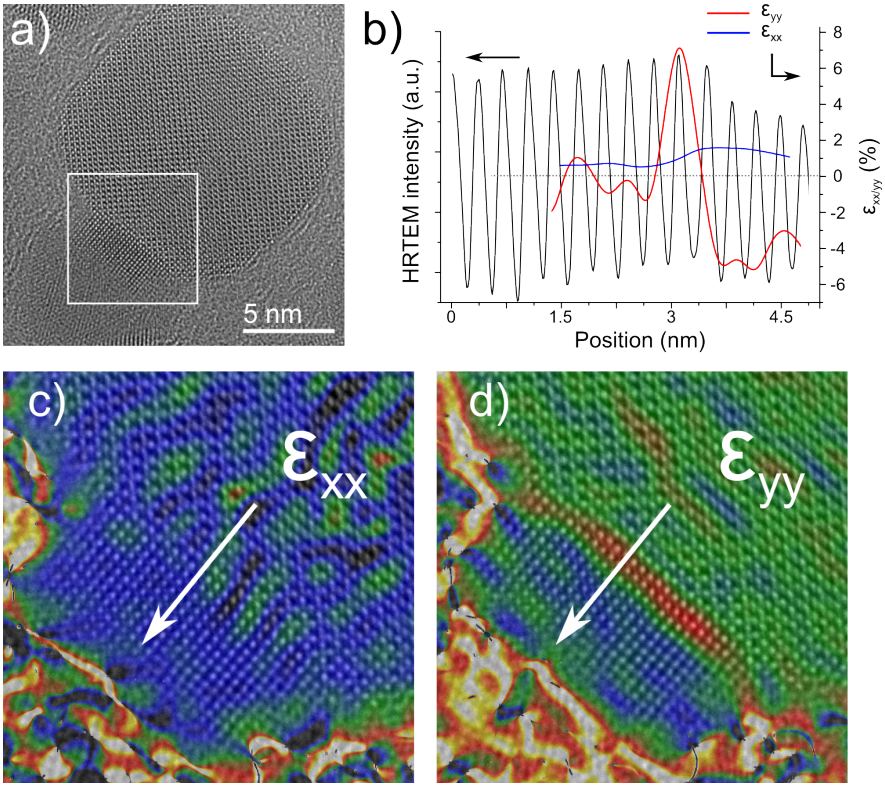

Figure 6.5 a) HRTEM image of a dimer. The highlighted are is studied by GPA. b) Overlapped profiles from HRTEM intensity, in-plane (ϵ_{xx}) and out-of-plane (ϵ_{yy}) components of the strain tensor. Ag grows fully adapted to Fe_3O_4 in the in-plane direction. c) ϵ_{xx} map in colour scale superimposed onto the HRTEM image. c) ϵ_{yy} map in colour scale superimposed onto the HRTEM image.

6.1.4 Antiphase boundaries in Fe_3O_4

Performing an analogous GPA analysis, using only the characteristic reflections of Fe_3O_4 revealed interesting features, as shown in figure 6.6. By mapping the amplitude of the reflections highlighted in the power spectrum, it was found that the corresponding lattice planes are located in the Fe_3O_4 particle only. In addition, a dark band crossing the particle is clearly seen, revealing that the lattice planes are missing in those regions. Phase shift maps show a phase inversion where the dark bands appear in the amplitude maps. This is a characteristic feature of an antiphase boundary (APB),

a type of planar defect often reported in Fe_3O_4. The calculated strain tensor component across the phase inversion line shows a sharp contrast line.

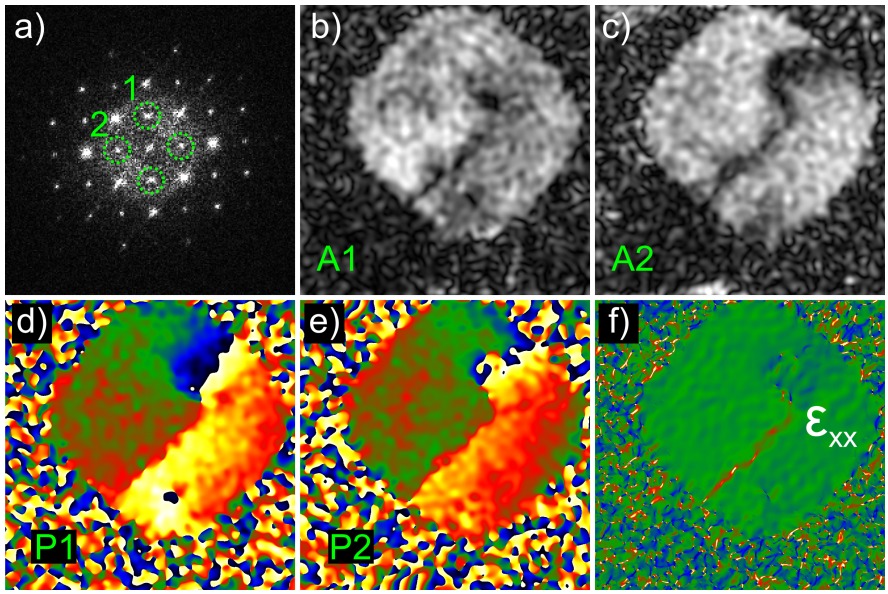

Figure 6.6 a) Power spectrum from the whole dimer. Highlighted in green, reflections corresponding to Fe_3O_4. b-c) Amplitude maps for the reflections labeled in the power spectrum. A discontinuity is seen as a band perpendicular to the interface. d-e) Phase shift maps for the reflections labeled in the power spectrum, showing a phase reversal across the line already observed in the amplitude maps. f) Resulting ϵ_{xx} map showing a sharp line with positive strain values.

An atomic model for the antiphase boundary is given in figure 6.7. The boundary can be described as a 2.05 Å displacement of the crystal lattice in either the [010] or [001] directions resulting in a missing plane at the interface. The two domains are shifted in such a way that the structural channels formed by the chains of Fe and Fe/O atoms do not match. This is evidenced by the superposition of the structural model, in panel (b), and the corresponding simulated HRTEM image, in panel (c), onto the experimental HRTEM image. The displacement introduced by the APB allows the simultaneous matching of the HRTEM contrast of Fe and Fe/O chains at both sides of the boundary. The positive strain across the APB observed in the ϵ_{xx} map is explained by the missing plane at the interface.

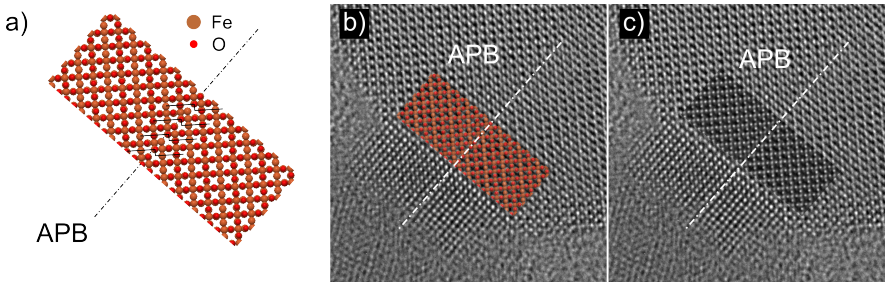

Figure 6.7 a) APB atomic model. b) APB model and c) simulated HRTEM image superimposed onto the HRTEM experimental image. Contrast corresponding to Fe and Fe/O columns is matched at both sides of the APB because of the introduced lattice shift.

6.1.5 Conclusions

- Dimers composed by 5 nm Ag nanoparticles attached to 10 nm Fe_3O_4 nanoparticles, with applications in magnetoplasmonics were studied by aberration corrected HRTEM.
- Dimer structure formation with only a single Ag particle attached to each cube was confirmed. Fe_3O_4 cubes present faceted corners. Ag particles present an irregular faceting.
- Epitaxial relationship between Ag and Fe_3O_4 was found to be [020]Ag(002) // [040]Fe_3O_4(004). The associated epitaxial strain due to lattice mismatch was characterized using GPA. Ag was found to be fully adapted to Fe_3O_4 in the in-plane direction and relaxed in the out-of-plane direction.
- Strain in the first two Ag atomic planes near the interface as determined by GPA was consistent with the observed increased intensity in the experimental HRTEM images, also confirmed by HRTEM image simulation.
- Discontinuity in the amplitude maps and reversal in the phase shifts maps obtained from GPA using only the Fe_3O_4 reflections revealed the presence of antiphase boundaries (APBs) in the cubes.
- A structural model for the APB was proposed and used to simulate HRTEM images. The resulting simulation matches

the HRTEM contrast at both sides of the APB. The missing plane in the APB is in good agreement with the sharp contrast line with positive ϵ_{xx} values in the strain maps.

6.2 Fe_3O_4 nanocubes for magnetic hyperthermia

Magnetic hyperthermia is a promising new therapy for cancer treatment, offering a complementary approach to radiotherapy and chemotherapy [17–19]. This technique offers the advantage of delivering a highly localized damage via the targeting of tumor cells with magnetic nanoparticles. By exciting these nanoparticles with a radio-frequency signal, local heating of the surrounding area is achieved, with lower full-system toxicity than chemotherapy and without ionizing radiation affecting healthy tissue, as in the case of radiotherapy. In spite of having shown some promising results on palliative care, the high particle concentration required rises concerns about the toxicity and side effects of the treatment [18]. Thus, improving efficiency by optimizing the magnetic response of nanoparticles is crucial in order to obtain therapeutic effects while keeping the number of nanoparticles as low as possible.

For applications such as magnetic hyperthermia, performance of magnetic nanoparticles is governed mainly by size distribution, saturation magnetization (M_S), and magnetic anisoptropy (K)[20, 21]. For a given excitation AC amplitude and frequency, these three are the parameters to tune in order to optimize the inductive specific absorption rate (SAR) of the system. The highest reported SAR values correspond to metallic Fe nanocubes [22]. However, the low chemical stability of metallic nanoparticles under physiological conditions make the magnetically softer magnetite (Fe_3O_4) a much more promising candidate for applications in magnetic hyperthermia [23]. Selecting Fe_3O_4 as the material of choice fixes a value for M_S. The particular application limits the range of particle sizes between the superparamagnetic limit ($\geq$ 15 nm) and the optimal size for internalization into mammalian cells ($\leq$ 50 nm) [24, 25]. Thus, the remaining free parameter in order to optimize the response of the nanoparticles is magnetic anisotropy (K) [26].

6.2.1 Optimizing the magnetic response of Fe_3O_4 nanoparticles

A way to increase magnetic anisotropy is by properly choosing the shape of the particles. Taking into account that a sphere is the geometric figure enclosing a volume with the minimum surface, cubic nanoparticles are already an improvement when compared to spherical ones due to their higher surface magnetic anisotropy. Another contribution to a larger surface anistropy is the presence of well-defined atomic planes at the surfaces [27]: this is also in favour of the cubic shape, considering the more irregular crystal facets of a spherical nanoparticle.

A consequence of the cubic shape is an increased tendency of the magnetic nanoparticles to arrange in chains by sharing cube faces. The formation of ensembles of nanoparticles is also a way of engineering magnetic response via the modification of the strength of the dipolar interaction between nanoparticles. Theoretical calculations for the hysteresis loops considering chains of Fe_3O_4 for different numbers of dipole-aligned nanocubes are shown in figure 6.8[28]. The simulations show an increasing area of the loop when increasing the number of aligned particles, and therefore an increase in SAR. Furthermore, the thermal stability gained by creating arrays, also shown by simulations of magnetic response versus temperature, displayed in the inset of figure 6.8[28], is an advantage when exploiting hysteresis losses. These results indicate a promising way to increase the hyperthermia performance by assembling cubic particles in elongated chains.

6.2.2 Synthesis and preliminary TEM characterization

Iron oxide nanocubes were synthesized by Dr. C. Martínez-Boubeta at the Electronics Department of Universitat de Barcelona. Nanocubes were prepared by heating a solution of iron (III) acetylacetonate ($Fe(acac)_3$), decanoic acid and dibenzylether. Size could be tuned over a wide range (15 nmto 180 nm) by choosing the suitable heating rate. Namely, for the preparation of 40 nm nanocubes (edge dimension), 0.353 g (1 mmol) of $Fe(acac)_3$ was mixed with 0.688 g (4 mmol) of decanoic acid in 25 mL of dibenzyl ether. After a short vacuum step at 60^{o}C (30 minutes),

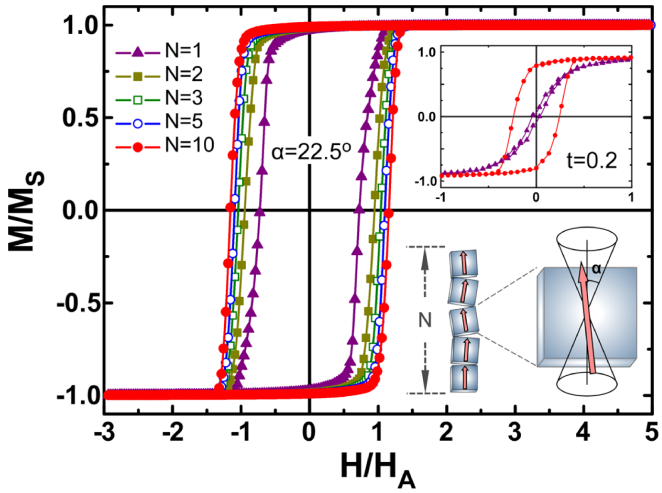

Figure 6.8 Computed hysteresis loops for arrays of nanoparticles of different lengths (values of N indicated), and the limit case of a single particle, where $H_A = 2K/M_S$ is the anisotropy field of the particles. The temperature was introduced in terms of the anisotropy energy barrier of the particles, $t = k_B T/2KV = 0.001$. The inset shows the magnetic response upon increasing the temperature for the N = 1 and N = 10 cases, illustrating the higher thermal stability of the chains. The schematic picture shows particles within a chain possessing easy axes contained within an angle of $\pi/4$.

the solution temperature was first raised up to 200 ^{o}C with a constant rate of 2.6 ^{o}C/min, and kept at this temperature for 2 h under an argon flow and vigorous stirring. In a second step, the solution was heated to reflux temperature with a heating rate of 1.7 ^{o}C/min. After 1 h the solution was cooled down and acetone was added. Nanoparticles were then collected by centrifugation at 8000 rpm and redispersed in chloroform. This procedure was repeated at least two times in order to get rid of the excess of surfactant.

Samples for TEM observation were prepared by dispersing a drop of the nanoparticle solution on a carbon coated copper grid. HRTEM experiments were carried out in a JEOL J2100 located at CCiT-UB.

TEM observations [28] reveal a generalized self-assembly of Fe_3O_4 nanocubes in chain-like structures (see Fig. 6.9(a)). Nano cubes are rather homogeneous in size, with $\sim$ 40 nm lateral dimension of the faces. The difference in contrast within the image

is due to the different diffraction conditions of the nanocubes. In this regard, there is no apparent contrast variation within each nanoparticle, thus suggesting that particles are completely oxidized during synthesis. HRTEM images show monocrystalline Fe_3O_4 nanocubes. HRTEM image in 6.9(b) is taken along the [001] zone axis. The corresponding FFT, shown in the inset is indexed according to the inverse spinel structure of iron oxide.

Electron tomography was used to reconstruct the 3D volume of a Fe_3O_4 nanoparticle chain. Data was collected in a FEI Tecnai F20-G2 at Cambridge University. A tilt series of HAADF images was acquired rotating the sample from -64^o to 64^o in steps of 4^o. Reconstruction was carried out using the simultaneous iterative reconstruction technique (SIRT). Results allow accessing the shape of the chain in 3D and, at the same time, segmentation of the information down to single particle level, as shown in figure 6.10. The cubic shape is confirmed by the 3D reconstruction, as well as cube alignment by sharing {100}-type flat faces. A separation in the order of $\sim$ 2 nm is found between adjacent cubes, corresponding to the organic ligand chains. At this surfactant layer thickness, van der Waals interaction between adjacent cubes is expected to be low [29], so the self-assembly is ascribed to the magnetic dipole-dipole interaction.

Structural and morphological TEM characterization at the nanoscale, as well as macroscopic magnetic measurements [28], are in good agreement with the proposed model and the corresponding simulation shown in figure 6.8. However, this constitutes an indirect evidence of the magnetic coupling of the nanostructures. Direct evidence, namely real space imaging of the magnetic ordering down to single particle level, can be provided by electron holography.

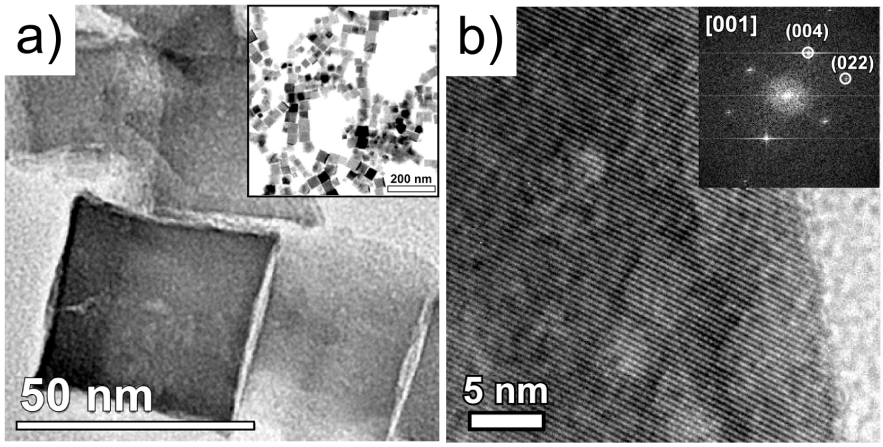

Figure 6.9 a) General TEM image of the Fe_3O_4 nanocubes. Inset shows the formation of chain-like structures. b) HRTEM image confirming the monocrystallinity of the particles. Inset: corresponding FFT.

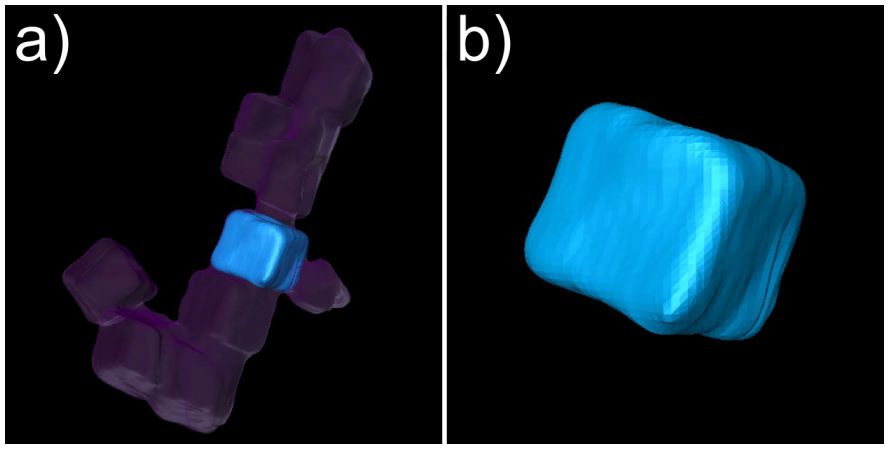

Figure 6.10 3D recostruction of a self-assembled chain obtained from a tilt series after 40 iterations of the SIRT algorithm. Neighboring cubes have {100} surfaces aligned face to face separated by $\sim$ 2 nm due to organic ligands. An individual member of the chain is highlighted in panel (a), and individually presented in panel (b).

6.2.3 Electron holography characterization

Electron holography experiments were carried out in the Hitachi I2TEM microscope at CEMES-CNRS in Toulouse. The I2TEM is a modified Hitachi HF3300C TEM equipped with a 300 kV cold FEG, with an aberration corrector in the objective system and a 4k x 4x CCD camera. It is especially designed for performing advanced electron holography experiments. It is also equipped with a second specimen holder port located above the objective lens, allowing the use of the aberration corrected objective lens without having its strong magnetic field affecting the sample when working in Lorentz mode. This feature allows an unprecedented spatial resolution for electron holography. It is also equipped with up to four electrostatic biprisms for electron beam splitting, granting the system a high flexibility when setting the parameters and reference areas for the holograms.

In order to assess the magnetic state of the Fe_3O_4 ensembles, up and down electron holography experiments were carried out using two electrostatic biprisms. As briefly explained in Chapter 2, up and down experiments consist in acquiring two sets of holograms (sample and vacuum reference) corresponding to the two possible orientations of the TEM specimen. This requires taking the sample out of the microscope and flipping it between the two acquisitions. Figure 6.11 panels (a) and (c) show the two flip-related holograms for an ensemble of nanocubes. The use of two electrostatic biprisms allows decoupling two important parameters: the width of the superposition region and the interference fringes spacing [30]. When working in a single biprism configuration, the applied voltage defines both parameters, so that a balance needs to be found. The use of two biprims allows controlling them separately by defining different voltages for each one of them. An additional advantage of this configuration is the elimination of Fresnel interference fringes in the holograms when the lower biprism is in the region shaded by the upper one. This can be seen in figure 6.11(b), where only the centerband and the sidebands are present. This results in a higher fringe contrast, which is a key parameter limiting the magnetic signal resolution. The obtained small fringe spacing and high contrast in the recorded holograms is illustrated in figure 6.11(d).

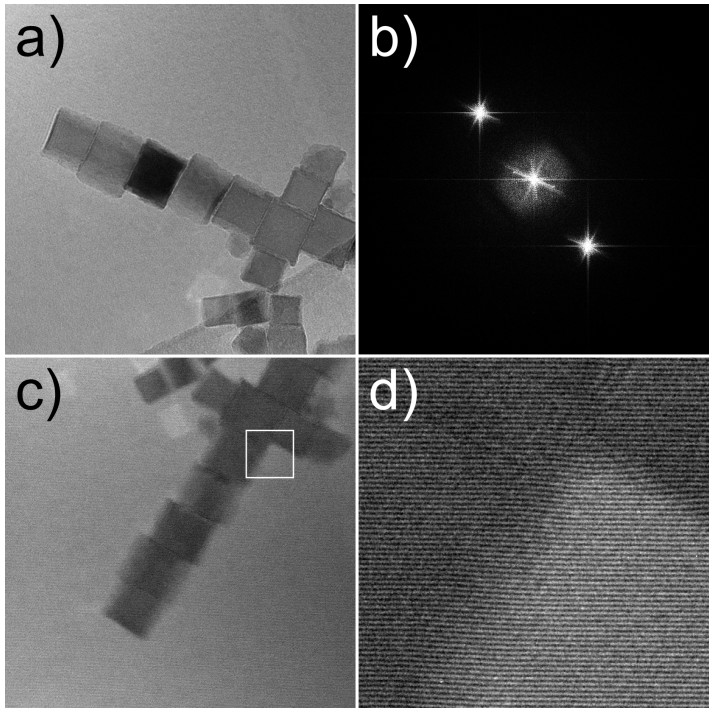

Figure 6.11 a) Hologram covering a nanoparticle ensemble formed by two crossing chains. b) FFT of the hologram showing the center band and sidebands. No spots correspoding to Fresnel fringes are visible due to the use of a two biprism configuration. c) Hologram of the same ensemble obtained after mechanical flipping of the sample. d) Detail of the interference fringes from the region highlighted in (c).

After substracting the constant phase term corresponding to the vacuum reference holograms for both the up and down configurations (not shown here), and correcting the images for the mechanical flip process, a mask is set on one of the sidebands and the corresponding amplitude and phase are calculated. The obtained phase shift maps for the up and down holograms of the ensemble under study are shown in figure 6.12 panels (a) and (c), respectively. Considering the experimental setup, the only actual contributions to the phase shift, of all the stated in equation 2.22 in Chapter 2, are the electrostatic phase and the magnetic phase. Each one of the phase maps will have contributions from both electrostatic (φ_E) and magnetic (φ_M) components

$$\varphi_{up} = \varphi_{E,up} + \varphi_{M,up} \tag{6.1a}$$
$$\varphi_{down} = \varphi_{E,down} + \varphi_{M,down} \tag{6.1b}$$

Given the flipping process between the two acquisitions and the nature of the electrostatic and magnetic fields, the phase shifts resulting from the two holograms will satisfy the following relationships

$$\varphi_{E,up} = \varphi_{E,down} \tag{6.2a}$$
$$\varphi_{M,up} = -\varphi_{M,down} \tag{6.2b}$$

So, after careful alignment of the phase shift maps, simple phase operations allow separating the magnetic phase

$$\varphi_M = \frac{\varphi_{up} - \varphi_{down}}{2} \tag{6.3}$$

from the electrostatic phase corresponding to the mean inner potential (MIP) of the sample

$$\varphi_E = \frac{\varphi_{up} + \varphi_{down}}{2} \tag{6.4}$$

The resulting phase sum and difference maps are shown in figure 6.12 panels (b) and (d), respectively. The dependence of the MIP is on the electric charge distribution and sample thickness so, considering an homogeneous material, an intensity profile across the sample can provide information on the third dimension. The MIP intensity profiles show sharper edges for the cube presenting a stronger diffraction contrast, as could be expected from a cube laying flat on one face and therefore closer to zone axis. The phase difference map corresponding to the magnetic signal shows a phase shift with a frontier laying along the direction of the nanocube chain. This magnetic phase difference, clearly shown in the intensity profile in the inset, is a clear signature of the magnetic behaviour of the nanocubes.

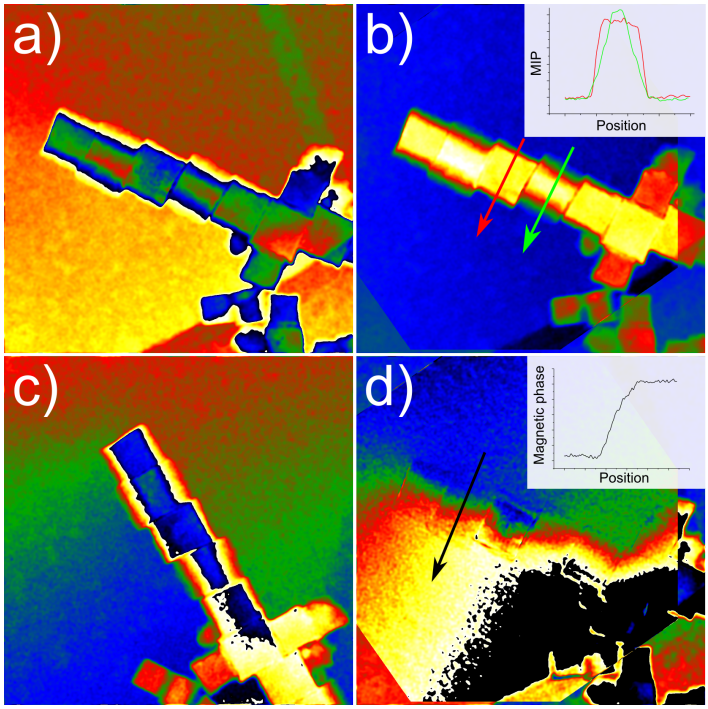

Figure 6.12 a,c) Phase shift maps corresponding to the 'up' and 'down' holograms, respectively. The 'down' image needs to be flipped so that it can be aligned with the 'top' image. b) Phase sum image, corresponding to the mean inner potential (MIP). d) Phase difference image, corresponding to the magnetic phase shift. The phase difference across the object, as shown in the inset, indicates its magnetic behaviour.

An easier way to visualize the magnetic coupling along the chain is by representing the magnetic phase shift as contour maps according to the expression $cos(n\varphi_M)$. The resulting contours constitute a map of the in-plane magnetic flux lines. The map for the ensemble under study is shown in figure 6.13a, superimposed to the amplitude map of the sideband as a geometrical reference. The magnetic signal is somewhat distorted in the nanocube showing a stronger diffraction contrast due to its crystal orientation, as mentioned before for the MIP map. Diffraction contrast decreases the interference fringes contrast, thus making the detection of the magnetic signal more difficult. The ensemble is formed by two crossing chains: a long chain with N = 7 along the horizontal direction and a shorter one with N = 3 along the vertical direction.

Magnetic flux lines follow the alignment of the chains and rotate $\sim 45^o$ in the 'node' nanocube where the two chains cross at 90^o. At the tip of the N = 7 chain, stray field lines are visible, going to closure away from the field of view. A sketch of the ensemble, in panel (b), represents the alignment of the magnetic dipoles of the cubes in the chains, as well as the stray field lines at the tip.

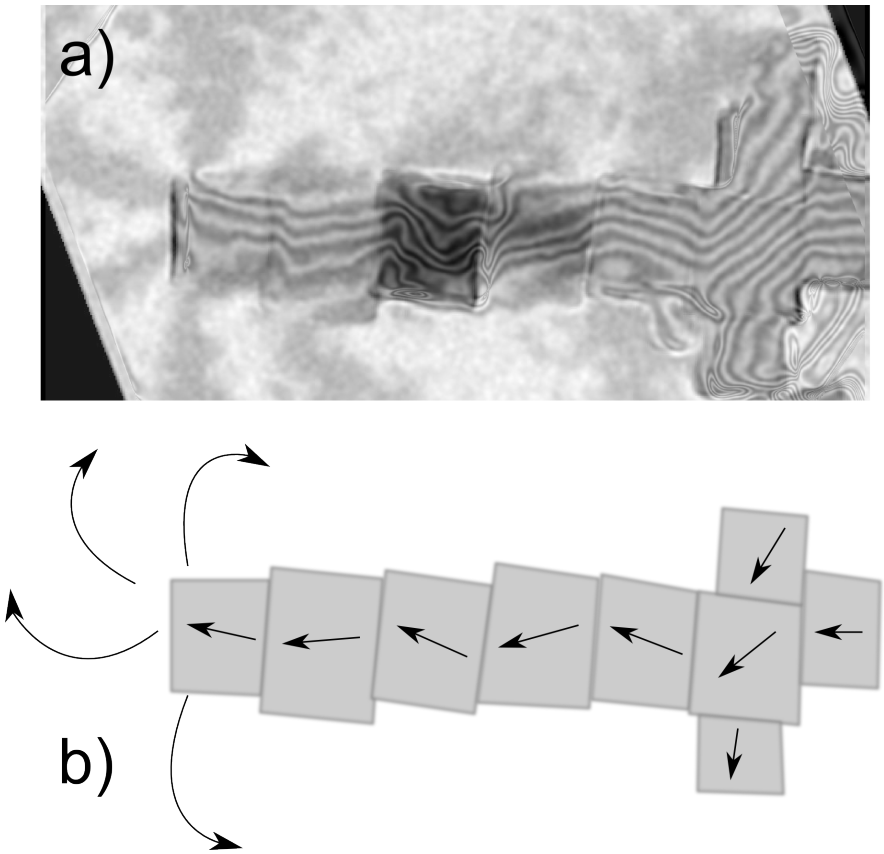

Figure 6.13 a) Magnetic phase signal visualized as a $cos(n\varphi_M)$ contour map superimposed to the amplitude image. Contours correspond to magnetic flux lines showing the magnetic coupling of the cubes, as schematically displayed in panel b). Stray field lines are visible at the tip of the chain.

An analogous processing was carried out for holograms from different chain-like assemblies and the resulting contour maps of the magnetic phase shift are shown in figure 6.14 and figure 6.15. Both of them present the predicted magnetic coupling

governed by dipole-dipole interaction. Individual nanocubes in strong diffraction contrast are also visible in these ensembles, making the characterization of the magnetic signal difficult at some points.

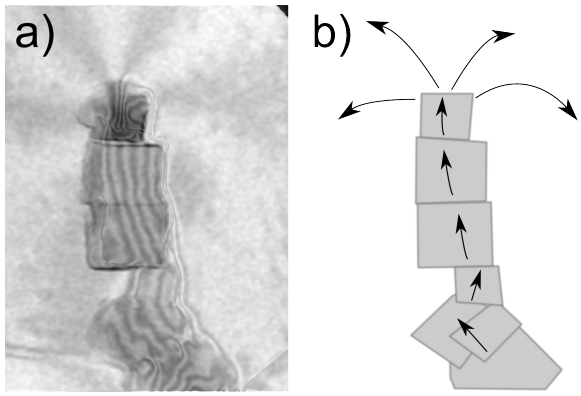

Figure 6.14 a) Magnetic phase contour map of a nanocube assembly showing the magnetic coupling and the stray field lines, as depicted schematically in panel b)

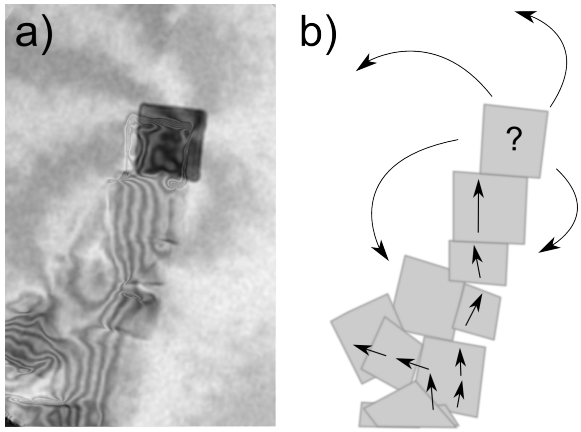

Figure 6.15 a) Magnetic phase contour map of a nanocube assembly showing the magnetic coupling of two chains and the stray field lines at the tip of the vertical one, as schematically depicted in panel b)

6.2.4 Conclusions

- 40 nm Fe_3O_4 nanocubes for applications in magnetic hyperthermia cancer treatment were studied. Macroscopic magnetic findings suggested the alignment of the cubes in chains by dipole-dipole interaction, thus increasing the specific absorption rate (SAR) due to a larger magnetic anisotropy coefficient (K).

- Preliminary HRTEM and electron tomography results showed the formation of nanoparticle chains.

- Electron holography experiments were carried out in order to obtain a magnetic characterization at the high resolution achieved by TEM, down to single particle level.

- Magnetic phase signal allowed confirming the magnetic coupling predicted for the self-assembled chains. Contour maps showed the magnetic flux lines along the nanocube chains and the stray fields in the vacuum.

Bibliography

[1] V.I. Safarov, V.A. Kosobukin, C. Hermann, G. Lampel, J. Peretti, and C. Marlière. Magneto-optical effects enhanced by surface plasmons in metallic multilayer films. *Phys. Rev. Lett.*, 73:3584–3587, 1994.

[2] C. Hermann, V.A. Kosobukin, G. Lampel, J. Peretti, V.I. Safarov, and P. Bertrand. Surface-enhanced magneto-optics in metallic multilayer films. *Phys. Rev. B*, 64:235422, 2001.

[3] S.A. Maier. *Plasmonics: fundamentals and applications*. Springer, New York, USA, 2007.

[4] W.L. Barnes, A. Dereux, and T.W. Ebbesen. Surface plasmon subwavelength optics. *Nature*, 424(6950):824–830, 2003.

[5] I.L. Lyubchanskii, N.N. Dadoenkova, M.I. Lyubchanskii, E.A. Shapovalov, and T. Rasing. Magnetic photonic crystals. *Journal of Physics D: Applied Physics*, 36(18):R277, 2003.

[6] M. Inoue, R. Fujikawa, A. Baryshev, A. Khanikaev, P.B Lim, H. Uchida, O. Aktsipetrov, A. Fedyanin, T. Murzina, and A. Granovsky. Magnetophotonic crystals. *Journal of Physics D: Applied Physics*, 39(8):R151, 2006.

[7] E. Ozbay. Plasmonics: Merging photonics and electronics at nanoscale dimensions. *Science*, 311(5758):189–193, 2006.

[8] D.K. Gramotnev and S.I. Bozhevolnyi. Plasmonics beyond the diffraction limit. *Nat. Photon.*, 4(2):83–91, 2010.

[9] A.I. Stockman. Nanoplasmonics: The physics behind the applications. *Physics Today*, 64(2):39, 2011.

[10] V.V. Temnov, G. Armelles, U. Woggon, D. Guzatov, A. Cebollada, A. Garcia-Martin, J.M. Garcia-Martin, T. Thomay, A. Leitenstorfer, and R. Bratschitsch. Active magneto-plasmonics in hybrid metal-ferromagnet structures. *Nat. Photon.*, 4(2):107–111, 2010.

[11] A.V. Kimel, A. Kirilyuk, P.A. Usachev, R.V. Pisarev, A.M. Balbashov, and T. Rasing. Ultrafast non-thermal control of magnetization by instantaneous photomagnetic pulses. *Nature*, 435(7042):655–657, 2005.

[12] B. Sepúlveda, A. Calle, L.M. Lechuga, and G. Armelles. Highly sensitive detection of biomolecules with the magneto-optic surface-plasmon-resonance sensor. *Opt. Lett.*, 31(8):1085–1087, 2006.

[13] Yanqiu L., Qiang Z., Arto V.N., , and Shouheng S. Enhanced magnetooptical response in dumbbell-like Ag-$CoFe_2O_4$ nanoparticle pairs. *Nano Letters*, 5(9):1689–1692, 2005.

[14] F.E. Moolekamp and K.L. Stokes. Magnetooptical response of gold-magnetite nanocomposite films. *IEEE Trans. Magne.*, 45(10):4888–4891, 2009.

[15] P.K. Jain, Y. Xiao, R. Walsworth, and A.E. Cohen. Surface plasmon resonance enhanced magneto-optics (SuPREMO): Faraday rotation enhancement in gold-coated iron oxide nanocrystals. *Nano Letters*, 9(4):1644–1650, 2009.

[16] R.K. Dani, H. Wang, S.H. Bossmann, G. Wysin, and V.R Chikan. Faraday rotation enhancement of gold coated Fe_2O_3 nanoparticles: Comparison of experiment and theory. *The Journal of Chemical Physics*, 135(22), 2011.

[17] K. Maier-Hauff, F. Ulrich, D. Nestler, H. Niehoff, P. Wust, B. Thiesen, H. Orawa, V. Budach, and A. Jordan. Efficacy and safety of intratumoral thermotherapy using magnetic iron-oxide nanoparticles combined with external beam radiotherapy on patients with recurrent glioblastoma multiforme. *Journal of Neuro-Oncology*, 103(2):317–324, 2011.

[18] C.S.S.R. Kumar and F. Mohammad. Magnetic nanomaterials for hyperthermia-based therapy and controlled drug delivery. *Advanced Drug Delivery Reviews*, 63(9):789 – 808, 2011.

[19] A. Jordan, P. Wust, H. Fähling, W. John, A. Hinz, and R. Felix. Inductive heating of ferrimagnetic particles and magnetic fluids: Physical evaluation of their potential for hyperthermia. *International Journal of Hyperthermia*, 9(1):51–68, 1993.

[20] K. Butter, P.H.H. Bomans, P.M. Frederik, G.J. Vroege, and A.P. Philipse. Direct observation of dipolar chains in iron ferrofluids by cryogenic electron microscopy. *Nature Materials*, 2(2):88–91, 2003.

[21] S.A. Majetich, T. Wen, and R.A. Booth. Functional magnetic nanoparticle assemblies: Formation, collective behavior, and future directions. *ACS Nano*, 5(8):6081–6084, 2011.

[22] B. Mehdaoui, A. Meffre, J. Carrey, S. Lachaize, L.M. Lacroix, M. Gougeon, B. Chaudret, and M. Respaud. Optimal size of nanoparticles for magnetic hyperthermia: A combined theoretical and experimental study. *Advanced Functional Materials*, 21(23):4573–4581, 2011.

[23] N.A. Usov. Low frequency hysteresis loops of superparamagnetic nanoparticles with uniaxial anisotropy. *Journal of Applied Physics*, 107(12), 2010.

[24] J.P. Fortin, F. Gazeau, and C. Wilhelm. Intracellular heating of living cells through Néel relaxation of magnetic nanoparticles. *European Biophysics Journal*, 37(2):223–228, 2008.

[25] S. Zhang, J. Li, G. Lykotrafitis, G. Bao, and S. Suresh. Size-dependent endocytosis of nanoparticles. *Advanced Materials*, 21(4):419–424, 2009.

[26] L.M. Lacroix, R. Bel Malaki, J. Carrey, S. Lachaize, M. Respaud, G. F. Goya, and B. Chaudret. Magnetic hyperthermia in single-domain monodisperse FeCo nanoparticles: Evidences for Stoner–Wohlfarth behavior and large losses. *Journal of Applied Physics*, 105(2), 2009.

[27] R. Skomski, X.H. Wei, and D.J. Sellmyer. Magnetization reversal in cubic nanoparticles with uniaxial surface anisotropy. *IEEE Trans. Magn.*, 43(6):2890–2892, 2007.

[28] C. Martinez-Boubeta, K. Simeonidis, A. Makridis, M. Angelakeris, O. Iglesias, P. Guardia, A. Cabot, L. Yedra, S. Estradé, F. Peiró, Z. Saghi, P.A. Midgley, I. Conde-Leborán, D. Serantes, and D. Baldomir. Learning from nature to improve the heat generation of iron-oxide nanoparticles for magnetic hyperthermia applications. *Scientific Reports*, 3:1652, 2013.

[29] H.G. Liao, L. Cui, S. Whitelam, and H. Zheng. Real-time imaging of Pt_3Fe nanorod growth in solution. *Science*, 336(6084):1011–1014, 2012.

[30] K. Harada, A. Tonomura, Y. Togawa, T. Akashi, and T. Matsuda. Double-biprism electron interferometry. *Applied Physics Letters*, 2004.

Chapter 7

Conclusions

The main goal of this thesis has been to apply TEM quantitative imaging techniques to solve materials science problems in a broad range of applications. The introductory Chapter 1 presents a review of the imaging formation theory. The different types of image contrast that can be obtained are explained and related to the corresponding electron-matter interactions. Chapter 2 presents the quantitative techniques that will be used in the characterization of the materials, namely HRTEM image simulation, electron holography and Geometric Phase Analysis (GPA). A detailed description of the theoretical and experimental basis is presented alongside a summary of the state of the art for each of them.

The results presented in the following chapters are grouped according to the decreasing dimensionality of the systems under study, including bulk (3D) crystals, thin films (2D), nanowires (1D) and nanoparticles (0D). In the following paragraphs we summarize the main findings for the studied materials.

7.1 3D materials

In chapter 3 cationic and anionic ordering in different functional oxides is addressed. The first case corresponds to a series of rare earth niobates (RE_3NbO_7, RE = Y, Er, Yb, Lu) for applications as proton conducting electrolites in solid oxide fuel cells. In order to explain their reduced conductivity values, in spite of the high amount of oxygen vacancies available, the microstructure of both

raw nanopowders and sintered pellets of the different compounds has been investigated through HRTEM and SAED experiments.

- HRTEM images show small domains with superstructure contrast modulation for all the compounds, doubling the expected fluorite unit cell dimensions. Diffuse features in the FFTs are found in the form of split spots and diffuse intensity rings.

- SAED experiments have been carried out systematically in order to characterize the reciprocal space of the crystal. SAED patterns have been acquired in several zone axes for all samples, both from nanopowders and sintered pellets samples. Diffuse scattering features in SAED patterns present split spots and diffuse rings at reciprocal positions doubling the fluorite unit cell.

- The experimental HRTEM and SAED results have been explained in terms of a microstructure model consisting in a fluorite matrix with randomly oriented pyrochlore domains. Pyrochlore is a second order superstructure of fluorite in which oxygen vacancies are ordered in alternating layers.

- The inherent oxygen vacancies of the niobates are short range ordered since long range ordering is avoided by the large cation radii difference. The finite size of the domains accounts for the diffuse nature of the pyrochlore reflections, and their random orientation accounts for the ring symmetry. All the experimental diffraction patterns can be explained by the cuts of the Ewald sphere with the fluorite spots and diffuse pyrochlore rings.

- Ordering of the oxygen vacancies in the domains explains the lower than expected conductivity values measured for these materials, through the shortening of conductive paths.

The second part of Chapter 3 focuses on the uniaxial ferroelectric relaxor $Sr_{0.67}Ba_{0.33}Nb_2O_6$ (SBN-67). The goal of the study is the characterization of structural and chemical disorder in the TTB crystal structure, which is responsible for the relaxor properties

of this material. This has been achieved by a combination of diffraction, imaging and spectroscopic techniques.

- SAED patterns acquired in the [100] zone axis of the TTB structure show interesting diffuse scattering features. First, a streaking of the intensity along the [010] direction, consistent with strain introduced by the presence of cation vacancies in the structure. Second, incommensurate superstructure modulation spots are found.

- The incommensurate nature of this modulation, which is not a multiple of SBN-67 reciprocal lattice vectors, makes the introduction of two additional reciprocal vectors necessary in order to describe the reciprocal lattice of the crystal, resulting in a 5D-superspace.

- Aberration corrected HAADF images taken in [001] zone axis show an elongated shape in the atomic columns corresponding to A2 sites. This is attributed to the projected view of slightly displaced cations in a preferential direction. Atomic displacements due to the random Sr or Ba occupation of these sites can explain the observed incommensurate structural modulation.

- Aberration corrected HAADF images taken in [100] zone axis shows the presence of cation vacancies in A1 sites. A full structural characterization has been completed by the use of ABF in order to observe the anion sublattice of the crystal.

- EELS spectrum imaging has been used in order to assess the chemical disorder in A2 sites. The use of very fast acquisition times has allowed obtaining chemical maps for large areas of the crystal oriented in [001] zone axis. In order to improve the low signal-to-noise ratio of the data, multivariate analysis techniques have been used. In particular, Principal Component Analysis (PCA) decomposition allows obtaining a new data set with reduced noise, from which the random occupation of A2 sites is confirmed.

- A1 site cation vacancies and random accupation of A2 sites lead to the charge disorder responsible for the formation of polar nanoregions and the macroscopic relaxor behaviour of SBN-67.

7.2 2D materials

Chapter 4 accounts for the elucidation of structural defects present in thin film materials used for spintronics and optoelectronics applications.

The first part covers a series of $LaNiO_3$ (LNO) thin films grown on different substrates (LAO, LSAT, STO and YAO). The different lattice parameter mismatch of LNO with respect to the different substrates induces a different stress in the thin film. This strain engineering strategy aims to the tuning of the electron transport properties of LNO. LNO films of 14 nm and 35 nm thicknesses have been studied by HRTEM, HAADF and GPA analysis of the obtained images.

- The strain state of all the films is assessed by GPA analysis of HAADF images. LNO films grown on LAO, LSAT and STO show a full adaptation of the in-plane lattice parameter to the in-plane substrate lattice parameter. Out-of-plane lattice parameters present values very similar to that of bulk LNO.

- For the case of LNO grown on YAO substrate, it has been found that the film is fully relaxed, due to the larger lattice mismatch and the different structure between the orthorhombic substrate and the cubic LNO.

- Planar defects are found in all films beyond the first ~ 3 nm. From HAADF contrast, it has been determined that they are Ruddlesden-Popper (RP) faults, consisting in the displacement of the crystal by half a unit cell along the [111] direction. A Ni-O plane is missing at the interface.

- Different geometries for RP faults in the LNO films have been characterized from the study of HAADF contrast. In

particular, the loss of contrast difference between the A and B sites of the perovskite can be used to detect the overlapping of the displaced domains along the electron beam direction. The sharp or gradual character of the A/B contrast difference loss can be used to determine whether there is a parallel orientation of the defect plane with respect to the electron beam.

- An oxygen defficient $LaNiO_{2.5}$ monoclinic phase has been detected in some regions of the 35 nm LNO films. Superstructure contrast modulation due to the ordering of oxygen vacancies was found, with an orientation depending on the sign of the stress induced by the substrate. By choosing the right cross section specimen preparation direction, the adequate zone axis for the direct imaging of the oxygen-deficient columns can be accessed.

- $LaNiO_{2.5}$ does not constitute the totality of the films. This is in good agreement with the macroscopic conduction measurements. A metallic behaviour is found for all the studied layers. This would not be possible if only $LaNiO_{2.5}$ was present in these samples, as the Ni coordination environment and octahedral connectivity is crucial for the transport properties of $LaNiO_3$.

The second part corresponds to the characterization of a distributed Bragg reflector (DBR) device, consisting in alternating layers of InAlN and GaN. By properly tuning the semiperiod thickness according to the different refractive index of the two III-V compounds, high reflectivity for the targeted wavelengths can be achieved. The goal is to explain the lower than expected reflectivity values observed for the system. The DBR has been characterized by SAED and HRTEM, with an important contribution of HRTEM image simulation in the data interpretation.

- Pure, defect free wurtzite structure has been found for all the AlN layers. On the other hand, a high density of planar defects, as well as Moirée patterns with different periodicities have been observed in GaN semiperiods.

- 6-fold Moirée patterns in GaN can be explained in terms of the superposition of wurtzite and zinc blende phases along the electron beam direction. Information extracted from HRTEM and SAED experiments has been used to create a structural model from which a simulated HRTEM image is produced. The simulated HRTEM contrast successfully matches the experimental HRTEM contrast.

- 3-fold Moirée patterns in GaN found in HRTEM images can be explained in terms of the superposition of two zone axis of the zinc blende phase. A structural model taking into account the possible different orientations for the growth of zinc blende GaN on top of a wurtzite AlN layer is proposed. HRTEM images have also been simulated for this model and the obtained contrast matches the experimental HRTEM contrast.

- The additional surfaces created by the planar defects associated to the differently oriented zinc blende GaN domains as well as the coexistence of wurtzite and zinc blende phases are responsible for the decrease of layer homogeneity, which is crucial in order to achieve higher reflectivity values.

7.3 1D materials

Chapter 5 covers the elucidationof structure, defective configuration and strain fields in 1D nanostructures. The material under study is Nb_2O_5, with the main focus of interest set on its humidity sensing properties. The structure and defects of Nb_2O_5 have been characterized by HRTEM and HRTEM simulation for contrast interpretation. First, isolated 500 nm long and 30-50 nm wide Nb_2O_5 nanorods have been studied.

- HRTEM images of the nanorods show complex contrast modulation bands oriented along the growth direction. This feature has been often reported as resulting from a high density of twins or stacking faults in the monoclinic C2 phase of Nb_2O_5. This structure is compatible with possible indexations of the FFTs. Following this approach, structural

models including such defects have been created and used to obtain simulated HRTEM images. Simulation results do not reproduce the experimentally observed contrast features.

- An alternative structural model is investigated by simulating HRTEM images from structural models of other Nb_2O_5 phases, also compatible with the indexation of the FFTs. The monoclinic phase belonging to space group C2/c is found to reproduce the experimental contrast in wide regions of the nanorods. Twin defects are present but with a low density. Nanorods have been ascribed to this phase and a much lower than expected density of defects has been obtained.

The second part of the chapter covers the characterization of engineered core-shell heterostructures aiming to optimize the functionality of the system. By combining the high sensitivity of a Nb_2O_5 shell and the good electron transport properties of a SnO_2 core, the recovery time and device integrability of the system are improved.

- Nb_2O_5 is found to grow on top of SnO_2 nanowires in the shape of truncated pyramids. The full coverage obtained after the deposition is not in the form of an homogeneous shell, but a rather irregular one.

- Heterostructures in an earlier stage of the growth process have been studied by HRTEM in order to characterize the contact surface between the two materials. Different kinds of defects are found in the interface, such as dislocation networks due to lattice parameter mismatch and twinned domains found oriented either parallel or perpendicular to the interface.

- Strain has been studied by GPA. It is found that strain relaxation through the formation of dislocations is not complete and that strain propagates into Nb_2O_5 in bands perpendicular to the interface. Twinned domains of ~ 2 nm laying parallel to the interface do account for the full relaxation of the epitaxial strain.

- The formation of twinned domains in the Nb_2O_5 islands, together with the observation of detached Nb_2O_5 crystals with the C2/c structure found for the nanorods points towards the existence of a critical length for which strain induces a structural transition.

- In addition to the contribution of the band alignment at the interface, the presence of defects accounts for part of the enhancement of the device functionality.

7.4 0D materials

Chapter 6 focuses on the relevance of the intimate structural configuration of 0-D systems, for the correct coupling of functional properties. The first system under study are dimers formed by a Fe_3O_4 particle and a Ag particle. Combining the properties of a ferromagnetic material with those of a noble metal allows enhancing and controlling the optical properties of the system via the magnetoplasmonic coupling. In order to understand both the optical properties of Ag, (mainly the plasmon ressonance) and the magnetic properties of Fe_3O_4, the precise knowledge of the morphology, structure and defects of the system is crucial.

- The interface of $\sim$10 nm Fe_3O_4 cubic particles with irregularly faceted $\sim$5 nm particles has been studied by HRTEM. The contact surface has been found to be atomically sharp, with no defects and no evidence of chemical diffusion.

- Analysis by GPA reveals the full in-plane adaptation of Ag to Fe_3O_4. The deformation in the out-of-plane direction can be seen in the first two atomic planes of Ag. This strain relaxation can also be seen in the increased brightness of those planes in HRTEM images.

- GPA phase maps and ϵ maps also reveal the presence of antiphase boundaries (APBs) inside Fe_3O_4 cubes. A structural model for one of these planar defects has been created and used to simulate HRTEM images, which match the experimental HRTEM contrast.

The second part of the chapter focuses on the characterization of the magnetic behaviour of Fe_3O_4 nanocubes, being the main interest its optimization for magnetic hyperthermia cancer treatment. In this sense, the chosen strategy is the increase of the magnetic anistropy coefficient by forming assemblies of nanocubes in the form of chains by dipole-dipole interaction.

- The formation of 3D chain-like assemblies of Fe_3O_4 40 nm had been previously confirmed by electron tomography. The cubes were found to be aligned sharing {100}-type faces. TEM results and macroscopic magnetic results are in good agreement with the proposed dipole-dipole interaction model. In order to obtain a nanoscale magnetic characterization, electron holography has been used.

- Electron holography experiments allow mapping the magnetic flux inside different nanocube assemblies. Magnetic coupling along the axis of the chain-like assemblies has been confirmed experimentally. This constitutes a direct confirmation of the theoretically predicted behaviour of the nanoparticle ensembles.

Appendix A

Aberration correction

This appendix, including the figures, closely follows some sections of Chapter 4 of the book *Aberration-Corrected Analytical Transmission Electron Microscopy*, edited by Rik Brydson [1].

A.1 Characterizing the aberrations of an electromagnetic lens

Aberrations, in general optics, are usually defined as the deviation of the real wavefront from the considered ideal, first order, or gaussian wavefront. The point-to-point distance between these two wavefronts is the *wave aberration*, W, and the resulting shift in the image plane of the real image point from the gaussian image point is the *ray aberration*, δ. This is schematically shown in figure A.1.

Making the reasonable assumption that aberrations tend to zero for paraxial rays, i.e. close to the optic axis, a mathematical 2D function in polar coordinates can be fitted to the aberrated surface of the wavefront, that corresponds to the angular aberration function of the lens

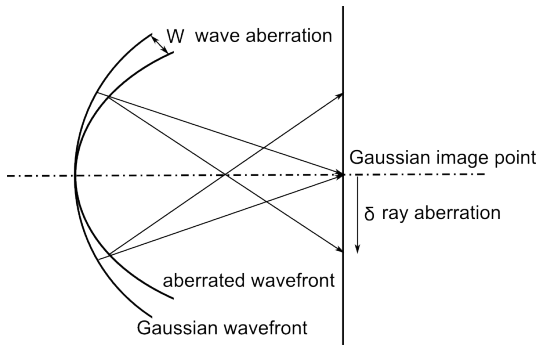

Figure A.1 Ray diagram showing the first order, gaussian, spherical unaberrated wavefront and the real wavefront. The difference between wave aberration and ray aberration is presented.

$$\begin{aligned}\chi(\theta,\varphi) = constant &+ \theta\{C_{01a}cos(\varphi) + C_{01b}sin(\varphi)\} \\ &+ \frac{\theta^2}{2}\{C_{10} + C_{12a}cos(2\varphi) + C_{12b}sin(2\varphi)\} \\ + \frac{\theta^3}{3}\{C_{23a}cos(3\varphi) &+ C_{23b}sin(3\varphi) + C_{21a}cos(\varphi) + C_{21b}sin(\varphi)\} \\ &+ \frac{\theta^4}{4}\{C_{30} + C_{34a}cos(4\varphi) + C_{34b}sin(4\varphi) \\ &\qquad + C_{32a}cos(2\varphi) + C_{32b}sin(2\varphi)\} + ... \quad \text{(A.1)}\end{aligned}$$

The numerical coefficients C_{NS} are called the aberration coefficients. N represents the *order* of the aberration and S represents the azimuthal dependence. If N is odd, S is even and vice versa. With that constraint, for each N, S takes values from 0 to $N+1$.

Aberrations are classified according to the power law dependence of the ray aberration, δ, which is proportional to the gradient of the wave aberration

$$\delta \propto \nabla W \qquad \text{(A.2)}$$

Table A.1 lists the aberration names corresponding to the lowest order aberration coefficients. Aberrations with the same azimuthal symmetry will result in similar effects on the wavefront, the only difference being the steepness of the deviation when

moving away from the optic axis. This means that low order aberrations dominate at low angles.

Aberration coefficient (Krivanek notation)	**Aberration coefficient** (Typke and Dierksen notation)	**Aberration name**
C_{01}	A0	Image shift
C_{10}	C1	Defocus
C_{12}	A1	Twofold astigmatism
C_{21}	B2	Coma
C_{23}	A2	Threefold astigmatism
C_{30} ($=C_s$)	C3	Spherical aberration
C_{32}	B3	Third order twofold astigmatism
C_{34}	A3	Third order fourfold astigmatism
C_{41}	B4	Fourth order coma
C_{43}	D4	Fourth order threefold astigmatism
C_{45}	A4	Fivefold astigmatism
C_{50}	C5	Fifth order spherical aberration
...	...	

Table A.1 Name of the aberrations corresponding to the coefficients of the lowest terms of equation A.1. Correspondence with the widely used Typke and Dierksen notation is added.

A.2 Diagnosing lens aberration

The first step in the process of correcting for aberrations, either in the condenser or the objective system, is to measure the aberration function $\chi(\theta, \varphi)$. Measuring χ directly can be difficult. However, considering the polynomial expression of equation A.1, measuring its derivatives and integrating afterwards can be an easier solution to fit the corresponding aberration coefficients to the experimental data. The first and second derivatives are, indeed, much easier to measure. The first derivative corresponds to the slope of the wavefront, and can be measured from the image shift associated with a tilted illumination. The second derivative corresponds to the curvature of the wavefront, and can be measured as the local defocus of an image induced by a tilted illumination. Measuring

derivatives, the constant term and the C_{01} coefficients are lost, but they constitute just an absolute phase term that is not relevant for the calculation.

The practical implementation of this idea is done through the acquisition of a series of images at different angles of the illumination, called a Zemlin tableau. In TEM correction, the tableau is recorded in an amorphous region (usually amorphous carbon film). The defocus and astigmatism for each image in the tableau, used to calculate the first and second derivatives of the aberrration function, can be calculated from the Thon rings in the Fast Fourier Transform of each image.

In STEM correction, the calibration sample is usually a distribution of approximately round Au particles on an amorphous carbon film, in order to achieve a high signal to background ratio in the HAADF detector. The Fast Fourier Transform of these images can be used in an analogous way to calculate the aberration function.

A.3 Aberration correctors

In order to break the rotational symmetry, and thus to avoid the presence of spherical aberration, the practical approach is the introduction of multipole lenses. They consist in an even number of poles, alternating N/S around the optical axis. In opposition to round lenses, for which the field lines are parallel to the beam, the resulting field lines are perpendicular to the electron beam, so an in-plane deflection of the beam can be achieved. The number of poles of the element determines the geometry of the distortion that it can induce. The distortion produced by the multipoles used in TEM aberration correctors are shown in figure A.2

There are two different implementations of aberration correctors in TEM: the quadrupole-octupole and the hexapole correctors.

A.3.1 Quadrupole-octupole corrector

The quadrupole-octupole configuration was proposed by Scherzer back in 1947 [2]. It was practically implemented with an improvement in resolution for the first time in 1999 by Krivanek [3], and it

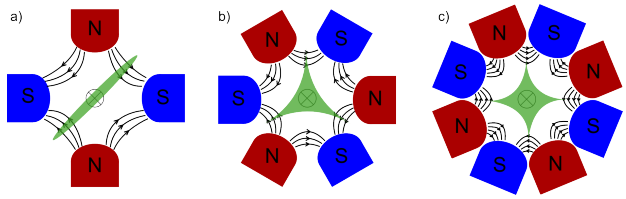

Figure A.2 Multipole elements, field lines and effect on the electron beam (green). The electron beam travels into the paper. a) Diagram of the quadrupole element. Its effect on the electron beam is the stretching in one direction, resulting in an elliptical beam. b) Diagram of the hexapole. Its effect results in a threefold symmetric beam. c) Diagram of the octupole. Its effect results in a fourfold symmetry of the electron beam.

is the dominant corrector for dedicated STEM systems. It consists in a total of four quadrupoles and three octupoles, as described in figure A.3.

The effect of an octupole on the electron wavefront has a cubic radial dependence with distance to the optical axis. This means the possibility of introducing a negative spherical aberration along two lines. The quadrupoles are then used to squeeze the beam along these two directions with negative C_s. The resulting beam is extremely elliptical in the first and third octupoles. This fourfold astigmatism is corrected by the remaining octupole. The problem with this configuration is the precision required in the correction of the extreme astigmatism introduced by the corrector itself.

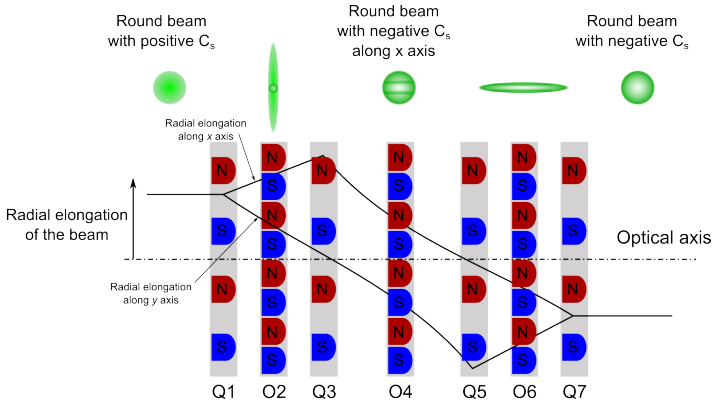

Figure A.3 Diagram of the quadrupole-octupole corrector. The state of correction of the electron beam is depicted on each optic element along the trajectory inside the detector.

New generation correctors by Nion are able to correct aberrations up to fifth order using a total of sixteen quadrupoles and 3 sets of the quadrupole-octupole systems described above.

A.3.2 Hexapole corrector

The hexapole corrector relies in a more subtle effect. By using long hexapoles, a second order effect appears with a cubic radial dependence that is not present in thin elements. The first order, undersired, effect with a quadratic radial dependence is cancelled by stacking two of these long hexapoles rotated 60^{o} with respect to each other. The second order effect, needed to introduce a negative C_s, is not cancelled but doubled. Two sets of projector round lenses (transfer doublets) are used to set the second order effects in equivalent optical planes so they can be canceled out. The layout is shown in figure A.4.

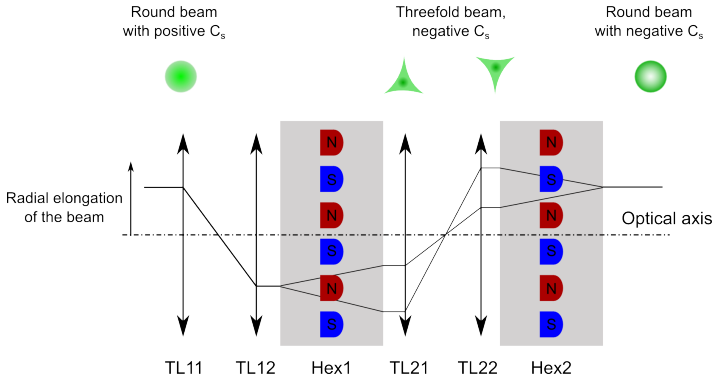

Figure A.4 Diagram of the hexapole corrector. Notice the thickness of the hexapole elements, responsible for the second order effect with cubic radial dependence needed for the negative C_s.

This corrector was introduced in 1998 by Haider et al.[4], and is the most widely used corrector. It can be used both in TEM and STEM correction. The new generation of hexapole correctors by the CEOS GmbH company uses a total of three hexapoles and three transfer doublets in order to correct aberrations up to fifth order.

Bibliography

[1] *Aberration-Corrected Analytical Transmission Electron Microscopy*, chapter 4. Lens Aberrations: Diagnosis and Correction. Wiley, 2011.

[2] O. Scherzer. Sphärische und chromatische korrektur von elektronenlinsen. *Optik*, 2, 1947.

[3] O.L. Krivanek, N. Delby, and A.R. Lupini. Towards sub-Å electron beams. *Ultramicroscopy*, (78):1–11, 1999.

[4] M. Haider, S. Uhlemann, E. Schwan, H. Rose, B. Kabius, and K. Urban. Electron microscopy image enhanced. *Nature*, 392(768), 1998.

Appendix B

Sample preparation

The observation in a TEM poses a series of requirements for the specimen. First, the region of interest needs to be electrotransparent since TEM is a transmission technique. Given the strong interaction of electrons with matter, this means that the sample needs to be thinner than 100 nm. Second, the mechanical constraint of the sample holder that is inserted in the TEM column. The standard sample holder design needs the sample to be mounted on a 3 mm metallic ring. Depending on the nature of the system under study, the fulfillment of these requirements demands different sample preparation procedures

B.1 Nano objects

Nanoscale 0D and 1D objects, i.e. nanoparticles, nanowires or equivalent nanosystems, are under 100 nm by definition. Given that they are already electrotransparent, the preparation procedure required consists just in the transfer to an adequate metallic grid to be mounted in the TEM sample holder.

The usual procedure followed in the present work is the dispersion of a droplet of an ethanol or hexane solution containing the nano-objects on a grid with a mesh of copper arms covered with an amorphous carbon holey film. After sonication of the solution in order to avoid aggregation, a droplet is dropped on top of the holey carbon grid. In the process, the objects adhere to the carbon membrane, as depicted in figure B.1. After mild heating in

a hot plate or under a light bulb in order to evaporate the solvent, the sample is ready to be observed. Hopefully, many objects will be adhered to the membrane but hanging on the edges of a hole so the electron beam travels just through the object. However, even if not optimal, observation is still possible for objects lying on the carbon membrane.

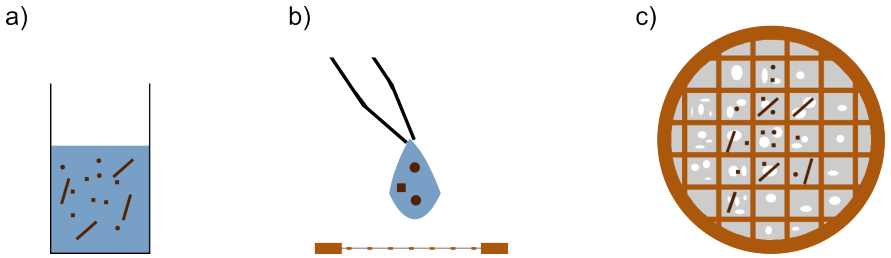

Figure B.1 a) Nano objects dispersed in an organic solvent. b) Droplet of the solution on the holey carbon copper grid (in cross section). c) The resulting sample with the adhered objects on the carbon membrane. Hopefully, some will be hanging on the holes.

The use of organic surfactant molecules in some wet synthesis routes results in contamination that aggregates under the electron beam and can render the TEM observation impossible. This contamination needs to be removed before putting the sample in the TEM column. An usual procedure is the cleaning of the sample by using an Ar/O plasma for a short time (< 20 s) in order not to destroy the carbon membrane. However, some samples can be affected by this process, specially for highly reactive surfaces. In such cases, more gentle procedures need to be considered, such as heating the grid (possibly in vacuum) in order for it to degas the organic contamination.

B.2 Mechanical polishing

For thin films grown on top of a substrate, or bulk crystals, a thinning process to electrotransparency is needed. Depending on the orientation of the film to be observed, the procedure is different for cross section or planar view geometries. This section covers mechanical polishing methods.

B.2.1 Cross section preparation

In order to obtain a sample in cross section geometry, the first step consists in cutting two pieces of the same dimensions and gluing them together, active face on. The polishing process is carried out, then, in the direction perpendicular to the cross section, as depicted in figure B.2. Depending on the hardness of the substrate material, polishing is achieved using SiC polishing paper or diamond covered lapping films.

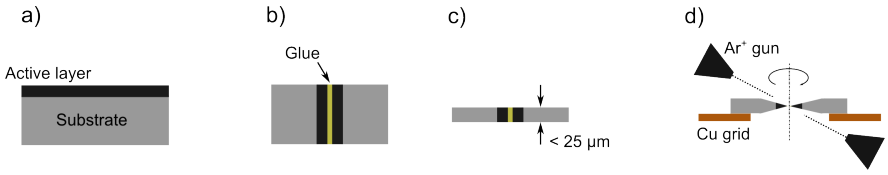

Figure B.2 a) Initial state of the sample. b) 'Sandwiched' sample. c) Mechanically flat polished sample in the direction perpendicular to the interface. d) Diagram of the resulting prepared sample on top of the Cu, grid with the central hole and the configuration of the ion guns.

Depending on the material and operator ability, the minimum achievable thickness in this flat polishing step may vary. For thicknesses around 25 μm, the sample is ready for the final thinning by ion milling. The sample is attacked by two Ar^+ guns at a low angle (4^o-6^o) and at $\sim$4.5 kV. The guns attack from top and bottom sides, so the redeposition of the material milled by one gun is cleaned by the other. The sample rotates at a variable speed in order to create an elongated hole in the direction of the cross section line. This results in a larger observable area on the edges of the hole. Figure B.3 presents three snapshots of the ion milling process of a silicon sample, taken with a visible light microscope.

B.2.2 Planar view preparation

Preparation of a thin film in planar view geometry starts directly with the mechanical polishing of the sample from the substrate side, following the same considerations as explained above for the cross section geometry. Once the target thickness is achieved in the flat polishing step, the ion milling is carried out in a similar

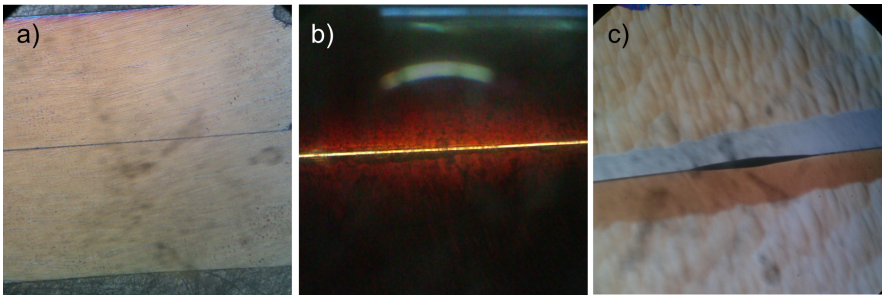

Figure B.3 a) A silicon sample after flat polishing. b) Optical transmission image of the sample during the milling process. Silicon thinned below 10 μm presents a color gradient from orange to yellow to white, as can be seen in the preferential attack region, i.e, the cross section line. c) Final elongated hole. Thin film and substrate in the edges of this hole are the thinnest observable regions.

way but attacking only from the substrate side and with no special need for modulation in the rotation speed. The active layer side needs to be covered in order to avoid redeposition of the material milled away from the substrate on top of the layer. As depicted in figure B.4, the final observable area will consist of a film region only and a superposition of film and substrate region.

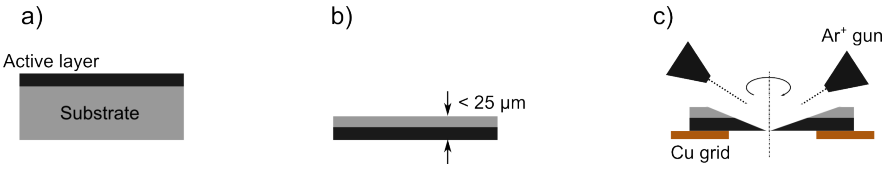

Figure B.4 a) Initial state of the sample. b) Flat sample polished on the substrate side. c) Ion milling configuration for milling from the substrate side only.

The preparation of bulk materials follows the same procedure, but with no need to protect the active layer; the attack can be, thus, performed from both top and bottom sides. Figure B.5 shows three snapshots of the ion milling process of a SBN single crystal.

For these mechanical preparation techniques, the final ion milling process may cause some degree of amorphization of the sample surface, especially near the edges. For particularly sensitive materials, lower accelerating energies or sample cooling using liquid nitrogen can reduce amorphization effects.

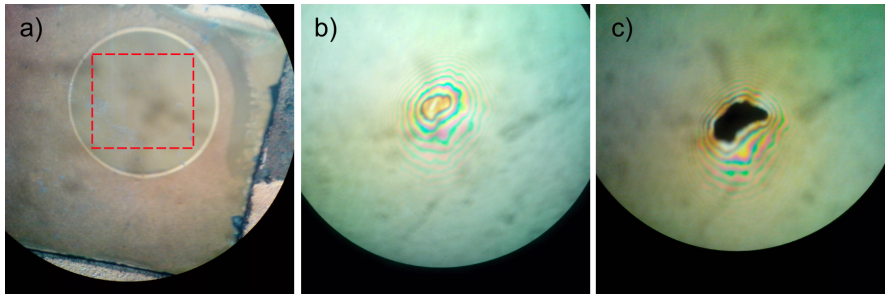

Figure B.5 a) A SBN-67 single crystal after flat polishing. Highlighted region corresponds to the zone depicted in the following images. b) Intermediate step of the thinning. Interference fringes in the optical reflection image from both sides of the sample shows that the hole is about to appear. c) Final state of the sample. The whole edge of the hole constitutes the observable region.

B.3 Focused Ion Beam (FIB)

Dual beam (SEM/FIB) systems have the imaging capabilities of a SEM microscope and the sample manipulation capabilities of an ion beam. For cases in which the amount of available material (or the available time) is not sufficient for mechanical preparation, or the region of interest in the sample needs to be precisely selected, FIB sample preparation is of great interest.

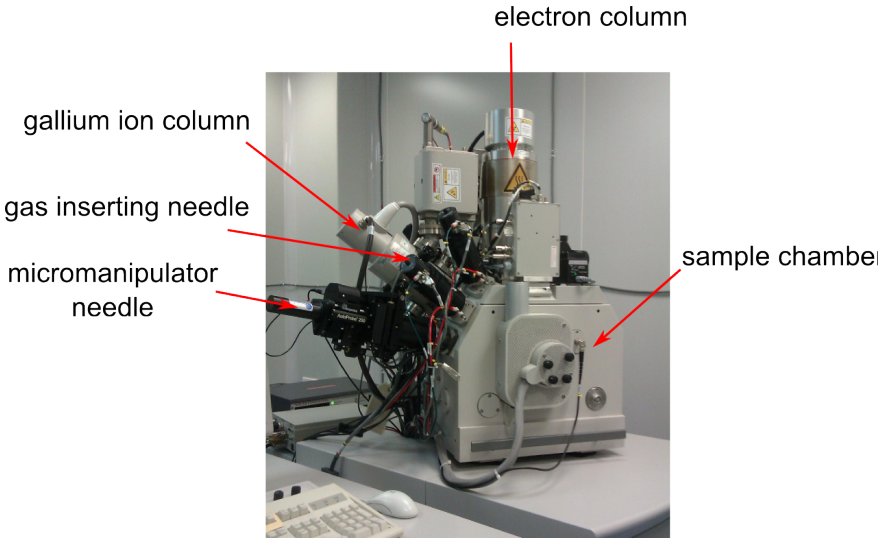

Figure B.6 The FIB FEI Strata Dual Beam at CCiT UB

In the context of this thesis, the particular TEM sample preparation procedure used is the so-called *in situ* lift-out technique. It is summarized in figure B.7. Once a region of interest is located in the sample, platinum is deposited to protect this region. Electron or ion beam induced deposition is achieved by decomposition of the molecules of a metalorganic gas precursor inserted in the chamber when the beam scans the selected region. Afterwards, the ion beam is used to cut trenches at both sides of the platinum deposit in order to get a lamella from the sample. This lamella is cut free from the substrate on the lower side and one of the lateral sides and is then attached to a micromanipulator tip by platinum deposition. Then it is released from the substrate by cutting on the other side, and taken to a special TEM copper half grid. This copper grid has three arms the lamella can be attached to, by platinum deposition. The lamella is cut free from the micromanipulator by means, again, of the ion beam, and finally thinned to electrotransparency.

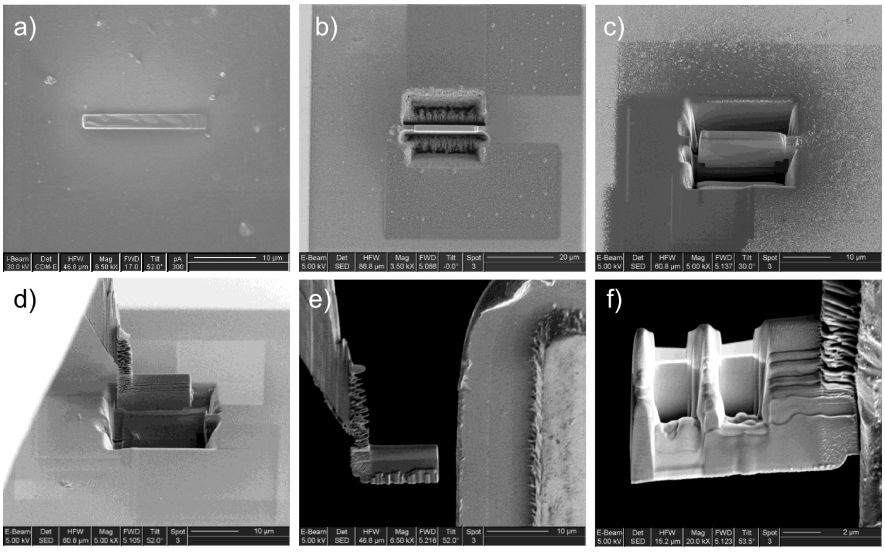

Figure B.7 Steps in the lift-out procedure. a) Protective Pt deposition. b) Lamella after cutting trenches at both sides. c) Lamella detached from the substrate on the left and bottom sides. d) Extraction of the lamella using the micromanipulator needle. e) Lamella about to be attached to the grid. f) Specimen ready for observation. Two observable windows have been thinned in the lamella.

Amorphization of the sample surface is also a possible complication from FIB sample preparation. The use of lower ion energy and/or current in the final steps of thinning of the lamella is important to minimize amorphization. Possible gallium implantation from the ion beam must be taken into account in cases where it can interfere with the experiment.

Appendix C

Resum en català

La reducció en l'escala espacial associada a la revolució de la Nanociència i la Nanotecnologia fa necessari comptar amb una sèrie d'eines capaces d'assolir una resolució sense precedents en una gran varietat d'àress, ja no tan sols com a control de qualitat, sinó per tal d'entendre les propietats de la matèria a la nanoescala. La correlació de la configuració estructural, la composició química i les distribucions de càrrega amb les propietats funcionals és imprescindible pel disseny de nous dispositius, tant des de la perspectiva 'top down' (reducció de les dimensions dels dispositius) com de la perspectiva 'bottom up' (fabricació d'estructures complexes a partir de blocs més petits, fins i tot àtoms). La capacitat de la Microscòpia Electrònica de Transmissió (TEM) de proporcionar diferents tipus d'informació amb una alta resolució espacial, situa les tècniques avançades de TEM com a peça clau en el desenvolupament d'aquest camp multidisciplinari i creixent.

L'objectiu principal d'aquesta tesi ha estat l'aplicació de tècniques quantitatives d'imatge TEM per la resolució de problemes en ciència dels materials. La tesi cobreix un espectre ampli pel que fa al tipus de materials estudiats i els seus camps d'aplicació. El Capítol 1 presenta una introducció general a la teoria de formació d'imatge aplicada a la microscopia TEM. S'hi exposen els diferents fenòmens d'interacció electró-matèria que són responsables dels diferents tipus de contrast que es poden trobar a les imatges TEM. El Capítol 2 presenta les tècniques experimentals que es faran servir en la caracterització dels materials, en concret la simulació d'imatges d'alta resolució (HRTEM), l'holografia electrònica i

l'anàlisi de la fase geomètrica (GPA). S'hi pot trobar una descripció del marc teòric i dels fonaments experimentals, juntament amb un resum dels resultats més recents en aquests camps.

Els resultats experimentals s'agrupen en els capítols posteriors segons la dimensionalitat dels sistemes estudiats. En ordre decreixent de dimensionalitat s'hi inclouen: materials massius (3D), capes primes (2D), nanofils (1D) i nanopartícules (1D).

El Capítol 3 conté la caracterització de dos òxids en forma de cristalls massius. El primer cas consisteix en una sèrie de niobats de terres rares ((RE_3NbO_7, RE = Y,Er,Yb,Lu) amb aplicacions en piles de combustible com a electròlit conductor de protons. Per tal d'explicar les propietats de conducció, s'ha investigat la microstructura de mostres en pols i en pastilles dels diferents compostos mitjançant HRTEM i SAED.

- Les imatges HRTEM de tots els compostos mostren dominis locals amb modulació del contrast per la presència d'una superestructura que dobla la periodicitat de la cel·la unitat de la fluorita. Els difractogrames digitals obtinguts a partir de les imates (FFT) mostren fenòmens de dispersió difusa en forma d'anells i reflexions satèl·lit.

- S'han dut a terme experiments de SAED sistemàticament per tots els compostos per tal de caracteritzar l'espai recíproc dels cristalls. S'han adquirit patrons de difracció en diferents eixos de zona tant per les mostres en pols com per les pastilles. Els fenòmens de dispersió difusa en forma d'anells i reflexions satèl·lit es troben a les posicions recíproques que doblen la cel·la unitat de la fluorita.

- Els resultats experimentals s'expliquen en termes d'un model microstructural consistent en una matriu amb estructura fluorita en la que hi ha immersos dominis amb estructura piroclor orientats aleatòriament. El piroclor és una superestructura de segon ordre de la fluorita en la que vacants d'oxigen s'ordenen en capes atòmiques alternes.

- Les vacants d'oxigen inherents als niobats amb la fórmula RE_3NbO_7 s'ordenen només a curt abast ja que la diferència en el radi dels cations impedeix l'ordenament a llarg abast.

La mida finita dels dominis explica el caràcter difús de les reflexions associades al piroclor en els patrons de difracció, i la seva orientació aleatòria explica la simetria en forma d'anell. Tots els patrons de difracció adquirits es poden explicar tenint en compte els talls de l'esfera d'Ewald amb els màxims de Bragg de la fluorita i els anells difusos del piroclor.

La segona part del Capítol 3 tracta sobre el relaxor ferroelèctric uniaxial $Sr_{0.67}Ba_{0.33}Nb_2O_6$. L'objectiu de l'estudi és la caracterització del desordre estructural i químic en l'estructura cristal·lina, que pertany a la família dels bronzes de tungstè tetragonals (TTB). En concret, la presència de vacants aleatòriament distribuïdes en les posicions catiòniques A1 i la ocupació aleatòria per part d'àtoms de Sr i Ba en les posicions catiòniques A2 són responsables del caràcter relaxor del material. L'estudi s'ha dut a terme amb una combinació de tècniques de difracció, imatge i espectroscòpia.

- Els patrons de difracció adquirits en l'eix de zona [100] mostren fenòmens interessants de dispersió difusa. En primer lloc, un allargament dels màxims de Bragg al llarg de la direcció [010], consistent amb la tensió introduïda al cristall per la presència de vacants catiòniques a l'estructura. En segon lloc, s'hi troben reflexions de superstructura incommensurables.

- El caràcter incommensurable de la superestrucura, que per tant no és un múltiple de l'estructura TTB, fa necessari introduir dos vectors recíprocs addicionals per tal de descriure la cel·la unitat recíproca del cristall, convertint-lo així en un superespai en 5D.

- Imatges HAADF amb resolució de columna atòmica en l'eix de zona [001] mostren una elongació en la forma de les columnes corresponents a les posicions A2. Això s'atribueix a la vista en projecció del desplaçament d'alguns cations en direccions preferencials. Els desplaçaments atòmics deguts a l'ocupació aleatòria per atoms de Sr i Ba d'aquestes posicions permeten explicar la superestructura incommnesurable que s'ha observat.

- Imatges HAADF amb resolució de columna atòmica en l'eix de zona [100] mostren la presència de vacants catiòniques en les posicions A1. La caracterització estructural s'ha completat mitjançant l'ús de la tècnica ABF per tal d'observar la subxarxa aniònica del cristall.

- Mapes químics obtinguts d'adquisicions EELS en mode d'adquisició hiperespectral (*spectrum image*) han permès estudiar el desordre químic en les posicions A2. L'ús de temps d'adquisicó molt curts ha permès obtenir mapes de regions extenses del cristall orientat en l'eix de zona [001]. Per tal de millorar la relació senyal-soroll de les dades, s'ha fet servir tècniques d'anàlisi multivariant. En concret, mitjançant la descomposició per Anàlisi de Components Principals (PCA) s'ha generat un conjunt de dades netes a partir de les quals l'ocupació aleatòria de la posició A2 per part de Sr i Ba ha estat confirmada.

El Capítol 4 correspon a la caracterització de dos estructures en capa prima. La primera part s'ocupa d'una sèrie de capes de niquelat de lantà ($LaNiO_3$, LNO) crescudes en diferents substrats (LNO, LSAT, STO i YAO). La diferència en el valor del paràmetre de xarxa entre el LNO i els diferents substrats indueix un estat de tensió diferent a la capa prima. Aquesta enginyeria de tensions es pot fer servir per tal de controlar les propietats de transport electrònica del LNO. Capes primes de 14 nm i 35 nm s'han estudiat mitjançant HRTEM, HAADF i anàlisi GPA de les imatges obtingudes.

- L'estat de tensió de les capes primes s'ha estudiat mitjançant l'anàlisi GPA de les imatges HAADF. Les capes primes de LNO crescudes sobre substrats de LAO, LSAT i STO mostren una adaptació total del paràmetre de xarxa del LNO en el pla al paràmetre de xarxa del substrat. El paràmetre de xarxa fora del pla presenta valors similars al LNO massiu.

- Pel cas de la capa prima de LNO crescuda sobre substrat de YAO, s'ha trobat que la capa creix totalment relaxada degut a la major diferència en els valors del paràmetres de xarxa i

a la diferència estructural entre el substrat (ortorròmbic) i el LNO (cúbic).

- S'han trobat defectes planars en totes les capes més enllà dels primers ~ 3 nm de creixement. S'ha pogut determinar, a partir del contrast de les imatges HAADF, que es tracta de defectes tipus Ruddlesden-Popper (RP) consistents en la translació del cristall $1/2$ de la cel·la unitat en la direcció [111]. Un pla de Ni-O es perd a cada defecte.

- L'estudi del contrast de les imatges HAADF ha permès caracteritzar la geometria d'aquests defectes RP dins de la capa prima. En concret, la pèrdua de la diferència de contrast entre les posicions A i B de la perovskita s'ha pogut fer servir per detectar la superposició dels dominis desplaçats al llarg de la direcció de propagació del feix d'electrons. El caràcter abrupte o gradual d'aquesta pèrdua de contrast s'ha fet servir per determinar l'orientació paral·lela o no paral·lela dels plans de defecte respecte del feix d'electrons.

- Una fase monoclínica deficient en oxigen, $LaNiO_{2.5}$, s'ha trobat en regions de les capes de 35 nm. El contrast de superestructura en les imatges HRTEM, degut a la ordenació de les vacants d'oxigen en aquesta fase, s'ha trobat amb orientacions diferents depenent del signe de la tensió exercida pel substrat sobre la capa. Triant adequadament la direcció de preparació de les seccions transversals, els eixos de zona necessaris per observar les columnes atòmiques amb deficiència d'oxigen s'han fet accessibles a l'observació .

La segona part correspon a la caracterització d'un reflector distribuït de Bragg (DBR), consistent en capes alternes de InAlN i GaN. Amb la tria adient del gruix dels semiperíodes d'acord amb els diferents índex de refracció dels dos compostos III-V, s'aconsegueix l'alta reflectivitat per la longitud d'ona desitjada. L'objectiu de l'estudi és explicar els valors de reflectivitats obtinguts pel dispositiu, sensiblement inferiors als esperats. El dispositiu ha estat caracteritzat mitjançant SAED i HRTEM, amb un paper important de la simulació d'imatge en la interpretació de les dades.

- Tots els semiperíodes de InAlN corresponen a la fase wurtzita, sense cap defecte estructural. D'altra banda, en els semiperíodes de GaN s'ha trobat una alta densitat de defectes planars, així com franges de Moirée amb diferents periodicitats.

- Un dels patrons de franges de Moirée, amb una periodicitat de 6x l'espaiat dels plans en la direcció de creixement, s'ha pogut explicar com a resultat de la superposició de les fases wurtzita i zinc blenda del GaN en la direcció de propagació del feix d'electrons. La informació extreta de les imatges de HRTEM i SAED s'ha fet servir per crear un model estructural que, al seu torn, s'ha simulat per tal d'obtenir imatges HRTEM. El resultat de les simulacions pel model proposat es correspon amb el contrast observat experimentalment.

- Un segon patró de franges de Moirée, amb una periodicitat de 3x l'espaiat dels plans en la direcció de creixement, s'ha pogut explicar per la superposició de dos dominis de GaN en la fase zinc blenda orientats en diferents eixos de zona. S'ha proposat un model estructural tenint en compte les diferents orientacions possibles del creixement de GaN zinc blenda sobre una capa wurtzita de InAlN. Les imatges HRTEM simulades a partir d'aquest model també coincideixen amb el contrast observat experimentalment.

- Les interfícies addicionals creades pels defectes planars associats als dominis zinc blenda amb orientacions diferents, així com la coexistència de dominis de GaN wurtzita i GaN zinc blenda, són responsables de la disminució de la homogeneïtat de la capa, un factor crucial per tal d'obtenir una alta reflectivitat.

El Capítol 5 tracta sobre la caracterització d'estructures unidimensionals, és a dir, nanofils. Diferents estructures basades en l'òxid de niobi Nb_2O_5 s'han estudiat per tal d'optimitzar les seves propietats com a sensor d'humitat. L'estructura i els defectes del Nb_2O_5 s'han caracteritzat mitjançant imatge HRTEM i les corresponents simulacions per tal d'interpretar el resultats. En primer

lloc, s'han estudiat nanofils de Nb_2O_5 de 500 nm de llargada i 30-50 nm de diàmetre.

- Les imatges HRTEM dels nanofils presenten una modulació de contrast en forma de bandes orientades al llarg de la direcció de creixement. Aquest tipus de contrast s'ha atribuït sovint a la presència d'una alta densitat de defectes d'apilament o plans de macla en la fase monoclínica, amb grup d'espai C2 del Nb_2O_5. Aquesta estructura és compatible amb una possible indexació dels difractogrames digitals (FFT). Seguint aquesta aproximació, s'han creat models estructurals incloent-hi aquests defectes i s'han obtingut les corresponents imatges HRTEM simulades. Els resultats de les simulacions no reprodueixen el contrast observat experimentalment.

- En la recerca de models estructurals alternatius per explicar el contrast HRTEM observat s'han dut a terme simulacions d'imatge HRTEM per altres fases del Nb_2O_5. La fase monoclínica amb grup d'espai C2/c, també compatible amb la indexació de les FFTs, reprodueix el contrast experimental en regions extenses dels nanofils sense haver d'introduir-hi defectes. Així, tot i que els defectes planars són presents i s'han pogut caracterizar, ho són amb una densitat molt més baixa de l'esperada.

La segona part del capítol es centra en la caracterització de nanofils amb estructures nucli-escorça dissenyades amb l'objectiu d'optimitzar la funcionalitat del sistema. La combinació de l'alta sensitivitat d'una capa externa de Nb_2O_5 i les bones propietats de conducció d'un nucli de SnO_2 fan que el temps de recuperació i la integrabilitat en dispositius del sistema siguin molt millors que els dels nanofils aïllats. A més de l'aliniament de l'estructura de bandes, la presència de defectes en la interfície entre els dos materials també explica una part de l'augment en la resposta del sistema.

- S'ha observat que el Nb_2O_5 creix sobre els nanofils de SnO_2 en forma de piràmides truncades. La cobertura total resultant

després del procés de dipòsit no és, doncs, homogènia sinó clarament irregular.

- Per tal de caracteritzar en detall la superfície de contacte entre els dos materials, s'han estudiat mitjançant HRTEM heterostructures en una fase intermitja de recobriment. S'ha trobat diferents tipus de defectes en aquestes interfícies, tals com xarxes de dislocacions periòdiques o plans de macla tant paral·lels com perpendiculars a la interfície.

- L'estat de tensió en les heteroestructures s'ha estudiat mitjançant GPA. S'ha trobat que la relaxació de tensió a través de la formació de dislocacions no és completa, i que la tensió es propaga a l'interior de les illes de Nb_2O_5 en forma de bandes perpendiculars a la interfície. En els dominis de ~ 2 nm, rotats a través d'un pla de macla paral·lel a la interfície, la relaxació de la tensió epitaxial és completa.

- La formació de dominis rotats per un pla de macla en les illes de Nb_2O_5, juntament amb la descoberta de cristalls de Nb_2O_5 separats dels nuclis de SnO_2 i pertanyents a la fase C2/c trobada pels nanofils aïllats, suggereixen la presència d'una longitud crítica a partir de la qual la tensió indueix una transició estructural.

El Capítol 6 correspon a la caraterització de sistemes 0D, és a dir, nanopartícules. El primer sistema consisteix en dímers formats per la unió d'una partícula de Fe_3O_4 i una partícula de Ag. La combinació de les propietats ferromagnètiques del primer material amb les propietats òptiques dels metalls nobles permet augmentar i controlar l'activitat òptica del sistema mitjançant l'acoblament magnetoplasmònic. Per tal d'entendre tant les propietats òptiques de la partícula de Ag (principalment la ressonància plasmònica) i les propietats magnètiques del Fe_3O_4 és necessària una descripció precisa de la morfologia, l'estructura i els defectes presents al sistema.

- La interfície entre les partícules de Fe_3O_4, cúbiques i d'aproximadament 10 nm de costat, i les partícules de Ag, amb un facetatge irregular i d'aproximadament 5 nm de diàmetre,

s'ha caracteritzat mitjançant HRTEM. La superfície de contacte entre els dos materials és abrupta, sense defectes ni evidències de difusió química.

- L'anàlisi mitjançant GPA mostra una total adaptació del paràmetre de xarxa, en el pla, de la plata respecte la partícula de Fe_3O_4. La deformació de la xarxa en la direcció fora del pla es pot veure en els dos primers plans atòmics de la partícula de Ag, tant en els mapes del tensor ϵ com en l'increment de contrast en aquests plans en la imatge HRTEM.

- Els mapes de GPA també revelen la presència de dominis d'antifase (APBs) als cubs de Fe_3O_4. S'ha proposat un model estructural per un d'aquests defectes planars i les imatges HRTEM simulades a partir d'aquest model reprodueixen el contrast experimental.

La segona part del capítol consisteix en la caracterització del comportament magnètic de nanocubs de Fe_3O_4, amb aplicacions en tractament del càncer mitjançant hipertèrmia magnètica. En aquest sentit, l'estratègia es basa en augmentar el coeficient d'anisotropia magnètica mitjançant la formació de cadenes de nanocubs alineades degut a la interacció dipol-dipol.

- La formació d'aquestes cadenes 3D de cubs de 40 nm de costat havia estat prèviament confirmada mitjançant experiments de tomografia electrònica. Els cubs es trobaven aliniats compartint cares del tipus {100}. Els resultats previs de TEM, així com la caracterització magnètica a escala macroscòpica són compatibles amb el model proposat d'interacció dipol-dipol. Per tal d'obtenir una caracterització magnètica a la nanoescala, s'han dut a terme experiments d'holografia electrònica.

- Els experiments d'holografia electrònica han permès obtenir mapes del flux magnètic dins de diferents cadenes de nanocubs. L'acoblament magnètic al llarg de l'eix de les diferents agrupacions ha estat confirmat experimentalment, tal com preveu el model teòric considerat i suggerien les mesures macroscòpiques.

En els diferents capítols de la tesi s'ha donat resposta a problemes de ciència de materials relacionats amb una varietat de propietats estructurals, químiques i magnètiques sobre les quals la microscopia TEM pot donar informació quantitativa amb una gran resolució espacial.

Appendix D

Scientific Curriculum

Education

2010 Llicenciatura en Física, Universitat de Barcelona

2011 MSc in Nanoscience and Nanotechnology, Universitat de Barcelona.

Appointments held

2011-2015 Formación de Personal Investigador (FPI) grant holder, as a PhD student at LENS (Laboratory of electron nanoscopies), Departament d'Electrònica, Universitat de Barcelona.

Research stages

2011 Departamento de Química Inorgánica y Ciencia de los Materiales, Universidad de Cádiz, Spain. June-July (1 month)

2011 Facultad de Química, Universidad Complutense de Madrid, Spain. November-December (1 month).

2013 Laboratorio de Microscopías Avanzadas Insituto de Nanociencia de Aragón (LMA-INA), Zaragoza, Spain. April-July (3 months).

2013 Centre d'Elaboration de Matériaux et d'Etudes Structurales (CEMES-CNRS), Toulouse, France. June-September (3 months).

2014 Laboratoire Structures, Proprietés et Modélisation des Solides (LSPMS), École Centrale Paris, France. March (2 weeks).

2015 NanoBioMedical Centre AMU, Adam Mickiewicz University, Poznan, Poland. July (1 week)

Workshops & schools

2011 11th TEM-UCA European Summer Workshop, Transmission Electron Microscopy of Nanomaterials. Universidad de Cádiz, Spain. July.

2011 Introducción a la Microscopia Electrónica de Transmisión, ICTS Centro Nacional de Microscopía Electrónica, Universidad Complutense de Madrid, Spain. December.

2012 Courses and seminars on Electronic Microscopy of Materials: Present and Future Institut de Nanociència de la Universitat de Barcelona (IN^2UB), Barcelona, Spain. September - June.

2012 Electron Chrystallography School - New methods and applications, Stockholm University, Department of Materials and Environmental Chemistry. Stockholm, Sweden. June.

2012-2013 Aprenent a ensenyar - Learning teaching, Institut de Ciències de l'Educació de la Universitat de Barcelona. Barcelona, Spain. Setember 2012 - June 2013.

2013 Introducció al Python, NumPy i SciPy, Universitat de Barcelona, Departament d'Electrònica. Barcelona, Spain. January.

2014 Advanced Analytical modes in the Nanoscale: Electron Energy Loss Spectrosocpy and Tomography in the TEM, Centres Científics i Tecnològics de la Universitat de Barcelona, Barcelona, Spain. June.

Grants, honors & awards

2011 Formación de Personal investigador (FPI) Grant BES-2011-043928 from Ministerio de Economia y Competitividad (Spain).

2013 Grant EEBB-I-13-07535 for a three month international research stage, from Ministerio de Economia y Competitividad (Spain).

MSc thesis supervision

2014 Advanced tools for Transmission Electron Microscopy, Josep Parra

Physics degree final project supervision

2015 Interpretation of HRTEM images of SBN-67 by simulations through the multislice approach, Sergi Plana

Reviewer for the following journals

- Plasmonics

Journal articles

1. J. López-Vidrier, S. Hernández, A.M. Hartel, D. Hiller, S. Gutsch, P. Löper, L. López-Conesa, S. Estradé, F. Peiró, M. Zacharias, and B. Garrido. Structural and optical characterization of size controlled silicon nanocrystals in SiO_2/SiO_xN_y multilayers. *Energy Procedia*, 10:43–48, 2011.

2. C. Martínez-Boubeta, A.S. Botana, V. Pardo, D. Baldomir, A. Antony, J. Bertomeu, J.M. Rebled, L. López-Conesa, S. Estradé, and F. Peiró. Heteroepitaxial growth of MgO(111) thin films on Al_2O_3(0001): Evidence of a wurtzite to rocksalt transformation. *Physical Review B*, 86(4):041407, 2012.

3. S. Albert, A. Bengoechea-Encabo, M.A. Sanchez-García, F. Barbagini, E. Calleja, E. Luna, A. Trampert, U. Jahn, P. Lefebvre, L. López-Conesa, S. Estradé, J.M. Rebled, F. Peiró, G. Nataf, P. De Mierry, and J. Zuniga-Pérez. Ordered Gan/Ingan Nanorods Arrays Grown By Molecular Beam Epitaxy for Phosphor-Free White Light Emission. *International Journal of High Speed Electronics and Systems*, 21(01):1250010, 2012.

4. M.A. Sanchez-Garcia, F. Peiró, G. Nataf, J. Zuniga-Perez, J.M. Rebled, L.L. López, A. Bengoechea-Encabo, E. Calleja, S. Albert, S. Estradé, and P. de Mierry. Selective area growth of a- and c-plane GaN nanocolumns by molecular beam epitaxy using colloidal nanolithography. *Journal of Crystal Growth*, 353(1):1–4, 2012.

5. C. Summonte, M. Canino, M. Allegrezza, M. Bellettato, A. Desalvo, R. Shukla, I.P. Jain, I. Crupi, S. Milita, L. Ortolani, L. López-Conesa, S. Estradé, F. Peiró, and B. Garrido. Boron doping of silicon rich carbides: Electrical properties. *Materials Science and Engineering: B*, 178(9):551–558, 2013.

6. J. M. Ramírez, Y. Berencén, L. López-Conesa, J. M. Rebled, F. Peiró, and B. Garrido. Carrier transport and electroluminescence efficiency of erbium-doped silicon nanocrystal superlattices. *Appl. Phys. Lett.*, 103(8):081102, 2013.

7. A. Eljarrat, L. López-Conesa, C. Magén, Z. Gacevic, S. Fernández Garrido, E. Calleja, S. Estradé, and F. Peiró. Insight into the compositional and structural nano features of AlN/GaN DBRs by EELS-HAADF. *Microscopy and Microanalysis*, 19:698–705, 2013.

8. L. López-Conesa, J. M. Rebled, M. H. Chambrier, K. Boulahya, J. M. González-Calbet, M. D. Braida, G. Dezanneau, S. Estradé, and F. Peiró. Local structure of rare earth niobates (RE_3NbO_7, RE=Y,Er,Yb,Lu) for proton conduction applications. *Fuel Cells*, 13(1):29–33, 2013.

9. A. Eljarrat, L. López-Conesa, J.M. Rebled, Y. Berencén, J.M. Ramírez, B. Garrido, C. Magén, S. Estradé, and F. Peiró. Structural and compositional properties of Er-doped silicon nanoclusters/oxides for multilayered photonic devices studied by STEM-EELS. *Nanoscale*, 5(20):9963–70, 2013.

10. A. Zelenina, S.A. Dyakov, D. Hiller, S. Gutsch, V. Trouillet, M. Bruns, S. Mirabella, P. Löper, L. López-Conesa, J. López-Vidrier, S. Estradé, F. Peiró, B. Garrido, J. Bläsing, A. Krost, D. M. Zhigunov, and M. Zacharias. Structural and optical properties of size controlled Si nanocrystals in Si_3N_4 matrix: The nature of photoluminescence peak shift. *Journal of Applied Physics*, 114(18):184311, 2013.

11. J. López-Vidrier, S. Hernández, J. Samà, M. Canino, M. Allegrezza, M. Bellettato, R. Shukla, M. Schnabel, P. Löper, L. López-Conesa, S. Estradé, F. Peiró, S. Janz, and B. Garrido. Structural, optical and electrical properties of silicon nanocrystals embedded in Si_xC_{1-x}/SiC multilayer systems for photovoltaic applications. *Materials Science and Engineering: B*, 178(9):639–644, 2013.

12. R. Fiz, F. Hernández-Ramírez, T. Fischer, L. López-Conesa, S. Estradé, F. Peiró, and S. Mathur. Synthesis, characterization, and humidity detection properties of Nb_2O_5 Nanorods and SnO_2 / Nb_2O_5 Heterostructures. *The Joournal of Physical Chemistry C*, 117(19), 2013.

13. D. Hiller, A. Zelenina, S. Gutsch, S.A. Dyakov, L. López-Conesa, J. López-Vidrier, S. Estradé, F. Peiró, B. Garrido, J. Valenta, M. Kořínek, F. Trojánek, P. Malý, M. Schnabel, C. Weiss, S. Janz, and M. Zacharias. Absence of quantum confinement effects in the photoluminescence of Si_3N_4–embedded Si nanocrystals. *Journal of Applied Physics*, 115(20):204301, 2014.

14. J. López-Vidrier, S. Hernández, D. Hiller, S. Gutsch, L. López-Conesa, S. Estradé, F. Peiró, M. Zacharias, and B. Garrido. Annealing temperature and barrier thickness effect on the structural and optical properties of silicon nanocrystals/SiO_2 superlattices. *Journal of Applied Physics*, 116(13):133505, 2014.

15. L. Caccamo, J. Hartmann, C. Fàbrega, S. Estradé, G. Lilienkamp, J.D. Prades, M.W.G. Hoffmann, J. Ledig, A.R Wagner, X. Wang, L. López-Conesa, F. Peiró, J.M. Rebled, H.H. Wehmann, W. Daum, H. Shen, and A. Waag. Band engineered epitaxial 3D GaN-InGaN core-shell rod arrays as an advanced photoanode for visible-light-driven water splitting. *ACS applied materials & interfaces*, 6(4):2235–40, 2014.

16. S. Hernández, J. López-Vidrier, L. López-Conesa, D. Hiller, S. Gutsch, J. Ibánez, S. Estradé, F. Peiró, M. Zacharias, and B. Garrido. Determining the crystalline degree of silicon nanoclusters/SiO2 multilayers by Raman scattering. *Journal of Applied Physics*, 115(20):203504, 2014.

17. L. Yedra, A. Eljarrat, J.M. Rebled, L. López-Conesa, N. Dix, F. Sánchez, S. Estradé, and F. Peiró. EELS tomography in multiferroic nanocomposites: from spectrum images to the spectrum volume. *Nanoscale*, 6(12):6646–50, 2014.

18. A. Eljarrat, L. López-Conesa, J. López-Vidrier, S. Hernández, B. Garrido, C. Magén, F. Peiró, and S. Estradé. Retrieving the electronic properties of silicon nanocrystals embedded in a dielectric matrix by low-los EELS. *Nanoscale*, 6:14971–14983, 2014.

19. C. Summonte, M. Allegrezza, M. Bellettato, F. Liscio, M. Canino, A. Desalvo, J. López-Vidrier, S. Hernández, L. López Conesa, S. Estradé, F. Peiró, B. Garrido, P. Löper, M. Schnabel, S. Janz, R. Guerra, and S. Ossicini. Silicon nanocrystals in carbide matrix. *Solar Energy Materials and Solar Cells*, 128:138–149, 2014.

20. A. Zelenina, A. Sarikov, D.M. Zhigunov, C. Weiss, N. Zakharov, P. Werner, L. López-Conesa, S. Estradé, F. Peiró, S.A. Dyakov, and M. Zacharias. Silicon nanocrystals in SiN_x/SiO_2 hetero-superlattices: The loss of size control after thermal annealing. *Journal of Applied Physics*, 115(24):244304, 2014.

21. M. Schnabel, C. Summonte, S.A. Dyakov, M. Canino, L. López-Conesa, P. Löper, S. Janz, and P.R. Wilshaw. Absorption and emission of silicon nanocrystals embedded in SiC: Eliminating Fabry-Pérot interference. *Journal of Applied Physics*, 117(4):045307, 2015.

22. M. Schnabel, M. Canino, S. Künhold, J. López-Vidrier, T. Klugermann, C. Weiss, L. López-Conesa, M. Zschintzsch-Dias, C. Summonte, P. Löper, S. Janz, and P. Wilshaw. Charge transport in nanocrystalline SiC with and without embedded Si nanocrystals. *Phys. Rev. B*, 91(19):195317, 2015.

23. M. Vila, C. Díaz-Guerra, J. Piqueras, L. López-Conesa, S. Estradé, and F. Peiró. Growth, structure, luminescence and mechanical resonance of Bi_2O_3 nano- and microwires. *CrystEngComm*, 17(1):132–139, 2015.

24. M. Estrader, A. López-Ortega, I.V. Golosovsky, S. Estradé, A.G. Roca, G. Salazar-Alvarez, L. López-Conesa, D. Tobia, E. Winkler, J. D. Ardisson, W.A.A. Macedo, A. Morphis, M. Vasilakaki, K.N. Trohidou, A. Gukasov, I. Mirebeau, O.L. Makarova, R.D. Zysler, F. Peiró, M.D. Baró, L. Bergström, and J. Nogués. Origin of the large dispersion of magnetic properties in nanostructured oxides: FeO/Fe_3O_4 nanoparticles as a case study. *Nanoscale*, 7(7):3002–3015, 2015.

Oral contributions in conferences

1. A. Eljarrat, L. López-Conesa, Z. Gacevic, S. Fernández-Garrido, E. Calleja, C. Magén, S. Estradé, and F. Peiró. AlN/GaN DBR layers low-loss EELS-HAADF compositional mapping. In *Workshop on EELS in Materials Science, Uppsala (SWE)*, 2012

2. A. Eljarrat, L. López-Conesa, J.M. Ramirez, Y. Berencén, S. Hernández, J. López-Vidrier, S. Estradé, C. Magén, B. Garrido, and F. Peiró. Chemical and structural characterization of Si-based electroluminescent and photovoltaic devices through HAADF-EELS. In *Jounées d'EELS, Aix-les-Bains (FRA)*, 2012

3. A. Eljarrat, L. López-Conesa, Z. Gacevic, S. Fernández-Garrido, E. Calleja, C. Magén, S. Estradé, and F. Peiró. EELS-HAADF combination for characterization of a new AlN/GaN DBRs growth method. In *European Microscopy Congress, Manchester (UK)*, 2012

4. L. López-Conesa, T. Fischer, R. Fiz, S. Mathur, F. Hernández-Ramírez, S. Estradé, and F. Peiró. Structural characterization of Nb_2O_5 nanorods and Nb_2O_5@SnO_2 heterostructures for humidity sensing applications. In *MRS Fall Meeting, Boston (USA)*, 2012

5. J. López-Vidrier, S. Hernández, D. Hiller, S. Gutsch, A.M. Hartel, M. Schnabel, P. Löper, M. Foti, L. López-Conesa, S. Estradé, F. Peiró, S. Janz, M. Zacharias, and B. Garrido. Silicon quantum dots embedded in SiO_2 for tandem solar cells. In *Workshop in Dielectric Materials, Dresden (GER)*, 2012

6. L. López-Conesa, J.M. Rebled, S. Estradé, K. Boulahya, J.M. González-Calbet, M.D. Braida, G. Dezanneau, and F. Peiró. Local structure study of rare earth niobates (RE3NbO7, RE=Y,Er,Yb,Lu) for proton conduction applications. In *EMRS Spring Meeting, Strasbourg (FRA)*, 2012

7. J. López-Vidrier, J. Samà, S. Hernández, M. Canino, M. Allegrezza, M. Bellettato, M. Schnabel, P. Löper, L. López-Conesa, S. Estradé, F. Peiró, S. Janz, C. Summonte, and B. Garrido. Structural, optical and electrical properties of silicon nanocrystals embedded in ´$Si_xC_{(1-x)}$/SiC multilayer systems for photovoltaic applications. In *EMRS Spring Meeting, Strasbourg (FRA)*, 2012

8. A. Eljarrat, L. López-Conesa, Z. Gacevic, S. Fernández-Garrido, E. Calleja, C. Magén, S. Estradé, and F. Peiró. EELS-HAADF spectrum imaging for characterization of (AlGa)N multilayer heterostructures. In *The 13th edition of Trends in Nanotechnology International Conference (TNT2012), Madrid (SPA)*, 2012

9. S. Estrade, J.M. Rebled, L. Yedra, A. Eljarrat, L. López-Conesa, and F. Peiró. Advanced transmission electron microscopy solutions for nanoscience problems. In *36th International Conference and Exposition on Advanced Ceramics and Composites (ICACC), Daytona Beach (USA)*, 2012

10. A. Eljarrat, L. López-Conesa, Z. Gazevic, S. Fernández-Garrido, E. Calleja, C. Magén, S. Estradé, and F. Peiró. Plasmon mapping for the analysis of III-V nitride distributed Bragg reflectors. In *Microscopy at the Frontiers of Science, Tarragona (SPA)*, 2013

11. LL. Yedra, A. Eljarrat, J.M. Rebled, L. López-Conesa, S. Estradé, and F. Peiró. EELS tomography: from spectrum images to spectrum volume. In *2nd Conference on Frontiers Of Aberration Corrected Electron Microscopy, Kaastel Vaalsbroek (NLD)*, 2013

12. L. López-Conesa, A. Eljarrat, J.M. Ramírez, Y. Berencén, j. López-Vidrier, S. Hernández, C. Magén, B. Garrido, S. Estradé, and F. Peiró. Si-based photonic and photovoltaic devices: a low-loss EELS analysis. In *Microscopy at the Frontiers of Science, Tarragona (SPA)*, 2013

13. R. Fiz, F. Hernández-Ramírez, T. Fischer, L. López-Conesa, S. Estradé, Peiró F., and S. Mathur. Nb_2O_5 nanorods and

SnO_2/Nb_2O_5 heterostructures as humidity sensors. In *37th International Conference and Expo on Advanced Ceramics and Composites, Daytona Beach (USA)*, 2013

14. A. Eljarrat, L. López-Conesa, Z. Gacevic, S. Fernández-Garrido, E. Calleja, C. Magén, S. Estradé, and F. Peiró. Electron Energy Loss Spectroscopy for the analysis of AlN/GaN distributed Bragg Reflectors. In *Microscopy of Semiconducting Materials, Oxford (UK)*, 2013

15. L. López-Conesa, A. Eljarrat, J.M. Ramírez, Y. Berencén, J. López-Vidrier, S. Hernández, S. Estradé, C. Magén, B. Garrido, and F. Peiró. Si-based electroluminescent and photovoltaic devices: EFTEM-HAADF-EELS characterization. In *Microscopy of Semiconducting Materials, Oxford (UK)*, 2013

16. J.M. Ramírez, Y. Berencén, L. López-Conesa, J.M. Rebled, A. Eljarrat, S. Estradé, F. Peiró, J.M. Fedeli, and B. Garrido. Optimizing Er-doped layer stacks for integrated light emitting devices. In *223rd Electrochemical Society Meeting, Toronto (CAN)*, 2013

17. A. Eljarrat, L. López-Conesa, Z. Gacevic, S. Fernández-Garrido, E. Calleja, C. Magén, S. Estradé, and F. Peiró. Electron Energy Loss Spectroscopy for the analysis of AlN/GaN interfaces in MBE grown distributed Bragg Reflectors. In *17th European Molecular Beam Epitaxy Workshop, Levi (FIN)*, 2013

18. P. Torruella, R. Arenal, Z. Saghi, L. Yedra, A. Eljarrat, L. López-Conesa, F. de la Pena, M. Estrader, G. Salazar-Álvarez, A. López-Ortega, J. Nogués, P.A. Midgley, F. Peiró, and S. Estradé. 3d mapping of oxidation states in heterostructured nanomaterials. In *MRS Fall Meeting, Boston (USA)*, 2014

19. A. Eljarrat, L. López-Conesa, J. López-Vidrier, S. Hernández, S. Estradé, C. Magén, B. Garrido, and F. Peiró. Optoelectronic properties of Si-NCs embedded in a dielectric matrix by low loss EELS. In *MRS Fall Meeting 2014, Boston (USA)*, 2014

20. Ll. Yedra, A. Eljarrat, J.M. Rebled, L. López-Conesa, N. Dix, F. Sánchez, J. Fontcuberta, S. Estradé, and F. Peiró. EELS and tomography: from EELS spectrum images to spectrum volumes. In *International Microscopy Conference, Prague (CZE)*, 2014

21. J. López-Vidrier, P. Löper, M. Schnabel, S. Hernández, M. Canino, L. López-Conesa, S. Estradé, F. Peiró, S. Janz, C. Summonte, and B. Garrido. Membrane cell devices containing silicon nanocrystals in silicon carbide. In *European Photovoltaic Solar Energy Conference, Amsterdam (NLD)*, 2014

22. J. López-Vidrier, S. Hernández, P. Löper, M. Schnabel, M. Canino, M. Allegrezza, L. López-Conesa, S. Estradé, F. Peiró, S. Janz, C. Summonte, and B. Garrido. Substrateless photovoltaic devices containing silicon nanocrystals in SiC. In *SPIE Photonics Europe, Brussels (BEL)*, 2014

23. A. Eljarrat, L. López-Conesa, J. López-Vidrier, S. Hernández, S. Estradé, C. Magén, B. Garrido, and F. Peiró. Phase identification, hyperspectral segmentation and MVA for EELS of Si-NC embedded in dielectric matrices. In *Symposium on Hyperspectral Imaging in Research and Engineering, Sheffield (UK)*, 2014

24. A. Eljarrat, L. López-Conesa, J. López-Vidrier, S. Hernández, S. Estradé, C. Magén, B. Garrido, and F. Peiró. EELS of Si nanocrystals by hyperspectral segmentation and multivariate factorization. In *9e edition des Journées EELS, Roscoff (FRA)*, 2014

25. L. López-Conesa, J.M. Rebled, C. Coll, E. Barrigón, I. Rey-Stolle, S. Estradé, and F. Peiró. Effect of Sb content in the ordering of $(In_{0.5}Ga_{0.5})P$ layers for tandem solar cells. In *Microscopy of Semiconducting Materials, Cambridge (UK)*, 2015

26. A. Eljarrat, L. López-Conesa, J.M. Ramirez, Y. Berencén, S. Hernández, J. López-Vidrier, S. Estradé, C. Magén, B. Garrido, and F. Peiró. Chemical and structural characteriza-

tion of Si-based electroluminescent and photovoltaic devices through HAADF-EELS. In *Journées d'EELS, Aix-les-Bains (FRA)*, 2012

27. A. Eljarrat, L. López-Conesa, Z. Gacevic, S. Fernández-Garrido, E. Calleja, C. Magén, S. Estradé, and F. Peiró. EELS-HAADF combination for characterization of a new AlN/GaN DBRs growth method. In *European Microscopy Congress, Manchester (UK)*, 2012

28. L. López-Conesa, T. Fischer, R. Fiz, S. Mathur, F. Hernández-Ramírez, S. Estradé, and F. Peiró. Structural characterization of Nb_2O_5 nanorods and Nb_2O_5@SnO_2 heterostructures for humidity sensing applications. In *MRS Fall Meeting, Boston (USA)*, 2012

29. A. Eljarrat, L. López-Conesa, C. Magén, N. García-Lepetit, Z. Gacevic, E. Calleja, S. Estradé, and F. Peiró. Valence EELS analysis of multiple InGaN-QW structure for electronic properties. In *10th Spanish Conference on Electron Devices, Aranjuez (SPA)*, 2015

30. P. Torruella, R. Arenal, Z. Saghi, L. Yedra, F. de la Peña, A. Eljarrat, M. Estrader, L. López-Conesa, G. Martín, A. López-Ortega, G. Salazar-Alvarez, J. Nogués, P.A. Midgley, F. Peiró, and Estradé S. Multidimensional EELS: from spectrum image to spectrum volume and beyond. In *Energy Materials Nanotechnology Spain, Donostia (SPA)*, 2015

31. P. Torruella, A. Eljarrat, C. Coll, L. López-Conesa, G. Martín, M. Vila, C Díaz-Guerra, J. Piqueras, S. Estradé, and F. Peiró. Energy Loss Spectroscopy of Bi_2O_3. In *Microscopy at the Frontiers of Science, Porto (POR)*, 2015

32. P. Torruella, R. Arenal, Z. Saghi, L. Yedra, F. de la Peña, A. Eljarrat, M. Estrader, L. López-Conesa, G. Martín, A. López-Ortega, G. Salazar-Alvarez, J. Nogués, P.A. Midgley, F. Peiró, and Estradé S. Accessing the chemical and optoelectronic properties of nanostructures in 3D: The EELS spectrum volume. In *Energy Materials Nanotecnology Open Acces Week, Cheng du (CHN)*, 2015

33. O. Blázquez, J.M. Ramírez, J. López-Vidrier, M. Busquets-Masó, L. López-Conesa, S. Hernández, S. Estradé, Peiró F., and B. Garrido. Luminescence of Al^{3+} and Tb^{3+} delta-doped silicon oxide thin films fabricated by electron beam evaporation. In *EMRS Spring Meeting, Lille (FRA)*, 2015

34. A. Eljarrat, L. López-Conesa, J. López-Vidrier, S. Hernández, S. Estradé, C. Magén, B. Garrido, and F. Peiró. Optoelectronic properties of Si-nanocrystals embedded in a dielectric matrix by low-loss EELS. In *EMRS Spring Meeting, Lille (FRA)*, 2015

35. L. López-Conesa, A. Eljarrat, J.M. Rebled, A. Ruiz-Caridad, G. Dezanneau, A. Torres-Pardo, L. Ruiz-González, J.M. González-Calbet, S. Estradé, and F. Peiró. Structural, chemical and dielectric characterization of the uniaxial relaxor SBN ($Sr_{0.67}Ba_{0.33}Nb_2O_6$). In *Microscopy at the Frontiers of Science, Porto (POR)*, 2015

Languages

Spanish and Catalan native level.

English spoken (well), read (well) and written (well). Proficient use of the language in a professional context.

French spoken (well), read (well) and written (sufficient).